Superconducting flux circuits for coherent quantum annealing

by

Xi Dai

A thesis
presented to the University of Waterloo
in fulfillment of the
thesis requirement for the degree of
Doctor of Philosophy
in
Physics - Quantum Information

Waterloo, Ontario, Canada, 2023

Examining Committee Membership

The following served on the Examining Committee for this thesis. The decision of the Examining Committee is by majority vote.

External Examiner:	Yasunobu Nakamura Professor, Dept. of Applied Physics, The University of Tokyo
Supervisor(s):	Adrian Lupascu Associate Professor, Dept. of Physics and Astronomy, University of Waterloo
Internal Member:	Matteo Mariantoni Associate Professor, Dept. of Physics and Astronomy, University of Waterloo
Internal-External Member:	Achim Kempf Professor, Dept. of Applied Mathematics, University of Waterloo
Other Member(s):	James Martin Associate Professor, Dept. of Physics and Astronomy, University of Waterloo

Author's Declaration

This thesis consists of material all of which I authored or co-authored: see Statement of Contributions included in the thesis. This is a true copy of the thesis, including any required final revisions, as accepted by my examiners.

I understand that my thesis may be made electronically available to the public.

Statement of Contributions

Xi Dai was the sole author of Chapters 1, 2, and 7, which were written under the supervision of Professor Adrian Lupascu, and were not written for publication.

This thesis consists in part of five manuscripts written for publication. All the research work was carried out as part of the Quantum Enhanced Optimization (QEO) program, supported by the Intelligence Advanced Research Projects Activity (IARPA), and the Quantum Annealing Feasibility Study (QAFS) program, supported by the Defense Advanced Research Projects Agency (DARPA). Under these two programs, the fabrication of the devices and experiments were carried out by colleagues and collaborators of Xi Dai, at MIT Lincoln Laboratory. Xi Dai's main role in these experiments is related to developing the experiment concepts, simulating the devices, as well as writing code for the experiments and data analysis. Specific contributions to each chapter are as follows:

Research presented in Chapters 3

This chapter consists of two related research works. This first one is based on the publication:

X. Dai, D. M. Tennant, R. Trappen, A. J. Martinez, D. Melanson, M. A. Yurtalan, Y. Tang, S. Novikov, J. A. Grover, S. M. Disseler, J. I. Basham, R. Das, D. K. Kim, A. J. Melville, B. M. Niedzielski, S. J. Weber, J. L. Yoder, D. A. Lidar, and A. Lupascu, Calibration of Flux Crosstalk in Large-Scale Flux-Tunable Superconducting Quantum Circuits, PRX Quantum 2, 040313 (2021).

The second is based on a preprint written for publication:

X. Dai, R. Trappen, R. Yang, S. M. Disseler, J. I. Basham, J. Gibson, A. J. Melville, B. M. Niedzielski, R. Das, D. K. Kim, J. L. Yoder, S. J. Weber, C. F. Hirjibehedin, D. A. Lidar, and A. Lupascu, Optimizing for periodicity: a model-independent approach to flux crosstalk calibration for superconducting circuits, arXiv:2211.01497.

In the first work, X. D., D. M. T., and A. J. Martinez. developed the experiment concepts. X. D. and A. J. Martinez. wrote the code for data analysis. X. D., D. M. T. wrote the measurement scripts. D. M. T. and R. T. performed the experiments. D. M., M. A. Y., Y. T., and S. N. contributed to the device design. D. M. T., R. T., J. A. G., S. M. D., J. I. B., and S. J. W. contributed to the experiment infrastructure. R. D., D. K. K., A. J. Melville, B. M. N., S. J. W., and J. L. Y. contributed to the device fabrication and packaging. D. L. supervised the QEO program and A. L. supervised the experiment. X. D. wrote the manuscript, with feedback from all co-authors.

In the second work, X. D., R. Y., and A. L. developed the experiment concepts. X. D. wrote the data analysis code and measurement scripts. R.T. performed the experiments. S. M. D., J. I. B., J. G., S. J. W., and C. F. H. contributed to the experiment infrastructure. A. J. Melville, B. M. N., R. D., D. K. K., S. J. W., and J. L. Y. contributed to the device fabrication and packaging. D. L. supervised the QEO program and A. L. supervised the experiment. X. D. wrote the manuscript, with feedback from all co-authors.

Research presented in Chapter 4

This chapter is based on the publication:

D. M. Tennant, X. Dai, A. J. Martinez, R. Trappen, D. Melanson, M. A. Yurtalan, Y. Tang, S. Bedkihal, R. Yang, S. Novikov, J. A. Grover, S. M. Disseler, J. I. Basham, R. Das, D. K. Kim, A. J. Melville, B. M. Niedzielski, S. J. Weber, J. L. Yoder, A. J. Kerman, E. Mozgunov, D. A. Lidar, and A. Lupascu, Demonstration of long-range correlations via susceptibility measurements in a one-dimensional superconducting Josephson spin chain, Npj Quantum Inf 8, 1 (2022).

In this work, D. M. T., A. J. Martinez, and R. T. performed the experiments. D. M. T., X. D., and A. J. Martinez wrote the measurement scripts. D. M. T., X. D., and R. Y. performed the data analysis. D. M. T., X. D., A. J. Martinez., D. M., and Y. T. performed numerical device simulations. A. J. Martinez., D. M., M. A. Y., Y. T., and S. N. designed the device. S. B., A. J. K., and E. M. provided theoretical guidance to the experiment. R. D., D. K. K., A. J. Melville, B. M. N., S. J. W., and J. L. Y. contributed to the device fabrication and packaging. D. L. supervised the QEO program and A. L. supervised the experiment. D. T. wrote the manuscript, with feedback from all co-authors.

Research presented in Chapter 5

This chapter is based on a manuscript written for publication:

R. Trappen, X. Dai, M. A. Yurtalan, D. Melanson, D. M. Tennant, A. J. Martinez, Y. Tang, J. Gibson, J. A. Grover, S. M. Disseler, J. I. Basham, S. Novikov, C. F. Hirjibehedin, K. Serniak, S. J. Weber, J. L. Yoder, W. D. Oliver, K. M. Zick, D. A. Lidar, and A. Lupascu, Decoherence of a tunable capacitively shunted flux qubit, manuscript in preparation.

In this work, R.T. performed the experiments. R.T. and X.D. performed the data analysis. X.D. performed the numerical simulations. D.M., M.A.Y., A.J. Martinez, and Y.T. designed the device. S.N. provided feedback on the device design. D.M.T., J.A.G.,

S.D., and J.B. contributed to the development of the experiment infrastructure. J.L.Y. lead the fabrication of the device. C.H., K.S., and S.J.W. contributed to the fridge and electronics operation. W. D. O., K. M. Z., and D.L. provided leadership and supervision of the QEO/QAFS program and A.L. conceived and supervised this work. All authors were involved in the discussion of experiments and data analysis. R.T. and X.D. wrote the manuscript with feedback from all authors.

Research presented in Chapter 6

This chapter is based on a preprint written for publication: X. Dai, R. Trappen, H. Chen, D. Melanson, M. A. Yurtalan, D. M. Tennant, A. J. Martinez, Y. Tang, E. Mozgunov, J. Gibson, J. A. Grover, S. M. Disseler, J. I. Basham, S. Novikov, R. Das, A. J. Melville, B. M. Niedzielski, C. F. Hirjibehedin, K. Serniak, S. J. Weber, J. L. Yoder, W. D. Oliver, K. M. Zick, D. A. Lidar, and A. Lupascu, Dissipative Landau-Zener tunneling: crossover from weak to strong environment coupling, arXiv:2207.02017.

In this work, R.T. performed the experiments. R.T. and X.D. performed the data analysis. X.D. performed the numerical simulations. H.C. provided guidance on the numerical simulations and theoretical models. D.M., M.A.Y., A.J. Martinez, and Y.T. designed the device. S.N. provided feedback on the device design. E. M. explored alternative explanations of the experimental data. J.G. J.A.G. and X.D. performed earlier versions of the experiments on a different device and setup. D.M.T., J.A.G., S.D., and J.B. contributed to the development of the experiment infrastructure. R.D., A.J.Melville, B.M.N., and J.L.Y. developed the fabrication process and fabricated the device. C.H., K.S., and S.J.W. contributed to the fridge and electronics operation. W.O. supervised the QEO/QAFS effort from Lincoln Laboratory, K.M.Z. led the coordination of the QEO/QAFS experimental effort, D.L. led the QEO/QAFS program and A.L. conceived and supervised this work. All authors were involved in the discussion of experiments and data analysis. X.D., R.T., and A.L. wrote the paper with feedback from all authors.

Abstract

Quantum annealing is a method with the potential to solve hard optimization problems faster than any classical method. In the near term, quantum annealing is particularly appealing due to its low control requirement, relative to gate-based quantum computation. However, despite the fact that large-scale quantum annealers containing more than 5000 qubits have been made commercially available, identifying a quantum advantage for practical problems has remained an elusive target. Amongst other issues, poor coherence is considered the main prohibitive factor for these annealers to take on the quest for quantum advantage.

In this thesis, we make progress in realizing a highly coherent quantum annealer, based on superconducting capacitively-shunted flux qubits (CSFQ). First, we are met with the challenge of crosstalk calibration when implementing individual control of the qubits and couplers in the annealer, which is important for exploring novel annealing protocols. Two different methods, relying on the symmetries of the superconducting circuits, are proposed and successfully implemented to tackle this challenge. Second, we experimentally demonstrate long-range correlation in a chain of couplers, which enables effective coupling of qubits over large distances. The coupler chain could be expanded to a coupler network to support high qubit connectivity, a highly desirable feature when embedding practical-scale optimization problems into the annealer hardware. Finally, we evaluate the noise properties of the CSFQ. Coherence time measurements reveal that the dominant noise in the system is intrinsic flux noise in the two control loops of the qubit. Landau-Zener transition, a toy model for quantum annealing, is investigated in a CSFQ, revealing a crossover from the weak to strong coupling to the environment. This crossover regime was not studied before in either theory or experiment, and we present a phenomenological spin bath model to elucidate this regime.

Acknowledgements

This thesis is the result of close to five years of exciting and challenging Ph.D. work, which would not have been possible without the support of many people, who I would like to acknowledge here.

Firstly I would like to thank my supervisor Adrian Lupascu for giving me the chance to pursue a Ph.D. at the Superconducting Quantum Devices (SQD) lab at IQC. He taught me everything I knew about superconducting circuits and how to conduct rigorous research. I am grateful to him for all the encouragement when research is not going well and all the challenging questions which pushed me to think harder about my work.

Secondly, I would like to thank Prof. Achim Kempf, Prof. James Martin, and Prof. Matteo Mariantoni for serving on my Ph.D. committee. The committee meetings allowed me to see my research from a broader perspective and constantly motivate me. I would like to express my gratitude to Prof. Yasunobu Nakamaru for agreeing to serve as the external examiner for my thesis. It is a great honor to have one of the pioneers in the field on my defense committee.

I am also grateful to colleagues who kindly provided feedback on the thesis draft, Lucas, Chi, and Rui.

All the work presented in this thesis is carried out as part of the Quantum Enhanced Optimization (QEO) program, supported by Intelligence Advanced Research Projects Activity (IARPA) [1]. I am fortunate to have worked with many amazing scientists in the program. First I would like to thank members of the SQD QEO team. Antonio and Denis, although we only worked together for less than 2 years, I want to let you know that all the work you have documented continues to be a great source of reference. It just feels surreal that whenever I have a question about a design, I can almost certainly find some simulation you have done that answers my question. I would also like to thank Antonio for the peer-coding sessions during the crosstalk calibration project. I learned a lot from you. Daniel and Robbyn, I am grateful to have worked closely with you on all the experiments. Without your hard work in Lincoln lab, all the achievements presented in this thesis wouldn't be possible. I am also thankful to previous members of the SQD QEO team, Ali, Yongchao, Rui, Salil, and Mehmet for all the stimulating discussions.

QEO has a large consortium of collaborators and I benefited a lot from their work and the frequent interactions. I would like to thank especially James, Steve, and Jeff. Your

[1] QEO later becomes the quantum annealing feasibility study, QAFS, supported by Defense Advanced Research Projects Agency (DARPA)

dedication to doing great science despite a tight program timeline is a constant source of inspiration for me. Thank you for setting up a rigorous experimental code repository and allowing us to build upon it. I learned a great deal from you all in the code reviews. I am also grateful to have interacted with the many brilliant theorists in the program, Jamie, David, and Daniel Lidar. I especially thank Jamie for answering numerous questions I had about circuit quantization. David, I am always impressed by the way you introduce new theoretical perspectives into the experiments and the way you bring up NBA updates after an intense meeting. These two things must be related. I am fortunate to have worked with students and post-docs from Prof. Daniel Lidar's group, Huo Chen, Jenia, and Mostafa. Thank you for sharing your in-depth understanding of open quantum systems and superconducting circuit modeling. I would like to thank everyone who has presented during the weekly QEO telecon, these talks have always been very inspiring. Finally, I would like to thank Prof. Daniel Lidar and Dr. Ken Zick for their empowering leadership during the QEO program.

The experimental progress made in this thesis and QEO wouldn't be possible without the people working behind the scenes to fabricate the devices and operate the fridge. For this, I would like to thank all the staff scientists in the MIT Lincoln Laboratory who were involved in the QEO program.

Outside QEO, I am fortunate to have worked with Noah, Lucas, Elena, Shaun, and Adam on the ultrastrong coupling and entanglement harvesting project. This work is not presented in this thesis. I am looking forward to seeing the results coming through. I am also grateful to Michal, Jae, Chi, and Chris for being such nice officemates. I would also like to thank Shlok for helping with the weekly IQC student seminar.

Outside work, I would like to thank the Chinese friends I met at IQC. Zhangdong, Nicky, thank you for sharing all the evening meals and allowing me to show off table tennis skills on the kitchen table. Jiahao, Shuoyuan, Junan, Junjie, I am glad we can share the camping trips, definitely one of the highlights of my life in Canada outside work. Chris, Cheng, Cindy, Guang, and Yingchi, glad to have enjoyed a few homecooked dinners and boardgame evenings together in the last year I am here, I hope we can stay in touch after I leave Canada.

Life outside IQC is made joyful by the companies of many people. I would like to thank in particular Ce Yang, who came to Waterloo together with me from Oxford. I am still amazed by how disciplined you are with work and that you finished your Ph.D. in less than three years! I would also like to thank Ce and Minglei for sharing dinners during quarantine. Working at home doesn't feel all that dreary because of your company. Special thanks go to my landlord, Xiaohui. Thank you for providing a hassle-free living

environment for the last four years, and showing me how to properly work in the kitchen like a diligent housewife/househusband.

Table tennis is an important part of my life outside work. I can't imagine a better table tennis club than MyTableTennis at Waterloo. Thank you Linda and James for offering such a friendly environment to play. It's sad to know that you are moving (and that I can't play for the next two months). I would also like to thank my table tennis buddies, Mung Mung and David Huo for all the training sessions we had together.

Finally, I would like to thank my family. I am forever indebted to my parents and grandparents, you have cultivated the physicist in me and supported me to be where I am now. The last three years have gone by too fast, and I can't wait to spend more time with you. I am grateful to be accompanied by Yijing, my fiancee. Thanks to you, the joy along the journey has doubled and the hardships have become more bearable. For every day in these five years, I am more and more certain that I want to spend the rest of my life together with you.

Dedication

This is dedicated to my grandparents.

论文献给我的婆婆，外婆，和已故的爷爷，外公。

Table of Contents

List of Figures

List of Tables

Chapter 1

Introduction

Quantum mechanics is one of the two paradigm shifts in physics that occurred in the last century, next to relativity. It began as a very much theoretical study to explain black-body radiation, and later helped us to understand a wide range of phenomena in the microscopic world. In the hundred years after its inception, quantum mechanics not only contributed to a large range of advancements in modern physics, but also served as the foundation for the development of semiconductor technologies, paving the way for the information age.

The 21st century holds promise for the second quantum revolution [1]. In the first quantum revolution, novel technologies are developed by understanding and exploiting states of matter existing in nature. In the second quantum revolution, we are growing our capability in manipulating and engineering more and more novel and complex quantum states. The landmark of such developments is celebrated in the 2012 Nobel Prize when Serge Haroche and David J. Wineland were recognized for developing experimental methods to manipulate and measure individual quantum systems [2]. Such capabilities promise to revolutionize several technological frontiers, in cryptography and secure communication [3], sensing and metrology [4], as well as computation [5], which is what this thesis focuses on.

It is widely believed that quantum computers will be able to solve certain problems more efficiently than classical computers. To a large extent, this is motivated by the insight, first due to Feynman, that classical simulation of quantum systems requires exponential run time and memory [6]. Later on, the power of quantum computers becomes widely appreciated when a few quantum algorithms were discovered that outperform the best classical algorithms [7, 8, 9, 10, 11](see Ref. [12] for a review), the most famous one being Shor's factoring algorithm [13, 9].

There are two main approaches to quantum computation: the gate-model quantum

computation and adiabatic quantum computation[1]. In gate-model quantum computation (GMQC), first formalized by Deutsch in 1989 [15], computation is carried out by a sequence of discrete quantum gates, much like classical digital computation. In adiabatic quantum computation (AQC) [16], computation is performed by slowly varying the system Hamiltonian from an initial Hamiltonian, with an easily prepared ground state, to a final Hamiltonian, the ground state of which corresponds to the solution of a computational problem. In general, it has been shown that AQC and GMQC can efficiently simulate each other with polynomial resource and time, although a huge overhead is required to simulate GMQC circuits using AQC [17].

The idea of mapping the ground state of a target Hamiltonian to a particular computational problem first arises around the 1990s in the context of solving optimization problems [18, 19, 20]. In analogy to simulated annealing [21], such optimization method that employs a quantum system is what is now known as quantum annealing (QA). In this sense, QA is closely related to AQC, with the distinction being that AQC is usually referring to the more general approach to quantum computation, and QA is more closely related to optimization.

There is a growing effort in the past twenty years to build a quantum computer. Among the various hardware platforms [22, 23, 24, 25, 26], superconducting circuits stand out due to its relative ease of control with commercial microwave electronics, and its fabrication technique built upon conventional nano- and micro-technologies [27, 22]. In the case of GMQC, since the first demonstration of coherent control of a superconducting qubit to more twenty years ago [28], tremendous progress has been made to engineer superconducting circuits that can be controlled and read out with high fidelity. A notable achievement in this field is the demonstration of a quantum speedup in sampling random quantum gate sequences [29].

Superconducting circuits, in particular superconducting flux circuits, are also one of the leading platforms for implementing QA [30]. The flux circuits are essentially superconducting metal loops, with the two relevant states being persistent currents flowing in clockwise and anti-clockwise directions. The persistent current is effectively a large magnetic dipole moment, making flux circuits behave much like spins in an external magnetic field. Thus, superconducting flux circuits are a natural realization of QA, with the target Hamiltonian encoded in the longitudinal fields of each flux circuit and coupling strengths among them. Such circuits have been built by the company DWave, which has commercialized quantum annealers containing as many as 5000 qubits [31]. These large-scale annealers also attracted a growing community of researchers, from both academia and industry, that try

[1]There are others such as measurement-based quantum computation [14]

to understand the power of these engineered quantum machines [30, 32, 33]. However, to this date, it is still an open question regarding whether the DWave quantum annealer can realize quantum advantage in solving commercially relevant problems.

One of the fundamental challenges in building a quantum computer is the balance between decoherence and control. Decoherence is a phenomenon through which a quantum system loses its quantumness as it interacts with the environment around it, which has degrees of freedom we cannot control and keep track of. The time scale over which this happens, the (de)coherence time, is set by how strongly the quantum system interacts with the environment. On the other hand, controlling and reading out the state of the quantum system necessarily requires it to have strong enough interactions among itself and with the control signals. This general tradeoff is relevant in both GMQC and QA. In GMQC, stronger interaction allows faster gates, and hence more gates can be performed within the coherence time of the device. For QA, stronger interaction increases the overall energy scale, reducing the relative control error when solving a particular target Hamiltonian.

This thesis explores superconducting flux circuits for coherent quantum annealing. The large persistent current of the flux circuits enables large tunable coupling which is desirable for QA. However, this large magnetic dipole moment and strong interaction pose challenges in precise control of the circuits and make them couple to noise strongly. Indeed, addressing the challenges in controlling strongly interacting flux circuits and understanding the effects of strong noise are the two main themes of this thesis.

1.1 Thesis outline

This thesis is organized as follows. In Chapter 2, we review the necessary background for this thesis. We begin with an introduction to superconducting circuits in Section 2.1, followed by an introduction to open quantum systems, focusing on different master equations used in the thesis. The last section of this chapter introduces quantum annealing and presents a review of the challenges and possible directions in this field.

Chapter 3 presents two systematic methods we developed to calibrate crosstalk in the flux biasing of superconducting circuits. Their general principles are first introduced, followed by a discussion of the experimental results. The first of the calibration methods are used to enable the demonstration of long-range coupling between two qubits, mediated by a chain of seven couplers, which is the subject of Chapter 4.

Chapters 5 and 6 study decoherence in a single flux qubit. In Chapter 5 we characterize the coherence times of the qubit at various operating points, and the dominant noise

channel. In Chapter 6 we looked at specifically the effect of noise on quantum tunneling, by studying the Landau-Zener transition measurements. The experimental result is compared with numerical open system simulations. Although the master equations failed to capture the full range of data, we present a phenomenological open system model based on a spin bath that captures the underlying physics.

We conclude this thesis in Chapter 7, where we highlight the significance of our work and discuss future directions.

Chapter 2

Background

2.1 Superconducting circuits

Superconductors, despite being macroscopic in nature, feature quantum mechanical properties just like atoms. This is because charge carriers in superconductors are Cooper pairs of electrons, condensed into a single macroscopic state described by a wavefunction [34, 35].. This condensate supports current flow without dissipation, hence electrical circuits made of superconductors in principle do not suffer from decoherence. The physics of superconducting circuits is enriched by the Josephson effect, which describes charge tunneling between two superconductors interrupted by a thin barrier. By combining linear circuit elements such as capacitors and inductors with the non-linear Josephson tunnel junction, complex superconducting circuits can be designed and fabricated, which allows the storage, manipulation, and readout of quantum states, forming the basis of quantum computing [27, 22].

In this section, we review the principles of general superconducting circuits, and then discuss the specific components that make up the annealing processor. We begin this section by introducing in Sec. 2.1.1 the basic building blocks of superconducting circuits, the harmonic oscillator, and the Josephson junction. In Sec. 2.1.2 we discuss the method to derive the Hamiltonian of a general complex superconducting circuit. Section 2.1.3 and 2.1.4 introduce the main type of superconducting qubit used in this thesis, the flux qubit, as well as the method to realize tunable coupling between flux qubits. This is followed by Sec. 2.1.5 which discusses the method used to read out the flux qubit.

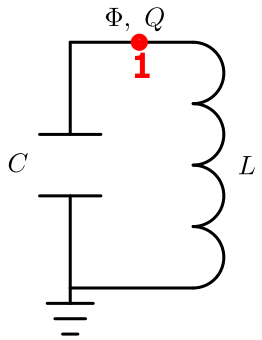

Figure 2.1: A harmonic oscillator circuit made of capacitance C and inductance L. The flux and charge at node 1 are denoted as Φ, Q respectively (see text for explanation).

2.1.1 Elements of superconducting circuits

The harmonic oscillator circuit. Physicists sometimes say that almost anything can be modeled as a harmonic oscillator. Indeed the simplest superconducting quantum circuit is a harmonic oscillator circuit, consisting of an inductance L and a capacitance C, as shown in Fig. 2.1. Its dynamics can be described in terms of the flux at node 1

$$\Phi(t) = \int_{-\infty}^{t} V(t')\mathrm{d}t', \tag{2.1}$$

where $V(t)$ is the node voltage. Applying Kirchhoff's law to the circuit then gives the equation of motion (EOM) for Φ,

$$\ddot{\Phi}C + \frac{\Phi}{L} = 0, \tag{2.2}$$

where the dot indicates the time derivative. This resembles the EOM of a mass attached to the end of a spring, where Φ is the displacement, and C and L play the role of mass and inverse spring constant. The above equation of motion corresponds to the Euler-Lagrange equations of motion for the Lagrangian

$$\mathcal{L}_{\mathrm{LC}} = \frac{\dot{\Phi}^2 C}{2} - \frac{\Phi^2}{2L}. \tag{2.3}$$

Performing the Legendre transformation leads to the Hamiltonian

$$H_{\mathrm{LC}} = \frac{Q^2}{2C} + \frac{\Phi^2}{2L}, \tag{2.4}$$

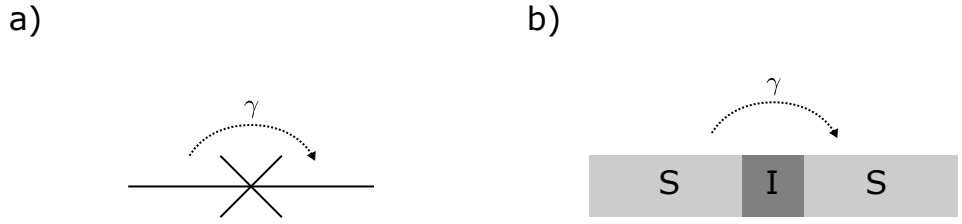

Figure 2.2: (a) The circuit symbol corresponding to an ideal Josephson junction is a cross. (b) The Josephson junction is usually made up of two pieces of superconductors, linked by a thin insulating barrier. Its properties are described in terms of the phase difference between the superconducting wavefunctions on either side of the barrier, denoted as γ.

where Q is the conjugate momentum $Q = \partial\mathcal{L}_{\mathrm{LC}}/\partial\dot{\Phi}$, which for the harmonic oscillator circuit is the charge stored in node 1.

To quantize the above Hamiltonian, one raises the variables Q, Φ to operators $\hat{Q}, \hat{\Phi}$ and identifies the canonical commutation relation

$$[\hat{\Phi}, \hat{Q}] = i\hbar, \tag{2.5}$$

where $\hbar$ is the reduced Planck's constant.

The Josephson Junction. The harmonic oscillator itself cannot be used as a qubit because it is made of linear circuit elements and has degenerate level spacing. To obtain non-degeneracy (or anharmonicity), a non-linear circuit element is required. The Josephson junction is such a non-dissipative, non-linear circuit element, first predicted by B. D. Josephson [36]. It is usually made up of two pieces of superconducting material, interrupted by a thin layer of insulator, as shown in Fig. 2.2. The current through and voltage across an ideal Josephson junction are given by the Josephson relations

$$I_j = I_c \sin\gamma \text{ and} \tag{2.6}$$
$$V_j = \phi_0\dot{\gamma}, \tag{2.7}$$

where I_c is the critical current of the junction, γ is the phase difference between the wavefunctions of the two superconductors, and $\phi_0 = \hbar/(2e)$ is the reduced flux quantum. The Josephson junction is often seen as a non-linear inductance, with Josephson inductance $L_j(\gamma)$ given by

$$\frac{1}{L_j} = \frac{1}{\phi_0}\frac{\mathrm{d}I}{\mathrm{d}\gamma} = \frac{I_c\cos\gamma}{\phi_0}. \tag{2.8}$$

It is also useful to introduce the Josephson energy

$$\int I_j V_j \mathrm{d}t = \int I_c \sin\gamma \phi_0 \mathrm{d}\gamma = -E_j \cos\gamma, \tag{2.9}$$

where $E_j = I_c \phi_0$ is the characteristic Josephson energy.

Before proceeding, it needs to be pointed out that there is a close relationship between the magnetic flux and the superconducting phase. Comparing Eq. 2.7 to Faraday's law across a linear inductor shows that the junction phase difference γ acts analogously a flux across the junction, with a proportionality constant ϕ_0. This can be more rigorously proven by introducing the gauge-invariant superconducting phase[1]. Therefore, we introduce the dimensionless flux variable, $\hat{\varphi} = \hat{\Phi}/\phi_0$, which can be seen as a generalized flux across either a linear or non-linear inductor. Combined with the fact that the superconducting currents are carried by Cooper pairs, the commutation relation in Eq. 2.5 is reintroduced using dimensionless quantities

$$[\hat{\varphi}, \hat{n}] = i, \tag{2.10}$$

where $\hat{n} = \hat{Q}/(2e)$ is the Cooper pair number, with e being the electron charge.

2.1.2 Circuit quantization

One of the first steps in modeling a superconducting circuit for quantum computation is to find the system Hamiltonian. The procedure to derive the Hamiltonian of a circuit is commonly known as circuit quantization. Various methods exist to achieve this, such as the method of nodes [38, 39, 40], the black-box quantization method[41] and the energy participation ratio method [42]. In this section, we review the method of nodes to quantize a generic circuit, consisting of inductors, capacitors, and junctions. This is the primary method used in this thesis, and it is valid given that the circuit elements are much smaller than the relevant wavelength, so they can be treated as lumped elements.

The starting point of circuit quantization through the method of nodes is to recognize that a circuit can be described by a graph $\mathcal{G}(\mathcal{N}, \mathcal{E})$, where the edges are the circuit elements such as capacitors, inductors, and Josephson junctions. Each node is associated with a generalized flux coordinate, defined similarly to Eq. 2.1, by the time integral of the node voltage relative to the ground node. The coordinates can be collected as a vector $\vec{\varphi}_N$ with dimension N_N, where N_N is the number of active nodes in the circuit (nodes

[1] See for example chpt.3.5 of Ref. [37]

except ground). Naively the potential or kinetic energy can be found by writing the energies stored in the inductors(junctions) or capacitors in terms of the difference of the superconducting phases of the two nodes connected by the element, or its time derivative. However superconducting circuits obey the fundamental relation that the total flux threading an enclosed loop, including external flux bias has to be quantized [43, 44]. To account for this condition algorithmically, we use the concept of spanning trees and closure branches. The spanning tree $\mathcal{S}$ for a graph is made of a set of edges such that there is a unique path joining every node to every other node through edges in $\mathcal{S}$. The remaining edges make the closure branches $\mathcal{C} = \mathcal{E} - \mathcal{S}$. The choice of spanning tree is not unique, as this choice corresponds to gauge choice in electromagnetism, and does not affect the underlying physics. Following [40], the convention we adopt here is that an inductive-like element (inductors or Josephson junctions) is always preferred to capacitors when choosing the spanning tree element between any two nodes, and a capacitor is chosen only when there is no inductive-like element between two nodes. This way, for each of the remaining inductive-like elements, which is not in the tree, there is an associated fundamental loop in the circuit. We collect these inductive-like elements not in the tree into a set $\mathcal{L} \in \mathcal{C}$. The external flux can then be conveniently assigned to each inductive-like element in $\mathcal{L}$. This allows us to write the phase difference across an edge $e_{k,l,m}$, connecting node k, l as

$$\varphi_{k,l,m} = \begin{cases} \varphi_k - \varphi_l - 2\pi f_{k,l,m}, & \text{if } e_{k,l,m} \in \mathcal{L} \\ \varphi_k - \varphi_l, & \text{otherwise} \end{cases}, \tag{2.11}$$

where m denotes for the m'th edge between nodes k, l. The external flux bias for a loop, normalized by the flux quantum $\Phi_0 = 2\pi\phi_0$, is assigned to the corresponding edge as $f_{k,l,m}$. The next step is to write down the kinetic and potential energy in the Lagrangian. The kinetic energy T_L is given by the sum of capacitive energies in the circuit, which can be succinctly given by

$$T_L = \frac{\phi_0^2}{2} \dot{\vec{\varphi}}_N^T \mathbf{C} \dot{\vec{\varphi}}_N, \tag{2.12}$$

where $\mathbf{C}$ is the so-called Maxwell node capacitance matrix, with dimension $N_N \times N_N$. Its off-diagonal elements are given by the negative of the capacitance connecting two nodes, and each diagonal element is given by the sum of capacitances connecting to a node, including capacitances to ground.

The potential energy is a sum of the inductive energy and Josephson energy in the

circuit. They are respectively

$$U_{\text{ind}} = \sum_{e_{k,l,m}} \phi_0^2 \frac{\varphi_{k,l,m}^2}{2L_{k,l,m}} \tag{2.13}$$

$$U_{\text{jos}} = -\sum_{e_{k,l,m}} E_{j,k,l,m} \cos \varphi_{k,l,m}, \tag{2.14}$$

where $E_{j,k,l,m}, L_{k,l,m}$ are the Josephson energy and inductance of the edge k, l, m. The sums are understood to run over all the inductances and Josephson junctions in the circuit, respectively.

Having found the Lagrangian, we next perform the Legendre transform and define the conjugate momentum of the i'th node coordinate as

$$p_{N,i} = \frac{\partial \mathcal{L}}{\partial \dot{\varphi}_i}. \tag{2.15}$$

The kinetic energy in the Hamiltonian is given by

$$T_H = \vec{p_N} \dot{\vec{\varphi}}_N - T_L \tag{2.16}$$

$$= \frac{1}{2\phi_0^2} \vec{p}_N^T \mathbf{C}_N^{-1} \vec{p}_N. \tag{2.17}$$

Combining the kinetic and potential energy together, we have the circuit Hamiltonian

$$H = T_H + U_{\text{ind}} + U_{\text{jos}}, \tag{2.18}$$

from which the properties of the circuit, such as transition frequencies and operator matrix elements can be extracted. In practice, choosing the appropriate basis to numerically represent the above Hamiltonian is challenging. Since this is fairly technical, we defer this discussion to Appendix. A, which also includes an example superconducting circuit to be quantized.

2.1.3 The flux qubit

Qubits are the fundamental building block for quantum computing. Various types of qubits can be realized with superconducting circuits [27, 22]. The flux qubit in particular is a class of superconducting circuits with states characterized by persistent current flowing in a superconducting loop, interrupted by Josephson junctions. As we will see in this and

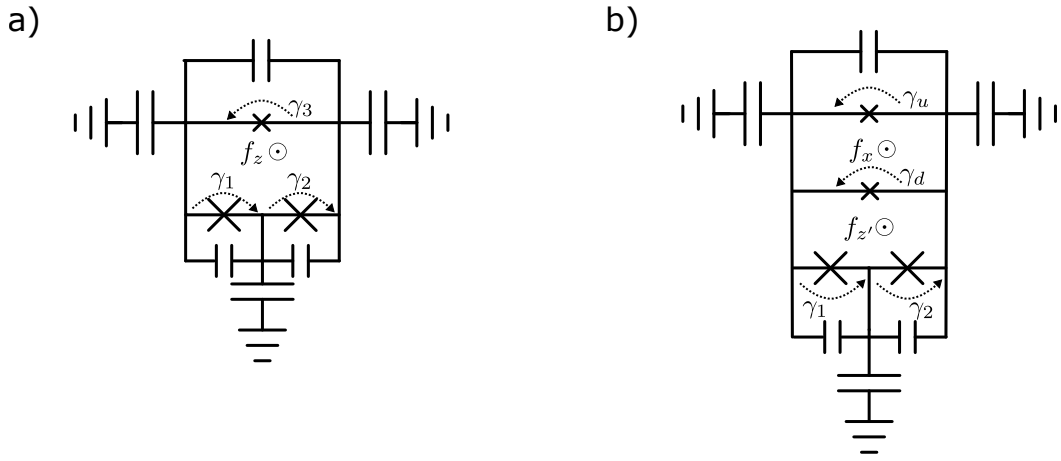

Figure 2.3: Circuit schematic of the (a) fixed-gap (three-junction) and (b) tunable-gap (four-junction) persistent current qubits.

the next subsection, coupled flux qubits emulate coupled spins under external magnetic fields, which makes it a natural platform to build a programmable quantum annealer. Our qubit design derives from the persistent current qubit [45, 46]. As shown in Fig. 2.3(a), it consists of a superconducting loop interrupted by three Josephson junctions, with two of them being identical in principle and the third one is smaller and often called the α junction. The flux quantization condition in the qubit loop leads to

$$\gamma_1 + \gamma_2 + \gamma_3 = -2\pi f_z, \tag{2.19}$$

where $f_z = \Phi_z/\Phi_0$ is the reduced flux bias in the qubit loop, $\gamma_{1,2}$ are the phase difference across the two larger junctions and γ_3 is the phase difference across the smaller α junction. Using the flux quantization condition to eliminate γ_3, the potential energy of the circuit is given as

$$U_{\rm fq} = -\sum_{i=1,2} E_{Ji} \cos\gamma_{1,2} - E_{J\alpha} \cos\left(\gamma_1 + \gamma_2 + 2\pi f_z\right) \tag{2.20}$$

$$= -2E_J \cos\varphi_m \cos\varphi_p - \alpha E_J \cos\left(2\pi f_z + 2\varphi_p\right) \tag{2.21}$$

where in the second line we have introduced $E_J = E_{J1} = E_{J2}$ assuming symmetry and $E_{J\alpha} = \alpha E_J$ and $\varphi_{p(m)} = (\varphi_1 \pm \varphi_2)/2$. The potential landscape for different values of the flux bias near $f_z = 0.5$ is shown in Fig. 2.4. The new coordinates $\varphi_{p(m)}$ are analogous to in(out of) phase oscillation normal modes of two coupled harmonic oscillators. Near the flux bias symmetry point and assuming low enough energy, the φ_m coordinate can be

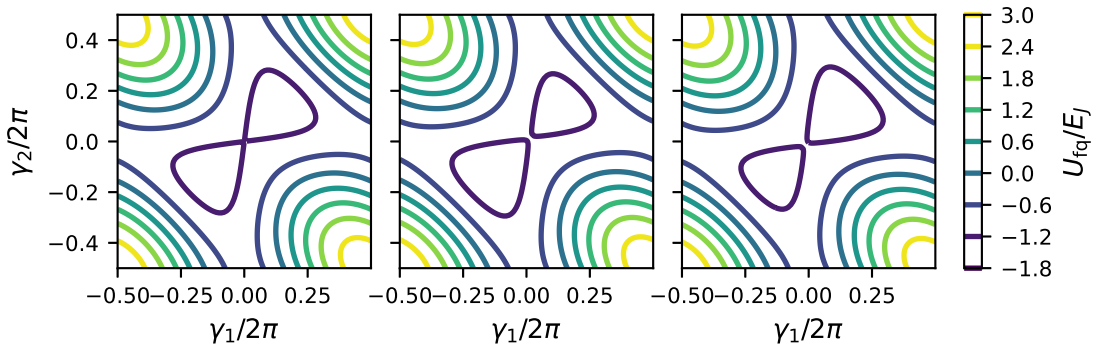

Figure 2.4: Contour plots of the potential energy $U_{\rm fq}$ of the three junction flux qubit with $\alpha = 0.8$, at different flux bias points, as a function of the phase difference across the two larger junctions, γ_1 and γ_2. From left to right they correspond to $f_z = 0.5, 0.49, 0.51$.

seen as almost fixed at $\varphi_m = 0$. The potential energy along φ_p is effectively a double-well potential, as illustrated in Fig. 2.5(a), with each well corresponding to persistent current flowing clock-wise and counter-clockwise in the qubit loops.

The capacitances in the circuit lead to the kinetic energy. It can be written in terms of conjugate variables to the $\varphi_\pm$ coordinates, following the method presented in Appendix A. This kinetic energy induces tunneling between the two wells. Assuming low enough energy so that only the lowest state of each well can be occupied, the flux qubit Hamiltonian can be well-approximated using the two-level system Hamiltonian

$$H_{fq}^{\rm TLS} = \frac{-\epsilon}{2}\sigma_z - \frac{\Delta}{2}\sigma_x, \tag{2.22}$$

$$\epsilon = 2I_p\Phi_0(f_z - 0.5) \tag{2.23}$$

where σ_α is the Pauli matrix in the persistent current basis, I_p is the persistent current. The tunneling amplitude is given by Δ, which is also known as the qubit gap, as it is the minimum qubit frequency obtained when the flux bias is at the symmetry point, $f_z = 0.5$ (see Fig. 2.5(b)). The tunneling amplitude Δ can be estimated analytically using the WKB (Wentzel-Kramers-Brillouin) approximation [47, 45]. More generally, the parameters I_p and Δ can be obtained by numerically. A simple method is to diagonalize the circuit Hamiltonian while sweeping f_z. The resultant transition frequency between the two lowest states can be fitted to the analytical two-level transition frequency expression,

$$\omega_{01}^{\rm TLS} = \sqrt{\Delta^2 + 2I_p\Phi_0(f - 0.5)}. \tag{2.24}$$

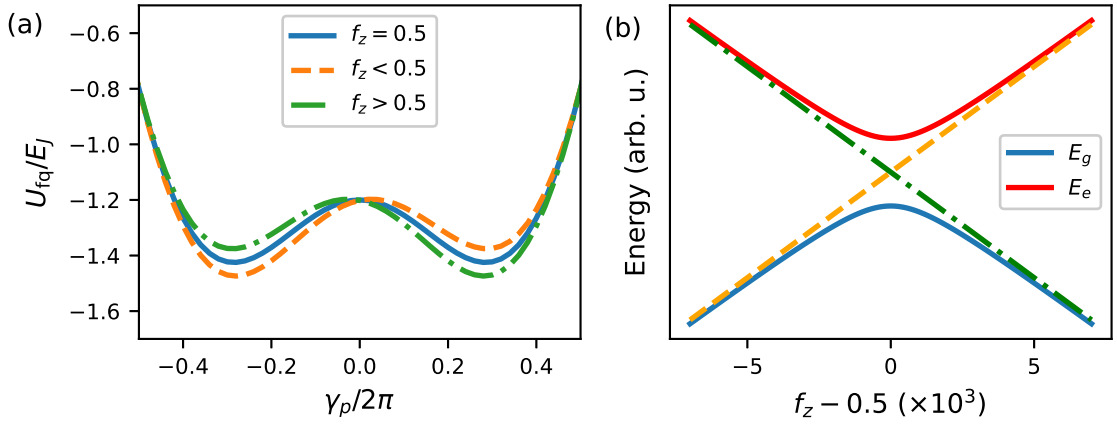

Figure 2.5: (a) Potential energy of the three junction flux qubit versus φ_p, assuming $\varphi_m = 0$ for different flux bias conditions. (b) Schematic of the energies of the ground and first excited state of the flux qubit as a function of flux bias f_z. The yellow dashed lines and blue dot-dashed lines indicate energies of the persistent current states $|L\rangle$ and $|R\rangle$ respectively.

The fitting results give the persistent current I_p and the minimum qubit gap Δ.

The qubit gap can be made tunable by replacing the α junction with a DC-SQUID, as illustrated in Fig. 2.3(b). For a symmetric DC-SQUID, each with Josephson energy βE_J, the potential energy of the tunable flux qubit is

$$U_{\text{tfq}} = -\sum_{i=1,2} E_J \cos\gamma_i - \beta E_J \cos\left(\gamma_1 + \gamma_2 + 2\pi f_{z'}\right) - \beta E_J \cos\left(\gamma_1 + \gamma_2 + 2\pi(f_{z'} + f_x)\right) \tag{2.25}$$

$$= -2E_J \cos\varphi_p \cos\varphi_m - 2\beta E_J \cos(\pi f_x)\cos(2\pi f_z + 2\varphi_m), \tag{2.26}$$

In the second line, we introduced $f_z = f_{z'} + f_x/2$. Comparing with Eq. 2.21, we see $f_z = 0.5$ is the symmetry point for the four-junction flux qubit, and $2\beta\cos(\pi f_x)$ plays the role of α. With f_x closer to zero, or equivalently with increasing α, the tunneling barrier of the double-well potential increases, which suppresses the tunneling amplitude Δ. The flux tunability of both ϵ and Δ in the two-level system Hamiltonian resembles that of an ideal spin under externally applied transverse and longitudinal fields.

Since the first introduction of the persistent current qubit, different variants of it have been attempted to improve it. Recently, Fei Yan et al [48] demonstrated significantly

improved qubit coherence times and reproducibility, achieved by shunting large capacitors across the α junction. This type of flux qubit is named the capacitively-shunted flux qubit (CSFQ), and our qubit design similarly adopts the capacitive shunt.

Another type of flux qubit that is often considered in the context of quantum annealing is the rf-SQUID qubit [49, 50], which is essentially a superconducting loop interrupted by a Josephson junction. The quadratic potential of the geometric inductance of the loop, added to the cosine potential of the junction leads to a double-well potential analogous to the persistent current qubit. The double-well potential only occurs when $\beta = I_c L/\phi_0 > 1$. Therefore, one disadvantage of the rf-SQUID qubit as compared to the persistent current qubit, is that a significant critical current I_c and/or inductance is required for the two-state approximation to be valid, whereas in the persistent current qubit, this large effective inductance is achieved through the Josephson inductances of the two large junctions. This means that the rf-SQUID qubit will likely be more sensitive to noise, due to larger I_p, or experiences more noise due to the larger size of the superconducting loop. A more recent variant of the rf-SQUID qubit is the fluxonium, where the large inductance is replaced by a super-inductance, typically realized by a long chain of Josephson junctions [51]. The fluxonium has one of the highest coherence times reported for a superconducting qubit [52]. Exploring the possibility of a fluxonium-based quantum annealer would be an interesting future work.

The flux basis definition. As discussed above, the two-level Hamiltonian parameters can be obtained by fitting the transition frequency between the lowest two levels in the flux qubit circuit model. However, this procedure does not provide any information about the basis in which the two-level system is defined. This basis definition becomes particularly important when considering interacting flux qubits. This section outlines an unambiguous method to reduce the flux circuit to its two-state description.

We first note that for any two-level system, its Hamiltonian can always be written as

$$H = \sum_{\alpha=\{x,y,z,I\}} h_\alpha \sigma_\alpha. \tag{2.27}$$

Then the computational basis is chosen such that the persistent current operator is diagonal in this basis. Formally we first look for a 2×2 unitary transformation V_1 such that,

$$V_1 \begin{pmatrix} \langle g|\partial_{f_z} H^{\text{circ}}|g\rangle & \langle g|\partial_{f_z} H^{\text{circ}}|e\rangle \\ \langle e|\partial_{f_z} H^{\text{circ}}|g\rangle & \langle e|\partial_{f_z} H^{\text{circ}}|e\rangle \end{pmatrix} V_1^\dagger = \begin{pmatrix} \langle L'|\partial_{f_z} H^{\text{circ}}|L'\rangle & 0 \\ 0 & \langle R'|\partial_{f_z} H^{\text{circ}}|R'\rangle \end{pmatrix}, \tag{2.28}$$

where $|g\rangle, |e\rangle$ are the ground and first excited state vectors found by diagonalizing the circuit Hamiltonian H^{circ}. The two states $|L'\rangle, |R'\rangle$ are distinguished by imposing the condition $\langle L'|\partial_{f_z} H^{\text{circ}}|L'\rangle < 0$ and $\langle R'|\partial_{f_z} H^{\text{circ}}|R'\rangle \geq 0$. Then we introduce two additional constraints following conventions for flux qubits:

- α_y is always zero;
- α_x is always positive.

They are realized by defining a unitary

$$V_2 = \begin{pmatrix} 1 & 0 \\ 0 & \exp(i\phi) \end{pmatrix}, \tag{2.29}$$

where $\phi = \arg[\langle R'|H^{\text{circ}}|L'\rangle]$. Combining things, the computational (persistent current) basis states $|L\rangle$ and $|R\rangle$ are given by

$$\begin{pmatrix} |L\rangle \\ |R\rangle \end{pmatrix} = V_2 V_1 \begin{pmatrix} |g\rangle \\ |e\rangle \end{pmatrix}. \tag{2.30}$$

We note that $|L\rangle, |R\rangle, |g\rangle, |e\rangle$ are state vectors in the Hilbert space of the flux qubit circuit.

2.1.4 The rf-SQUID coupler

Realizing tunable coupling between qubits is necessary for both gate-based quantum computing and programmable quantum annealing. For superconducting flux qubits, coupling is usually achieved by forming mutual inductances between the qubits' z-loops, due to the flux generated by each qubit's persistent current. Tunable mutual inductance can be effectively realized by inserting an intermediate coupler between the qubits, which has flux-tunable susceptibility [53, 54]. A schematic of two three-junction flux qubits coupled by an rf-SQUID coupler is depicted in Fig. 2.6. In this subsection, we review the working principle of the rf-SQUID coupler, which is used in this thesis.

The susceptibility picture. The rf-SQUID coupler has potential energy

$$U_{\text{co}}(\varphi_J) = -I_c^{\text{co}} \phi_0 \cos(\varphi_J) + \frac{\phi_0^2}{2L^{\text{co}}} (\varphi_J - 2\pi f_{cz})^2, \tag{2.31}$$

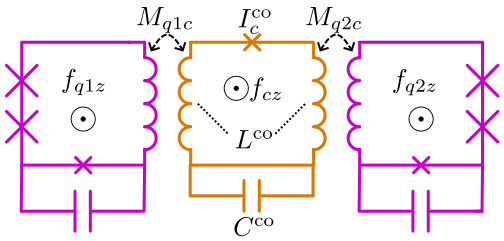

Figure 2.6: Two flux qubits coupled by an rf-SQUID coupler.

where I_c^{co} and L^{co} are the junction critical current and geometric inductance of the SQUID, and f_{cz} is the reduced flux bias applied to the SQUID. When the rf-SQUID has non-linearity parameter $\beta = I_c^{co} L^{co}/\phi_0 < 1$, its potential energy is monostable, with the position of the potential minimum dependent on the external flux bias. As the external bias deviates from the symmetry point, a finite circulating current arises in the coupler loop. Therefore, by inductively coupling the rf-SQUID to two qubits, the rf-SQUID mediates the flux signal of one qubit to another.

Given that the coupler is designed to have a large excitation frequency, it can be assumed, in the spirit of Born-Oppenheimer approximation, that the coupler remains in the ground state throughout any qubit operation. This allows writing the effective interaction between qubits mediated by the coupler as

$$H_{\text{int}} = \chi M_{\text{q1c}} M_{\text{q2c}} I_{p1} I_{p2} \sigma_{z1} \sigma_{z2}, \tag{2.32}$$

where χ is the susceptibility of the rf-SQUID coupler. Further assuming that the qubit flux signal is small and the coupler responds linearly to the qubit flux signal, the susceptibility is given by

$$\chi = \frac{1}{\Phi_0} \frac{\partial I_g}{\partial f_{cz}}, \tag{2.33}$$

with I_g being the ground state current flowing through the coupler loop. In Fig. 2.7, we show the ground state current, as well as the susceptibility for typical parameters of the rf-SQUID coupler.

The susceptibility of the rf-SQUID coupler, and hence the qubit coupling strength can be tuned by adjusting the external flux bias f_{cz} in the coupler. Away from the coupler symmetry point, $f_{cz} = 0.5$, it has a non-zero ground state current and thus induces a finite flux bias to the adjacent qubit. This interdependence of the coupling strength and the qubit flux bias is undesirable as it makes calibrating the system more difficult. To overcome this

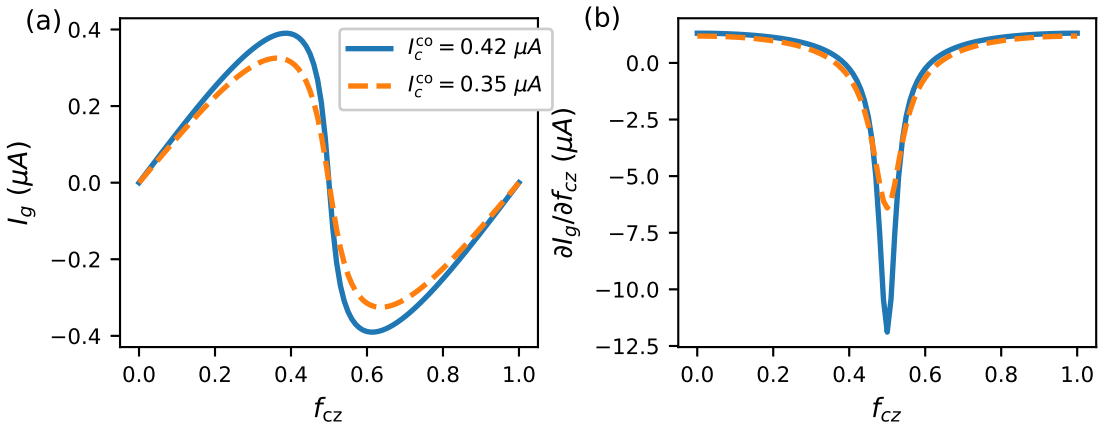

Figure 2.7: The ground state current I_g (a) and the susceptibility of the rf-SQUID coupler as a function of the external flux bias f_{cz}. The parameters used for this coupler is $L^{\text{co}} = 750$ pH, , $C^{\text{co}} = 8.4$ fF

problem, the single-junction can be replaced by a DC-SQUID [55]. The DC-SQUID allows the coupler to be always operated at the symmetry point and achieves tunable susceptibility by tuning the effective critical current of the SQUID. This design minimizes the effective crosstalk from the coupler to the qubit and simplifies calibration [55].

Schrieffer-Wolff transformation for effective interaction. When designing couplers that mediate strong coupling between flux qubits, it is often the case that the susceptibility description, relying on the linear response of the coupler breaks down. In Ref. [56], the authors developed analytical corrections accounting for the non-linearity of the coupler susceptibility when the mediated coupling becomes strong. In our work, to compute the coupling strength, we follow a numerical approach based on the Shrieffer-Wolff transformation (SWT), developed in Refs [57, 58]. As compared to the analytical corrections developed in Ref. [56], although computationally more expensive, the SWT-based approach is a more general method for finding low-energy effective Hamiltonian of the subsystem of interest, and hence more easily accounts for effects such as the renormalization of qubit energy due to coupling and non-ZZ type interactions. Here we outline the procedure to find the low-energy effective Hamiltonian of two qubits coupled by a coupler, using the SWT.

First, we consider the total system Hamiltonian without and with the interaction terms,

in the basis of the circuits. They are given by

$$H_0 = \sum_\alpha \overline{H}_\alpha, \tag{2.34}$$

$$H_{\text{full}} = H_0 + H_{\text{int}}. \tag{2.35}$$

In the expressions above α is an index denoting the subcircuit (either qubit circuit or coupler circuit), and the overline indicates we consider the loading effect in H_0[2]. Then we define the qubit space projection operators, for the non-interacting and interacting circuits respectively,

$$P_0 = \sum_{i=0}^{2^N-1} |E_i^0\rangle\langle E_i^0| \tag{2.36}$$

$$P = \sum_{i=0}^{2^N-1} |E_i\rangle\langle E_i|, \tag{2.37}$$

where the eigenstates $|E_i^0\rangle$ and $|E_i\rangle$ are found by diagonalizing H_0 and H_{full} respectively. These are the lowest 2^N states, which are the qubit-like excitations in a circuit containing N qubit circuit. Then the SWT matrix is defined as

$$U_{\text{SW}} = \sqrt{(2P_0 - I)(2P - I)}, \tag{2.38}$$

and the effective Hamiltonian is

$$H_{\text{eff}} = P_0 U_{\text{SW}} H_{\text{full}} U_{\text{SW}}^\dagger P_0. \tag{2.39}$$

Finally, the effective Hamiltonian can be decomposed into multi-qubit Pauli operators, with coefficients,

$$h_{\vec{\alpha}} = \frac{1}{2^N}\text{Tr}(H_{\text{eff}} \cdot S_{\vec{\alpha}}), \tag{2.40}$$

where $S_{\vec{\alpha}} = \sigma_{\alpha_1}^1 \otimes \sigma_{\alpha_2}^2 \otimes \cdots \otimes P_c$. The operator $\sigma_{\alpha_i}^i$ is a Pauli operator of the i'th qubit circuit, expressed in the circuit Hamiltonian basis, and P_c is a projection operator which projects all coupler circuits into the ground state of the non-interacting, but loaded couplers.

[2]Loading refers to the change of the effective inductance(capacitance) of a subcircuit when it is inductively(capacitively) coupled to another subcircuit. See also Appendix A for details of the loading effect

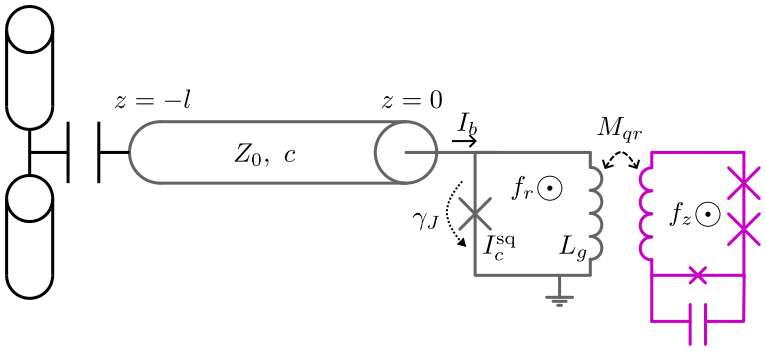

Figure 2.8: Schematic of the readout circuit. The flux-sensitive resonator (grey) is coupled to a flux qubit (purple) on the one end and an open transmission line (black) on the other

2.1.5 Readout of the flux qubit

Reading out the qubit state is a necessary process for any form of quantum computation and various ways exist to read out the flux qubit. Early methods rely on measuring the magnetic signal generated by the two distinct persistent current states by detecting the switching current of a DC-SQUID [59]. However, such a readout scheme leads to a large number of quasi-particles as the DC-SQUID switches to the voltage state and thus becomes unfavorable as the need for qubit coherence increases. Later schemes usually embed the DC-(or rf-)SQUID as part of a resonant circuit, and rely on the magnetic-field-dependent non-linear SQUID inductance [60, 61, 62]. The resonant circuit can be formed by either shunting the SQUID with a large capacitance or terminating a waveguide resonator with the SQUID. As realizing large on-chip capacitance can be challenging, we adopt the latter method of combining SQUID and waveguide resonator as the readout method used in this thesis. We note that the energy eigenstate of the flux qubit can also be read out by coupling to linear resonators in a standard circuit-QED architecture [63, 64]. However, such a method usually becomes ineffective near $\Delta = 0$, due to the vanishingly small state overlap between two computational states, making them unsuitable for annealing applications. Though it needs to be pointed out that readout with linear resonators is still viable by using a more complex readout protocol, involving higher energy states of the qubit circuit [65].

Next, we present the basic principles of the flux-sensitive resonator readout. This is followed by a method to quantize a waveguide resonator terminated by a SQUID (see Fig. 2.8). As we will see, this quantization procedure facilitates a quantum mechanical treatment of the interaction between the qubit and the tunable resonator.

Qubit state dependent resonance. The SQUID can be first approximated as an ideal linear inductance L_{sq}. For a classical rf-SQUID [66] with bias current I_b, its effective inductance is given by

$$L_{\text{sq}} = \phi_0 \frac{\partial \varphi_J}{\partial I_b}, \tag{2.41}$$

The phase across the junction φ_J can be found by minimizing the classical SQUID potential

$$U_{\text{sq}}(\varphi_J) = -I_c^{\text{sq}} \phi_0 \cos(\varphi_J) + \frac{\phi_0^2}{2L_g} (\varphi_J - 2\pi f_r)^2 - I_b \varphi, \tag{2.42}$$

where I_c^{sq} and L_g are the junction critical current and geometric inductance of the SQUID, and f_r is the reduced flux bias applied to the SQUID.

The next step is to find the resonance frequency for the resonator, which is set by the boundary condition

$$I(z = -l) = 0, V(z = 0) = i\omega L_{\text{sq}} I(z = 0). \tag{2.43}$$

Combined with the telegrapher's equations for the waveguide [67], the $\lambda/4$ resonance can be found by solving the equation

$$\exp\left(\frac{2i\omega_r l}{c}\right) = \frac{i\omega_r L_{\text{sq}} - Z_0}{i\omega_r L_{\text{sq}} + Z_0}, \tag{2.44}$$

where l, c, Z_0 are the waveguide length, phase velocity, and characteristic impedance respectively. By inductively coupling the SQUID to the qubit, the SQUID has a different effective flux bias depending on the qubit's persistent current state and has different effective inductance. Hence the resonator has different resonance frequencies for different qubit states. They can be distinguished by measuring the transmission of a probe tone through the open transmission line coupled to the resonator.

Tunable resonator quantization. A Hamiltonian description of the waveguide and SQUID inductor system can be obtained by first writing the energies stored in the resonator system in terms of forward and backward propagating voltages, and then identifying a transformation that turns the voltages into conjugate variables. First, at the SQUID (inductor) end, the ratio between backward and forward propagating voltage is given by

$$\frac{V^-}{V^+} = \Gamma = \frac{i\omega_r L_{\text{sq}} - Z_0}{i\omega_r L_{\text{sq}} + Z_0}. \tag{2.45}$$

Then the time-dependent voltages and currents on the transmission line at point z is

$$\begin{aligned} V(z,t) &= V^+ \{\exp[i\omega_r(t-z/v)] \\ &\quad +\Gamma \exp[i\omega_r(t+z/c)]\} + \text{c.c.}, \end{aligned} \tag{2.46}$$

$$\begin{aligned} I(z,t) &= i\frac{V^+}{Z_0} \{\exp[i\omega_r(t-z/c)] \\ &\quad -\Gamma \exp[i\omega_r(t+z/v)]\} + \text{c.c.}, \end{aligned} \tag{2.47}$$

where c.c. stands for complex conjugate, added to ensure the voltage and current on the line is real. The total energy stored in the transmission and the inductor is

$$H_\text{r} = \int_{-d}^{0} \left[\frac{c_0}{2}V(z,t)^2 + \frac{1}{2l_0}I(z,t)^2\right] dz + \frac{L_\text{sq}I(0,t)^2}{2},, \tag{2.48}$$

where $c_0 = 1/(cZ_0), l_0 = Z_0/c$ are the characteristic capacitance and inductance of the line. For the $\lambda/4$ resonator, The total energy can be succinctly written in quadratic form

$$H_\text{r} = \begin{pmatrix} \widetilde{V^+} & \widetilde{V^+}^* \end{pmatrix} \begin{pmatrix} 0 & \frac{1}{2}\left(\frac{l}{cZ_0} + \frac{L_\text{sq}}{Z_0^2+L_\text{sq}^2\omega_r^2}\right) \\ \frac{1}{2}\left(\frac{l}{cZ_0} + \frac{L_\text{sq}}{Z_0^2+L_\text{sq}^2\omega_r^2}\right) & 0 \end{pmatrix} \begin{pmatrix} \widetilde{V^+} \\ \widetilde{V^+}^* \end{pmatrix}, \tag{2.49}$$

where we have introduced the dynamical variable $\widetilde{V^+} = V^+\exp(i\omega_r t)$. We then aim to find the variable transformation $q = \kappa\widetilde{V^+} + \kappa^*\widetilde{V^+}^*$ and $p = i\omega_r\kappa\widetilde{V^+} - i\omega_r\kappa^*\widetilde{V^+}^*$, such that

$$H_\text{r} = \begin{pmatrix} q & p \end{pmatrix} \begin{pmatrix} \frac{1}{2}\omega_r^2 & 0 \\ 0 & \frac{1}{2} \end{pmatrix} \begin{pmatrix} q \\ p \end{pmatrix}. \tag{2.50}$$

Applying the transformation to Eq. 2.49 we have

$$H_\text{r} = \begin{pmatrix} q & p \end{pmatrix} \begin{pmatrix} \frac{1}{4\kappa\kappa^*}\left(\frac{l}{cZ_0} + \frac{L_\text{sq}}{Z_0^2+L_\text{sq}^2\omega_r^2}\right) & 0 \\ 0 & \frac{1}{4\kappa\kappa^*\omega_r^2}\left(\frac{l}{cZ_0} + \frac{L_\text{sq}}{Z_0^2+L_\text{sq}^2\omega_r^2}\right) \end{pmatrix} \begin{pmatrix} q \\ p \end{pmatrix}. \tag{2.51}$$

Comparing Eqn.2.50 and Eqn.2.51 allows us to obtain the magnitude of κ. The phase of κ will be determined later.

Next, to establish that p and q are indeed conjugate variables, it needs to be checked that they obey Hamilton's equations of motion,

$$\frac{dp}{dt} = -\omega_r^2\kappa\widetilde{V^+} - \omega_r^2\kappa^*\widetilde{V^+}^* = -\omega_r^2 q = -\frac{\partial H_\text{r}}{\partial q}; \tag{2.52}$$

$$\frac{dq}{dt} = i\omega_r\kappa\widetilde{V^+} - i\omega_r\kappa^*\widetilde{V^+}^* = p = \frac{\partial H_\text{r}}{\partial p}. \tag{2.53}$$

Thus p, q can be promoted to operators. By introducing the harmonic ladder operators,

$$p = i\sqrt{\frac{\hbar\omega_r}{2}}\left(a^\dagger - a\right); \tag{2.54}$$

$$q = \sqrt{\frac{\hbar}{2\omega_r}}\left(a^\dagger + a\right), \tag{2.55}$$

the harmonic oscillator Hamiltonian is recovered $H_r = \hbar\omega_r(a^\dagger a + 1/2)$. Hereafter we omit the hat on operators, assuming it is clear from the context.

This quantization procedure gives an expression for the bias current flowing through the SQUID inductance in terms of the creation and annihilation operators, through Eq. 2.47 and the variable transformation. We also use our freedom in choosing the phase of κ to ensure that $\kappa^* = \kappa/\Gamma$. This gives

$$I_b = I_{b0} i(a^\dagger + a), \tag{2.56}$$

$$\text{with } I_{b0} = \frac{\sqrt{c\hbar\omega_r Z_0}}{\sqrt{cL_{\text{sq}}Z_0 + l\left(L_{\text{sq}}^2\omega_r^2 + Z_0^2\right)}}. \tag{2.57}$$

Since in our design, the qubit is coupled inductively to the geometric inductance of the rf-SQUID, we need to further relate the SQUID bias current to the current flowing through the SQUID geometric inductance. Assuming small I_b, which is justified when the energy in the resonator is low, we have

$$I_g(f_r, I_b) = \left[\varphi_J(I_b, f_r) - 2\pi f_r\right]\frac{\phi_0}{L_g} \tag{2.58}$$

$$= I_{g0}(f_r) + r_1(f_r)I_b + r_2(f_r)I_b^2 + \mathcal{O}(I_b^3), \tag{2.59}$$

where in the second line we performed a Taylor expansion of I_g around $I_b = 0$. The coefficients of the Taylor expansion can be found numerically by minimizing the SQUID potential Eq. 2.42 at a range of I_b. The term I_{g0} corresponds to screening current in the SQUID and effectively shifts the qubit bias. The coefficients r_1, and r_2 are SQUID bias dependent and give rise to linear and non-linear interactions between the resonator and the qubit. Finally, the interaction Hamiltonian between the resonator and the qubit is

$$H_{\text{qr}} = M_{qr}\frac{\partial H_q}{\partial f_z}\left[ir_1 I_{b0}(a^\dagger - a) - r_2 I_{b0}^2(a^\dagger - a)^2\right], \tag{2.60}$$

where M_{qr} is the mutual inductance between the qubit and the SQUID geometric inductance, and $\partial H_q/\partial f_z$ is the qubit operator participating in the interaction.

2.2 Open quantum systems

One of the fundamental challenges of building a quantum computer is that the external environment that the system is coupled to can destroy the quantum state of the latter. The field of open quantum systems is concerned with studying such systems that couple to an environment, but still preserves some quantum mechanical properties [68, 69]. Due to the requirement of large coupling strength between qubits to encode problem Hamiltonians, annealing-compatible flux qubits couple more strongly to the environment than state-of-the-art superconducting qubits used in GMQC. Thus, flux qubits provide unique opportunities to develop our understanding of noise in superconducting devices and test open quantum system theories, and in return, these improved understandings could be used to mitigate the adverse effect of noise on the computational power of annealers.

In this section, we review the theories used in this thesis to study the open system behaviors observed in annealing-compatible qubits. In particular, we focus on the master equation approach, which gives a time-local equation for the reduced density operator of the system. In the first subsection, we review the derivation of the Lindblad-form master equation for a time-independent system Hamiltonian, assuming weak system-bath coupling. This allows us to relate the qubit coherence times to the coupling and noise properties of the bath. In the second subsection, we look at how to obtain a similar master equation for a time-dependent Hamiltonian, which is particularly useful when considering annealing. In the third subsection, we look at a different master equation that is applicable in the strong coupling limit. This equation is particularly useful for describing quantum tunneling subjected to strong noise, a situation that is closely related to annealing. We note that there are other approaches for modeling open quantum systems, such as the Nakajima-Zwanzig equations [70, 71], influence functionals [72], hierarchical equations of motion [73]. These methods are more general, but usually not as numerically efficient as master equations. For a more complete review of theories on open systems, the readers are referred to Ref. [74, 68, 69].

2.2.1 Redfield and Lindblad master equations

We start by considering a general system-bath Hamiltonian

$$H = H_S + H_B + H_I, \tag{2.61}$$

where H_S and H_B are the system and bath Hamiltonian respectively. The interaction Hamiltonian can be given in the form

$$H_I = g \sum_\alpha A_\alpha \otimes B_\alpha, \tag{2.62}$$

where A_α and B_α are system and bath operators respectively, with unit norm, and g is some constant characterizing the coupling strength. The evolution of the total density operator (system + bath) follows the Von Neumann equation

$$\dot{\rho}(t) = -\frac{i}{\hbar}[H(t), \rho(t)]. \tag{2.63}$$

In the interaction picture, we have

$$\dot{\widetilde{\rho}}(t) = -\frac{i}{\hbar}[\widetilde{H}_I(t), \widetilde{\rho}(t)], \tag{2.64}$$

where the tilde denotes operators in the interaction picture. The solution to Eq. 2.64 is

$$\widetilde{\rho}(t) = \frac{-i}{\hbar} \int_0^t \mathrm{d}s[\widetilde{H}_I(s), \widetilde{\rho}(s)] + \widetilde{\rho}(0). \tag{2.65}$$

Substituting the solution back into Eq. 2.64 and tracing out the bath, we obtain an integral-differential equation for the reduced density operator of the system,

$$\dot{\widetilde{\rho_S}}(t) = -\frac{1}{\hbar^2} \int_0^t \mathrm{d}s \mathrm{Tr}_B \left\{ \left[\widetilde{H_I}(t), [\widetilde{H_I}(s), \widetilde{\rho}(s)] \right] \right\} - \frac{i}{\hbar} \int_0^t \mathrm{d}s \mathrm{Tr}_B \left\{ [\widetilde{H_I}(s), \widetilde{\rho}(0)] \right\}. \tag{2.66}$$

Assuming factorizable initial condition, $\rho(0) = \rho_S(0) \otimes \rho_B(0)$, the integrand in the second term in Eq. 2.66 becomes

$$g \sum_\alpha [A_\alpha(s), \widetilde{\rho_S}(0)] \mathrm{Tr}_B \left\{ B_\alpha(s), \rho_B(0) \right\}, \tag{2.67}$$

noting the interaction picture and Schrodinger picture operator coincide at $t = 0$. The trace in the above expression can always be brought to zero since any non-zero component can be absorbed into H_S. Therefore, the second term in Eq. 2.66 is ignored hereafter.

We next make the Born-Markov approximations. The Born approximation assumes that the bath state is negligibly affected by the system and the system-bath state remains

factorizable. This is reasonable if for example the bath has a large number of degrees of freedom and remains in thermal equilibrium. Using this approximation, we can write

$$\widetilde{\rho}(s) = \widetilde{\rho_S}(s) \otimes \rho_B. \tag{2.68}$$

The time dependence on the bath state is dropped hereafter. The Markov approximation is to assume that the evolution at time t does not depend on the system state at any $s < t$, in other words, information about the system's past is lost in the bath and never comes back to the system. This amounts to replacing $\widetilde{\rho_S}(s)$ with $\widetilde{\rho_S}(t)$, allowing us to obtain

$$\dot{\widetilde{\rho_S}}(t) = -\frac{1}{\hbar^2}\int_0^t \mathrm{d}s \mathrm{Tr}_B \left\{ \left[\widetilde{H_I}(t), [\widetilde{H_I}(s), \widetilde{\rho_S}(t) \otimes \rho_B] \right] \right\}. \tag{2.69}$$

Next, we substitute in the form of interaction Hamiltonian, as given in Eq. 2.62, which allows us to obtain

$$\dot{\widetilde{\rho_S}}(t) = -\frac{g^2}{\hbar^2}\sum_\alpha [A_\alpha(t), \Lambda_\alpha(t)\widetilde{\rho_S}(t)] + \text{h.c.}, \tag{2.70}$$

where h.c. stands for Hermitian conjugate. The operator $\Lambda_\alpha(t)$ is given by

$$\Lambda_\alpha(t) = \sum_\beta \int_0^t \mathrm{d}s C_{\alpha\beta}(t,s) A_\beta(s) \mathrm{d}s, \tag{2.71}$$

with the bath correlation function defined as

$$C_{\alpha\beta}(t,s) = \langle B_\alpha(t) B_\beta(s) \rangle = \mathrm{Tr}\left[B_\alpha(t) B_\beta(s) \rho_B \right]. \tag{2.72}$$

In deriving Eq. 2.70 we used the property of the correlation time

$$C_{\alpha\beta}(t, t-s) = C_{\alpha\beta}(s,0) = C^*_{\beta\alpha}(0,s), \tag{2.73}$$

arising from the assumption that the bath is stationary [75].

Equation 2.70 is known as the Redfield equation [76]. It is still not fully Markovian because the evolution at time t has implicit initial condition dependence. To remove this dependence, the lower limit of the integral in $\Lambda_\alpha(t)$ can be extended to minus infinity, justified if the bath correlation function decays fast enough. Replacing s with $t - s$, we have

$$\Lambda_\alpha(t) = \sum_\beta \int_0^\infty \mathrm{d}s C_{\alpha\beta}(s,0) A_\beta(t-s) \mathrm{d}s. \tag{2.74}$$

Evaluating Eq. 2.74 requires knowledge of the bath correlation function, which is usually not directly accessible by experiments. This inconvenience can be avoided by going into the frequency domain. First, the interaction picture system operator, assuming a time-independent system Hamiltonian $H_S(t) = H_S$, can be decomposed with matrix elements,

$$\begin{aligned} A_{\alpha,ij}(t) &= \langle i|A_\alpha(t)|j\rangle \\ &= \exp\left(i\omega_{ij}t\right)\langle i|A_\alpha|j\rangle \\ &= \exp\left(i\omega_{ij}t\right)A_{\alpha,ij}, \end{aligned} \tag{2.75}$$

where $|i\rangle$ is the i'th system eigenstates, $\omega_{ij} = \omega_i - \omega_j$ is the angular transition frequency between states i and j. Second, the noise correlation can be given by its one-sided Fourier transform, the spectral density matrix

$$\Gamma_{\alpha\beta}(\omega) = \int_0^\infty \mathrm{d}s \exp\left(i\omega s\right)C_{\alpha\beta}(s), \tag{2.76}$$

which can always be decomposed with

$$\Gamma_{\alpha\beta}(\omega) = \frac{1}{2}\gamma_{\alpha\beta}(\omega) + iS_{\alpha\beta}(\omega), \tag{2.77}$$

$$\gamma_{\alpha\beta}(\omega) = \int_{-\infty}^\infty \mathrm{d}s e^{i\omega s}C_{\alpha\beta}(s), \tag{2.78}$$

$$S_{\alpha\beta}(\omega) = \int_{-\infty}^\infty \frac{\mathrm{d}\omega'}{2\pi}\gamma_{\alpha\beta}(\omega')\mathcal{P}\left(\frac{1}{\omega-\omega'}\right), \tag{2.79}$$

where $\mathcal{P}$ denotes principal value. Furthermore, for a bath in thermal equilibrium at temperature T_B, $\gamma_{\alpha\beta}(\omega)$ satisfies

$$\gamma_{\alpha\beta}(-\omega) = \exp\left(\frac{-\hbar\omega}{k_B T_B}\right)\gamma_{\alpha\beta}(\omega), \tag{2.80}$$

where k_B is the Boltzmann constant. As we will see later, $\gamma_{\alpha\beta}$ is directly related to the decoherence rate in the system, which can be directly measured experimentally, and $S_{\alpha\beta}$ gives rise to Lamb shift to the system Hamiltonian[3].

Now collecting the result of $\Lambda_\alpha(t)$ in Eq. 2.74, $A_\alpha(t)$ in Eq. 2.75, and using the definition of the spectral density matrix in Eq. 2.76, we can expand Eq. 2.70 and get a Markovian

[3]The notations here follows the textbook [68]. Note that often one uses $S(\omega)$ as the noise spectral density, which is denoted by $\gamma(\omega)$ here.

equation for the evolution of the interaction picture system density operator

$$\dot{\widetilde{\rho_S}}(t) = -\frac{g^2}{\hbar^2} \sum_{\alpha,\beta,i,j,k,l} \Gamma_{\alpha\beta}(\omega_{ji}) A_{\alpha,kl} A_{\beta,ij} e^{i(\omega_{kl}+\omega_{ij})t} \left[(|k\rangle\langle j|)\delta_{il}\widetilde{\rho_S}(t) - |i\rangle\langle j|\widetilde{\rho_S}(t)|k\rangle\langle l| \right] + \text{h.c.}. \tag{2.81}$$

Furthermore, if the system Hamiltonian is non-degenerate, we can apply the secular approximation, which discards terms with $\omega_{kl} + \omega_{ij} \neq 0$, because they are fast rotating and average to zero. This is equivalent to inserting $(\delta_{kl}\delta_{ij} + \delta_{kj}\delta_{il}(1-\delta_{ik}))$ to Eq. 2.81. We get

$$\begin{aligned} \dot{\widetilde{\rho_S}}(t) = -\frac{g^2}{\hbar^2} \{ & \sum_{\alpha,\beta,i,k} \Gamma_{\alpha\beta}(0) \left[L_{\alpha ii} L_{\beta kk} \tilde{\rho_S}(t) + L_{\beta ii} \widetilde{\rho_S}(t) L_{\alpha kk} \right] \\ & \sum_{\alpha,\beta,i\neq k} \Gamma_{\alpha\beta}(\omega_{ki}) \left[L_{\alpha ki} L_{\beta ik} \widetilde{\rho_S}(t) + L_{\beta ik} \widetilde{\rho_S}(t) L_{\alpha ik} \right] \} + \text{h.c.}, \end{aligned} \tag{2.82}$$

where we introduced

$$L_{\alpha,ij} = A_{\alpha,ij} |i\rangle\langle j|. \tag{2.83}$$

Using the decomposition of $\Gamma_{\alpha\beta}$ introduced in Eq. 2.77, we can rewrite Eq. 2.82 into the more familiar form

$$\begin{aligned} \dot{\widetilde{\rho_S}}(t) = & -\frac{i}{\hbar} \left[H_{\text{LS}}, \widetilde{\rho_S}(t) \right] \\ & + \frac{g^2}{\hbar^2} \sum_{\alpha\beta} \sum_{i\neq k} \gamma_{\alpha\beta}\left(\omega_{ki}\right) \left[L_{\beta,ik} \widetilde{\rho}_{\text{S}} L^\dagger_{\alpha,ik} - \frac{1}{2} \left\{ L^\dagger_{\alpha,ik} L_{\beta,ik}, \widetilde{\rho}_{\text{S}} \right\} \right], \\ & + \frac{g^2}{\hbar^2} \sum_{\alpha\beta} \sum_{ik} \gamma_{\alpha\beta}(0) \left[L_{\beta,ii} \widetilde{\rho}_{\text{S}} L^\dagger_{\alpha,kk} - \frac{1}{2} \left\{ L^\dagger_{\alpha,ii} L_{\beta,kk}, \widetilde{\rho}_{\text{S}} \right\} \right] \end{aligned} \tag{2.84}$$

where $\{\cdot\}$ denotes the anti-commutator and the Lamb shift is given by

$$H_{\text{LS}} = \frac{g^2}{\hbar} \sum_{\alpha\beta} \sum_{ik} L^\dagger_{\alpha,ik} L_{\beta,ik} S_{\alpha\beta}\left(\omega_{ik}\right), \tag{2.85}$$

which is diagonal in the system eigenbasis. Rotating back into the Schrodinger picture, we

have

$$\begin{aligned}\dot{\rho_S}(t) = &-\frac{i}{\hbar}\left[H_S + H_{\mathrm{LS}}, \rho_S(t)\right] \\ &+ \frac{g^2}{\hbar^2}\sum_{\alpha\beta}\sum_{i\neq k}\gamma_{\alpha\beta}\left(\omega_{ki}\right)\left[L_{\beta,ik}\rho_S(t)L^\dagger_{\alpha,ik} - \frac{1}{2}\left\{L^\dagger_{\alpha,ik}L_{\beta,ik}, \rho_S(t)\right\}\right] \\ &+ \frac{g^2}{\hbar^2}\sum_{\alpha\beta}\sum_{ik}\gamma_{\alpha\beta}(0)\left[L_{\beta,ii}\rho_S(t)L^\dagger_{\alpha,kk} - \frac{1}{2}\left\{L^\dagger_{\alpha,ii}L_{\beta,kk}, \rho_S(t)\right\}\right]\end{aligned} \tag{2.86}$$

Here the first term describes the unitary evolution of the system density operator under the system Hamiltonian and the Lamb shift H_{LS}. The second term describes transitions between populations in different energy eigenstates, and the third term describes the loss of phase coherence between eigenstates. The Equation 2.86 is in the Lindblad form. A particular property of the Lindblad master equation is that it is completely positive and trace preserving [5]. This ensures that $\rho_S(t)$ is a valid density operator at all times.

Lindblad equation for the qubit. Next, to make connections to the qubit experiments, we apply Eq. 2.86 to a qubit. The qubit Hamiltonian under consideration is

$$H_q = -\frac{\epsilon}{2}\sigma_z - \frac{\Delta}{2}\sigma_x, \tag{2.87}$$

with ϵ and Δ being the longitudinal and transverse fields respectively. we consider longitudinal qubit-bath interaction, that is the interaction operator is proportional to qubit σ_z. This is because the Z basis usually corresponds to a macroscopic degree of freedom, for example, the persistent current basis in flux qubit, and is hence more easily affected by noise. Therefore we write

$$H_{\mathrm{int}} = g\sigma_z \otimes B_z. \tag{2.88}$$

Introducing the angle between persistent current basis and energy basis

$$\theta = \arctan\frac{\Delta}{\epsilon}, \tag{2.89}$$

The Lindblad master equation becomes

$$\begin{aligned}\dot{\rho_q}(t) = &-\frac{i}{\hbar}\left[H_q + H_{q\mathrm{LS}}, \rho_q(t)\right] \\ &+ \frac{g^2 \sin^2\theta}{\hbar^2} \sum_{k=+,-} \gamma_{zz}\left(\pm\omega_q\right)\left[\sigma_k \rho_q(t) \sigma_k^\dagger - \frac{1}{2}\left\{\sigma_k^\dagger \sigma_k, \rho_q(t)\right\}\right] \\ &+ \frac{g^2 \cos^2\theta}{2\hbar^2}\gamma_{zz}(0)\left[\sigma_z \rho_S(t) \sigma_z^\dagger - \frac{1}{2}\left\{\sigma_z^\dagger \sigma_z, \rho_S(t)\right\}\right],\end{aligned} \tag{2.90}$$

where $\sigma_{+(-)} = |e(g)\rangle\langle g(e)|$ is the qubit raising (lowering) operator in the energy basis and ω_q is the qubit angular transition frequency. The noise at the qubit frequency causes qubit energy relaxation, with an exponential time scale denoted as T_1, where

$$\frac{1}{T_1} = \frac{g^2 \sin^2\theta}{\hbar^2}\left[\gamma_{zz}(\omega_q) + \gamma_{zz}(-\omega_q)\right]. \tag{2.91}$$

The zero frequency component causes pure dephasing, with an exponential time scale denoted as T_ϕ, given by

$$\frac{1}{T_\phi} = \frac{g^2 \cos^2\theta}{\hbar^2}\gamma_{zz}(0). \tag{2.92}$$

It can be seen that as a function of the longitudinal field ϵ, relaxation is suppressed by a Lorentzian factor as ϵ increases. The opposite is true for dephasing, which is first-order protected from dephasing at $\epsilon = 0$ and approaches the maximum value of $g^2/\hbar^2\gamma_{zz}(0)$ as $\epsilon \gg \Delta$.

2.2.2 The adiabatic master equation

Next, we discuss an extension of the derivation of the master equation to the case of a time-dependent system Hamiltonian, closely following [77]. For this, we need to revisit the definition for $\Lambda_\alpha(t)$ given in Eq. 2.74. For the time-dependent system Hamiltonian, evaluating Eq. 2.74 becomes computationally inefficient. This can be seen by considering the definition of the interaction picture system coupling operator

$$A_\alpha(t) = U_S^\dagger(t,0) A_\alpha U_S(t,0), \tag{2.93}$$

where

$$U_S(t,0) = \mathcal{T}\exp\left[\int_0^t -\frac{iH_S(\tau)}{\hbar}\mathrm{d}\tau\right] \tag{2.94}$$

is the system propagator, with $\mathcal{T}$ denoting time ordering. Therefore, evaluating the Eq. 2.74 requires evaluating the time-ordered system unitary. To avoid this, we need to work in the adiabatic limit. The adiabatic approximation is to make the following replacement

$$\begin{aligned} U_S(t-s,0) &= U_S^\dagger(t,t-s)U_S(t,0) \\ \rightarrow \exp\left(i\frac{H_S(t)s}{\hbar}\right)&U_S^{\mathrm{ad}}(t,0). \end{aligned} \tag{2.95}$$

In the above, $U_S(t,t-s)$ is replaced by the propagator generated by the Hamiltonian at time t, which is valid if the correlation time of the bath is shorter than the time taken for the system Hamiltonian to change significantly. The propagator $U_S(t,0)$ is replaced by the corresponding propagator in the adiabatic limit, which can be written as

$$U_S^{\mathrm{ad}}(0,t) = \sum_i e^{i\phi(t)}|i\rangle\langle i| \tag{2.96}$$

$$\phi_i(t) = \int_0^t \mathrm{d}\tau\omega_i(\tau)\mathrm{d}\tau. \tag{2.97}$$

Here $|i\rangle, \omega_i$ are the i'th instantaneous eigenstate and eigenvalue of the system Hamiltonian $H_S(t)$. We next substitute the approximated propagator Eq. 2.95 into Eq. 2.74, which gives

$$\Lambda_\alpha(t) = \sum_\beta \int_0^\infty \mathrm{d}s C_{\alpha\beta}(s) \sum_{ij} e^{-i\omega_i(t)s}e^{i\phi_i}|i\rangle\langle i|A_\beta|j\rangle\langle j|e^{-i\phi_j}e^{i\omega_j(t)s} \tag{2.98}$$

$$= \sum_{\beta,i,j} e^{-i\phi_{ji}}\Gamma_{\alpha\beta}(\omega_{ji})A_{\beta,ij}|i\rangle\langle j|. \tag{2.99}$$

Putting this back into Eq. 2.70 and transforming back into the Schrodinger picture, we have

$$\dot{\rho_S}(t) = -\frac{i}{\hbar}[H_s(t),\rho_S(t)] - \frac{g^2}{\hbar^2}\sum_{\alpha,\beta,ij}\Gamma_{\beta,ij}(\omega_{ji}(t))[A_\alpha, L'_{\beta,ij}(t)\rho_S(t)] + \mathrm{h.c.}, \tag{2.100}$$

where

$$L'_{\alpha,ij} = e^{-i\phi_{ji}}A_{\alpha,ij}U_S(t,0)|i\rangle\langle j|U_S^\dagger(t,0). \tag{2.101}$$

Eq. 2.100 is referred to as the one-sided adiabatic master equation (AME), which has been implemented numerically in an open source package [78]. This is the main equation that

will be used later in the thesis. Its main drawback is that it is not in Lindblad form and does not preserve the trace of the system density matrix. This could lead to negative probabilities when the evolution time is long.

To obtain a Lindblad form master equation for time-dependent Hamiltonian, we further apply the adiabatic approximation on $A_\alpha(t)$ and employ the secular approximation. The final form is exactly the same as Eq. 2.86, with the understanding that the relevant frequencies and states at each time step are the instantaneous system transition frequencies and eigenstates.

The adiabatic frame. The AME is most conveniently solved in the adiabatic frame, which diagonalizes the instantaneous system Hamiltonian since this is the basis in which decoherence occurs. Therefore, we also write the system Hamiltonian in this frame.

$$H_S^{\text{ad}}(t) = U^\dagger(t)H_S(t)U(t) + i\hbar\dot{U}^\dagger(t)U(t) \tag{2.102}$$

$$= \sum_i \hbar\omega_i(t)|i\rangle\langle i| + \sum_{ij} W_{ij}(t)|i\rangle\langle j|, \tag{2.103}$$

where $U(t)$ is the unitary which diagonalizes the instantaneous Hamiltonian, W is often known as the non-adiabatic transition operator, arising from the time-dependence of the system Hamiltonian and hence the unitary $U(t)$. The states $|i\rangle, |j\rangle$ are the instantaneous energy eigenstates of the system.

2.2.3 The polaron transformed master equation

Polaron is a concept used in condensed matter that describes quasi-particles formed due to interaction between electrons and phonons. The polaron transformed master equation (PTRE) exploits this concept to study the dynamics of spins coupled to baths of harmonic oscillators, i.e. the spin-boson problem [79]. In this section, the PTRE is introduced. To simplify the presentation, the discussion is restricted to the single qubit case, which is most relevant to the thesis. We note that in the single qubit case, the PTRE gives results similar to that of taking the non-interacting blip approximation [80, 81]. For a more general treatment applied to a multi-qubit annealer, the readers are referred to Ref. [82, 83, 78].

We start by considering the total Hamiltonian of a qubit coupled to a harmonic bath,

$$H = H_q + H_B + H_{qB} \tag{2.104}$$

$$H_q = -\frac{\Delta}{2}\sigma_x - \frac{\epsilon}{2}\sigma_z, \tag{2.105}$$

$$H_B = \sum_k \hbar\omega_k b_k^\dagger b_k, \tag{2.106}$$

$$H_{qB} = \frac{\sigma_z}{2}\sum_k g_k(b_k^\dagger + b_k). \tag{2.107}$$

The bath of harmonic oscillators is in addition characterized by the bath spectral density

$$J(\omega) = \frac{1}{\hbar^2}\sum_k \pi g_k^2 \delta(\omega - \omega_k), \tag{2.108}$$

usually taken in the continuous limit. The polaron transform displaces each oscillator conditioned on the qubit state and diagonalizes the total Hamiltonian except the qubit σ_x term. The unitary is

$$U^{\mathrm{PF}} = \exp\left(-\frac{i}{2}\sigma_z\Omega\right), \tag{2.109}$$

$$\Omega = -i\sum_k \frac{g_k}{\omega_k}(b_k^\dagger - b_k). \tag{2.110}$$

The transformed Hamiltonian is

$$H^{\mathrm{PF}} = U^{\mathrm{PF}\dagger} H U^{\mathrm{PF}} = -\frac{\epsilon}{2}\sigma_z^{\mathrm{PF}} - \frac{\Delta}{2}(\sigma_+^{\mathrm{PF}}\xi_+ + \sigma_-^{\mathrm{PF}}\xi_-) + H_B, \tag{2.111}$$

$$\xi_\pm = \exp\left(\pm i\Omega\right). \tag{2.112}$$

After this transformation, the system-bath coupling is of the order Δ. When Δ is small enough, we can again apply the Born-Markov and secular approximations. This results in a master equation that is similar to Eq. 2.86, with a few differences which we discuss here. First, besides the Lamb shift term, the unitary part of the evolution gets an additional term due to the finite expectation value of the bath coupling operator $\xi_\pm$. This is commonly known as the renormalized tunneling amplitude

$$H_{\mathrm{renorm}} = -\frac{\kappa\Delta}{2}\sigma_x^{\mathrm{PF}}, \tag{2.113}$$

where $\kappa = \langle\xi_\pm\rangle$. The factor κ is always smaller than 1 so that the polaron-dressing always reduces the tunneling rate. Second, the interaction operator in the polaron frame does not

cause pure dephasing as it is completely off-diagonal. The resultant master equation is therefore

$$\dot{\rho_S}(t) = -\frac{i}{\hbar}[-\frac{\epsilon}{2}\sigma_z - \frac{\kappa\Delta}{2}\sigma_x + H_{\rm LS}, \rho_S(t)] \tag{2.114}$$

$$+ \frac{\Delta^2}{4\hbar^2}\gamma_{+-}(\omega_{10})\left[\sigma_-\rho_S(t)\sigma_+ - \frac{1}{2}\left\{\sigma_+\sigma_-, \rho_S(t)\right\}\right] \tag{2.115}$$

$$+ \frac{\Delta^2}{4\hbar^2}\gamma_{-+}(\omega_{01})\left[\sigma_+\rho_S(t)\sigma_- - \frac{1}{2}\left\{\sigma_-\sigma_+, \rho_S(t)\right\}\right] \tag{2.116}$$

where we have dropped the superscript PF on the qubit operators for simplicity. Next, we need to find the noise spectrum $\gamma_{\pm(\mp)}(\omega)$ in the polaron frame, which will be used to calculate the transition rate and the Lamb shift term using Eq. 2.79, 2.85. Using standard results for harmonic oscillator bath[4], the following expressions can be found for the operator expectation values in the polaron frame,

$$\langle\xi_\pm\rangle = \exp\left\{-\int_0^\infty \frac{J(\omega)}{2\pi\hbar^2\omega^2}\coth(\beta\hbar\omega/2)\mathrm{d}\omega\right\}, \tag{2.117}$$

$$\langle\xi_\pm(t)\xi_\mp(0)\rangle = e^{-Q(t)}, \tag{2.118}$$

$$Q(t) = \int_0^\infty \mathrm{d}\omega\frac{J((\omega)}{\pi\hbar^2\omega^2}\left\{i\sin(\omega t) + \coth(\beta\hbar\omega/2)\left[(1-\cos(\omega t))\right]\right\}, \tag{2.119}$$

where $\xi_\pm(t)$ is the interaction picture polaron frame bath operator, $\beta = 1/(k_B T_B)$ is the inverse bath temperature. The last expression can be compared with the correlation function in the lab frame, given by the Fourier transform of the noise power spectral density $\gamma(\omega)$,

$$C(t_2, t_1) = \frac{1}{2\pi}\int_{-\infty}^{\infty}\gamma(\omega)e^{-i\omega(t_2-t_1)}\mathrm{d}\omega \tag{2.120}$$

$$= \sum_{k,l} g_k g_l \left\langle\left[b_k^\dagger(t_2) + b_k(t_2)\right]\left[b_l^\dagger(t_1) + b_l(t_1)\right]\right\rangle \tag{2.121}$$

$$= \int_0^\infty \frac{J(\omega)}{\pi}\mathrm{d}\omega\left[\cos(\omega(t_2-t_1))\coth(\frac{\beta\hbar\omega}{2}) - i\sin(\omega(t_2-t_1))\right] \tag{2.122}$$

where in the second line we use the definition of the lab frame bath correlation function, with $b^{(\dagger)}(t)$ being the interaction picture harmonic oscillator operators, and in the third line we use the definition of $J(\omega)$, together with the expectation values evaluated assuming

[4]See for example Eq. 4.3.11 of Ref. [84].

the bosons are in thermal equilibrium. Comparing Eq. 2.119 and Eq. 2.122, we can find that

$$Q(t) = -\frac{1}{\hbar^2}\int_0^t \mathrm{d}t_2 \int_{-\infty}^0 \mathrm{d}t_1 C(t_2,t_1) \tag{2.123}$$

$$= -\frac{1}{2\pi\hbar^2}\int_0^t \mathrm{d}t_2 \int_{-\infty}^0 \mathrm{d}t_1 \int_{-\infty}^{\infty} \gamma(\omega) e^{-i\omega(t_2-t_1)}\mathrm{d}\omega \tag{2.124}$$

$$= -\frac{1}{2\pi}\int_{-\infty}^{\infty} \frac{e^{-i\omega t}-1}{\hbar^2\omega^2}\gamma(\omega)\mathrm{d}\omega. \tag{2.125}$$

Therefore, the correlation function, and hence the noise spectrum in the polaron frame is indeed related to the lab frame noise spectrum $\gamma(\omega)$.

The master equation can be further simplified if the noise is strong. First, strong noise leads to a small κ so that the renormalized tunneling can be ignored. Second, coherence between the two-qubit computational states is expected to decay fast so that the qubit density operator commutes with its Hamiltonian. As a result, we only need to consider the dynamics between the populations in the two-qubit computational states. This is described by

$$P_L = -\Gamma_{LR}P_L + \Gamma_{RL}P_R, \tag{2.126}$$

$$P_L + P_R = 1. \tag{2.127}$$

Here the left and right states are states in the polaron frame, but from the qubit observable point of view, they are essentially the same as the bare qubit's left and right state, as the polaron transformation commutes with the qubit computational basis. The left to right (right to left) transition rate $\Gamma_{LR(RL)}$ is given by

$$\Gamma_{\mathrm{LR}}(\epsilon) = \frac{\Delta^2}{4\hbar^2}\int_{-\infty}^{\infty} dt e^{i\epsilon t}\langle \xi_-(t)\xi_+(0)\rangle \tag{2.128}$$

$$= \frac{\Delta^2}{4\hbar^2}\int_{-\infty}^{\infty} dt e^{i\epsilon t} \exp\left\{\int d\omega \frac{\gamma(\omega)}{2\pi}\frac{e^{-i\omega t}-1}{\hbar^2\omega^2}\right\}, \tag{2.129}$$

$$\Gamma_{\mathrm{RL}}(\epsilon) = \Gamma_{\mathrm{LR}}(-\epsilon). \tag{2.130}$$

We note that this transition rate can also be obtained by directly applying Fermi's Golden rule to the coupled qubit and bath, assuming strong noise [85].

The noise environment of flux qubits generally consists of a strong low-frequency $1/f$ noise and a weaker high-frequency noise, typically with an ohmic spectrum. Following

Ref. [83], we decompose the noise power spectrum into low and high-frequency components

$$\gamma(\omega) = \gamma_{\mathrm{LF}}(\omega) + \gamma_{\mathrm{HF}}(\omega). \tag{2.131}$$

For the low-frequency components, a second-order Taylor expansion in Eq. 2.129 is justified, which leads to transition rates with a Gaussian lineshape,

$$\Gamma_{\mathrm{LR,LF}}(\epsilon) = \sqrt{\frac{\pi}{8}} \frac{\Delta^2}{\hbar W} \exp\left\{ \frac{-(\epsilon - \epsilon_p)^2}{2W^2} \right\}. \tag{2.132}$$

The width and peak position are given by integrals of γ_{LF},

$$W^2 = \int_{-\infty}^{\infty} \frac{\mathrm{d}\omega}{2\pi} \gamma_{\mathrm{LF}}(\omega) \tag{2.133}$$

$$\epsilon_p = \mathcal{P} \int_{-\infty}^{\infty} \frac{\mathrm{d}\omega}{2\pi} \frac{\gamma_{\mathrm{LF}}(\omega)}{\hbar\omega}. \tag{2.134}$$

These two quantities, in the context of flux qubits, are commonly known as the macroscopic resonant tunneling (MRT) width and the reorganization energy [85]. The MRT width (reorganization energy) is dependent on the (anti-)symmetric component of the noise spectrum $\gamma_{\pm} = [\gamma(\omega) \pm \gamma(-\omega)]/2$. If the low-frequency noise is in thermal equilibrium, the fluctuation-dissipation theorem relates the symmetric and anti-symmetric component via $\gamma_{-}(\omega) = \gamma_{+}(\omega) \tanh(\beta\hbar\omega/2)$. Given the relevant frequencies satisfy $\hbar\omega < k_B T$, this relates the MRT width and reorganization energy via $\epsilon_p = W^2/(2k_B T_B)$.

The high-frequency component of the noise modifies the transition rate to

$$\Gamma_{\mathrm{LR}}(\epsilon) = \frac{\Delta^2}{4\hbar^2} \int \mathrm{d}\tau \mathrm{e}^{\mathrm{i}(\epsilon-\epsilon_p)\tau/\hbar - W^2\tau^2/2\hbar^2} \exp\left[\int \frac{\mathrm{d}\omega}{2\pi} \frac{\gamma_{\mathrm{HF}}(\omega)}{\hbar^2\omega^2} \left(\mathrm{e}^{-\mathrm{i}\omega\tau} - 1 \right) \right], \tag{2.135}$$

which is just the low-frequency contribution multiplied by an exponential factor determined by the high-frequency component. Using the convolution theorem, Eq. 2.135 can be written as

$$\Gamma_{\mathrm{LR}}(\epsilon) = \frac{\Delta^2}{4\hbar^2} \int \frac{\mathrm{d}\omega}{2\pi} G^L(\frac{\epsilon}{\hbar} - \omega) G^H(\omega), \tag{2.136}$$

$$G^L(\omega) = \sqrt{\frac{2\pi\hbar^2}{W^2}} \exp\left[-\frac{(\omega - \epsilon_p/\hbar)^2}{2W^2/\hbar^2} \right], \tag{2.137}$$

$$G^H(\omega) = \int_{-\infty}^{\infty} \mathrm{d}\tau \mathrm{e}^{\mathrm{i}\omega\tau} \exp\left[\int \frac{\mathrm{d}\Omega}{2\pi} \frac{\gamma_{\mathrm{HF}}(\Omega)}{\hbar^2\Omega^2} \left(\mathrm{e}^{-\mathrm{i}\Omega\tau} - 1 \right) \right]. \tag{2.138}$$

In particular the high frequency part $G^H(\omega)$, under the assumption $\gamma_{\rm HF}(\omega)/(\hbar^2\omega) \ll 1$, can be approximated by [83]

$$G^H(\omega) = \frac{\gamma_{\rm HF}(\omega)/\hbar^2}{\omega^2 + [\gamma_{\rm HF}(0)/\hbar^2]^2}. \tag{2.139}$$

2.3 Quantum annealing

Quantum annealing was first envisioned as a heuristic optimization tool, as the quantum analog to simulated thermal annealing [19, 20, 86]. In thermal annealing, one starts a system in a high-temperature state, and by gradually reducing the temperature, hopes to find the energy minimum of a complex cost landscape. In quantum annealing, thermal fluctuation is replaced by quantum fluctuations. As shown in Fig. 2.9(a), quantum annealing is often expected to outperform thermal annealing, due to the ability to quantum mechanically tunnel out of local minima. A few years after the theory proposal, experimental implementation of quantum annealing on magnetic materials revealed that quantum annealing leads to faster convergence towards low energy states than thermal annealing [87].

The development of quantum annealing is also closely related to the development of adiabatic quantum computation (AQC) [16]. In contrast to standard gate-based quantum computation, where evolution is decomposed into a set of unitaries acting on qubits, AQC encodes the computational process in a continuously changing system Hamiltonian. Such forms of computation were first developed in the context of solving optimization problems [88]. Later on, it has been shown that AQC has the same quadratic speed up on the oracular Grover search [10], just as gate-based quantum computing, and that in general, AQC is polynomially equivalent to gate-based quantum computing [17].

Prompted by both experiments in quantum annealing and algorithmic development, we see a growing interest in developing a programmable quantum system that implements quantum annealing. The primary objective is to find a potential quantum advantage in solving hard, industry-relevant optimization problems, using a programmable quantum annealer.

The general prescription for quantum annealing is to implement a time-dependent Hamiltonian of the form

$$H(s) = A(s)H_d + B(s)H_p, \tag{2.140}$$

where $s = t/T_f$ is the annealing time divided by the total time T_f. The annealing schedules $A(s)$ and $B(s)$ go from $A(0) \gg B(0)$ initially, to $A(1) = 0$ in the end. In figure 2.9(b), the annealing schedule as implemented in one of the D-Wave devices is shown. The Hamiltonian H_p is the target Hamiltonian we are interested in, which usually encodes an optimization problem, with its ground state being the solution. It usually only consists of commuting terms, so its eigenstates are classical states that can be easily read out. The Hamiltonian H_d does not commute with H_p and implements the quantum fluctuation. In

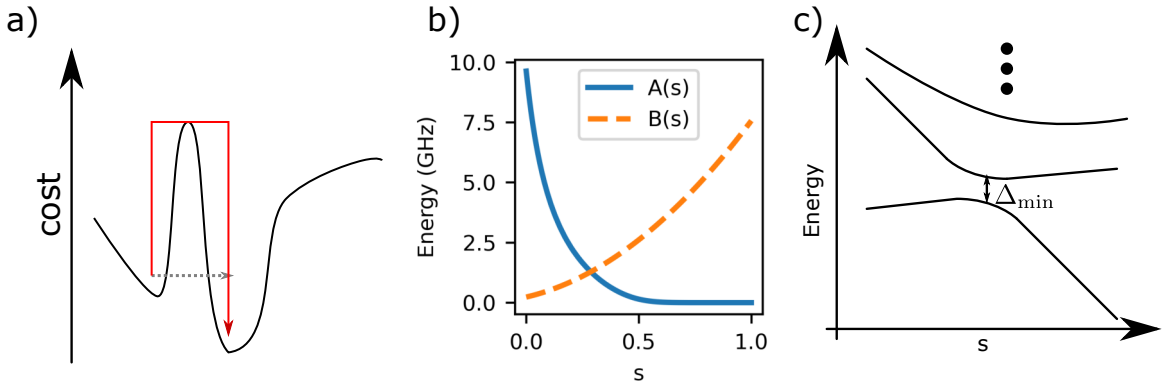

Figure 2.9: (a) An illustration of cost landscape (continuous black curve) for some optimization problem. The grey dashed line and red solid line indicate paths for quantum tunneling and thermal escape from a local minimum to the global minimum. (b) The annealing schedules as in the D-Wave Advantage system 4.1 [31]. (c)An illustration of the annealing energy spectra, with the minimum gap between the ground and the first excited state, indicated as $\Delta_{\min}$.

the standard setting, H_d and H_p are respectively given by

$$H_d = -\sum_i h_x^i \sigma_x^i \text{ and} \tag{2.141}$$

$$H_p = \sum_i h^i \sigma_z^i + \sum_{j>i} J^{ij} \sigma_z^i \sigma_z^j. \tag{2.142}$$

Therefore, at $s = 0$, assuming $A(s)h_x \gg k_B T$, the system is prepared in the ground state of H_d, which is an equal superposition of all computational states. If the system is annealed slowly enough, it eventually reaches the ground state of H_p, by virtue of the adiabatic theorem. The form of the annealing Hamiltonian consisting of Eq. 2.141, 2.142 is known as the transverse field Ising model (TFIM). Although it looks restrictive, H_p can in fact encode NP-hard optimization problems via the quadratic unconstrained binary optimization (QUBO) formalism, and no efficient classical algorithms are known for this class of problems.

To give an example of how to map an optimization problem, we can consider the number partitioning problem. The optimization problem is that given a set of N real numbers $\{n_1, n_2, \ldots, n_N\} \in \mathcal{S}$, to partition it into two sets $\mathcal{S}_1, \mathcal{S}_2$, such that the difference between the sums of the individual sets is minimized. To solve this problem on a quantum annealer, each number is associated with a binary variable s_i, taking the value of either 0

or 1, indicating whether n_i it belongs to $\mathcal{S}_1$ or $\mathcal{S}_2$. Then the optimization problem amounts to minimizing the function

$$f(\{s_i\}) = \left[\sum_i 2(s_i - 0.5)n_i\right]^2 . \tag{2.143}$$

Minimization of $f(\{s_i\})$ is an example of a QUBO problem, meaning the target expression to be minimized contains at most quadratic terms of the binary variables and the minimization task has no additional constraint. The QUBO problem can be mapped to the Ising Hamiltonian by identifying $2(s_i - 0.5)$ with the qubit Pauli operator σ_z^i. For the number partitioning problem, the corresponding Ising coefficients are

$$h^i = 0, \;\; J^{ij} = n_i n_j. \tag{2.144}$$

The adiabatic theorem gives a lower bound on how fast quantum annealing could solve a problem. For the evolution to remain adiabatic, the adiabatic theorem requires that the total evolution time to satisfy

$$\frac{1}{T_f} \max_{s\in[0,1]} \frac{|\langle \varepsilon_0(s)| \partial_s H(s) |\varepsilon_i(s)\rangle|}{|\varepsilon_0(s) - \varepsilon_i(s)|^2} \ll 1 \quad \forall i \neq 0, \tag{2.145}$$

where $|\varepsilon_i\rangle, \varepsilon_i$ are the i'th eigenstate and energy. The adiabatic criterion is sometimes loosely referred to as the inverse gap squared criterion for the evolution time. As shown in Fig 2.9(c), the gap refers to the minimum energy difference between the ground and the first excited states $\Delta_{\min} = \min_s [\varepsilon_1(s) - \varepsilon_0(s)]$. This criterion is useful when analyzing the complexity of problems, but has little practical value since in general it is hard in itself to know where $\Delta_{\min}$ occurs and how large it is.

One of the main advantages of quantum annealing is its low requirement for control. Compared to gate model devices which require highly tuned pulses per qubit to carry out the desired unitaries, standard quantum annealing only requires global control of the transverse field. This prompts the rapid development in hardware implementation of quantum annealing, using superconducting qubits [89], Rydberg atoms [90] and trapped ions [91]. Superconducting flux qubit is a natural platform for quantum annealing, as the large persistent current allows strong programmable Ising interaction, and annealing can be performed by a single time-dependent signal that controls the X-flux of all qubits together. Relying on the rf-SQUID flux qubit, the D-Wave company has commercialized a few generations of quantum annealers, with the most recent generation containing more than 5000 qubits [92]. These D-Wave devices have been extensively studied, both in terms of their fundamental capabilities [30, 32], and also potential applications in a wide range of real-world problems [93].

2.3.1 Challenges in quantum annealing

To put the research of this thesis into context, we review in this section the challenges and possible research directions in the field of quantum annealing. They are categorized into five different topics: maintaining adiabaticity, classical simulability, decoherence, analog error, and connectivity. The first two points concern more the algorithmic side and the last three points are concerned primarily with the hardware implementation, though it needs to be noted that different points are interrelated. These are synthesized based on the author's research exposure, as well as a few recent reviews on quantum annealing [16, 30, 32, 33].

Maintaining adiabaticity and avoiding small gaps. The minimum gap during annealing, and hence the run time required for quantum annealing, is closely related to phase transitions [94]. It is generally believed that first-order phase transitions lead to exponentially small minimum gap with system size [95], while second-order phase transitions lead to polynomially small gap [96], although counterexamples exist [97, 98, 99]. One of the main research directions in quantum annealing is to find annealing protocols alternative to the conventional TFIM forward annealing paradigm, that can circumvent first order phase transitions. One strategy that is often explored is inhomogeneous driving, where the annealing schedule is made different for different qubits [100, 101, 102, 103]. Another strategy is the addition of catalyst Hamiltonian, which is a time-dependent term that is zero at the beginning and end of a Hamiltonian, but finite in between [104, 105, 106]. These methods have been found to be effective at avoiding first order phase transitions in specific instances where symmetries of the problem can be exploited. In general, their usefulness in improving the solution quality of QA remains elusive.

A more recent development around novel annealing protocols is reverse annealing, which comes in different variants [107, 108]. In adiabatic reverse annealing, the time-dependent Hamiltonian becomes,

$$H(s) = (1-s)\left[1-\lambda(s)\right]H_{\text{init}} + (1-s)\lambda(s)H_0 + sH_p, \tag{2.146}$$

where $\lambda(s=0)=0$ and $\lambda(s=1)=1$. The initial Hamiltonian H_{init} is usually a simple diagonal Hamiltonian that sets the desired initial state of the qubits. The idea is that by exploiting knowledge of the structure of the solution, we can initialize the annealer into a state close to the final solution, and the reverse annealing procedure allows an efficient local search around the initial solution [107]. Another variant of reverse annealing is called iterative reverse anneal, where the initial and final diagonal Hamiltonian are the same, and the initial state is the final state of the previous round of reverse anneal. Such protocols

have been implemented in D-Wave devices and enabled efficient simulation of topological phases of matter [109, 110].

A related approach to avoid the slow evolution time due to small gaps is called counter-diabatic drives [111]. Consider the Schrodinger equation in the adiabatic frame

$$i\hbar\partial_t|\psi^{\text{ad}}\rangle = \left[U(t)H(t)U^\dagger(t) - i\hbar U(t)\frac{\partial U^\dagger(t)}{\partial t}\right]|\psi^{\text{ad}}\rangle, \tag{2.147}$$

where U is the unitary that diagonalizes the instantaneous Hamiltonian $H(s)$. In Eq. 2.147, the first term on the right-hand side is diagonal and the second term is off-diagonal and causes non-adiabatic transitions. The idea of counter diabatic driving is then to modify the original Hamiltonian to $H_{\text{CD}} = H(s) + A(t)$, with

$$A(t) = i\hbar\frac{\partial U^\dagger(t)}{\partial t}U(t). \tag{2.148}$$

Then the dynamics generated by H_{CD} becomes equivalent to the dynamics generated by the adiabatic evolution of $H(t)$, no matter how fast $H(t)$ changes. The problem with this method is that $A(t)$ is in general a highly non-local operator and it is not experimentally feasible beyond a small number of qubits. Therefore, recent literature focuses on approximate implementations of counter diabatic drives with variational parameters [112]. Although it is shown to be effective in improving ground state fidelity for small-scale problems, the effectiveness of such approximate counter-diabatic driving in large-scale problems remains to be tested.

Classical simulability. A common challenge that standard quantum annealing faces is that very often equilibrium properties of the TFIM can be efficiently simulated using path integral Quantum Monte Carlo (PI-QMC)technique [113, 114]. This is due to the TFIM being in a class of Hamiltonian called stoquastic Hamiltonian. A Hamiltonian is stoquastic in a particular basis if there is no positive off-diagonal terms [115]. Although specific instances of stoquastic Hamiltonians can be constructed where PI-QMC fails to equilibrate efficiently [116], it is often believed that computation involving only the ground state of stoquastic Hamiltonian has limited power [32]. This belief to some extent is evidenced by the fact all known construction of equivalence between adiabatic quantum computing and gate-model quantum computing requires non-stoquastic interactions [17, 117].

One way to enhance quantum annealing is thus to introduce non-stoquastic interactions. Experimentally, non-stoquastic interaction, of the form $\sigma_y\sigma_y$, has been demonstrated by coupling flux qubits together both capacitively and inductively [118] (see Fig. 2.10(a,

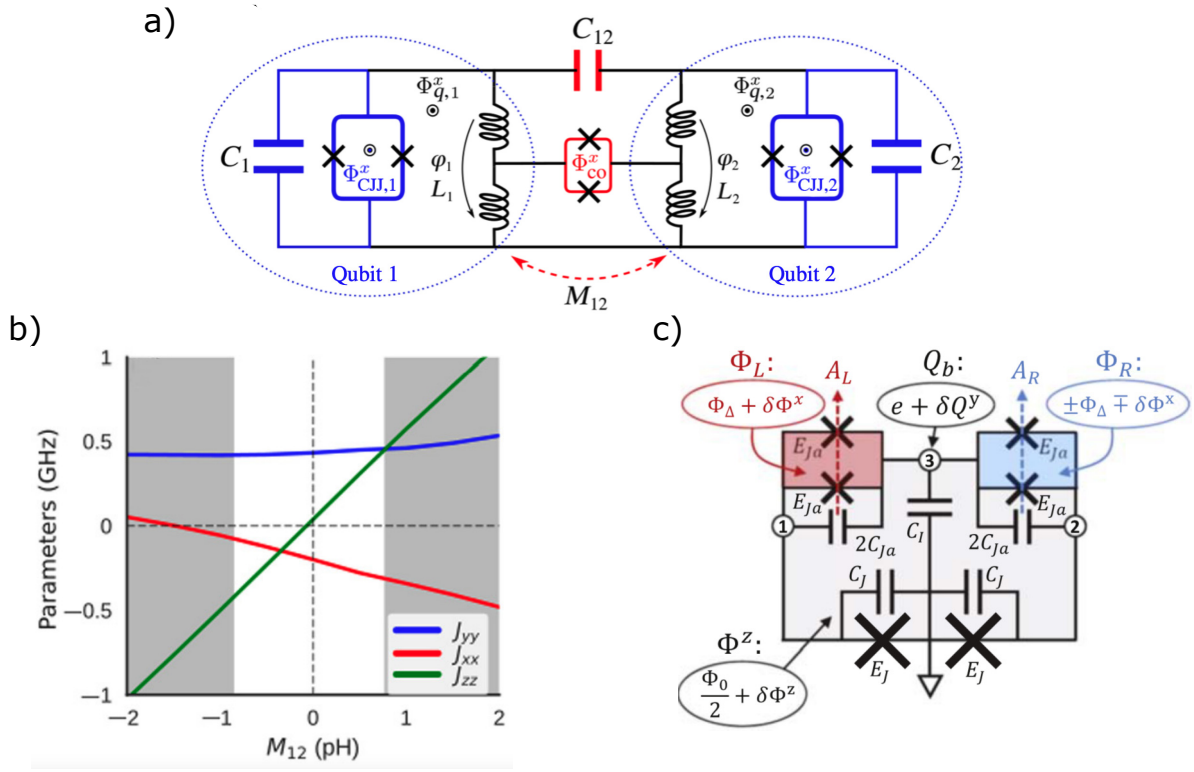

Figure 2.10: Two ways to realize non-stoquastic interaction between flux qubits. (a) Two rf-SQUID flux qubits coupled by a coupler and a capacitor simultaneously. (b) The measured coupling strength between the two qubits is shown in panel (a), as a function of the tunable mutual inductance M_{12} mediated by the coupler. Panels (a) and (b) are reproduced from [118]. (c) The Josephson phase slip qubit circuit, reproduced from Ref. [119].

b)). However, such implementations are limited in that the non-stoquastic interaction is only strong when the qubit transverse field is large. To obtain arbitrary tunability of the non-stoquastic interaction, a new qubit, named the Josephson-phase-slip qubit was proposed [119] (see Fig. 2.10(c)). However experimental realization of this qubit has been challenging, as it requires charge bias tunability, which opens the qubit to large charge fluctuations. On the theory side, further understanding of how non-stoquasticity can improve annealing is also needed. Although it has been shown that adding non-stoquastic catalyst avoids first-order phase transition in some cases [120, 106], recent results show that generically having the same interactions, but with the opposite sign and hence being stoquastic, tend to have larger minimum gap compared to their non-stoquastic counterpart [121].

The other approach to enhance the computational power of current annealers is to go beyond adiabatic evolution [32]. This is motivated by the fact that Monte Carlo techniques are restricted to equilibrium properties, and allowing excited state evolution leads to stoquastic Hamiltonians becoming universal [122]. Moreover, studies of QAOA, a quantum-annealing-inspired optimization algorithm that runs on gate-based machines, show that by combining two diabatic transitions, the ground state can be reached faster than a pure ground state evolution [123]. This has yet to be realized on a quantum annealer, likely due to the limited bandwidth and poor coherence of the annealers available.

Decoherence. Any physical realization of quantum annealing suffers from noise and decoherence. Early studies of the open system effect of quantum annealers mainly rely on the Redfield equation, which is applicable in the weak coupling limit [124, 125, 126, 127]. In this limit, quantum annealing is protected from dephasing if the system remains close to the ground state, because decoherence only occurs in the instantaneous energy eigenbasis in the weak-coupling limit. On the other hand, in the long time limit, the system tends towards the Gibbs state at some temperature T_B due to coupling to the environment, which in some cases leads to an improvement to the ground state probabilities [126]. This so-called thermally-assisted quantum annealing regime was also tested by inserting intentional pauses during the anneal, which again could lead to increased ground state probabilities [128, 129]. These examples show how differently QA and GMQC are affected by decoherence. While in GMQC decoherence almost always causes errors in the computation, QA could sometimes benefit from decoherence. However, so far none of the studies indicate that thermal relaxation could lead to any scaling advantage.

Later on, it becomes recognized that in the later stage of the anneal, especially around the minimum gap, the weak-coupling approximation breaks down [130, 82, 83, 131]. In this limit, the energy eigenstate of the system is no longer meaningful, due to polaronic

dressing by the environment. However, despite the expectation that polaronic dressing suppresses tunneling, it has been experimentally demonstrated that multi-qubit tunneling is possible, and leads to an advantage over either simulated thermal annealing or classical simulation that involves only product states [82, 130].

Recently, it has been demonstrated in D-Wave devices that coherent annealing is possible, if the annealing time is brought down to about ~ 10 ns [132, 133], comparable to the decoherence times of the constituent qubits. This allows the demonstration of a scaling advantage of QA in solving 3D spin glass problems over simulated quantum annealing and thermal annealing. Further reducing noise and extending the coherent regime of annealing to longer times are necessary for quantum annealers to be competitive in solving industry-relevant optimization problems.

Beyond improving qubit coherence, large-scale annealing applications will likely require some error correction schemes to mitigate noise. Unlike gate-model devices, which could rely on intermediate measurement and classical processing to correct errors during arbitrarily long computation, quantum annealing typically relies on Hamiltonian error suppression schemes [134], which use energy penalty to suppress thermal transitions out of the ground state. Such error schemes usually require novel interactions beyond the TFIM, such as two body XX interactions or four body interactions [134, 135].

Analog error. Quantum annealing is a type of analog computation, as it encodes the problem to be solved into a set of controls that can be continuously varied. This means that quantum annealing inevitably suffers from analog errors, such that the problem represented by the hardware is different from the problem that one wants to solve. It has been shown that for a constant error magnitude, the annealing success probability decreases as fast as exponentially with system size, for hard optimization problems [136]. The typical solution to this problem is to use classical repetition code, which essentially increases the energy scale of the problem relative to the errors by ferromagnetically coupling copies of physical qubits to a penalty qubit [137, 138]. Recently, it has also been shown that by linking antiferromagnetically physical qubits that encode multiple copies of the problem Hamiltonian, the parameter precision can be effectively improved by several orders of magnitude [139].

Besides the intrinsic resolution of the controls that limits the accuracy, one important source of analog error is environment polarization [140]. The idea is that persistent current in the qubit biases the environment spins, which in turn acts as an external bias to the qubit. Due to this environment polarization, when the same anneal sequence is repeated over a short interval, the result of the new run will be biased toward the previous result. Further mitigating this effect requires better understanding the response of the environment

to external biases at a wide range of timescales, and the nature of flux noise in general.

Connectivity. When mapping real-world problems to the annealing hardware, an embedding procedure is usually needed to allow the physical hardware, with limited connectivity to represent the real problem, which has more complicated connectivity. This is typically done through a procedure called minor embedding [141, 142], where strong ferromagnetic interactions are imposed among neighboring physical qubits, so that they are likely to stay in the same spin states and behave as a single logical spin. In general, to represent N logical qubits with all-to-all connectivity, $\Omega(N^2)$ physical qubits are required and the physical connectivity graph has to be non-planar [142]. There are two main issues with minor embedding. First, the chain of physical qubits that encodes the logical qubit could break in large-scale applications, due to the finite interaction energy available [143]. Often one has to discard results with broken chains or perform a majority vote to determine the state of the logical qubit. Either of these lowers the probability of obtaining the optimum result. The second issue is that minor embedding changes the energy landscape of the logical problem. It has been pointed out that quantum annealing is advantageous when compared to simulated thermal annealing if the cost landscape involves thin and tall barriers, since in this case tunneling is more efficient than thermal escape [130]. However, in the embedded problem, the barriers widen by the number of physical qubits used to encode the logical qubit, which makes tunneling much harder and simulated thermal annealing more advantageous.

One way to improve qubit connectivity, while keeping the physical size of the qubits small, proposed in Ref. [144, 146] is the paramagnetic coupler tree concepts. As shown in Fig. 2.11(b), the qubits are coupled to a network of couplers along the circumference, and the couplers essentially act as paramagnets that propagate qubit magnetization and hence mediate coupling between qubits. A prototype device exploring this idea, involving two qubits coupled by a chain of couplers is presented in Chapter. 4 of this thesis. An alternative approach to improve connectivity is the so-called LHZ scheme [145], named after the authors (see Fig. 2.11). The idea is to embed the $N(N-1)/2$ interaction terms into the local fields of the same number of qubits. The redundant physical states, which do not have a corresponding logical state, can be suppressed by 4-body interaction terms. This embedding scheme does not allow local fields on the logical qubits, but is likely to have the same computational power, since many NP-complete problems, such as number partitioning, can be mapped with zero local field terms. Experimentally the main challenge is to engineer 4-body interaction, for which there have been proposals and preliminary experiments based on Kerr non-linear oscillators [147] and flux qubits [148, 149].

Finally, I would like to conclude the above discussions with a list of directions, with

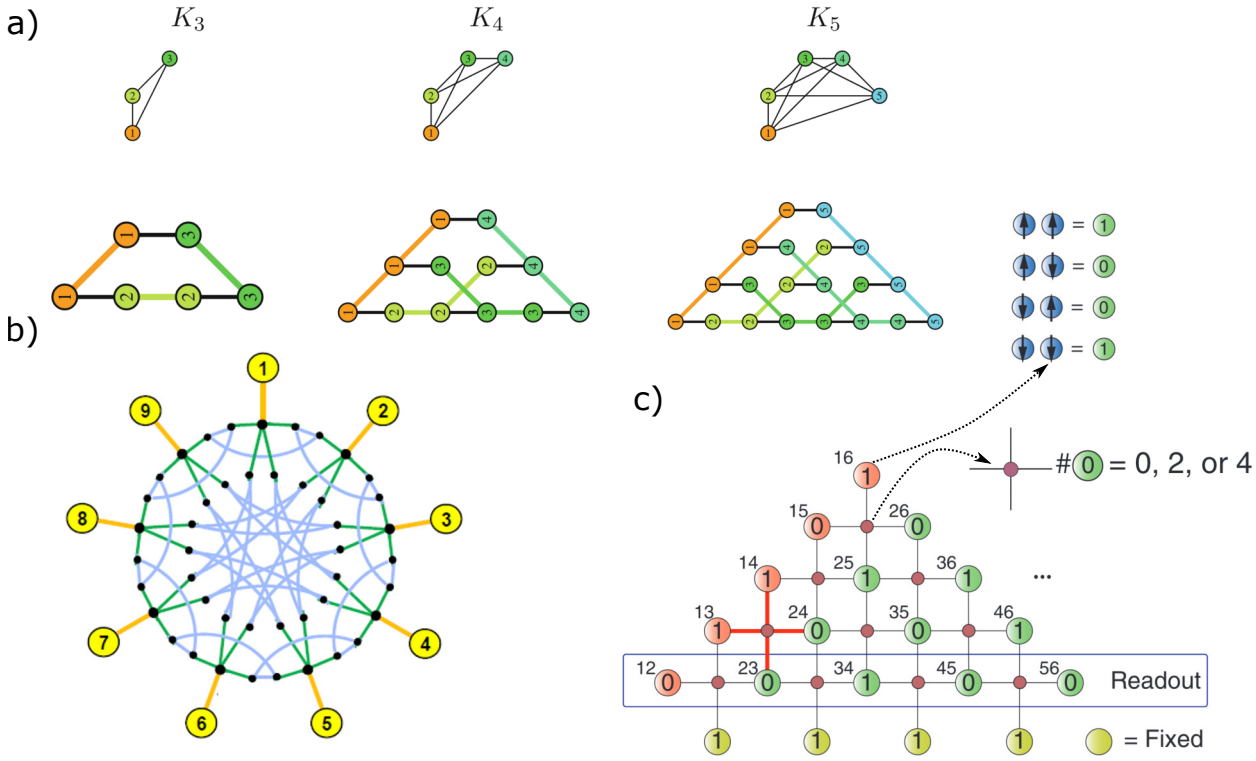

Figure 2.11: Illustrations of different schemes to improve annealer connectivity. (a) Minor embedding. The three sub-panels show a progression of constructing K_n graph from K_{n-1} graph using minor embedding, where K_n stands for all-to-all connected graph with n vertices. This construction keeps the length of the edges bounded, hence amenable to physical implementation. Reproduced from Ref. [142]. (b) Coupler tree. The qubits (yellow solid circles) are coupled via a network of couplers (black dots). Reproduced from Ref. [144] (c) The LHZ scheme. In this scheme, each physical qubit (circles) state represents the parity of two coupled logical qubit, and the physical four-body $ZZZZ$ interaction (dots) constrains the physical system into the logical subspace. The readout is only needed on a subset of physical qubits to decode the logical states. Reproduced from Ref. [145].

a focus on experimental ones on how to improve quantum annealing as an optimization algorithm:

1. Improving qubit coherence and understanding of noise. These are necessary in extending the coherent regime of QA to longer times and will very likely improve the multi-qubit tunneling rate.

2. Improve control capabilities. These are relevant for implementing the various annealing protocols proposed to avoid exponentially small gaps.

3. Developing novel interactions. These are relevant both as a tool towards reaching universality and classical intractability, as well as realizing error suppression.

4. Improving qubit connectivity. These are relevant for reducing the embedding overhead of solving real-world problems.

Relative to this list, this thesis makes progress on points 1, 2, and 4. In particular, Chapter 3 deals with flux crosstalk, which paves the way towards annealing with arbitrary schedules. Chapter 4 demonstrates an architecture for long-range interaction between flux qubits, which when extended to a network could enable high connectivity. Chapters 5 and 6 provide detailed characterization and modeling of noise on a single flux qubit and offers insights into the effect of noise on an annealer.

Chapter 3

Crosstalk calibration

Flux control is an important engineering resource for superconducting-qubit-based quantum computers. In gate-model quantum computing implementations, flux tunability is used to realize high-fidelity gates [150, 151, 152, 153, 154, 155, 156, 157], tunable couplers [53, 54, 158, 159, 160, 161, 162], avoiding frequency crowding [29] and two-level-system defects [163], For quantum annealers, flux-based control is essential [164] and independent dynamic flux control has been identified as an important resource for quantum enhancement [165, 166, 102, 167, 168, 108, 169].

Flux crosstalk in superconducting circuits arises due to the physical proximity between circuit elements and control lines, as well as reasons associated with the electromagnetic environment hosting the circuits, such as ground loops. For most large-scale superconducting circuits today, which are based on transmons, solving the calibration problem is often helped by the fact that transmons interact via the charge degree of freedom and the interaction strength is weak [170, 171, 172, 173]. Commercial quantum annealers rely on local magnetic memory elements to feed static flux to qubits and couplers, with crosstalk reduced using suitable integrated superconducting circuit design. Dynamic crosstalk is reduced because a single, global bias control acts all qubits to execute the annealing process. [164, 174].

The annealers developed in this thesis have individual controls for each qubit and coupler loop, allowing the exploration of novel annealing protocols. In this setting, calibration is challenging because of the strong flux interaction between circuit elements, which makes it hard to directly measure the coupling between bias lines and flux loops. In an alternative quantum annealer implementation using fluxmon qubits [65], the authors outlined a procedure for measuring crosstalk between two coupled fluxmons, based on fitting to analytical

circuit models. However, it is unclear whether the method could be easily extended to other systems, where it is hard to obtain an accurate analytical model.

In this chapter, we propose and implement two different methods to address this challenge. Both methods are circuit-model-independent and rely only on the symmetries of superconducting circuits. Hence, both of them can be readily applied to superconducting circuits used outside the context of this thesis, such as those used for GMQC.

In the first method, we rely on an iterative process to gradually improve calibration accuracy and minimize systematic errors due to inductive coupling between loops. This method is automated and implemented on two quantum annealing devices, containing 9 and 27 superconducting control loops respectively. We also introduce a method to characterize the error through a different set of measurements, which we executed on the smaller device. The error was measured to be lower than 0.17% for all crosstalk coefficients.

In the second method, crosstalk calibration of N flux channels is treated as N independent optimization problems, with the objective functions being the periodicity of a measured signal depending on the compensation parameters. The periodicity analysis is automated, allowing a closed-loop optimization to be performed. This method is implemented on a small-scale quantum annealing circuit with three loops, achieving comparable accuracy with the first method. We also show that the objective function usually has a nearly convex landscape, allowing efficient optimization.

The rest of this chapter is organized as follows. In Sec. 3.1, we begin with a formal description of the problem of flux crosstalk and the symmetries involved, which applies to both methods and arbitrary superconducting circuits with individual flux control. In Sec. 3.2 we give a brief account of the simple translation based method for crosstalk calibration, and why it is not suitable for strongly coupled circuits, such as the annealers. In Sec. 3.3 and 3.4 we introduce the device and the general methodology for the iterative method. The device is introduced first because the calibration method used in each iteration has some particularities to the device, though the general idea of exploiting symmetry and iteration is applicable to devices beyond those measured here. In Sec. 3.5 we discuss the experimental results of implementing the iterative method. Next in Sec. 3.6 we introduce the second method, later referred to as the periodicity optimization method. In Sec. 3.7 we discuss the experimental results for the periodicity optimization method. This is followed by conclusions for this chapter in Sec. 3.8. Additional details about circuit modeling and further experimental results for the two methods are given in Sec. 3.9 and 3.10.

3.1 The crosstalk problem and the symmetries

The properties of superconducting circuits depend on the external flux biases of the superconducting loops. For a superconducting circuit with N flux bias loops, the external fluxes are usually controlled by N bias lines, which are mutually coupled to the flux loops. We denote the external flux bias in loop i, reduced by the flux quantum Φ_0, as f_i, and the corresponding bias line current as I_i. The fluxes $\{f_i\}$ in all loops and currents $\{I_i\}$ on all bias lines can be written as vectors $\mathbf{f}$ and $\mathbf{I}$ respectively, and they are in general related by a linear transformation

$$\mathbf{f} = \mathbf{M}\mathbf{I} + \mathbf{f}_0, \tag{3.1}$$

where $\mathbf{M}$ is the $N \times N$ mutual matrix describing the coupling between bias lines and flux loops, and $\mathbf{f}_0$ is the vector of flux offsets arising from spurious sources. Often, and in particular in the context of our experiment, bias currents are controlled by voltage sources. For a more direct representation of the experiment, we will refer to the relation between fluxes and voltages, written as

$$\mathbf{f} = \mathbf{C}\mathbf{V} + \mathbf{f}_0, \tag{3.2}$$

where $\mathbf{V}$ is the vector of voltages with each element controlling the corresponding element in $\mathbf{I}$, and $\mathbf{C} = \mathbf{M}\mathbf{R}^{-1}$ with $\mathbf{R}$ a diagonal matrix consisting of the resistances between the voltage sources and the bias lines. From here onward we will work with voltage controls and the crosstalk matrix $\mathbf{C}$.

Measurements on the superconducting qubits can be considered as a function mapping the flux biases to the signal R_l, where l denotes a particular readout channel. Note that the number of readout channels is not restricted to the number of physical signal processing units; rather each channel corresponds to reading out the signal of an experiment, with a particular set of experimental parameters. The experiment could consist of one quadrature of a transmission measurement at a particular frequency or more complex experiments involving microwave excitations of the system.

Fundamentally there are two symmetries that one could exploit for calibration. First superconducting circuits respond periodically to external bias fluxes, with the period of one flux quantum [175, 176]. Second, the device possesses mirror symmetry with respect to the plane of the chip, meaning the response of the superconducting circuits should not change upon changing the sign of all external flux biases. We denote the readout data as $\mathbf{R}$, which is a vector with the dimension of the number of readout channels. Then the

periodicity and mirror symmetry condition can be formally stated as

$$\mathbf{R}(\{f_k\}) = \mathbf{R}(\{f_k + m_k\}) = \mathbf{R}(\{-f_k\}), \forall k = 1, 2, \ldots, N \tag{3.3}$$

where m_k is an integer.

3.2 Simple translation-based approach to flux crosstalk calibration

Most previously developed approaches to flux crosstalk calibration assume that one can identify a particular readout channel l that depends on the external flux in a single loop i, $R_l(\{f_k\}) \approx R_l(f_i)$. This allows estimating the coupling coefficient from bias line j to loop i, C_{ij}, by measuring the translation of R_l as a function of V_j. For this reason, we denote such calibration methods as the translation-based approach. When a simple model for $R_l(f_i)$ exists, the method becomes particularly effective as one only requires measurements at a few voltage bias values to extract the coupling parameters, and the model can be fitted to the data to obtain the coupling C_{ij}. This is the case for many calibration methods used in tunable transmons, with the readout channel being the frequency of the transmon or its readout resonator [170, 172], or the Ramsey phase shift [171, 172, 173]. However, this method would only work if the circuit elements interact weakly, and each superconducting loop can be sufficiently decoupled from the other loops. We also note that the work presented in Ref. [177] uses an optimization-based crosstalk calibration approach, however, this too relies on simplifying the full superconducting circuit to an effective description in terms of weakly coupled harmonic oscillators.

3.3 The iterative method: device

We experimentally demonstrate the iterative method on two devices consisting of tunable flux qubits, tunable couplers, and flux detectors. These devices are designed to explore high-coherence quantum annealing, based on coupled capacitively-shunted flux qubits (CSFQs) [161, 178]. A circuit schematic of the first device (device A) is shown in Fig. 3.1(a). It contains two CSFQs and a coupler. Each qubit is formed of a main loop and a secondary loop, named z-loop and x-loop respectively, in line with their functionality to control the corresponding Pauli terms in the persistent current basis. The coupler has a similar configuration, with a main inductive loop and a secondary split Josephson junction loop. In

analogy to the qubit, these loops are named z-loop and x-loop respectively as well. The z-loop of the coupler is inductively coupled to the qubits' z-loop, thus acting as a tunable coupler [55, 161]. A set of bias lines is used, with each line designed to couple primarily to a corresponding loop.

Flux readout devices are coupled to each of the qubits and the coupler. Readout of the persistent current of the qubits is required for standard annealing experiments [62, 179]. The additional flux readout of the coupler was added here to aid with the calibration of the operation point of the coupler. Each readout device is formed of a tunable rf-SQUID terminating a coplanar waveguide resonator (see Fig. 3.1(a)), with the rf-SQUID loop coupled to the corresponding z-loop of each qubit or the coupler. The resonators are coupled to a common transmission line. They can be probed by sending a microwave signal at probe frequency ω_p through the transmission line and measuring the complex transmission coefficient S_{21}. In the semi-classical picture, the persistent current in the qubit or coupler z-loop generates fluxes threading the resonator rf-SQUID, which changes its effective inductance, leading to a change in the resonator's resonance frequency. For a weak enough probing signal, the magnitude of the transmission $|S_{21}|$ has a minimum when ω_{p} coincides with the resonator's resonance frequency.

Device B consists of two CSFQs coupled by a chain of seven tunable rf-SQUID couplers. Each coupler has its z-loop coupled to its neighboring couplers or qubits. The seven couplers act as a coupler chain that mediates flux signals between the end qubits. Fig. 3.1(b) shows a cartoon representation of this device. It has the potential to realize long-range coupling without trading it off with coherence(see Chapter 4).

The devices are fabricated at MIT Lincoln Laboratory, based on the fabrication process outlined in Ref. [180], combining a high coherence chip hosting qubits, an interposer chip, and a multi-layer chip for control and readout wiring. In the work presented here, the devices were realized using only the qubit and interposer chips (see Fig. 3.1 (c,d)), as a preliminary step towards high-density annealing circuits including the full three-tier process described in Refs. [180, 181].

Each device is placed in a sample holder anchored to the mixing chamber plate of a dilution refrigerator. All on-chip flux bias lines are connected to arbitrary waveform generators (AWGs) operating at room temperature through twisted-pair wiring. The connections are appropriately attenuated at room temperature to generate a flux range of a few flux quanta (see Appendix B for a complete wiring diagram).

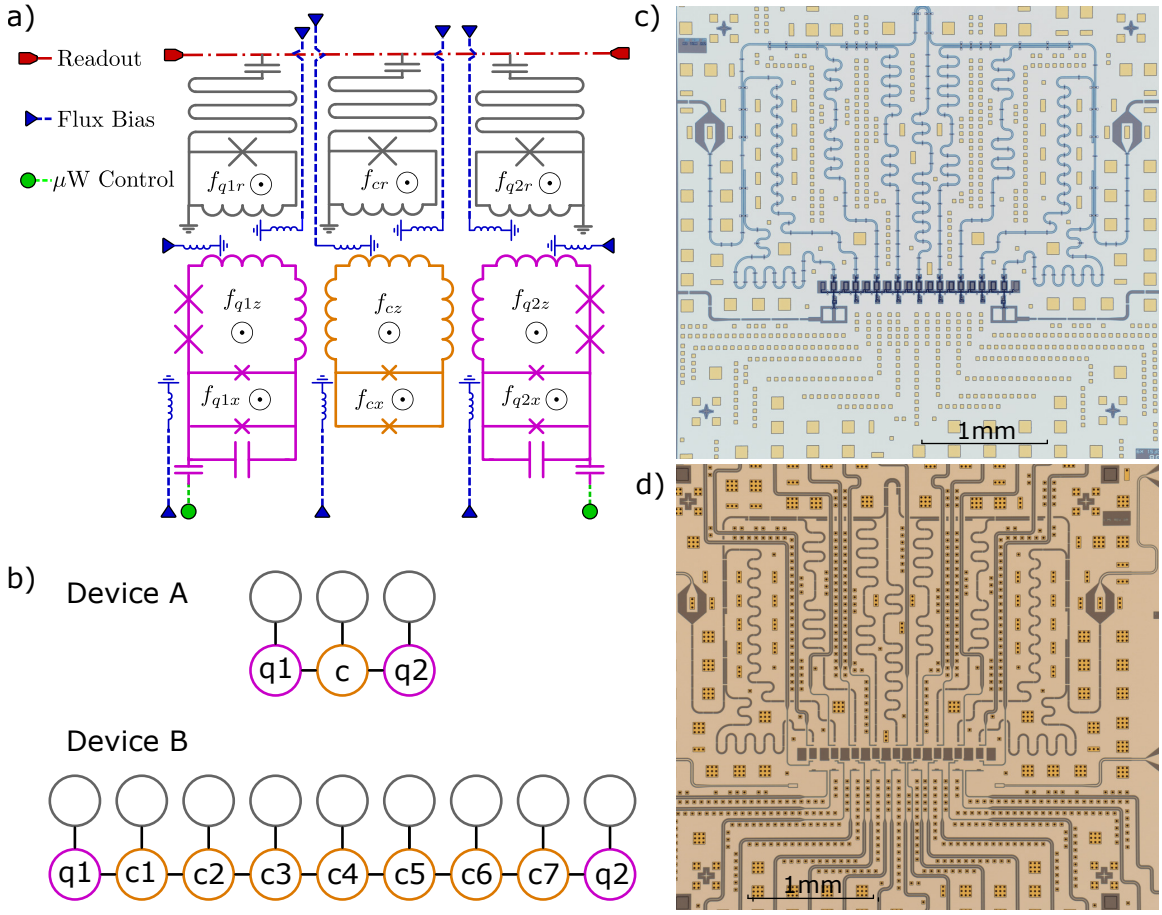

Figure 3.1: (a) Circuit schematic of device A. The qubit circuits (left and right, purple) are tunable CSFQs. The coupler circuit (middle, orange) is a tunable rf-SQUID. Each qubit and coupler has two control loops and is coupled to a tunable resonator (top, gray). All resonators are coupled to a joint feedline (top, red). Fluxes in each loop are controlled via the on-chip bias lines (triangles, blue). The design also includes microwave control by capacitively coupling microwave lines (circle, green) to the qubit, allowing for spectroscopy measurement of the device (not used in this work). (b) Diagram representation of devices A and B. Device A contains two qubits (left and right units, purple), the coupler (insider cell, orange), and a tunable resonator for each cell (top, gray). Device B contains two qubits and seven couplers. Device B has the same qubit and coupler circuit schematic and control capabilities as device A, shown in panel (a). (c, d) Microscope image of the qubit and interposer chips of device B. The qubit chip (c) hosts the qubit and readout circuitry and the interposer chip (d) hosts the flux bias lines. The square features (yellow boxes) correspond to indium bumps used to connect the two chips.

3.4 The iterative method: methodology

In general terms, the iterative method works as follows. In the first iteration, it is assumed that when one bias voltage is changed, it only changes the external flux of the loop being addressed, while changes in external fluxes in other loops do not cause any appreciable change in the measured quantity. Using the estimates from the first iteration, subsequent iterations can improve the accuracy of these estimates.

Devices A and B have a design commonality, in that, qubits and couplers are similar circuits, each coupled to a flux tunable resonator. It is useful to group each qubit or coupler with its resonator into a unit cell. This makes it so that each cell has three superconducting loops; z, x on the qubit or coupler, and r on the resonator rf-SQUID. We use $C_{p\alpha,q\beta}$ to represent the flux to voltage ratio between the bias line β in cell q and the loop α in cell p, where $\alpha, \beta \in \{z, x, r\}$ and $p, q \in [1, m]$. Here m is the total number of unit cells, given by $m = 3(9)$ for device A(B). The flux offset in loop α in cell p is denoted by $f_{0,p\alpha}$. Similarly, $f_{p\alpha}$ ($V_{p\alpha}$) represents the flux (voltage) on loop (bias line) α in cell p. This double index notation facilitates the analysis of this circuit, where each readout resonator is nominally coupled to each qubit or coupler. However, the methods discussed below apply to more general circuits. Note that we continue to sometimes use the single index notation (V_i, f_i, and $C_{i,j}$) below. The difference between the single and the double index notations should be clear from the context.

Distinguishing between estimated values and the corresponding variables is very important in particular in the discussion of the iterative procedure below. We use a prime to denote the estimated value for a specific quantity. For example, $C'_{p\alpha,q\beta}$ refers to the estimated value for $C_{p\alpha,q\beta}$. With the estimated coupling matrix and the estimated flux offsets, we can define an estimated flux vector $\mathbf{f}'$ as

$$\mathbf{f}' = \mathbf{C}'\mathbf{V} + \mathbf{f}'_0. \tag{3.4}$$

In the subsections below, we first introduce the procedure for one iteration and then discuss how further iterations are carried out.

3.4.1 CISCIQ

We devise a procedure to obtain estimates of the coupling matrix named CISCIQ (an acronym for "crosstalk into SQUIDs, crosstalk into qubit"). In general terms, it consists of

first measuring the coupling elements between bias lines and the SQUID detectors, which is subsequently used to keep the resonator SQUID at nearly fixed operation points, as needed in order to maintain a consistent level of sensitivity to changes in the states of qubits and couplers induced by external biases. This procedure has four stages, discussed below.

Stage 1. In the first stage, the resonator direct bias element $C_{pr,pr}$ is measured for each unit p. Ignoring the resonator interaction with other quantum elements (qubits, couplers, or other resonators), the resonator frequency is periodic with respect to its own bias line control voltage. By measuring the resonator spectrum as a function of its own bias voltage, we can extract its periodicity, denoted by P_{pr}, and the voltage coordinate corresponding to zero flux in the resonator SQUID, denoted by V^*_{pr}. Based on these quantities, we estimate

$$C'_{pr,pr} = \frac{1}{P_{pr}}, \text{ and } f'_{0,pr} = -\frac{V^*_{pr}}{P_{pr}}. \tag{3.5}$$

Stage 2. In the second stage, the crosstalk coefficients $C_{pr,q\alpha}$ for all p, q, α are measured. A similar measurement as in Stage 1 is carried out. All voltages except $V_{q\alpha}$ and V_{pr} are set to zero. The readout response is measured as a function of V_{pr} for a set of different values of $V_{q\alpha}$. The added flux in the probed resonator due to crosstalk from $V_{q\alpha}$ shifts the resonator frequency as a function of V_{pr}. For δV_{pr} amount of shift per $\delta V_{q\alpha}$, the crosstalk element is given by

$$C'_{pr,q\alpha} = -C'_{pr,pr}\frac{\delta V_{pr}}{\delta V_{q\alpha}}. \tag{3.6}$$

Stage 3. After Stage 2, we have control of the fluxes in the resonator SQUIDs from all the bias lines. In Stage 3, the 3×3 sub-matrix formed of the elements $C_{p\alpha,p\beta}$ and the flux offsets $f_{0,pz}, f_{0,px}$ for each unit p are measured. In the remainder of this stage, $V_{q\alpha}$ for all $q \neq p$ and all α are set to zero. To simplify notation, the subscript denoting the cell index is dropped since we are only concerned with intra-unit crosstalk. With this simplified notation we write

$$\begin{pmatrix} f_z \\ f_x \\ f_r \end{pmatrix} = \begin{pmatrix} C_{z,z} & C_{z,x} & C_{z,r} \\ C_{x,z} & C_{x,x} & C_{x,r} \\ C_{r,z} & C_{r,x} & C_{r,r} \end{pmatrix} \begin{pmatrix} V_z \\ V_x \\ V_r \end{pmatrix} + \begin{pmatrix} f_{0,z} \\ f_{0,x} \\ f_{0,r} \end{pmatrix}. \tag{3.7}$$

This stage consists of two measurements. In *measurement (a)*, we measure the fluxes in the qubit or coupler, f_z and f_x by measuring the coupled resonator's transmission at a fixed frequency, while sweeping x and z bias voltages, V_x, V_z. During the measurement, the resonator flux bias needs to be fixed, leading to a constraint on the resonator bias voltage,

$$f'_r = \sum_\alpha C'_{r,\alpha} V_\alpha + f'_{0,r} = 0, \tag{3.8}$$

where f'_r is the approximate resonator flux from external sources, given by the estimates from Stages 1 and 2. Note that the errors in the estimates of Stages 1 and 2 lead to uncompensated crosstalk into the resonator, which can affect the measured transmission, in addition to the changes in transmission due to the changes in f_z and f_x. To avoid this complication, we choose to fix f'_r to zero, which makes the resonator first order insensitive to the residual uncompensated crosstalk, allowing us to associate the change in transmission solely with changes in f_z and f_x. While setting the resonator flux bias away from zero can increase the overall interaction strength between the resonator and qubit or coupler, potentially leading to more sensitive measurement, we empirically find the benefits of avoiding complication due to uncompensated crosstalk outweighs the cost of slightly weaker sensitivity.

Since V_r is constrained to satisfy the requirements on f'_r, the 3-dimensional voltage and flux space are reduced to an effective 2-dimensional relation, such that

$$\begin{pmatrix} f_z \\ f_x \end{pmatrix} = \begin{pmatrix} C^{\text{eff}}_{z,z} & C^{\text{eff}}_{z,x} \\ C^{\text{eff}}_{x,z} & C^{\text{eff}}_{x,x} \end{pmatrix} \begin{pmatrix} V_z \\ V_x \end{pmatrix} + \begin{pmatrix} f^{\text{eff}}_{0,z} \\ f^{\text{eff}}_{0,x} \end{pmatrix}. \tag{3.9}$$

Specifically, the effective matrix and offsets are related to the actual matrix elements and

offsets via

$$C^{\text{eff}}_{z,z} = C_{z,z} - \frac{C'_{r,z}C_{z,r}}{C'_{r,r}}, \tag{3.10}$$

$$C^{\text{eff}}_{z,x} = C_{z,x} - \frac{C'_{r,x}C_{z,r}}{C'_{r,r}}, \tag{3.11}$$

$$C^{\text{eff}}_{x,z} = C_{x,z} - \frac{C'_{r,z}C_{x,r}}{C'_{r,r}}, \tag{3.12}$$

$$C^{\text{eff}}_{x,x} = C_{x,x} - \frac{C'_{r,x}C_{x,r}}{C'_{r,r}}, \tag{3.13}$$

$$f^{\text{eff}}_{0,z} = f_{0,z} + \frac{C_{z,r}}{C'_{r,r}}(f'_r - f'_{0,r}) \text{ and} \tag{3.14}$$

$$f^{\text{eff}}_{0,x} = f_{0,x} + \frac{C_{x,r}}{C'_{r,r}}(f'_r - f'_{0,r}). \tag{3.15}$$

Measurement (a) can be shown to have point reflection symmetry about every half-integer flux point due to both symmetries about the chip plane and periodicity in external fluxes (see Sec. 3.9.1). These points form a lattice and allow us to find the affine transformation defined by the effective matrix $\mathbf{C}^{\text{eff}}$ and the effective flux offsets $f^{\text{eff}}_{0,z}, f^{\text{eff}}_{0,x}$. However, as implied by Eqs. (3.10)-(3.15), knowing the effective matrix and offsets is insufficient to determine the complete set of coupling coefficients for this unit. Hence another measurement is needed.

Stage 3 *measurement (b)* repeats *measurement (a)*, but setting $f'_r = \pm 1$. Since the resonator flux is changed by 1 Φ_0, due to the flux periodicity, the resonator response remains the same, up to some translation in the V_x, V_z coordinates. Such translations could be understood in terms of the change in effective flux offsets of the $z(x)$ loop, $f^{\text{eff}}_{0,z(x)}$ due to crosstalk from the resonator bias line. From Eqs. (3.14) and (3.15), we can write the change in effective flux offset $\delta f^{\text{eff}}_{0,z(x)}$ due to change in resonator flux $\delta f'_r$ as,

$$\delta f^{\text{eff}}_{0,z(x)} = \frac{C_{z(x),r}}{C'_{r,r}}\delta f'_r. \tag{3.16}$$

Measurement of the offset shift $\delta f^{\text{eff}}_{0,z(x)}$ is used to determine $C_{z(x),r}/C'_{r,r}$, which in combination with Eqs. (3.10)-(3.15) enables identifying all the coupling elements and flux offsets in a unit cell.

To extract the offset shifts $\delta f^{\text{eff}}_{0,z}$ and $\delta f^{\text{eff}}_{0,x}$, an effective procedure is to rely on the shifts of the measured two-dimensional datasets quantified along the V_z and V_x coordinates. These

shifts are denoted by δV_z and δV_x respectively and are related to the effective offset shifts via

$$\begin{pmatrix} \delta f_{0,z}^{\text{eff}} \\ \delta f_{0,x}^{\text{eff}} \end{pmatrix} = \begin{pmatrix} (C_{z,z}^{\text{eff}})' & (C_{z,x}^{\text{eff}})' \\ (C_{x,z}^{\text{eff}})' & (C_{x,x}^{\text{eff}})' \end{pmatrix} \begin{pmatrix} -\delta V_z \\ -\delta V_x \end{pmatrix}. \tag{3.17}$$

Combining Eqs. (3.16) and (3.17) gives

$$\begin{pmatrix} C'_{z,r} \\ C'_{x,r} \end{pmatrix} = C'_{r,r} \begin{pmatrix} (C_{z,z}^{\text{eff}})' & (C_{z,x}^{\text{eff}})' \\ (C_{x,z}^{\text{eff}})' & (C_{x,x}^{\text{eff}})' \end{pmatrix} \begin{pmatrix} -\frac{\delta V_z}{\delta f'_r} \\ -\frac{\delta V_x}{\delta f'_r} \end{pmatrix}. \tag{3.18}$$

Then by inverting Eqs. (3.10)-(3.15), the actual 2-dimensional qubit or coupler coupling and offsets can be written in terms of the effective matrix elements and offsets,

$$\begin{pmatrix} C'_{z,z} & C'_{z,x} \\ C'_{x,z} & C'_{x,x} \end{pmatrix} = \begin{pmatrix} (C_{z,z}^{\text{eff}})' & (C_{z,x}^{\text{eff}})' & \frac{C'_{z,r}}{C'_{r,r}} \\ (C_{x,z}^{\text{eff}})' & (C_{x,x}^{\text{eff}})' & \frac{C'_{x,r}}{C'_{r,r}} \end{pmatrix} \begin{pmatrix} 1 & 0 \\ 0 & 1 \\ C'_{r,z} & C'_{r,x} \end{pmatrix}, \tag{3.19}$$

$$f'_{0,z} = (f_{0,z}^{\text{eff}})' + \frac{C'_{z,r}}{C'_{r,r}} f'_{0,r} \text{ , and} \tag{3.20}$$

$$f'_{0,x} = (f_{0,x}^{\text{eff}})' + \frac{C'_{x,r}}{C'_{r,r}} f'_{0,r}. \tag{3.21}$$

To summarize Stage 3, *measurement (a)* allows us to estimate the effective 2×2 matrix $\mathbf{C}^{\text{eff}}$ and the effective flux offsets $f_{0,z}^{\text{eff}}, f_{0,x}^{\text{eff}}$, and *measurement (b)* extracts the shifts of the resonator response as a function of V_z, V_x. Together with the results from Stages 1 and 2, they complete the flux offsets and 3×3 block diagonal matrix in each unit cell.

Stage 4. In the last stage, all the remaining crosstalk elements are measured. This is done by performing a measurement similar to Stage 3 *measurement (b)* for each cell p, but this time stepping an out-of-cell bias voltage $V_{q\alpha}$. To fix the resonator flux bias during the measurement, the resonator bias voltage for cell p, V_{pr} is constrained so that

$$f'_{pr} = \sum_{\beta \in \{z,x,r\}} C'_{pr,p\beta} V_{p\beta} + C'_{pr,q\alpha} V_{q\alpha} + f'_{0,pr} = 0. \tag{3.22}$$

Changes in $V_{q\alpha}$ induce shifts of the measured response in the V_{pz}, V_{px} plane. To find the relation between the crosstalk elements and the shifts, we consider the change in the z and x fluxes in cell p, δf_{pz} and δf_{px} due to changes in the bias voltages $\delta V_{pz}, \delta V_{px}$ and $\delta V_{q\alpha}$. They are given by

$$\begin{pmatrix} \delta f_{pz} \\ \delta f_{px} \end{pmatrix} = \begin{pmatrix} C^{\text{eff}}_{pz,pz} & C^{\text{eff}}_{pz,px} & C^{\text{eff}}_{pz,q\alpha} \\ C^{\text{eff}}_{px,pz} & C^{\text{eff}}_{px,px} & C^{\text{eff}}_{px,q\alpha} \end{pmatrix} \begin{pmatrix} \delta V_{pz} \\ \delta V_{px} \\ \delta V_{q\alpha} \end{pmatrix}, \tag{3.23}$$

where we introduced $C^{\text{eff}}_{pz,q\alpha}$ and $C^{\text{eff}}_{px,q\alpha}$, given by

$$C^{\text{eff}}_{pz,q\alpha} = C_{pz,q\alpha} - C'_{pz,pr}\frac{C'_{pr,q\alpha}}{C'_{pr,pr}}, \text{ and} \tag{3.24}$$

$$C^{\text{eff}}_{px,q\alpha} = C_{px,q\alpha} - C'_{px,pr}\frac{C'_{pr,q\alpha}}{C'_{pr,pr}}. \tag{3.25}$$

A change $\delta V_{q\alpha}$ in the out-of-cell bias voltage $q\alpha$ induces shifts $\delta V_{pz}, \delta V_{px}$ in the resonator response. The effective crosstalk elements can be found by setting $\delta f_{pz} = \delta f_{px} = 0$ in Eq. (3.23), yielding

$$\begin{pmatrix} \left(C^{\text{eff}}_{pz,q\alpha}\right)' \\ \left(C^{\text{eff}}_{px,q\alpha}\right)' \end{pmatrix} = \begin{pmatrix} (C^{\text{eff}}_{pz,pz})' & (C^{\text{eff}}_{pz,px})' \\ (C^{\text{eff}}_{px,pz})' & (C^{\text{eff}}_{px,px})' \end{pmatrix} \begin{pmatrix} -\frac{\delta V_{pz}}{\delta V_{q\alpha}} \\ -\frac{\delta V_{px}}{\delta V_{q\alpha}} \end{pmatrix}. \tag{3.26}$$

Finally, combining Eqs. (3.25) and (3.26) gives

$$\begin{aligned} \begin{pmatrix} C'_{pz,q\alpha} \\ C'_{px,q\alpha} \end{pmatrix} = & \begin{pmatrix} (C^{\text{eff}}_{pz,pz})' & (C^{\text{eff}}_{pz,px})' \\ (C^{\text{eff}}_{px,pz})' & (C^{\text{eff}}_{px,px})' \end{pmatrix} \begin{pmatrix} -\frac{\delta V_{pz}}{\delta V_{q\alpha}} \\ -\frac{\delta V_{px}}{\delta V_{q\alpha}} \end{pmatrix} \\ & + \begin{pmatrix} C'_{pz,pr}\frac{C'_{pr,q\alpha}}{C'_{pr,pr}} \\ C'_{px,pr}\frac{C'_{pr,q\alpha}}{C'_{pr,pr}} \end{pmatrix}. \end{aligned} \tag{3.27}$$

3.4.2 Limitations of CISCIQ

The CISCIQ procedure relies on assuming that when a circuit element (a qubit, coupler, or SQUID) is measured, its properties as a function of an externally applied flux are negligibly affected by the interaction with other circuit elements. For example, in Stage 1, it is assumed that the tunable resonator frequency is periodic in its own bias voltage.

However, due to crosstalk from the resonator bias line to the coupler loop, the coupler properties change over the range of the resonator bias swept, which in turn changes the resonator due to their inductive interaction. In Stage 2, while the coupler z bias is swept, its resonator SQUID flux changes not only because of the finite crosstalk from the z bias line to the SQUID loop but also because of the state of the coupler changing.

To illustrate the expected role of circuit interactions, we use a simple model to calculate the effect of the resonator-coupler interaction on the resonator response. The interaction is modeled via the inductive loading of the rf-SQUID inductance by the coupler effective quantum inductance. We consider a single coupler-resonator cell, and assume only coupling between the r and z bias lines and the resonator and coupler loops. By numerically finding the coupler circuit's effective inductance and solving the classical rf-SQUID equation, the resonator spectrum in terms of the resonator and coupler z bias can be calculated (see Sec. 3.9.2 for additional details). Figure 3.2 shows the resonator spectrum as a function of its bias voltage V_r, for two different values of coupler z bias voltage V_z. The dominant feature is the resonator frequency change due to a change in its own bias. However, due to crosstalk, the coupler flux bias also changes as a function of V_r, which changes its inductive loading effect on the resonator and hence the resonator frequency. Therefore the translational symmetry in V_r that is used for calibration in Stages 1 and 2 is broken. We note here that the inductive loading model does not capture the full interaction between the resonator and coupler, rather it serves as an example to highlight the increased complexity of calibration due to strong interactions between circuit elements.

The above analysis can be extended to other stages of CISCIQ, where the coupler's effective inductance loads the qubit and the coupler ground state current acts as an effective bias seen by the qubit. Based on the single qubit and coupler persistent current and their mutual inductances, such an effect could produce an error of tens of $\mathrm{m}\Phi_0$ (see Sec. 3.9.3). While it is possible to develop models to capture the interaction for small systems, developing an accurate model for a large system is a daunting task. Apart from the qubit-coupler, qubit-resonator, or coupler-resonator interactions, since the different resonators are coupled to a single transmission line for readout, resonance collisions also distort the readout signal. Larger devices are particularly prone to this problem. Therefore, CISCIQ alone does not provide a good enough measurement of the coupling matrix and flux offsets.

3.4.3 CISCIQi

To reduce the errors in calibration coefficients found with CISCIQ, which are due to the systematic effects discussed in the previous subsection, we propose an iterative approach,

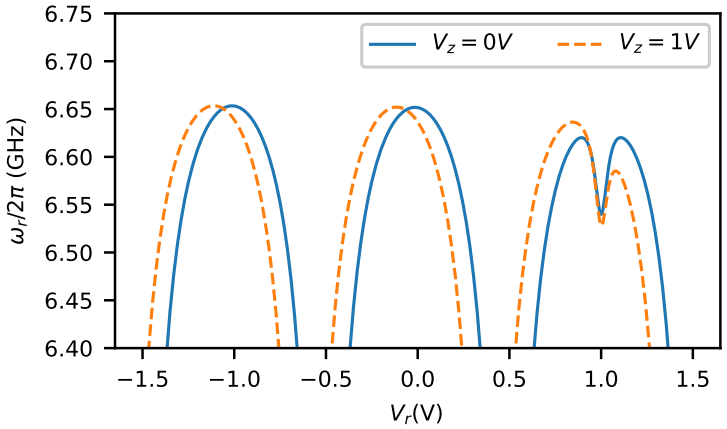

Figure 3.2: The simulated readout resonator spectrum as a function of its bias voltage, using the inductive loading model to describe the interaction between the resonator and the coupler (see text). The solid (blue) and orange (dashed) lines correspond to the coupler coupled to the resonator being biased at two different V_z values, of 0 and 1 Volt respectively. The coupling coefficients and flux offsets used for this model are $C_{z,z} = C_{r,r} = 1\ \Phi_0/V, C_{r,z} = C_{z,r} = 0.1\ \Phi_0/V, f_{0,r} = 0, f_{0,z} = 0.4$, which are realistic in our devices. Translational symmetry is broken due to the coupler resonator interaction.

abbreviated as CISCIQi. With this procedure, the measured coupling coefficients and flux offsets from CISCIQ are taken as an initial estimate. Further iterations of CISCIQ are carried out to gradually improve the initial estimates. In each iteration, one controls directly not the voltages but a set of new coordinates - which are the fluxes applied to the loops, calculated based on the estimated coupling coefficients and offsets. More specifically, the first iteration can be considered as giving the estimates of $\mathbf{C}$ and $\mathbf{f}_0$ as $\mathbf{C}^{(1)\prime}$ and $\mathbf{f}_0^{(1)\prime}$ respectively. In the absence of interactions between individual qubits, coupler, and resonator circuits, these estimates are accurate, limited only by experimental noise. However, this is not the case for the reasons explained in the previous section. Nevertheless, the quantities

$$\mathbf{f}^{(1)} = \mathbf{C}^{(1)\prime}\mathbf{V} + \mathbf{f}_0^{(1)\prime}, \tag{3.28}$$

where $\mathbf{C}^{(1)\prime}$ and $\mathbf{f}_0^{(1)\prime}$ are the estimates of the coupling matrix and flux offsets obtained from iteration 1, are a good approximation for fluxes in the loops. Then the flux relation in Eq. (3.2) can be recast into the form

$$\mathbf{f} = \mathbf{C}^{(2)}\mathbf{f}^{(1)} + \mathbf{f}_0^{(2)} \tag{3.29}$$

where we introduced

$$\mathbf{C}^{(2)} = \mathbf{C}\left(\mathbf{C}^{(1)\prime}\right)^{-1} \tag{3.30}$$

and

$$\mathbf{f}_0^{(2)} = -\mathbf{C}\left(\mathbf{C}^{(1)\prime}\right)^{-1}\mathbf{f}_0^{(1)\prime} + \mathbf{f}_0. \tag{3.31}$$

The task in iteration 2 is to estimate $\mathbf{C}^{(2)}$ and $\mathbf{f}_0^{(2)}$ by sweeping the components of $\mathbf{f}^{(1)}$ and measuring the circuit response. Because the basis vectors in the estimated flux coordinate $\mathbf{f}^{(1)}$, as compared to those in the voltage coordinates V, are closer to the corresponding basis vectors in the real flux coordinates $\mathbf{f}$, the assumptions made in CISCIQ on periodicity with respect to controls are better justified. For example, when repeating Stage 1 during iteration 2, the resonator frequency as a function of $f_{pr}^{(1)}$ has smaller departures from periodicity than $f_{pr}^{(1)}$ as a function of V_{pr} in iteration 1. In Stage 2, one measures the crosstalk from a source bias to a target resonator by stepping the source biases with integers of flux quanta according to the estimated coupling coefficients. By doing this the resonator spectrum better obeys translational symmetry over different source bias settings, because the effect of the interactions with the rest of the circuit is reduced when changes in applied fluxes are close to the circuit periodicity. In Stage 3, the data is expected to have better point reflection symmetry in the $f_{pz}^{(1)}, f_{px}^{(1)}$ plane as compared to V_{pz}, V_{px}. In

Stage 4, similarly to Stage 2, we choose integer flux quanta steps in the crosstalk source bias to null out modulations within a period. In all stages, resonance collisions become less likely in the second iteration, as the resonators' bias points are better controlled, due to the reduced changes in flux coupled from other elements.

At the n-th iteration, this procedure yields the estimates for the coupling matrix $\mathbf{C}^{(n)\prime}$ and the offset vector $\mathbf{f}_0^{(n)\prime}$. Combining the coupling matrix and offsets measured at each iteration, the estimates after n iterations for the coupling matrix and the flux offset are

$$\mathbf{C}' = \mathbf{C}^{(n)\prime}\mathbf{C}^{(n-1)\prime}\dots\mathbf{C}^{(1)\prime} \tag{3.32}$$

and

$$\mathbf{f}_0' = \mathbf{C}^{(n)\prime}\left(\mathbf{C}^{(n-1)\prime}\left(\dots\left(\mathbf{C}^{(2)\prime}\mathbf{f}_0^{(1)\prime} + \mathbf{f}_0^{(2)\prime}\right) + \dots\right) + \mathbf{f}_0^{(n-1)\prime}\right) + \mathbf{f}_0^{(n)\prime}. \tag{3.33}$$

3.4.4 Fast offsets calibration

The coupling matrix is expected to remain constant in the course of an experiment while the device is kept cold inside a dilution refrigerator. However, the flux offsets change over time due to flux noise and trapped flux. Therefore a time-efficient method is desired to recalibrate flux offsets. Here we introduce such a procedure, which relies on the knowledge of the estimate of the coupling matrix, assumed to remain constant. The method makes use of similar measurements as in Stages 1 and 3 of CISCIQ. To measure the offset of the resonator, the corresponding approximate flux coordinate f'_{pr} is swept around 0, and at each flux setting the resonator transmission is measured over a frequency range around resonance. The signal is expected to be mirror reflection symmetric about a value, denoted by f'^{*}_{pr}, which corresponds to the flux in the resonator being equal to zero. Based on this, the new estimated flux offset is related to the old estimated flux offset $f'_{0,pr}$ by

$$f'_{0,pr} \to f'_{0,pr} - f'^{*}_{pr}. \tag{3.34}$$

Similarly, to find the new offset of the qubit or coupler, the estimated flux coordinates f'_{pz}, f'_{px} are swept while probing resonator transmission close to the peak frequency of the resonator for unit p. The signal is point reflection symmetric about some point $(f'^{*}_{pz}, f'^{*}_{px})$. The new estimated flux offset and the old ones are related analogously to the resonator offset in Eq. (3.34). If this set of measurements reveals that the offset drifts are large, the procedure can be iterated to eliminate the apparent offset shifts due to circuit interactions.

3.4.5 The error of the calibration procedure

There are several sources of errors for the CISCIQi calibration procedure. Firstly, all the data collected has noise contributions from the microwave amplifiers, and flux drifts occur while taking the data. Secondly, the fitting algorithms applied to identify translational and point reflection symmetries have estimate errors arising from the finite range and sampling for the collected data. Last and most significantly, systematic errors arise from circuit interactions, which are only partially mitigated even after the application of multiple iterations in the calibration procedure. To characterize the errors in the crosstalk matrix and flux offsets considering all the sources of errors is therefore a complex task. Conventional error propagation analysis is not suitable for our method because the output of the analysis, i.e. the periodicities and translations extracted, depends linearly on the coupling coefficients, as well as nonlinearly on the interactions between circuit elements. As an example, Stage 3(b) measurement of CISCIQ relies on couplings measured in Stage 1 and 2. The errors in the resonator bias from Stage 1 and 2 would result in resonator frequencies being different for $f'_r = 0, \pm 1$ when doing Stage 3 measurements. This causes transmissions at different resonator flux biases not being simply translated versions of each other. The errors in the extracted translations and crosstalk in Stage 3 thus have a substantially nonlinear dependence on the errors from Stage 1 and 2. Given the above consideration, we propose an error characterization method that is motivated by the purpose of crosstalk calibration, which is to gain independent control of each flux bias.

The error characterization relies on a set of measurements performed to determine to what extent the fluxes can be controlled independently. Ideally, when a change $\Delta f'_j$ in the estimated flux f'_j is applied to loop j, the flux in other loops should remain unaffected. Any change in flux can be conveniently measured using the abbreviated offset measurement procedure discussed in Sec. 3.4.4. For $i, j \in [1, N], i \neq j$, the quantity

$$\Theta_{i,j} = \frac{\Delta f'_{0,i}}{\Delta f'_j} \tag{3.35}$$

is a measure of the remaining control crosstalk. To measure this quantity in a way that is robust against systematic errors from circuit interactions, one can set $\Delta f'_j$ to be integer flux quanta. This leads to a reduced effect of circuit interaction, due to their periodic dependence on applied fluxes.

3.5 The iterative method: experiments

3.5.1 Implementation of the CISCIQ method

In this section we discuss the experimental implementation of the first iteration in the CISCIQi iterative procedure. We discuss this iteration in detail, given that the analysis tools carry over to subsequent iterations. We present measurements for calibration of device A as examples. Measurements on device B are carried out similarly.

Stage 1

In Stage 1, for each resonator, the transmission is measured versus the probe frequency and resonator bias voltage. The voltage bias sweep is chosen to cover a few flux quanta, in order to allow determination of the periodicity. We note that in the first iteration we choose bias voltage ranges that are relatively large, to allow determining the period in the presence of relatively strong, uncompensated spurious flux generated by other circuit elements.

Figure 3.3(a) shows a color plot of the transmission magnitude versus bias voltage and probe frequency. At resonance, the magnitude of transmission has a dip relative to the background. To extract the periodicity and offset, one could extract the resonance frequencies as a function of bias voltage and fit it to the resonator model or a simpler periodic function. However, this method becomes difficult to automate due to the presence of other features in the transmission arising from other readout resonators and spurious package resonances. In addition, fitting the transmission requires small frequency steps and an analytical transmission model can be hard to obtain when the tunable resonator is driven at high power. Hence, an image-processing-based method is used instead. The transmission data can be considered as an image with the first dimension being the bias voltage V_{cr}, the second dimension being the probe frequency ω_p, and the third dimension being the magnitude of the transmission $|S_{21}|$. Before extracting the period of the data, edge detection techniques are applied to enhance the resonance features (see Sec. 3.10.1). To extract the period of the resonator bias, recurrence plot analysis is used [182]. Recurrence plots are a method to visualize symmetries in time series data and are adapted here to identify periodicities within an image and translations between two different images. Given two

images $A(i_1, i_2)$ and $B(j_1, j_2)$, the recurrence plot is a new dataset $R(i_1, j_1)$ defined as

$$R(i_1, j_1) = \begin{cases} 1, \text{if} \sqrt{\sum_{i_2, j_2} (A_{i_1, i_2} - B_{j_1, j_2})^2 \delta_{i_2, j_2}} \leq \epsilon \\ 0, \text{otherwise} \end{cases}, \tag{3.36}$$

where δ_{i_2, j_2} is the Kronecker delta and ϵ is a threshold chosen to maximize the contrast in the recurrence plot (see Sec. 3.10.1). The arguments in A, B, and R are integer-valued indices. We apply the recurrence plot to the case where both the A and B images are the acquired dataset. The y-intercept of 45-deg lines in the plot corresponds to the amount of translation needed on one of the images to overlap with the other. We use line detection via the Hough transform to extract the translations from the recurrence plot. An example resonator transmission image and its corresponding recurrence plot are shown in Fig. 3.3(a) and (b).

To extract the flux offset, the reflection symmetry of the data is analyzed. The measured transmission magnitude $|S_{21}|$ can be considered as an image $A(i_1, i_2)$ of dimensions (m_1, m_2). The correlation coefficients between image A and its reflection about all bias indices are calculated. The reflected image $B(i_1, i_2; j)$ about a particular bias index j is given by

$$B(i_1, i_2; j) = A(2j - i_1, i_2). \tag{3.37}$$

The correlation coefficient $\rho(j)$ is given by

$$\rho(j) = \frac{\sum_{i_1, i_2} [A(i_1, i_2) - \bar{A}(j)][B(i_1, i_2; j) - \bar{B}(j)]}{\sqrt{\sum_{i_1, i_2} [A(i_1, i_2) - \bar{A}(j)]^2 \sum_{i_1, i_2} [B(i_1, i_2; j) - \bar{B}(j)]^2}}, \tag{3.38}$$

where the summations range over $i_1 \in [\text{Max}(1, 2j - m_1), \text{Min}(m_1, 2j - 1)]$ and $i_2 \in [1, m_2]$, and $\bar{A}(j), \bar{B}(j)$ are the average values of A, B over the same range. The ranges serve to pick out the overlap region between the original and reflected images. The correlation coefficient used here is adapted from the Pearson correlation coefficient applied to samples. It is normalized to lie between $[-1, 1]$, so images with different overlap sizes can be fairly compared. The peaks in $\rho(j)$ correspond to points of reflection symmetry in the image, identified with half and whole integer flux quanta in the resonator loop. Figure 3.3(c) shows the result of this calculation. Finally, the integer flux quanta points can be distinguished from the half-integer flux quanta points by checking whether there is a dip in transmission within the frequency range swept, at that bias point.

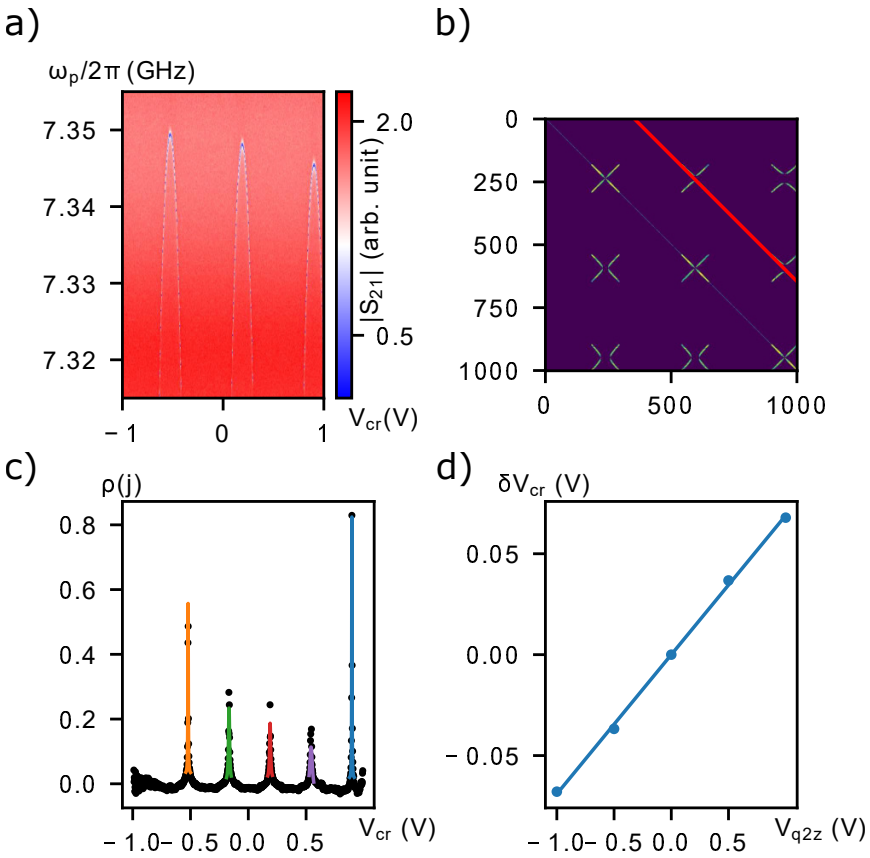

Figure 3.3: (a) Transmission magnitude $|S_{21}|$ versus bias voltage V_{cr} and probe frequency ω_p for the unit cell c of device A. (b) Recurrence plot of the image in (a) with detected line (red). The horizontal and vertical axes correspond to pixel indices in the bias voltage dimension in (a). (c) Reflection symmetry correlation coefficient $\rho(j)$ versus bias voltages V_{cr}. Each local maximum is locally fitted to a Lorentzian line shape (orange, green, red, purple, and blue curves) to obtain sub-pixel accuracy in the offset. (d) Shifts of resonator response δV_{cr} versus crosstalk source bias voltages V_{q2z}. The dots are data points and the line is the fit result.

Stage 2

In Stage 2, for each resonator, the transmission is measured versus the resonator direct bias and probe frequency, at a few voltages of each indirect bias line, with all other bias voltages set to zero. Recurrence plots are used to extract the translations in the two-dimensional data for each value of the applied indirect bias voltage. The translation versus indirect voltage is fit by a line, whose slope represents the amount of crosstalk. Figure 3.3(d) shows an example of such a fit. While the translations versus crosstalk source voltage follow a linear dependence to a good approximation, small systematic errors are observed due to interactions of the resonator with the rest of the circuit.

Stage 3

In Stage 3(a), for each unit cell, the resonator transmission is probed at a fixed probe frequency, with the resonator external flux held constant while sweeping its directly coupled qubit or coupler x and z biases. Typically, the probe frequency is below the peak frequency by about half of its linewidth to maximize contrast. The bias ranges are typically swept over two to four periods in both directions and the step size is of the order of 1 % of the observed periodicity. The resonator flux is kept at zero during the sweep. At this bias point, the resonator is flux-insensitive to first order. This choice of the resonator bias minimizes the frequency change of the resonator due to residual crosstalk when the z and x biases are swept, thus preventing deterioration of the measurement signal. This measurement generates an image that has point reflection symmetry about integer and half-integer flux points (see Sec. 3.9.1). The measured transmission magnitude $|S_{21}|$ can be considered as an image $A(i_1, i_2)$ of dimensions (m_1, m_2). To extract the point reflection symmetry centers, the correlation coefficient between the image and the image inverted about some point (j_1, j_2) is calculated. The inverted image $B(i_1, i_2; j_1, j_2)$ is given by

$$B(i_1, i_2; j_1, j_2) = A(2j_1 - i_1, 2j_2 - i_2). \tag{3.39}$$

The correlation coefficient $\rho(j_1, j_2)$ is given by

$$\rho(j_1, j_2) = \frac{\sum\limits_{i_1,i_2} [A(i_1, i_2) - \bar{A}(j_1, j_2)][B(i_1, i_2; j_1, j_2) - \bar{B}(j_1, j_2)]}{\sqrt{\sum\limits_{i_1,i_2} [A(i_1, i_2) - \bar{A}(j_1, j_2)]^2 \sum\limits_{i_1,i_2} [B(i_1, i_2; j_1, j_2) - \bar{B}(j_1, j_2)]^2}}, \tag{3.40}$$

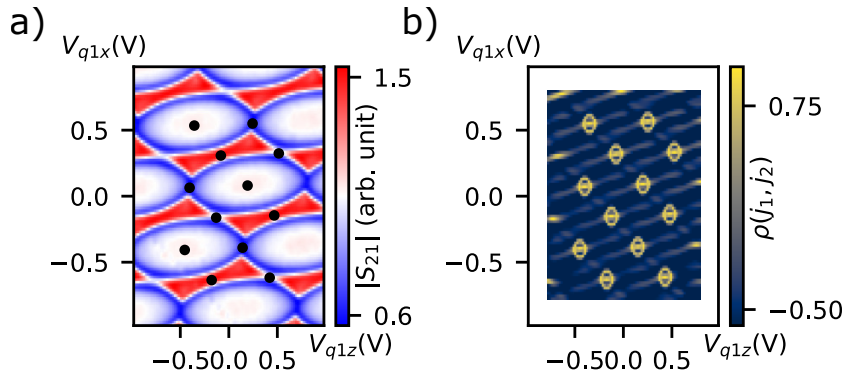

Figure 3.4: (a) Resonator transmission magnitude $|S_{21}|$ versus z, x bias voltages for unit cell $q1$. The detected inversion symmetry centers are shown by the black dots. (b) Correlation coefficient $\rho(j_1, j_2)$ for the image in (a). Each local maximum in the image corresponds to one KAZE feature (highlighted circles). We note that for a range up to about half the expected periodicity from the edge of the transmission measurement, the correlation coefficients are not calculated and plotted as white. This is because the correlation becomes an unreliable measure of symmetry near the edge.

where the summations range over $i_{1(2)} \in [\mathrm{Max}(1, 2j_{1(2)} - m_{1(2)}), \mathrm{Min}(m_{1(2)}, 2j_{1(2)} - 1)]$, and $\bar{A}(j_1, j_2)$, $\bar{B}(j_1, j_2)$ are the average values of A, B over the same range. Local maxima in the image $\rho(i_1, i_2)$ correspond to points with maximum point reflection symmetry. Instead of simple peak detection, KAZE feature recognition [183] is applied to the image ρ, which detects blobs in the image. Then, by filtering out features that are not close to any local maximum, the coordinates of the remaining features can then be identified with point reflection symmetry centers. It is empirically found that the KAZE feature detection outperforms simple local maximum detection, in cases where resonator collision causes the measured transmission to deviate from the expected symmetry. The feature detection also allows sub-pixel precision, which removes the need to take time-consuming, high-density measurements. Fig. 3.4(a) shows the point reflection symmetry centers plotted on the measured data, ordered by their distances to the origin and Fig. 3.4(b) shows the point reflection correlation coefficients calculated, with the KAZE features overlaid.

The inversion symmetry centers are coordinates in z and x bias voltages corresponding to half-integer flux quantum in z and x loops. The next task is to identify an affine transformation that converts these inversion symmetry centers to coordinates in external fluxes. In principle, any three inversion symmetry centers that are not co-linear are sufficient to

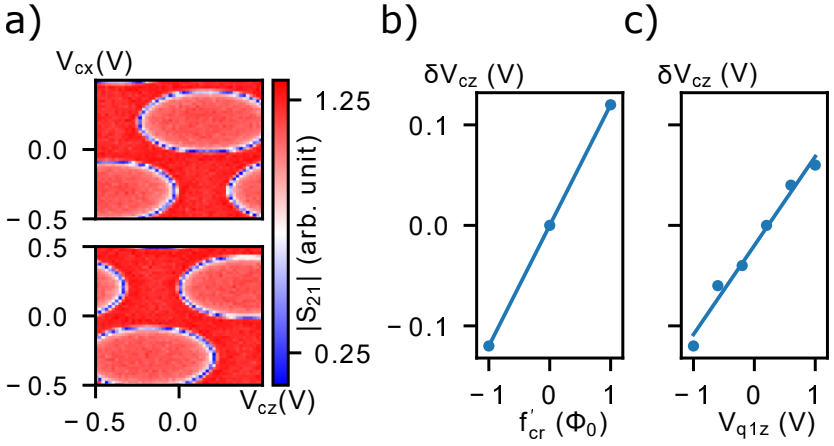

Figure 3.5: (a) Coupler resonator transmission measurement versus V_{cz}, V_{cx}, at $f'_{cr} = -1$ (top) and $f'_{cr} = 1$ (bottom). (b) Shifts of the coupler 2d scan in z direction, δV_{cz} versus resonator bias f'_{cr}. (c) Shifts of the coupler 2d scan in z direction versus crosstalk source V_{q1z}. In both (b) and (c) the dots are data points and the line is the fit result.

define such a transformation. However, due to various noise sources, it is likely that different choices of inversion centers will lead to slightly different transformations. To make use of the full lattice of inversion symmetry centers, the affine transformation parameters can be treated as fitting parameters. The optimal transformation is found by minimizing the distance between transformed lattice coordinates and the ideal lattice coordinates [178].

In Stage 3(b), for each unit, the resonator transmission is probed at a fixed frequency, while sweeping the unit x and z bias voltages and maintaining $f'_r = \pm 1$. Fig. 3.5(a) shows the measured data for the coupler unit. Translations between images in both the z and x directions are simultaneously extracted using *scikit-image* image registration routine [184, 185]. The translations versus resonator bias values are fitted to a line and the slope can be related to the crosstalk value as discussed in Sec.3.4.1 Stage 3.

Stage 4

In Stage 4, measurements similar to those in Stage 3(b) are performed. For each unit, the resonator transmission is probed while fixing the resonator flux bias and sweeping the unit's x, z biases, and stepping another crosstalk source bias voltage. The ranges

for crosstalk source voltage are chosen to cover more than one flux quantum flux bias in the corresponding loop, to ensure the translations measured are not biased due to the modulation of circuit interaction within a period. An example of translations extracted versus crosstalk source bias voltages and the corresponding fits are shown in Fig. 3.5(c). The slope of the line fit is then related to the crosstalk coupling via Eq. (3.27).

3.5.2 Calibration results for devices A and B

CISCIQi

After the application of CISCIQ as discussed above, further iterations are performed by sweeping the approximate flux coordinates, where fluxes are calculated according to the estimates of the coupling matrix and flux offset obtained in the previous iteration. Three complete iterations are completed for both devices A and B. The estimated values of coupling coefficients at the end of each iteration are calculated using Eq. (3.32).

To illustrate how the coupling elements change with iteration, we show in Fig. 3.6 a subset of the coupling matrix elements for iterations 1-3 for devices A and B. Note that the coupling elements shown correspond to units at the center of devices A and B, which are most affected by systematic crosstalk errors due to interactions with other circuit elements. We observe that all the coupling elements change, with typically a smaller change between iterations 2 and 3 than between iterations 1 and 2. To further illustrate the effectiveness of the iterations, in Fig. 3.7(a) we show the statistical box plots of coupling coefficients and flux offsets in $\mathbf{M}^{(n)\prime}, \mathbf{f}^{(n)\prime}$ for $n = 2, 3$. It is clear from the plot that the coupling matrices in iterations 2 and 3 are approaching identity, and the flux offsets are approaching zero.

For device A, it is worth noting that the corrections in off-diagonal matrix elements in iteration 2 are about $10\,\mathrm{m}\Phi_0/\Phi_0$, and the correction in flux offsets are about $10\,\mathrm{m}\Phi_0$. Assuming 60 pH mutual inductance between circuit elements, which is the typical value, the required persistent current to generate $10\,\mathrm{m}\Phi_0$ flux is $0.34\,\mu$A. This number is comparable to the maximum ground state current in the coupler z-loop, which is $0.45\,\mu$A. As the persistent current gets modulated by flux bias, corrections on the order of $10\,\mathrm{m}\Phi_0/\Phi_0$ in iteration 2 are consistent with the level of interactions between circuit elements (see Sec. 3.9.3 for a more detailed comparison). In iteration 3, the matrix element corrections are below $2\,\mathrm{m}\Phi_0/\Phi_0$ and the flux offsets corrections are below $2\,\mathrm{m}\Phi_0$. Since the flux drifts measured (see Sec. 3.5.3) are also about $2\,\mathrm{m}\Phi_0$, this suggests that further iterations would be limited by random flux jumps and not improve the calibration measurement much further.

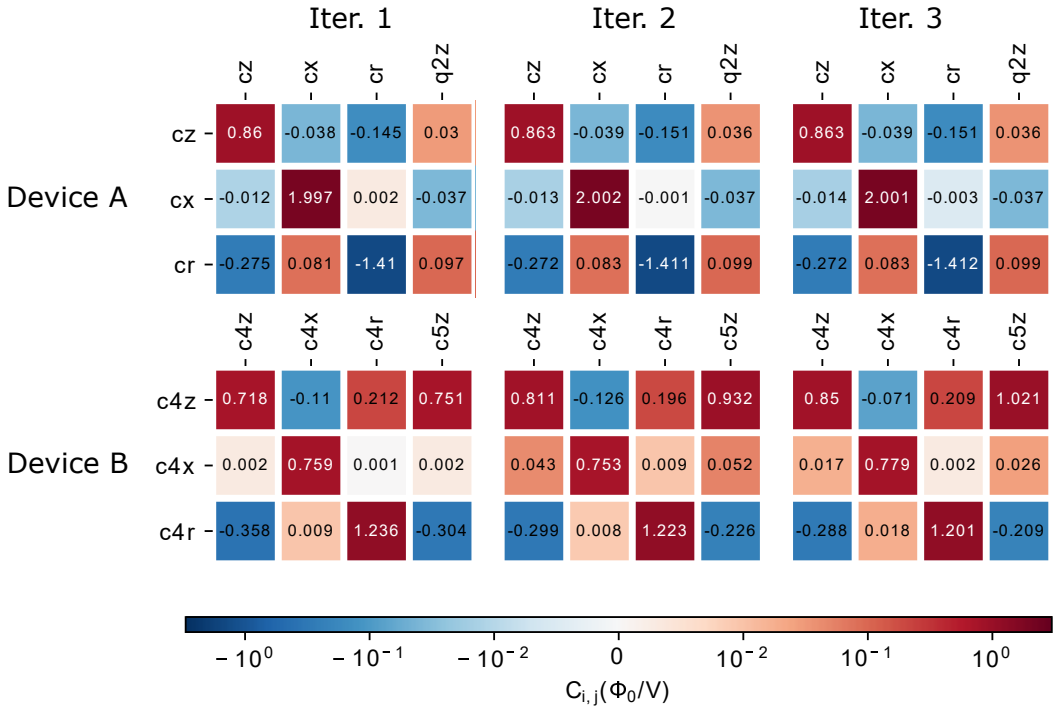

Figure 3.6: A selection of the coupling coefficients for each iteration for devices A (top) and B (bottom). From left to right they correspond to iteration 1, 2 and 3. For each image, the column and row labels correspond to source and target loops, respectively.

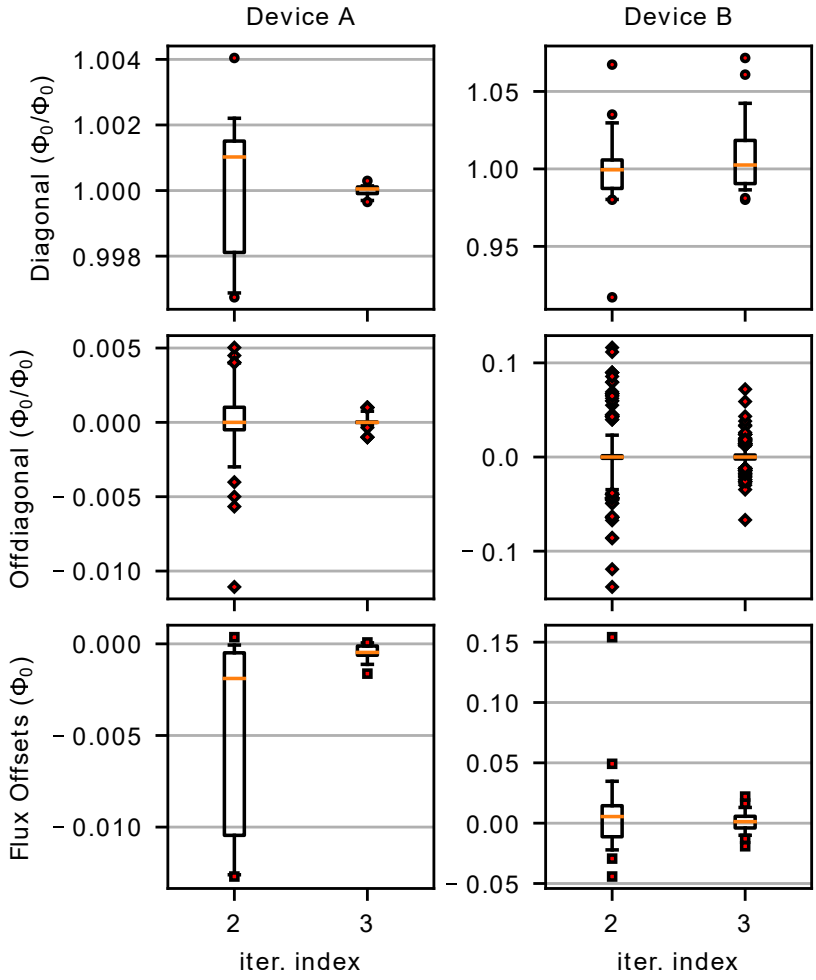

Figure 3.7: For device A (left), and B (right) respectively, the statistical box plots of the diagonal (top), off-diagonal (middle) coupling coefficients in $\mathbf{C}^{(n)\prime}$, and the flux offsets (bottom) in $\mathbf{f}_0^{(n)\prime}$, for iteration 2 and 3. The orange bar is the median, the black box corresponds to the lower and upper quartiles, the segments contain the 5 to 95 percentile of the data and the dots are outliers. For device B, the coupling coefficients and offsets corresponding to the $c2$ unit are excluded in the plots due to device failure (see text).

When compared to device A, device B has three times as many control loops. In addition, device B has overall stronger circuit interactions, because the couplers are designed to have about three times as large a persistent current and flux sensitivity compared to the qubit (see Sec. 3.9.3). This is compounded by the fact that more resonators are on the same feedline in device B, leading to increased errors in resonator readout. Besides, device B also suffered from a partial device failure: the resonator SQUID in cell $c2$ could not be tuned. This cell, including the resonator and the coupler, remained uncalibrated during the CISCIQi procedure (additional techniques were used to calibrate this unit for other experiments, which we do not discuss in this work).

Therefore, it is expected that iteration 1 of CISCIQ for device B gives less accurate estimates of the actual coupling coefficients and flux offsets. This is made apparent by simply examining the measured data. As shown in Fig. 3.8(a, b), the Stage 1 measurement for the resonator in unit $c5$ and Stage 3(a) measurement for unit $c1$ are far from the expected periodic behavior. Fig. 3.8 (c) and (d) show the same scan taken during iteration 2. The periodic behavior is restored.

3.5.3 Flux offset drift

As noted earlier, the flux offsets drift even when the device is kept cold. It is important to understand the magnitude and timescale over which the flux drifts occur. To perform annealing experiments on the device, the flux offsets need to be stable over a duration that is much longer than any annealing experiment itself.

To check the flux offset stability for device B, after the initial CISCIQi calibration, the flux offsets are recalibrated twice using the method described in Sec. 3.4.4. Figure 3.9 shows the change in flux offsets relative to the initial calibration. After two days, the root mean square (RMS) change in flux offsets for different loops is $1.3\,\mathrm{m}\Phi_0$. After 17 days, one of the resonator SQUID fluxes changed by $20.0\,\mathrm{m}\Phi_0$. The others have an RMS change of $2.0\,\mathrm{m}\Phi_0$. Similar shifts were observed in device A. This suggests that the device can remain well-calibrated for a few days. Over a longer period of time, the flux drifts can be large. Such fluctuations could have various sources, which should be investigated in future work.

3.5.4 Characterization of the errors of the calibration protocol

The error measurement discussed in Sec. 3.4.5 is applied to device A. The measured errors are displayed in Fig. 3.10. The RMS of the errors is $0.5\,\mathrm{m}\Phi_0/\Phi_0$ and the maximum error

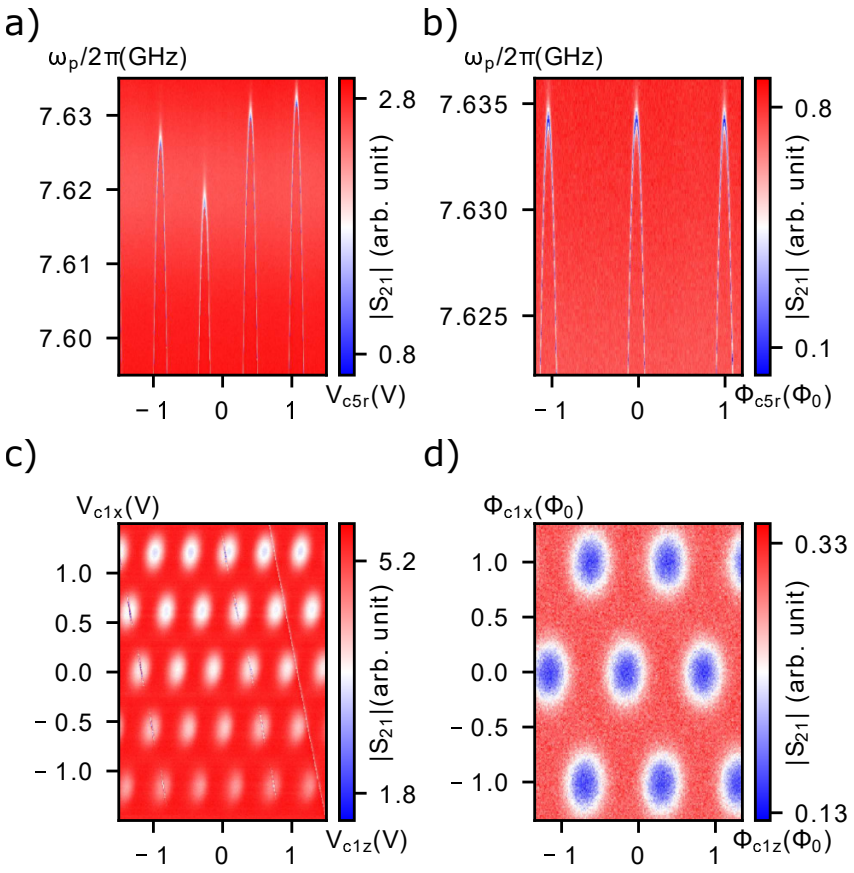

Figure 3.8: (a, b) Resonator transmission measurement versus probe frequency and resonator bias voltage for unit $c5$ in iteration 1(a) and 2 (b). (c, d) Resonator transmission measurement sweeping z, x biases for unit $c1$ in iterations 1(c) and 2(d). Clearly, the iteration 2 measurement has much better symmetry as compared to iteration 1.

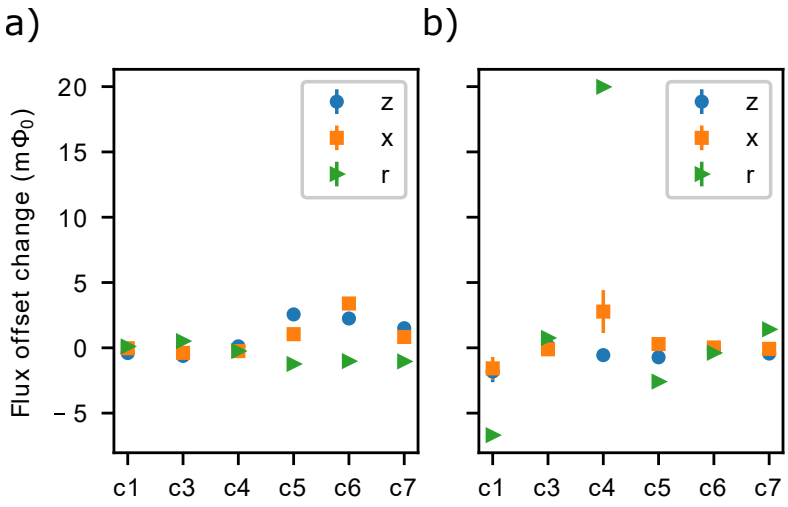

Figure 3.9: The changes in flux offsets for the z (blue, circle), x (orange, square) and r (green, triangle) loops for each unit. Panel (a) is the change in flux offset after 2 days and panel (b) is after 17 days. The errors are obtained in two steps. First, the errors of offsets extracted are computed by first resampling the transmission measurement data with typical measurement noise. The errors in offset changes are obtained by adding in quadrature the offset errors at different times. Only the coupler unit flux offsets are recalibrated in experiments (except $c2$ which had a non-functioning resonator).

magnitude is below $1.7\,\mathrm{m}\Phi_0/\Phi_0$. This means that when the estimated flux f_i' is changed by $1\,\Phi_0$ for some loop i, while keeping others constant, the actual external flux f_j differs from the approximate coordinate f_j' by at most $1.7\,\mathrm{m}\Phi_0$. In comparison, if no crosstalk compensation is applied, the control error can be lower bounded by the ratio of the final measured crosstalk coefficients $C'_{i,j}$ to the direct coupling coefficients $C'_{j,j}$, which has an RMS value of $75\,\mathrm{m}\Phi_0/\Phi_0$. If only one iteration is performed, the errors can be lower bounded by the values of the off-diagonal elements in iteration 2 matrix $C^{(2)\prime}$, which has an RMS value of $2.3\,\mathrm{m}\Phi_0/\Phi_0$ and maximum magnitude of $11\,\mathrm{m}\Phi_0/\Phi_0$.

The calibration accuracy achieved here is comparable to recent work in Ref. [186], where a systematic study of crosstalk calibration was done on a system of superconducting transmon qubits. It is worth mentioning that similar accuracy was achieved in Ref. [186] using more complex control, involving microwave pulses applied to the qubits. In contrast, the method we proposed here only uses resonator transmission measurements.

It is also instructive to compare the calibration error with the quasi-static noise due to low-frequency flux noise intrinsic to the system. Based on flux noise measured in similar devices [161] and the qubit loop size in our device, the estimated flux noise power spectral density on the qubit z-loop is $S_{f_z}(\omega) = A_{f_z}^2/(\omega/2\pi)^\alpha$, with $A_{f_z} = 14.4\,\mu\Phi_0/\sqrt{\mathrm{Hz}}$ and $\alpha = 0.91$. The noise magnitude is obtained by integrating the power spectral density over a frequency range determined by the experimentally relevant time scales, which is taken to be $\omega/2\pi \in [1\text{ Hz}, 1\text{ GHz}]$. This gives the fluctuation due to flux noise, which is about $281\,\mu\Phi_0$. In comparison, as the maximum variation of flux in any single loop is $1/2\,\Phi_0$, the RMS error due to calibration inaccuracy is $0.5 \times 1/2 = 0.25\,\mathrm{m}\Phi_0$, which is comparable to the intrinsic flux noise.

3.5.5 Calibration time

In this subsection we discuss the time taken to complete the calibration protocol. For device A, the first iteration takes about 22 hours while each further iteration takes about 8 hours. Offsets calibration takes about an hour. For device B, the first iteration takes about 80 hours while further iteration takes about 50 hours each. Offsets calibration takes about 2 hours.

We note that the data acquisition time, which takes about two orders of magnitude more than the data analysis time, is highly specific to the current setup. Firstly, improving the signal-to-noise ratio could reduce the signal integration time required. This could be done by optimizing the readout frequency and power. Secondly, there is overhead in the

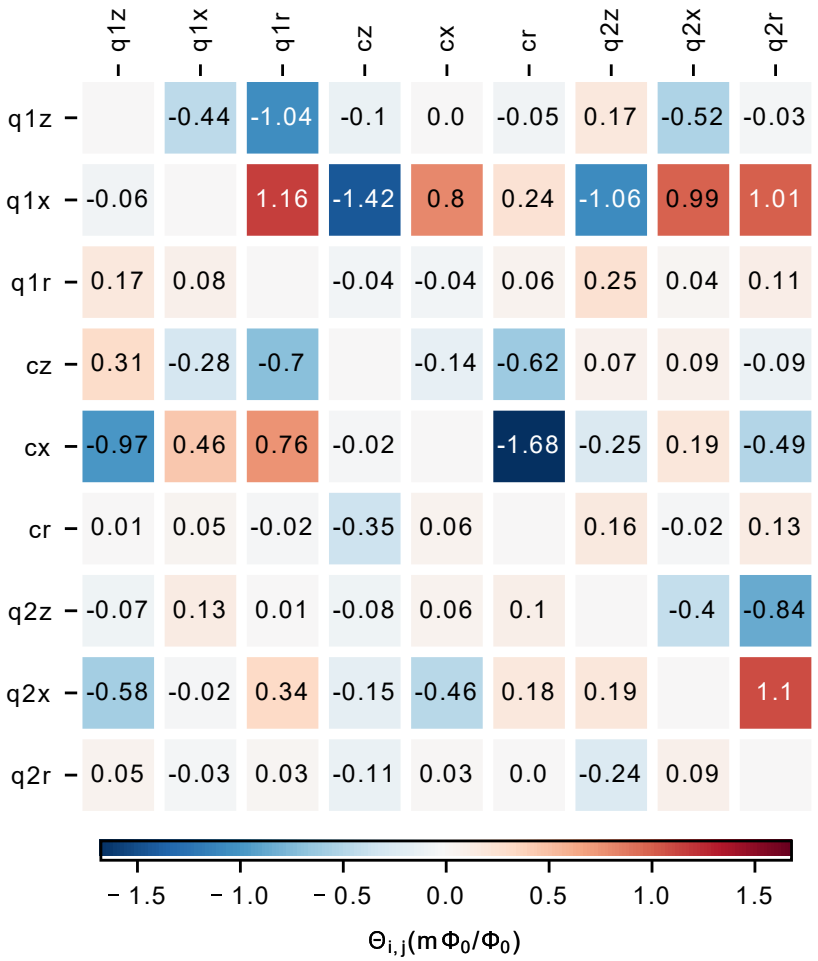

Figure 3.10: The measured crosstalk error coefficients $\Theta_{i,j}$ for each pair of sources (column) and targets (row).

Table 3.1: Comparison of simulated and measured (in brackets) values of mutual inductances between bias lines and loops.

	z bias line	x bias line	r bias line
Qubit Loop z' [1]	$-1.6(-1.9)$ pH	$-0.65(-1.3)$ pH	$-0.21(-0.2)$ pH
Qubit Loop x	$0.0098(-0.065)$ pH	$1.4(2.5)$ pH	$0.0003(-0.0068)$ pH
Resonator Loop	$0.25(0.31)$ pH	$-0.021(-0.028)$ pH	$-1.4(-1.7)$ pH

software controlling the AWGs. Optimizing the software stack can lead to significant measurement speedup, especially when the number of AWG channels becomes large. Beyond this, improving the measurement protocol by incorporating multiplexed readout could also reduce the measurement time.

3.5.6 Comparison with targeted mutual inductances

The calibration measurement also provides valuable feedback to circuit design. One important aspect of the design process is to be able to predict the mutual inductances between bias lines and control loops. The measured coupling coefficients can be converted into mutual inductances using the measured resistances along the bias lines in the fridge. This is compared to the mutual inductances extracted by simulating the device with an electromagnetic solver. As the computational resources required for such a simulation scale poorly with the size of the chip, we chose to simulate a single flux cell consisting of a single CSFQ coupled to a resonator SQUID, and their corresponding bias lines in the full two-tier environment (see Sec. 3.9.4).

Table 3.1 shows a comparison of the simulated mutual inductances and the measured mutuals on qubit 1 of device A. There is reasonable agreement between the simulated and measured values. Discrepancies could arise due to more complex return current paths through the ground plane, which are not accounted for when simulating only a restricted area of the chip. Given that all the bias lines are connected to the ground plane in the interposer chip, which is facing the qubit, it is not unexpected that the return current effect becomes important. This could be partially mitigated if the connection between bias line and ground is made further away from the control loops. However, this is ultimately limited by the density of control lines and loops in the circuit. In future designs using the three-tier architecture, there will be more flexibility in designing the ground current return path. We expect such an architecture to give better agreement between designs and actual devices.

3.6 Periodicity optimization: methodology

In this section, we introduce the periodicity optimization approach to crosstalk calibration. We will first discuss the framework used to treat the calibration task as an optimization problem. Then we will discuss the measurement and analysis required to quantify periodicity.

3.6.1 Crosstalk calibration as an optimization problem

The task of crosstalk calibration is to obtain estimates of the coupling matrix $\mathbf{C}$ and independent control of the external flux biases. This is equivalent to finding N independent control coordinates, such that the circuit responds periodically to changes in each of them. To do this, we break the calibration task into N independent optimization problems, as described below.

We start by introducing initial estimates of the crosstalk and flux offsets, given by $\mathbf{C}^{\text{init}}$ and $\mathbf{f}_0^{\text{init}}$. Introducing them makes it convenient to discuss the optimization with or without prior knowledge on the same footing. When no prior knowledge is available, the initial estimates are identity and zeros for the crosstalk matrix and flux offsets respectively. The initial estimates allow us to define the initial control coordinates $\mathbf{f}^{\text{init}}$,

$$\mathbf{f}^{\text{init}} = \mathbf{C}^{\text{init}}\mathbf{V} + \mathbf{f}_0^{\text{init}}. \tag{3.41}$$

The initial control coordinates $\mathbf{f}^{\text{init}}$ are related to the actual fluxes $\mathbf{f}$ via the residual crosstalk and flux offsets,

$$\mathbf{f} = \mathbf{C}^{\text{res}}\mathbf{f}^{\text{init}} + \mathbf{f}_0^{\text{res}}, \tag{3.42}$$

where $\mathbf{C}^{\text{res}} = \mathbf{C}(\mathbf{C}^{\text{init}})^{-1}, \mathbf{f}_0^{\text{res}} = \mathbf{f}_0 - \mathbf{C}^{\text{res}}\mathbf{f}_0^{\text{init}}$.

To calibrate the ith control coordinate, we define a trial control flux variable $\mathbf{f}'$,

$$\mathbf{f}' = (\mathbf{I} - \mathbf{O}')\mathbf{C}^{\text{init}}\mathbf{V} + \mathbf{f}_0^{\text{init}}, \tag{3.43}$$

where the compensation matrix $\mathbf{O}'$ has elements O'_{jk} with

$$O'_{jk} = \begin{cases} 0, & \text{if } k \neq i \text{ or } j = k, \\ \Omega_{jk}, & \text{otherwise.} \end{cases} \tag{3.44}$$

[1]Due to the specific convention used, z-loop does not refer to a physical loop in the device, therefore z'-loop is used instead (see Appendix D).

There are $N-1$ non-zero elements in the matrix $\mathbf{O}'$, denoted as $\{\Omega_{ji}\}$. These are the compensation parameters to be optimized when calibrating the ith control coordinate. The objective of the optimization problem is to maximize the periodicity of the measured signal when varying the ith coordinate of the trial flux, f_i'. This can be done by performing measurements varying f_i', and quantifying the periodicity using the metric discussed in Sec. 3.6.2. A schematic for one iteration of the optimization step is shown in Fig. 3.11(a).

The maximum periodicity of the signal is achieved when compensation parameters satisfy specific relations relative to the residual crosstalk $\mathbf{C}^{\text{res}}$. To see this, consider the relation between the trial control fluxes and the actual fluxes, which follows from Eq. (3.41, 3.42, 3.43),

$$\mathbf{f} = \mathbf{C}^{\text{res}}(\mathbf{I}+\mathbf{O}')\mathbf{f}' + \mathbf{f}_0', \tag{3.45}$$

where $\mathbf{f}_0' = \mathbf{f}_0 - \mathbf{C}^{\text{res}}(\mathbf{I}+\mathbf{O}')\mathbf{f}_0^{\text{init}}$. It can be seen that when the following condition is satisfied

$$\Omega_{ji} = \frac{[(\mathbf{C}^{\text{res}})^{-1}]_{ji}}{[(\mathbf{C}^{\text{res}})^{-1}]_{ii}},\ \forall j \neq i, \tag{3.46}$$

one has

$$f_i = \frac{f_i'}{[(\mathbf{C}^{\text{res}})^{-1}]_{ii}} + \sum_{j\neq i} C_{ij}^{\text{res}} f_j' + f_{0,i}' \tag{3.47}$$

$$f_{l\neq i} = \sum_{j\neq i} C_{lj}^{\text{res}} f_j' + f_{0,l}', \tag{3.48}$$

where $f_i, f_i', f_{0,i}'$ and C_{ij}^{res} are elements of $\mathbf{f}, \mathbf{f}', \mathbf{f}_0'$ and $\mathbf{C}^{\text{res}}$ respectively. The relations between the actual fluxes $\mathbf{f}$ and trial control fluxes $\mathbf{f}'$ given by Eqs. (3.47, 3.48) indicate that when the ith control flux f_i' is being varied, only the ith actual flux f_i changes. In other words, the residual crosstalk from the ith control coordinate to other coordinates $l \neq i$ is completely canceled out by setting the compensation parameters $\{\Omega_{ji}\}$ satisfying Eq. 3.46. Since the circuit response is periodic to each flux f_i with period 1, the circuit also responds periodically with respect to f_i', with period $[(\mathbf{C}^{\text{res}})^{-1}]_{ii}$. Hence, optimizing the periodicity for the ith coordinate gives the optimized compensation parameters approximately satisfying Eq. 3.46, and they are denoted as Ω_{ji}'. After completing the optimization for all N control coordinates, we obtain $N(N-1)$ optimized compensation parameters, and another N parameters corresponding to the periods of the N control coordinates. Using Eq. 3.46, estimates for residual crosstalk matrix can be obtained, which we denote as $\mathbf{C}^{\text{res}\prime}$.

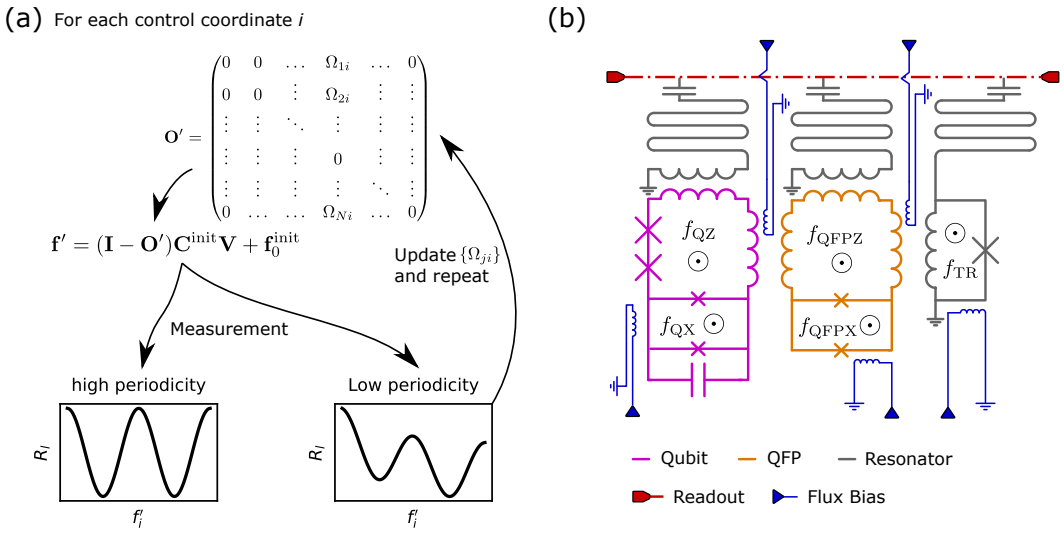

Figure 3.11: (a)Schematic representation of the optimization step. For each loop i, the optimization parameters are elements of a trial compensation matrix $\mathbf{O}'$, which defines the trial flux coordinates $\mathbf{f}'$. Then the measurement is done by sweeping f_i' and the periodicity of the measurement signal is determined. If the periodicity is high, the compensation parameters give good estimates of the ratio between the crosstalk matrix elements, otherwise, the compensation parameters are updated and the optimization is repeated until the periodicity is high. (b) Schematic of the subcircuit of the device measured, with the tunable flux qubit on the left (purple), the quantum flux parametron (QFP) in the middle (yellow), and the tunable resonator on the right (grey). In addition, the qubit and the QFP are each coupled to a fixed-frequency resonator (grey). All resonators are coupled to a joint feedline (red). External flux biases in the loops are controlled via the on-chip bias lines (blue).

3.6.2 Quantifying periodicity

The objective function for the optimization is the periodicity of the readout data with respect to f_i'. To measure the periodicity, the readout data is collected sweeping a large enough range of f_i' to cover a few periods, while keeping $\{f'_{j\neq i}\}$ fixed. The readout data is denoted as $R_l(f'_{i,s})$, where $s = 1, 2, \ldots, m$ goes over the values of f_i' taken during the sweep and m is the total number of f_i' steps. Readout data from different channels is first normalized, by applying the operation

$$R_l(f'_{i,s}) \to \frac{R_l(f'_{i,s}) - \overline{R_l}}{\sqrt{\sum_s \left[R_l(f'_{i,s}) - \overline{R_l}\right]^2}}, \tag{3.49}$$

where $\overline{R_l}$ is the average of the readout data from channel l over all values of f_i' taken. The periodicity can be quantified by first computing the correlation of the signal and its own with a translation of t steps along the f_i' coordinates. Defining the translated signal as

$$R_{l,t}(f'_{i,s}) = R_l(f'_{i,s+t}), \tag{3.50}$$

the correlation is

$$\rho_i(t\delta) = \frac{\sum_{l,s\in\mathcal{S}} \left[R_l(f'_{i,s}) - \overline{R_l}\right] \left[R_{l,t}(f'_{i,s}) - \overline{R_{l,t}}\right]}{\sqrt{\sum_{l,s\in\mathcal{S}} \left[R_l(f'_{i,s}) - \overline{R_l}\right]^2 \sum_{l,s\in\mathcal{S}} \left[R_{l,t}(f'_{i,s}) - \overline{R_{l,t}}\right]^2}} \text{ and} \tag{3.51}$$

$$\mathcal{S} = \{1, 2, \ldots, m - t\}, \tag{3.52}$$

where δ is the step size of the f_i' sweep and t is an integer for the translation considered. The $\overline{R_l}, \overline{R_{l,t}}$ refer to averages of the readout data over $\mathcal{S}$ for a particular readout channel l. From the definition of correlation, we have the range of $\rho \in [-1, 1]$, with 1 for perfect correlation, -1 for perfect anti-correlation, and 0 for no correlation.

The correlation for a periodic signal is largest when the translation is an integer multiple of the period. However, since the period of the signal is in general not commensurate with the step size δ, we fit the following function around the maximum of ρ_i

$$\rho_i(\tau\delta) = \rho_i^{\max} + b \times \text{abs}(\tau_i - \tau_i^{\max}), \tag{3.53}$$

where τ can take non-integer values and $\tau_i^{\max}$ corresponds to the period of the signal. The fit parameter $\rho_i^{\max}$ could be identified with the periodicity of the measurement signal. However, to be more precise, we choose to do another measurement where the sweep range is shifted from the original measurement by $\tau_i^{\max}\delta$, giving $R_l(f_i' + \tau_i^{\max}\delta)$. The correlation between this signal and the original one is then computed and denoted as P, which is the objective function used in the optimization.

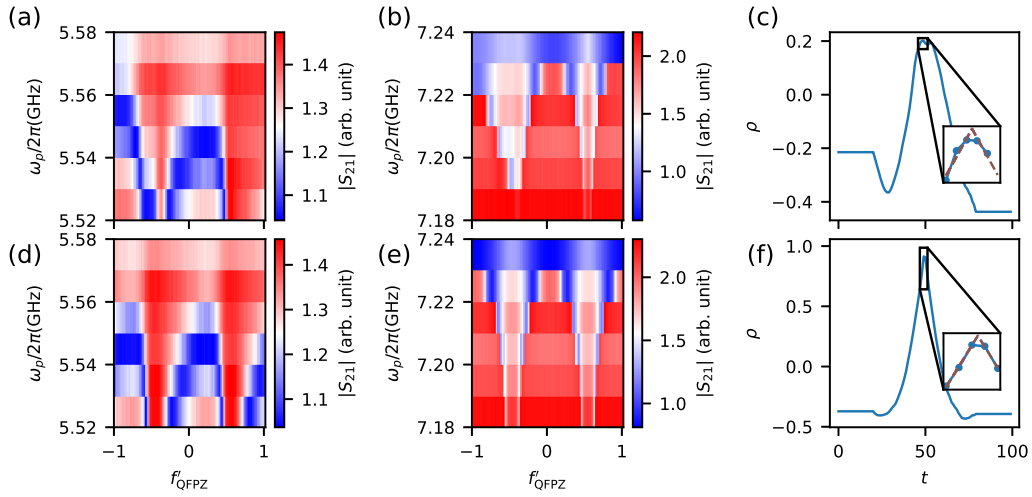

Figure 3.12: Transmission versus probing frequency ω_p and trial flux coordinate f'_{QFPZ}, through the fixed-frequency (a,d) and tunable (b,e) resonator, at the first (top) and last (bottom) step in the optimization. The plots on panels (c, f) show the corresponding correlation versus translation, with the inset showing the absolute value linear fit around the maxima.

3.7 Periodicity optimization: experiments

We implement the optimization procedure outlined above on subcircuits of a small prototype coherent quantum annealer. This device is different from the first two devices used in the demonstration of the iterative method in this chapter, and is named device C. The device consists of two coupled tunable capacitively-shunted flux qubits [48], fabricated using a three-stack process in Lincoln Laboratory [187]. Each qubit is coupled to a quantum flux parametron (QFP), which is in turn coupled to a flux-tunable resonator for readout. The QFP acts as an amplifier for the flux signal of the qubit, hence ensuring high-fidelity readout in the qubit flux basis, which is critical for quantum annealing applications [62]. In addition, each qubit and QFP is inductively coupled to a fixed-frequency resonator to assist crosstalk calibration. A schematic of one qubit unit cell consisting of the qubit, the QFP, and the tunable resonator is shown in Fig. 3.11(b). The full two-qubit system, including its readout circuits, has been calibrated using the iterative translation-based method. The result is presented in Sec. 3.10.4 and the crosstalk matrix obtained via this method is denoted as the reference crosstalk matrix, $\mathbf{C}^{\mathrm{ref}}$.

3.7.1 Optimization of a subcircuit with three flux biases

For a proof-of-principle demonstration of the periodicity optimization approach, we start with a subcircuit consisting of just the QFP and the tunable resonator. The subcircuit has strong coupling due to the large persistent current of the QFP and the resonator, which makes it very time-consuming to calibrate using the translation-based method. The three flux biases in the subcircuit are denoted as QFPZ, QFPX and TR. The optimization starts with the initial crosstalk $\mathbf{C}^{\text{init}} = \mathbf{C}^{\text{ref}}$. This allows setting the qubits and couplers outside the subcircuit in a flux bias such that they are decoupled from the measured subcircuit. Using the reference crosstalk also allows systematic investigation of the performance of the optimization relative to particular initial conditions and bounds on the trial compensation parameters. We have also demonstrated the optimization starting with $\mathbf{C}^{\text{init}}$ given by a single iteration of the translation-based method, which is discussed in Sec. 3.10.5.

For the readout channel, we choose to measure transmission through the resonators. Both the fixed-frequency and tunable resonators are measured, each at six different readout frequencies. The readout frequencies are chosen to be around the bare resonator frequencies and the step size is around their resonance linewidth. The flux bias sweep range is chosen to cover about two periods and the step size is about 20 $\text{m}\Phi_0$. The other flux biases not being swept are set to values that avoid the flux-insensitive bias points of the QFP and tunable resonator. This is needed to avoid the tunable resonator and the QFP coincidentally being in flux-insensitive spots, which would make the measurement signal insensitive to crosstalk. Such settings can be achieved without accurate initial estimates of the crosstalk or flux offsets.

As examples for the measurement and analysis at a single step in the optimization, we show the transmission measurement results at the start and the end of the optimization for the QFPZ control periodicity in Fig. 3.12(a,b,d,e). It is clear that the measurement signal is more periodic after the optimization. This is also reflected in the maximum correlations with respect to translations of the signal, which are shown in Fig. 3.12(c,f).

We use primarily an optimization algorithm based on Bayesian optimization [188], which is a global optimizer suited for black-box optimization with objective functions which are expensive to evaluate. The algorithm uses a Gaussian process to approximate the objective function, which is called the prior. At each step, the optimizer samples the distribution at a new point in the parameter space, which is probabilistically chosen according to the prior to improve upon the existing samples while minimizing the uncertainties of the prior [189]. The Gaussian process is then updated according to the Bayesian inference rule, and is used as the prior for the next iteration. The compensation parameters Ω_{ji}'s are bounded to within $[-0.2, 0.2]$, and the optimization is initialized with evaluations

at 20 random points in the parameter space. The bounds correspond to typical levels of crosstalk in large-scale devices [190]. We defer to Sec. 3.7.2 for a discussion of how the bounds and initial conditions could affect the optimization. In Fig. 3.13(a), the trial compensation parameters and the periodicity is plotted versus the optimization step. It can be seen that the optimum parameters have been found after about 40 iterations. In Fig. 3.13(b), the landscape of the objective function, predicted by the final Gaussian process model is shown, together with markers for the parameter values sampled during the optimization. The minimum is at around $(\Omega_{\text{QFPZ QFPX}}, \Omega_{\text{TR QFPX}}) = (0, 0)$, which is the expected optimum compensation parameter given $\mathbf{C}^{\text{init}} = \mathbf{C}^{\text{ref}} \approx \mathbf{C}$ and hence $\mathbf{C}^{\text{res}} \approx \mathbf{I}$. In Fig. 3.13(c), we show the difference between elements of $\mathbf{C}^{\text{res}\prime}$ with the identity matrix. The magnitudes of the elements are all below 3×10^{-3}, which is about the error of the iterative method [190]. This shows that the crosstalk matrix obtained by the optimization method is comparable to the crosstalk matrix obtained by the iterative calibration method. We also note that the differences are much smaller than the flux sweep step size, which shows that the method does not require high-resolution scans to be accurate. As a result of this, the optimization-based measurements required less data as compared to one iteration of the translation-based method.

Using the same optimizer setting but starting the optimization with estimated crosstalk from one iteration of the translation-based method, the estimated crosstalk obtained converged with a similar level of accuracy, as compared to starting the optimization with the reference crosstalk matrix, obtained from multiple iterations of translation-based method. The result is presented in Sec. 3.10.5.

3.7.2 Optimization landscape

After demonstrating that the optimizations converge with high accuracy to the expected compensation parameters, we examine the structure of the optimization problem. First, we looked at how periodicity changes as the compensation parameters deviate from the optimized values. We define the distance from the optimized compensation parameters as

$$\|\Omega_i\| = \sum_{j \neq i} (\Omega_{ji} - \Omega'_{ji})^2 \tag{3.54}$$

and plot the periodicities measured during the optimization versus $\|\Omega_i\|$ in Fig. 3.14. It can be seen that for all of the loops measured, when $\|\Omega_i\| \lesssim 0.001$, the periodicity function plateaus at about 0.99, This suggests given the current set of readout channels, the optimized compensation parameters would allow us to control each bias coordinate to 1 $\text{m}\Phi_0$

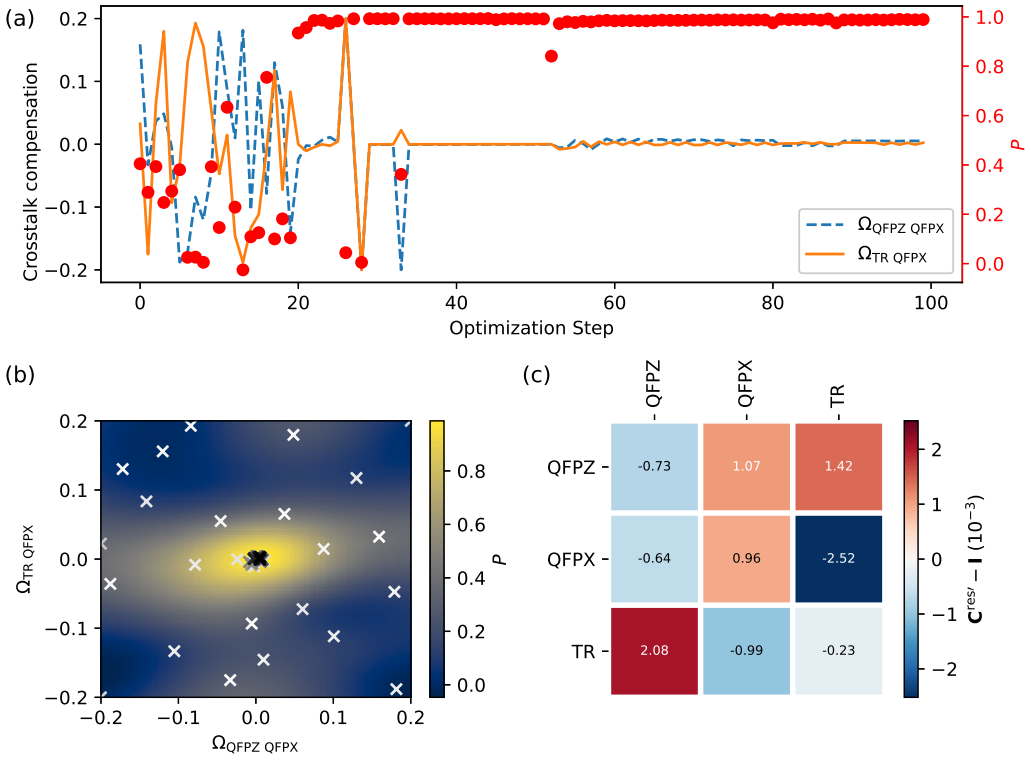

Figure 3.13: (a) Trial compensation parameters (left axis), $\Omega_{\text{QFPZ QFPX}}$ (dashed line), $\Omega_{\text{QFPZ QFPX}}$ (solid line) and periodicity P (red dots, right axis) versus optimization step. (b) A Gaussian process model of periodicity versus the compensation parameters. The cross markers correspond to parameters sampled by the optimizer and the gray scale of the markers indicates the sequence at which they are sampled, with darker color markers being sampled later. (c) Difference between the estimated residual crosstalk matrix $\mathbf{C}^{\text{res}\prime}$ and the identity matrix.

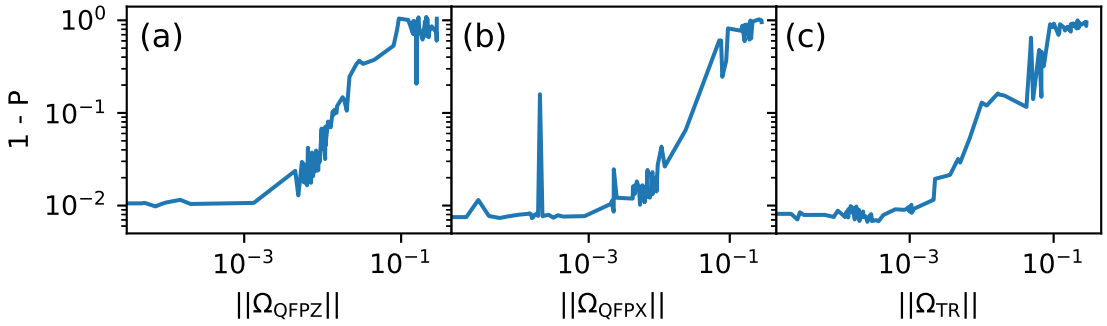

Figure 3.14: 1 minus the periodicity P versus the distance from the trial compensation parameters to the optimized compensation parameters for the three loops, QFPZ (left), QFPX (center), TR (right)

accuracy over one flux quantum range. The sharp peak for the QFPX loop is likely due to hysteresis of the QFP, which can be avoided by choosing a different set of independent flux control coordinates (see Sec. 3.10.7). When $\|\Omega_i\| \gtrsim 0.1$, the periodicity $P \approx 0$. This means that the sampled trial compensation parameters are only informative when they satisfy $\|\Omega_i\| \lesssim 0.1$. Hence, the optimization method is likely only efficient when initial crosstalk is known to within 10% accuracy, relative to the diagonal coupling elements. Various sources of estimation could provide such accuracies, such as one single iteration of the translation-based calibration method, measurement on different copies of the same device, or potentially careful electromagnetic simulation of the device.

We further characterize the landscape of the periodicity function by directly measuring it. This is done by first updating the initial crosstalk matrix with the optimized parameters, according to

$$\mathbf{C}^{\text{init}} \rightarrow \mathbf{C}^{\text{res},\prime}\mathbf{C}^{\text{init}}, \tag{3.55}$$

and then doing measurement in the updated f^{init} coordinates. For each loop, the periodicity is measured sweeping one trial compensation parameter, while keeping the other at zero. These measured periodicities are plotted in Fig. 3.15(a). It can be seen that the periodicity is mostly a smooth function of the compensation parameters with a single maximum. There are two features outstanding. First, the periodicity relative to the QFPX loop has a rugged landscape. This is likely due to the QFP becoming hysteric and not responding to flux bias variations fast enough compared to the experiment time. The hysteresis is caused by the discontinuous change in the ground state wavefunction of the QFP at the flux bias

symmetry points. This can be systematically avoided by choosing a different set of linearly independent flux bias coordinates, along which the ground state wavefunction changes smoothly (see Sec. 3.10.7 for more detailed discussion). Second, the periodicity maxima for the compensations to TR loop are slightly deviated from zero. The reason for this still requires further investigation. One possibility could be that the periodicity function, under the measurement setting used, is sensitive to drifts in flux offsets, which could occur between the optimization measurement and the landscape measurement. The offsets therefore need to be kept track of in future implementations of the optimization, otherwise the accuracy of the crosstalk calibration based on periodicity optimization could be limited. The periodicity along the TR flux bias is also measured sweeping a two-dimensional grid of values for the trial compensations $\Omega_{\mathrm{QFPZ,TR}}, \Omega_{\mathrm{QFPX,TR}}$, over the range of $[-0.1, 0.1]$. The result is plotted in Fig. 3.15(b). It confirms that the periodicity is a smooth function over the entire range, and has a single maximum at around (0, 0). Such characteristics of the objective function mean the optimization problem is likely convex in general. This opens the possibilities of using optimization algorithms that approximate and make use of the local gradients [191, 192, 193]. We successfully implement one such optimization method, called simultaneous perturbation stochastic approximation (SPSA) [191] and the result is discussed in Sec. 3.10.6.

3.7.3 Optimization of a subcircuit with five flux biases

To understand the feasibility of the periodicity optimization on larger devices, we implement the procedure incorporating the qubit that is directly coupled to the QFP. The qubit loops are denoted as QZ and QX. In Fig. 3.16(a) we show the four compensation parameters and the periodicities with respect to the QFPZ loop versus the optimization steps. It is noted that an increased number of initial evaluations, 50, is required for the optimization algorithm to approach the reference compensation parameters. The optimizations for other loops in the system did not approach the reference compensation parameters with the same optimizer hyperparameters. One possible explanation for the relative success of the QFPZ loop periodicity optimization, compared to the other loops, is that the QFPZ loop is special, both because of its large persistent current and it being directly coupled to most other loops in the subcircuit (except QX). The effectiveness of the optimization in larger circuits can potentially be improved by exploring different readout channels and optimization algorithms, which we didn't pursue in this proof-of-principle work.

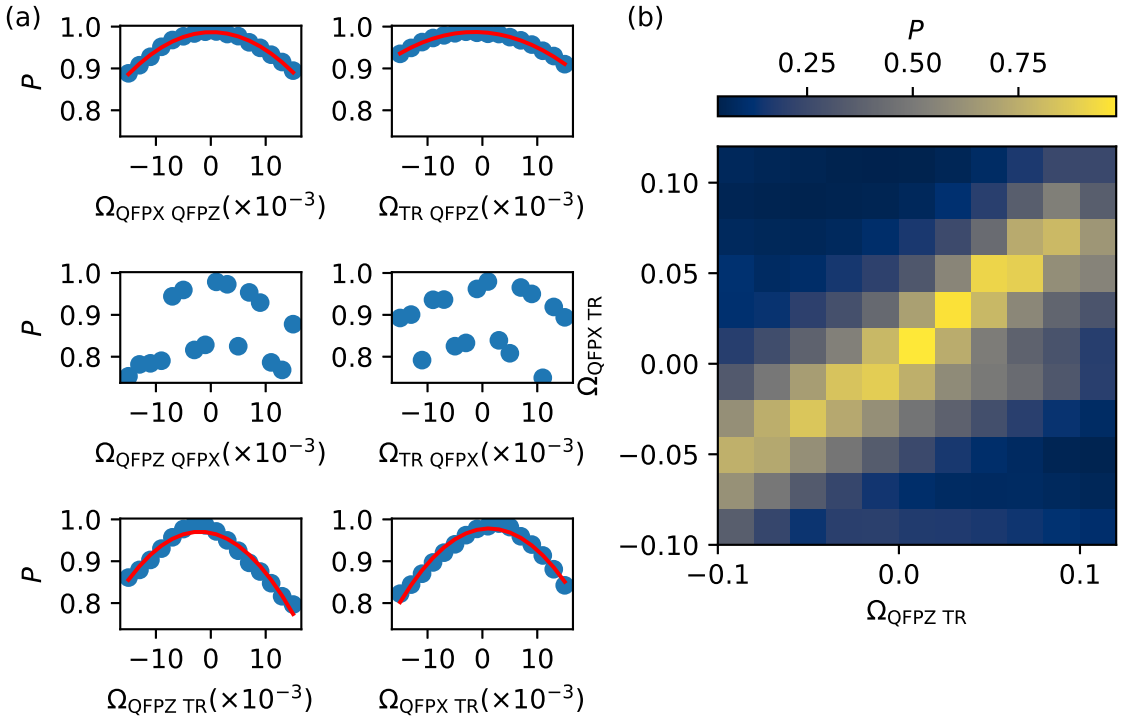

Figure 3.15: (a) Measured (blue dots) periodicity versus deviation of the compensation parameters from the optimized value for each of the six off-diagonal parameters in the 3×3 matrix, with a quadratic fit (red curve) on top. (b) Measured periodicity along the f'_{TR} bias versus deviation of the compensation parameters $\Omega_{\mathrm{QFPZ,TR}}, \Omega_{\mathrm{QFPX,TR}}$ from their optimized values.

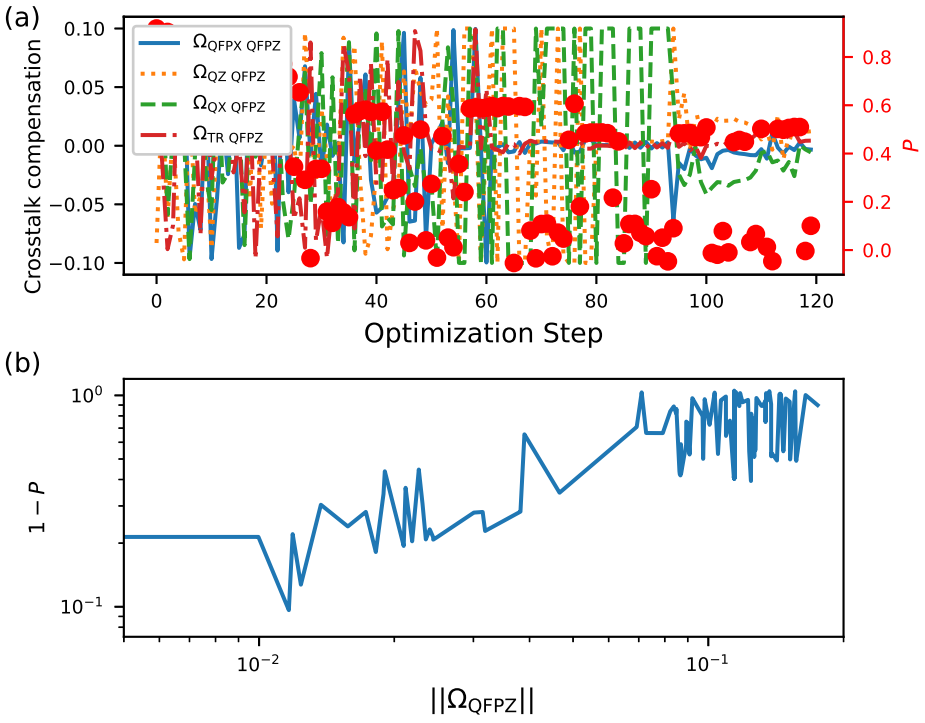

Figure 3.16: Optimization including the qubit loops. (a) Trial compensation parameters (left axis) from QZ, QX, QFX, and TR to the QFPZ loop and periodicity P (right axis) versus optimization steps. (b) 1 minus the periodicity P versus the distance from the trial compensation parameters to the optimized compensation parameters for the QFPZ loop.

3.8 Conclusion and discussion

In summary, we proposed and implemented two methods to calibrate flux crosstalk, which only relies on the symmetry properties of superconducting circuits, without needing a full model of the device. For the iterative method, the efficacy is clearly validated by the convergence of the crosstalk and offsets measured in each iteration, as well as the independent error measurement. The iterations address the errors due to strong inductive coupling within the circuit. Comparing the calibration results between devices A and B, it is clear that device B, which has more couplers, requires more iterations to achieve the same level of convergence. Indeed, when performing the iterative procedure on device C, which contains elements with a stronger persistent current, the QFP, 7-8 iterations are required (see Sec. 3.4.1). This highlights the importance of iteration when calibrating devices with strong inter-element interaction.

For the periodicity optimization method, we successfully demonstrate it on a coupled QFP-tunable-resonator system, with an accuracy that is comparable to the iterative calibration method. Although the current implementation of the periodicity optimization is limited when used to calibrate devices with a larger number of loops, it can already be utilized as a subroutine for calibrating parts of a larger system. Such a hybrid calibration strategy is particularly useful for strongly interacting systems such as the quantum annealing circuits investigated here, where the iterative method alone would require more data to converge. The landscape measurement shows that the problem is nearly convex within some bounds on the optimization parameters. This points to exploring other optimization algorithms, such as momentum-based optimizations [192, 193] to speed up the convergence, which is crucial for extending the optimization-based calibration to larger devices. Another attractive future direction could be adaptive measurements, where different experiment parameters can be used to give different optimization landscapes. For example, an optimization landscape with a broad maximum could afford large tolerance to the initial guess of the crosstalk matrix, while an optimization landscape with a narrow maximum could lead to higher accuracy for the optimized results.

When considering applying the calibration methods in this chapter to future large-scale quantum processors, there are a few things to be noted. First, from the design and fabrication perspective, future devices are likely to incorporate multi-tier architectures such as the ones in Ref. [181]. Such architecture allows current signals to be routed away from the circuit loops before they are grounded. With this advance we expect the crosstalk to be more spatially localized so that the number of crosstalk elements to be measured should only scale as N, instead of N^2. This, however, would not eliminate the need for iteration or optimization-based calibration, which addresses the issue of strong inter-

element interaction. Secondly, from a measurement perspective, we expect further technical developments to speed up the data acquisition, as discussed in Sec. 3.5.5. In addition to improving the design and measurement setup, an important future direction is to look at the frequency dependence of the crosstalk, which could arise due to the frequency dependence of the transmission through the signal delivery chain from room temperature to the target loops. As a complete characterization of this frequency-dependent crosstalk might not be feasible, an optimization-based method designed for a specific annealing protocol might be needed.

The crosstalk calibration methods developed in this chapter were applied to devices developed specifically for quantum annealing applications. Compared to commercial quantum annealers [164, 174, 92], we explore an implementation with independent local high-bandwidth control of qubits and couplers, enabling advanced annealing protocols, and simplified circuits without built-in compensation for variation in fabrication parameters, leading to increased coherence. While creating new opportunities for quantum annealing, this design approach leads to the increased complexity of flux crosstalk calibration, a challenge that can be tackled with the methods we developed here.

3.9 Additional details on device modelling

3.9.1 Symmetries in external fluxes in CSFQs and couplers

In Stage 3(a) of CISCIQ, we use the fact that the CSFQs and the couplers exhibit point reflection symmetries with respect to half-integer flux quanta points in both the x and z' loops (see Appendix D for the flux bias conventions). This property is derived from two underlying symmetries in the circuit. First, a single flux cell has mirror symmetry about the chip plane, so that the resonator frequency should have $\omega_r(f_{z'}, f_x, f_r) = \omega_r(-f_{z'}, -f_x, -f_r)$. Second, superconducting loops have properties periodic in Φ_0, so that $\omega_r(f_{z'}, f_x, f_r) = \omega_r(f_{z'} + 1, f_x + 1, f_r + 1)$. Combining these two relations we find that $\omega_r(f_{z'} + N_z/2, f_x + N_x/2, f_r + N_r/2) = \omega_r(-f_{z'} + N_z/2, -f_x + N_x/2, -f_r + N_r/2)$, where $N_{(z',x,r)}$ are integers.

In Stage 3 we assumed that each flux cell is isolated from the rest, and the resonator calibration is exact, so that $f_r = 0$. The fluxes $f_{z'}$ and f_x are completely specified by the affine transformation (see Sec. 3.4.1).

$$\begin{pmatrix} f_{z'} \\ f_x \end{pmatrix} = \begin{pmatrix} 1 & -\frac{1}{2} \\ 0 & 1 \end{pmatrix} \begin{pmatrix} f_z \\ f_x \end{pmatrix} \tag{3.56}$$

$$= \begin{pmatrix} C^{\text{eff}}_{z,z} & C^{\text{eff}}_{z,x} - \frac{1}{2}C^{\text{eff}}_{x,z} \\ C^{\text{eff}}_{x,z} & C^{\text{eff}}_{x,x} \end{pmatrix} \begin{pmatrix} V_z \\ V_x \end{pmatrix} + \begin{pmatrix} f^{\text{eff}}_{0,z} - \frac{1}{2}f^{\text{eff}}_{0,x} \\ f^{\text{eff}}_{0,x} \end{pmatrix}. \tag{3.57}$$

The analysis for Stage 3(a) data relies on the fact that the data has point reflection symmetry in the V_z, V_x coordinates. Hence, we need to show that point reflection symmetries are preserved under affine transformation. To show this, consider two sets of points A and B, related by an affine transformation $\mathcal{F}$, such that $\mathcal{F}(B) = A$. It is also known that A has point reflection symmetry so that $\mathcal{R}(A) = A$. Here $\mathcal{R}$ is the point reflection operation with the property $\mathcal{R} = \mathcal{R}^{-1}$. To show that B also possesses some point reflection symmetry, we need to a) find some operation $\mathcal{R}'$ which satisfies the symmetry condition $\mathcal{R}'(B) = B$ and b) show that $\mathcal{R}'$ is indeed a point reflection operation. To find $\mathcal{R}'$ we write

$$\mathcal{F}(B) = A = \mathcal{R}(A) = \mathcal{R} \circ \mathcal{F}(B), \tag{3.58}$$

$$\mathcal{F}^{-1} \circ \mathcal{R} \circ \mathcal{F}(B) = B. \tag{3.59}$$

Hence $\mathcal{R}' \equiv \mathcal{F}^{-1} \circ \mathcal{R} \circ \mathcal{F}$ satisfies the symmetry condition. To show that $\mathcal{R}'$ is indeed a point reflection operation, we just need to show that it is isometric and involutive. It is involutive because we can write

$$\mathcal{F}^{-1} \circ \mathcal{R} \circ \mathcal{F} \circ \mathcal{F}^{-1} \circ \mathcal{R} \circ \mathcal{F} = \mathcal{I}, \tag{3.60}$$

where $\mathcal{I}$ is the identify operation and we used $\mathcal{R} \circ \mathcal{R} = \mathcal{I}$. It can be shown that $\mathcal{R}'$ is also isometric because it is composed of $\mathcal{F}^{-1}$, $\mathcal{R}$ and $\mathcal{F}$, which are individually isometric. Therefore point reflection symmetry holds both in the flux coordinates f'_z, f_x as well as the voltage coordinates V_z, V_x.

3.9.2 Coupler-resonator inductive loading model

This section describes in detail the inductive loading model between a single coupler and its coupled tunable resonator used in Sec. 3.4.1. We start by defining the effective quantum inductance of the coupler, L^{eff}_C, based on [161],

$$\frac{1}{L^{\text{eff}}_C} = \frac{1}{\Phi_0} \frac{\partial \langle I^C \rangle}{\partial f_{cz}}, \tag{3.61}$$

where L_C^{eff} is the coupler effective inductance, $\langle I^C \rangle$ is the ground state current in the coupler z-loop and f_{cz} is the z-flux bias for the coupler. The quantity L_C^{eff} is obtained using the full circuit model of the coupler (see Sec. 4.5.1) and a quantum circuit simulation package [40].

The tunable resonator can be modeled as a waveguide terminated to ground through the effective inductance of the rf-SQUID. For a classical rf-SQUID with junction critical current I_c and geometric inductance L_g, its effective inductance is given by

$$\frac{1}{L_{\text{SQUID}}^{\text{eff}}} = \frac{1}{L_g} + \frac{2\pi I_c \cos\varphi}{\Phi_0}, \tag{3.62}$$

where φ is the phase across the junction. The phase φ can be found by minimizing the SQUID classical potential

$$U(\varphi) = -\frac{I_c \Phi_0}{2\pi}\cos(\varphi) + \frac{\Phi_0^2}{2L_g}\left(\frac{\varphi}{2\pi} - f_r\right)^2. \tag{3.63}$$

Then the resonance frequency ω_r for the $\lambda/4$ waveguide together with the rf-SQUID is found by numerically solving the equation

$$\exp\left(\frac{2i\omega_r l}{c}\right) = \frac{i\omega_r L_{\text{SQUID}}^{\text{eff}} - Z_0}{i\omega_r L_{\text{SQUID}}^{\text{eff}} + Z_0}, \tag{3.64}$$

where l, c, Z_0 are the waveguide length, phase velocity, and characteristic impedance respectively.

With inductive loading, the geometric inductance of the SQUID changes via

$$L_g \to L_g - \frac{M_{\text{coupler,SQUID}}^2}{L_C^{\text{eff}}}, \tag{3.65}$$

where $M_{\text{coupler,SQUID}}$ is the mutual inductance between coupler z and rf-SQUID loops. As the coupler bias changes, its effective inductance also changes, which then changes the SQUID effective inductance and resonator frequency.

3.9.3 Circuit parameters

To give more concrete numbers on the strength of circuit interaction, Tab.3.2 tabulates the range of persistent currents for the qubits, couplers resonator SQUIDs as well as their geometric mutual inductances in Devices A and B. For comparison, we also present the design

Table 3.2: Persistent current and mutual inductances between different circuit elements

Circuit parameter	Value
I_p(qubit)	within $\pm 0.14\mu$A
$\langle I^C \rangle$(coupler)	within $\pm 0.45\mu$A
I_p(SQUID)	within $\pm 1.2\mu$A
I_p(QFP)	within $\pm 2.0\mu$A
$M_{\text{qubit,SQUID}}$	$29.5(\text{m}\Phi_0/\mu\text{A})$
$M_{\text{coupler,SQUID}}$	$28.7(\text{m}\Phi_0/\mu\text{A})$
$M_{\text{qubit,coupler}}$	$30.2(\text{m}\Phi_0/\mu\text{A})$
$M_{\text{coupler,coupler}}$	$31.0(\text{m}\Phi_0/\mu\text{A})$
$M_{\text{QFP,SQUID}}$	$32.5(\text{m}\Phi_0/\mu\text{A})$
$M_{\text{QFP,qubit}}$	$32.5(\text{m}\Phi_0/\mu\text{A})$

numbers for the QFP based on Ref. [62]. We note the QFP in device C has slightly different target persistent current and mutual inductance to the qubit, but we do not disclose them here. For the qubit and couplers, the persistent currents are found by numerically solving the quantum circuit Hamiltonian. For the resonator, the current is calculated by solving the classical rf-SQUID equation. A complete list of the circuit parameters is presented in the next chapter, Sec. 4.5.1.

The maximum possible induced flux from one circuit element to another is $36\,\text{m}\Phi_0$. This is consistent with the fact that about $10\,\text{m}\Phi_0$ of error is measured on device B when only one iteration of CISCIQ is applied.

3.9.4 Simulation of mutual inductances using Sonnet

To simulate the mutual inductances, the design drawings are first imported into Sonnet, a microwave modeling software for 3D planar circuits. The model includes both the interposer and qubit layer, as well as all the bump bonds and air bridges. Gaps in the superconducting loop left for Josephson junctions are connected in the simulation. Ports are assigned to each superconducting loop and bias line. The inductances are extracted by computing the impedance matrix at 1 GHz. It is also found that there is little dependence on frequency.

3.10 Additional experimental results

3.10.1 Recurrence analysis and line detection

This section discusses the various image processing applied during the analysis of Stage 1 of CISCIQ. In this stage, resonator transmission is measured as a function of probe frequency and resonator bias. As the background transmission is different at different frequencies, a background filter is applied, which is specified by,

$$S'_{21}(\omega_p, V_r) = \frac{S_{21}(\omega_p, V_r)}{\mathbb{M}\left(S_{21}(\omega_p)\right)}, \tag{3.66}$$

where S'_{21} stand for the filtered results and $\mathbb{M}$ stand for taking the complex median over the V_r dimension.

Furthermore, to enhance the resonance dip feature relative to the background, a median filter is applied to the image along the frequency axis. The raw measurement data and the data after applying the background and median filters are shown in Fig. 3.17(a) and (b).

To obtain the recurrence plot, the first step is to compute the pair-wise distance between the columns of the image. This calculation results in Fig. 3.17(c). Then the pair-wise distance image goes through Sobel horizontal and vertical filters sequentially to enhance the features that correspond to translational symmetry. This results in Fig. 3.17(d). Finally, the filtered image is thresholded using Otsu thresholding [194] to give the recurrence plot, which is Fig. 3.3(d) in the main text. To identify lines and thus translations, the Hough transform is applied. This then completes our custom implementation of translational symmetry detection. Compared to readily available image registration functions, the custom algorithm allows specifying ranges within which to look for translations, hence avoiding finding translations that are multiple periods away.

3.10.2 Iterative calibration results on Devices A and B

Figure 3.18 presents coupling matrices $\mathbf{M}^{(n)\prime}$ and flux offsets $\mathbf{f}_0^{(n)\prime}$ measured at each iteration of CISCIQ for both devices A and B. As can be seen from the iteration 2 and 3 results, for both devices, the convergence is indicated by the decreased intensity of the colors on the off-diagonal elements and flux offsets, as well as the diagonal elements approaching 1.

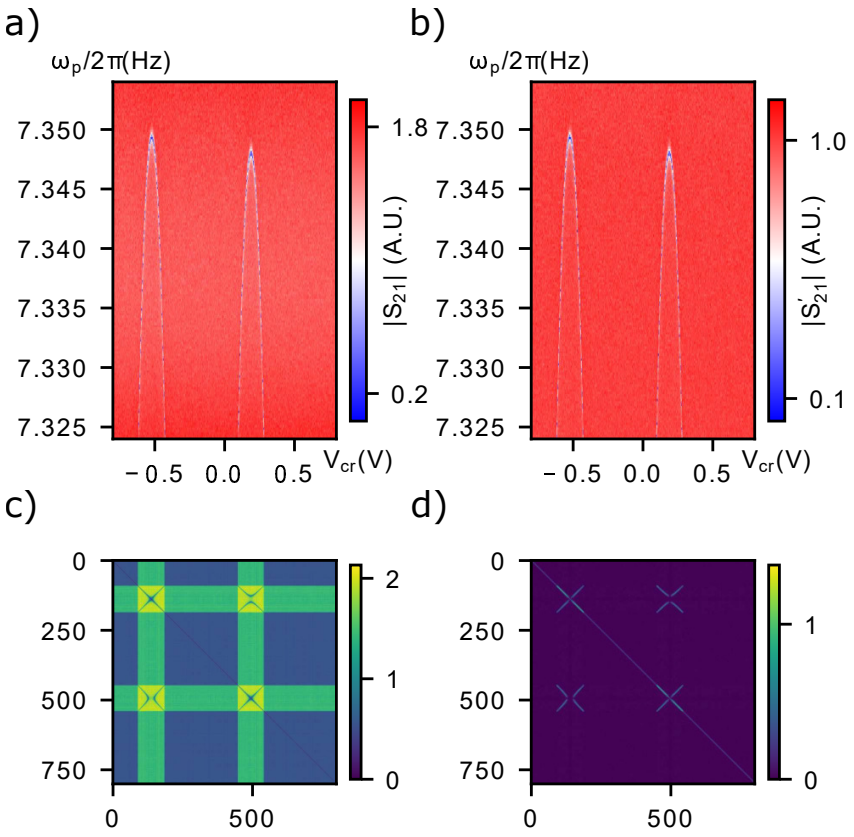

Figure 3.17: Top row shows the resonator S21 measurement before (left) and after (right) the image processing routines. The bottom left plot shows the corresponding column pair-wise distance for the top right image. The recurrence plot (bottom right) for the top right image is obtained by thresholding the column pair-wise distances image.

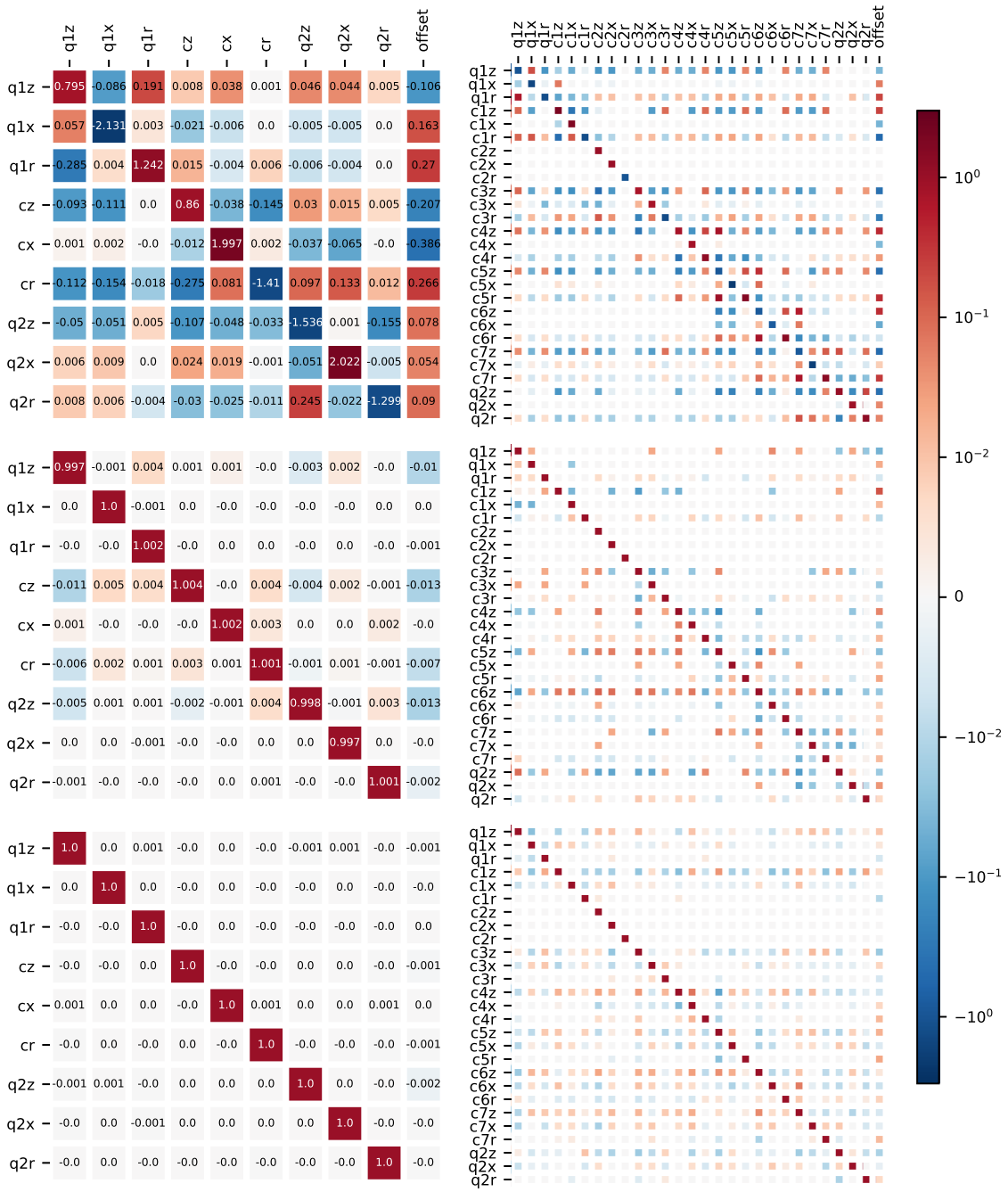

Figure 3.18: Left (right) three panels show for device A (B) the coupling matrices and flux offsets measured for iteration 1 (top), 2 (middle) and 3 (bottom)

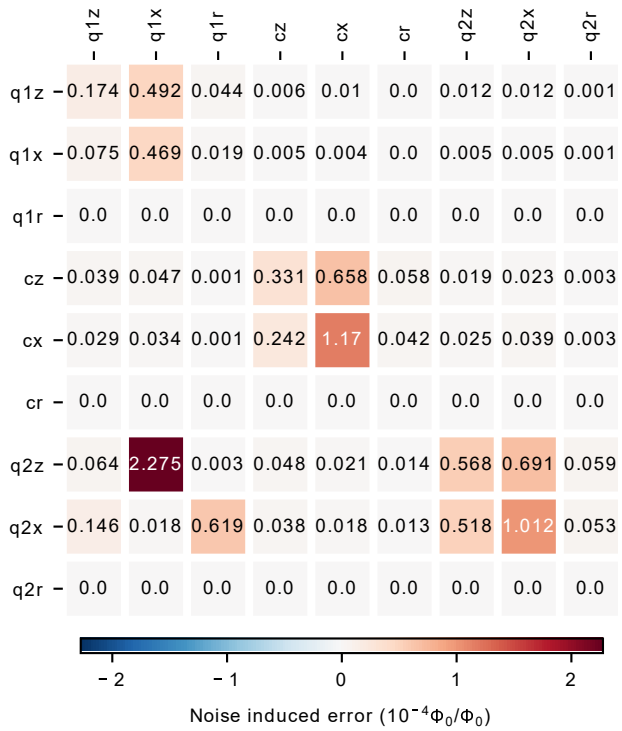

Figure 3.19: Measurement-noise-induced error in the coupling matrix for device B. The induced errors on the measured crosstalk to resonators are much smaller than on the qubits.

3.10.3 Error due to measurement noise

Since the analysis of CISCIQ data relies heavily on identifying symmetries in the measured S_{21} images, one could ask whether the fluctuations in S_{21} due to measurement noise cause significant errors. For this reason, we characterized the error of the coupling coefficients solely due to measurement noise. This is done by resampling the measurement data with added Gaussian noise on measured $|S_{21}|$. The noise parameters are chosen to reflect typical values at the choice of measurement parameters, such as the number of repetitions and readout integration time. We apply re-sampling on the data taken during the last iteration of device B. After applying the analysis procedure on 100 sets of resampled data, the standard deviation of the resultant coupling matrix is plotted in Fig. 3.19. The largest element is $0.2\text{m}\Phi_0/\Phi_0$, about 10 times lower than the total error measured in the main text. This shows that the error of calibration is not limited by the measurement noise.

3.10.4 Iterative calibration results for device C

The iterative calibration method is applied to device C, the two-qubit circuit used to demonstrate the periodicity maximization method. In Fig. 3.20 we show how the measured crosstalk and flux offsets converge towards identity and zeros. In Fig. 3.21 we show the final crosstalk matrix from the iterative procedure for the qubit, QFP, and tunable resonator, on which the periodicity optimization approach is implemented.

3.10.5 Optimization initialized with single iteration of translation-based calibration

In this section, we describe the results obtained by performing the periodicity optimization, starting from the estimated crosstalk of one iteration of the translation-based approach. In Fig. 3.22(a) we show the estimated crosstalk matrix obtained by a single iteration. This can be compared with the reference matrix elements plotted in Fig. 3.21. It can be seen that after a single iteration, the estimated crosstalk still deviates from the reference values, by as large as $\sim 10\%$.

In Fig. 3.22(b), we plot the deviation between the reference crosstalk matrix and the estimated crosstalk matrix after the optimization. Most of the deviation is about or less than 3×10^{-3}. This is comparable to the accuracy of the results discussed in the main text, which starts the optimization directly from $\mathbf{C}^{\text{ref}}$. The only exception is the QFPZ diagonal element, which corresponds to its period. This is probably due to the hysteresis of the QFP, which can be resolved by repeating the QFPZ periodicity measurement at a different QFPX biasing point.

3.10.6 Optimization with SPSA

In this section, we discuss the optimization results using an alternative optimizer called the Simultaneous Perturbation Stochastic Approximation (SPSA) [191]. This algorithm approximates the gradient of the objective function by measuring the finite difference due to a perturbation vector along a random direction in the parameter space, and performs gradient descent. We start the SPSA optimization with $\mathbf{C}^{\text{ref}}$ and the initial point is chosen uniformly randomly in the range $[-0.1, 0.1]$. In Fig. 3.23(a) a typical optimization process is shown, plotting the compensation parameters to QFPX and the periodicity versus the optimization step. The optimization converges after about 60 iterations and oscillates afterward. The optimized compensation parameters are used to compute the estimated

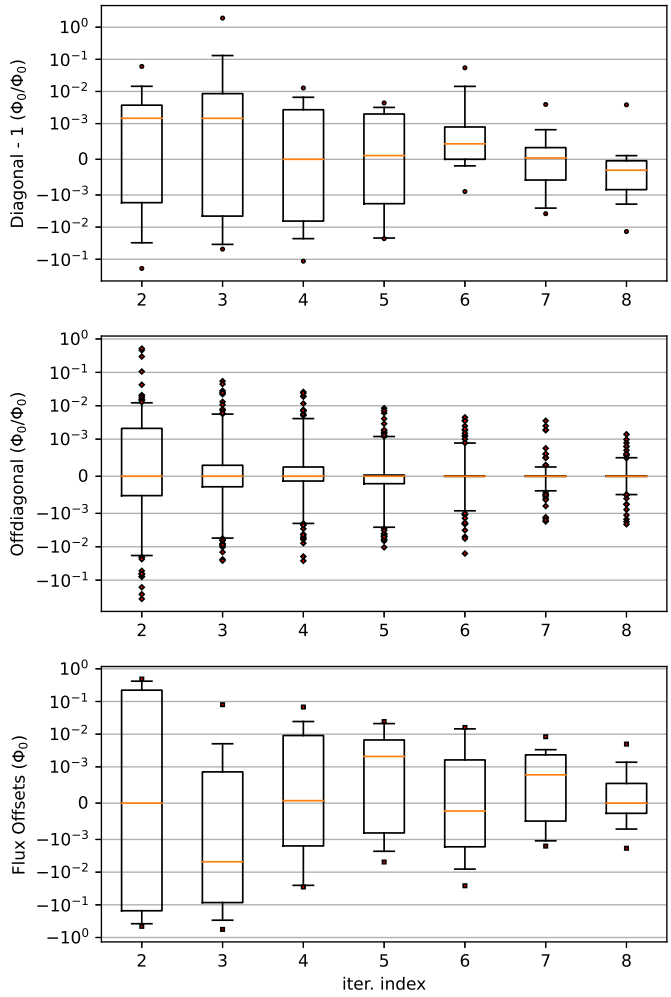

Figure 3.20: For device C, statistical box plots of the diagonal (top), off-diagonal (middle) coupling coefficients in $\mathbf{C}^{(n)\prime}$, and the flux offsets (bottom) in $\mathbf{f}_0^{(n)\prime}$ versus the iteration number. The orange bar is the median, the black box corresponds to the lower and upper quartiles, the segments contain the 5th to 95th percentiles of the data and the dots are outliers.

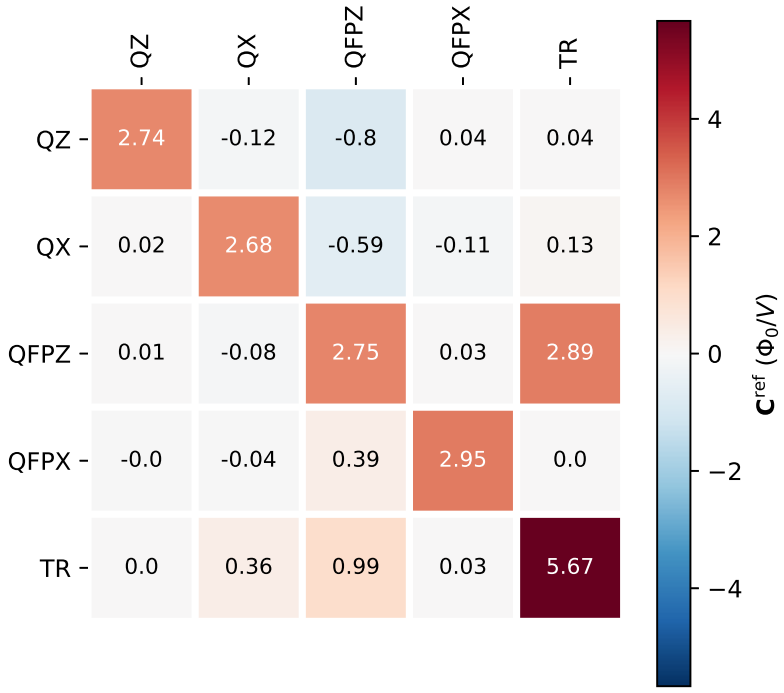

Figure 3.21: Final crosstalk matrix $\mathbf{C}^{\mathrm{ref}}$ obtained from the iterative procedure for the qubit, QFP, and tunable resonator subcircuit in device C, on which the periodicity optimization is applied.

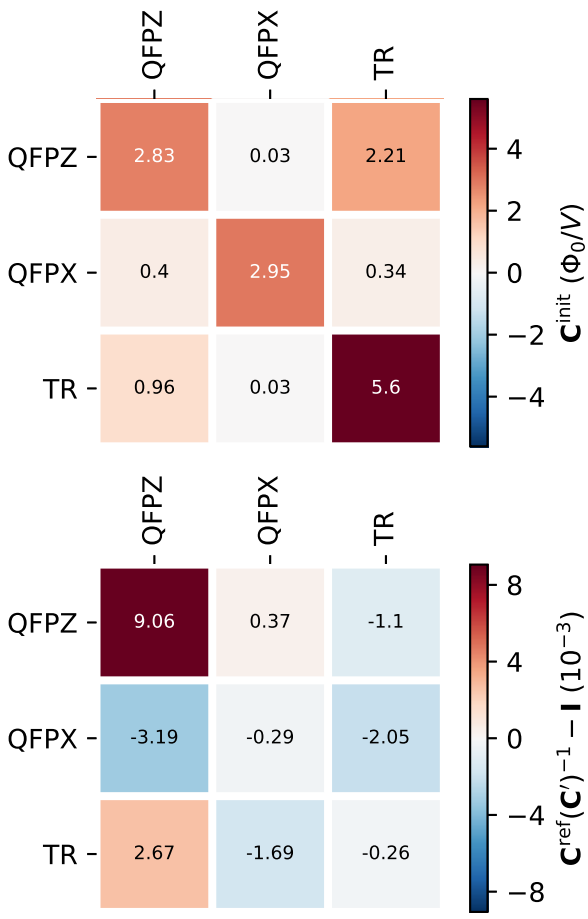

Figure 3.22: Top: $\mathbf{C}^{\mathrm{init}}$ as given by the first iteration of the translation-based calibration method. Bottom: The deviation between the optimized crosstalk matrix $\mathbf{C}'$ and the reference crosstalk matrix $\mathbf{C}^{\mathrm{ref}}$, defined as $\mathbf{C}^{\mathrm{ref}}(\mathbf{C}')^{-1} - \mathbf{I}$. The optimized crosstalk matrix $\mathbf{C}' = \mathbf{C}^{\mathrm{res}\prime}\mathbf{C}^{\mathrm{init}}$ is obtained by starting the optimization with the matrix given in the top panel.

$\mathbf{C}^{\text{res}\prime}$ and its difference from the identity matrix is shown in Fig. 3.23(b). The difference is about twice as large as compared to the results obtained using Bayesian optimization. We expect the results to improve by using better hyper-parameters for the optimization, such as the magnitude of the perturbation, which would likely remove the parameter oscillations near the end of the optimization.

3.10.7 Evidence for hysteresis of QFP and how to resolve it

It is found that the optimization landscape for the periodicity of the QFPX loop is often not well-behaved. As mentioned in Sec. 3.7, this is attributed to the hysteresis of the QFP. In this section, we briefly discuss the evidence of the hysteresis in the data and the solution to this problem based on the double-well potential of the QFP.

We first note that during the demonstration of the optimization-based calibration, we follow the convention in which all flux biases are defined based on external fluxes in a fundamental loop. This is in contrast to most applications in annealing, where the Z loop bias takes a compensated bias convention, such that the Z symmetry bias, corresponding to a symmetric double-well potential, is independent of X bias. The benefit of working with the fundamental loop bias is that the periodicity with respect to the bias is 1, as opposed to 2 in the compensated Z bias (see Appendix D).

In Fig. 3.24(a) we show the transmission versus the probing frequency and the QFPX bias at two different values of the compensation parameter $\Omega_{\text{QFPZ QFPX}} = \pm 0.001$, during the landscape measurement discussed in Sec. 3.7.2. It can be seen that when $\Omega_{\text{QFPZ QFPX}} = 0.001$, there are three periodically separated resonance traces while when $\Omega_{\text{QFPZ QFPX}} = -0.001$, the resonance trace at around $f'_{\text{QFPX}} \approx -1$ is missing. This suggests that QFP is not responding to the flux bias variations within the experiment time.

Due to the fundamental flux bias convention, when the X flux is being swept, both the tunneling and the biasing between the two persistent current states are changing. Due to the large persistent current of the QFP ($\sim 1\mu$A), there is a region in flux bias where the tunneling is small and the QFP could not tunnel to the persistent current state with lower energy. To solve this problem, we could work with the compensated Z bias convention (see Appendix D). In this convention, when sweeping f_{X}, one can avoid switching the sign of the bias between the two persistent current states, and hence avoiding the need for tunneling to occur for the QFP to respond to changes in flux biases. The periodicity along X bias increases to 2 in this convention.

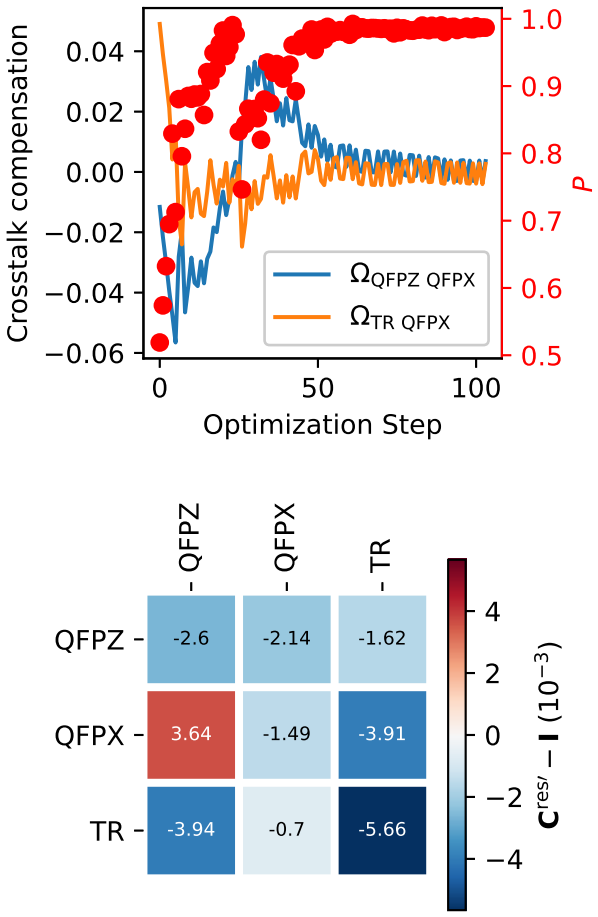

Figure 3.23: Top: Trial compensation parameters (left axis), $\Omega_{\mathrm{QFPZ\ QFPX}}$, $\Omega_{\mathrm{TR\ QFPX}}$ and periodicity P (right axis) versus SPSA optimization step. Bottom: Difference between the estimated residual crosstalk matrix $\mathbf{C}^{\mathrm{res}\prime}$, obtained using SPSA optimization, and the identity matrix.

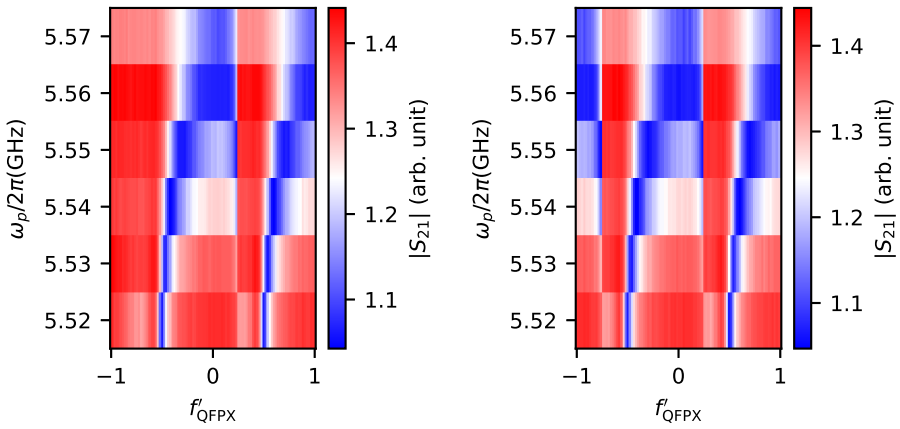

Figure 3.24: Transmission versus the probing frequency and the QFPX bias, at two different values of the compensation parameter $\Omega_{\mathrm{QFPZ\ QFPX}} = -0.001$ (left) and 0.001 (right).

Chapter 4

Demonstration of long-range correlations via susceptibility measurements in a one-dimensional superconducting Josephson spin chain

Long-range, high-degree connectivity between qubits is a highly-desired feature for quantum annealers. However, the simple approach of extending the size of the qubit or the coupler which mediates the interaction faces challenging drawbacks. On the one hand, extending the qubit size increases the noise experienced by the qubit, which negatively affects coherence. On the other hand, extending the size of the coupler leads to a reduction in its energy scale, which could affect the qubit dynamics. In this chapter, we explore the properties of a spin chain, made of a chain of rf-SQUID couplers, designed to act as a connectivity medium between two superconducting qubits. The susceptibility of the chain is probed and shown to support long-range, cross-chain correlations. In addition, interactions between the two end qubits, mediated by the coupler chain, are demonstrated. This work has direct applicability in near-term quantum annealing processors as a means of generating long-range, coherent coupling between qubits.

4.1 Introduction

Superconducting quantum information platforms have reached a level of maturity where tens of individual qubits, comprising a computational device, can provide proof of principle demonstrations of quantum simulations, quantum algorithms, and basic error correction functionality [22]. As these devices, and the tasks they seek to address, scale in size and complexity, so does the need for realizing qubit networks with increased dimensionality and expanded connectivity. These two desired features of future quantum processors prompt the development of long-range, qubit coherence preserving interactions [195, 196]. Quantum spin chains have been proposed as an effective medium for qubit interactions with these desired properties [197, 198, 199, 200, 201, 202]. In this chapter, we explore the possibility of long-range interactions supported by quantum spin chains for superconducting qubits [146, 144]. This architecture has direct application in recently proposed quantum annealing platforms based on superconducting capacitively shunted flux qubits [161, 178], rf-SQUIDs [203], fluxmon qubits [65], and fluxonium qubits [204].

Quantum annealing is emerging as a promising paradigm for near-term quantum computing [205, 206, 30, 16]. An initial Hamiltonian, whose ground state is straightforward to prepare, is transformed continuously to the problem Hamiltonian. The prepared state of the problem Hamiltonian is located in the vicinity of the true ground state and represents a useful solution to the optimization problem. In the limit of weak coupling to the environment, adiabatic quantum computing has been shown to be immune to dephasing in the energy basis, making it a particularly attractive candidate for near-term, noisy quantum computing platforms [207]. Commercial quantum annealers, based on superconducting Josephson flux qubits [89, 208, 209], have recently become available to the larger community and are beginning to make their mark as a valuable research tool, see e.g., Refs. [210, 211, 212].

There are strong motivations for improving upon the performance of quantum annealing processors [213], in particular with respect to how their constituent qubits interact with one another. Increasing both the graph dimensionality of qubit networks [195, 214], and improving connectivity [215], the degree to which the qubits are coupled to one another, would greatly reduce physical hardware overhead by increasing the types and sizes of optimization problems that can be natively embedded. Existing quantum annealing processors based on superconducting qubits possess either nearest neighbor [216] or a combination of inter- and intra- unit cell interactions [217] between qubits. Commercial annealers, possessing this combination of inter- and intra- unit cell interactions, currently rely on minor embedding [141, 142], a procedure of extending logical qubits over multiple physical qubits to implement problems that require higher dimensionality or connectivity than the

processor's hardware natively allows.

As each connection made to a qubit introduces additional noise and decoherence channels, expanding qubit connectivity in quantum annealing processors must be balanced against the need to maintain the qubits' coherence properties. Developing quantum annealing processors that support improved qubit coherence times would allow greater functionality in computation. Higher precision flux control, afforded by improved coherence, is required by many computational problems of interest [218, 108, 219]. In general, just how much of a computational advantage greater qubit coherence provides in quantum annealing processes is itself an open scientific question [130, 220]. Furthermore, more coherent quantum annealers will enable diabatic annealing protocols that require a greater degree of qubit coherence throughout the annealing process [221, 222, 32].

These two, often competing, improvements - creating qubit networks with higher dimensionality and expanded connectivity and maintaining qubit coherence - call for further development of long-range qubit interactions. One proposed scheme that accomplishes this dual need is utilizing spin chains as the qubit interaction medium [197, 199, 200]. Gapped spin chains, in the context of semiconducting quantum dots [198, 201, 202], have been proposed to support long-range, Ruderman-Kittel-Kasuya-Yoshida (RKKY) type qubit interactions [223]. Recent progress in this direction includes a demonstration of adiabatic quantum state transfer along a linear array of four electron spin qubits [224]. In addition to the possibility of supporting coherent coupling between two distant qubits, the spin chain architecture lends itself to higher connectivity schemes. Multiple qubits can be simultaneously interacting with a single 1-D chain [198]. Additionally, paramagnetic trees, formed by spin chains forking into multiple paths, offer another possible scheme for higher qubit connectivity [146, 144].

This work presented in this chapter demonstrates the viability of this coupling scheme in the context of superconducting Josephson qubit hardware. In the following, we discuss long-range coupling mediated by quantum spin chains in a hardware-independent fashion. This is a more natural language to describe long-range coupling as a consequence of the system's underlying quantum phase transition [225, 226, 227] [1]. Following this discussion, we demonstrate a realization of the quantum spin model with superconducting circuits. To accomplish this, we design a system of two qubits, coupled together through a chain of seven spin units. The spin chain, shown in Fig. 4.1, is realized by a one-dimensional array of seven tunable rf-SQUIDs [228, 229, 54, 230, 231, 161] inductively coupled to their nearest neighbor through the SQUIDs' main loops. Each end coupler is inductively coupled

[1] More precisely, these parameters are where the quantum phase transition happens for an infinite system.

to a tunable, capacitively shunted, superconducting flux qubit [45, 232, 233, 48]. Finally, to illustrate the viability of mediating long-range, coherent qubit interactions with our device, we characterize the non-local susceptibility of the coupler chain, demonstrate long-range qubit-qubit interactions, and identify the parameter region where both long-range correlations exist and the detrimental effects of low-frequency flux noise are negligible.

The Hamiltonian for the quantum spin chain is the one-dimensional Ising model. Incorporating the two end qubits, it can be written as

$$H = H_{\mathrm{q}} + H_{\mathrm{c}} + H_{\mathrm{int}}, \tag{4.1}$$

with

$$H_{\mathrm{q}} = \sum_{i=1}^{2} \left(\frac{\epsilon_{\mathrm{q_i}}}{2}\sigma_{\mathrm{q_i}}^{z} + \frac{\Delta_{\mathrm{q_i}}}{2}\sigma_{\mathrm{q_i}}^{x}\right), \tag{4.2}$$

$$H_{\mathrm{c}} = \sum_{i=1}^{7} \left(\frac{\epsilon_{\mathrm{c_i}}}{2}\sigma_{\mathrm{c_i}}^{z} + \frac{\Delta_{\mathrm{c_i}}}{2}\sigma_{\mathrm{c_i}}^{x}\right) + \sum_{i=1}^{6} J_{\mathrm{c_i c_{i+1}}}\sigma_{\mathrm{c_i}}^{z}\sigma_{\mathrm{c_{i+1}}}^{z}, \tag{4.3}$$

and

$$H_{\mathrm{int}} = J_{\mathrm{q_1 c_1}}\sigma_{\mathrm{q_1}}^{z}\sigma_{\mathrm{c_1}}^{z} + J_{\mathrm{q_2 c_7}}\sigma_{\mathrm{c_7}}^{z}\sigma_{\mathrm{q_2}}^{z}. \tag{4.4}$$

In the previous equations, $\Delta_{\mathrm{q_i}}/2$ ($\Delta_{\mathrm{c_i}}/2$) and $\epsilon_{\mathrm{q_i}}/2$ ($\epsilon_{\mathrm{c_i}}/2$) are the transverse and longitudinal components of the qubits' (couplers') spin while $J_{\mathrm{c_i c_{i+1}}}$ and $J_{\mathrm{q_i c_j}}$ represent the coupling strength between adjacent coupler units and between qubits and their nearest coupler unit. For the remainder of this chapter, we will assume the coupler units are operated homogeneously, that is $\epsilon_{\mathrm{c_i}} = \epsilon_{\mathrm{c}}$, $\Delta_{\mathrm{c_i}} = \Delta_{\mathrm{c}}$ and $J_{\mathrm{c_i c_{i+1}}} = J_{\mathrm{cc}}$.

Virtual excitations of the coupler chain can be integrated over to derive an expression for the coupler-chain-mediated effective qubit-qubit interaction strength, $J^{\mathrm{eff}}_{\mathrm{q_1 q_2}}$. By considering the qubit-adjacent coupler unit interaction, $J_{\mathrm{q_i c_j}}$, to be a weak perturbation to the coupler Hamiltonian, the interaction energy can be calculated to second order as the shift of the ground state energy of the coupler Hamiltonian. As the operating temperature of the device will be much less than the coupler chain excitation energy, it is reasonable to assume that the coupler chain remains in its ground state and the cross-chain interactions are supported by virtual excitations [199, 202]. This is reminiscent of the RKKY interaction whose long-range interaction between magnetic impurities is mediated by virtual excitations of conduction electrons above the Fermi surface [223].

By taking these above-stated approximations into account it is possible to derive an expression for the chain-mediated effective coupling strength between the end qubits (see

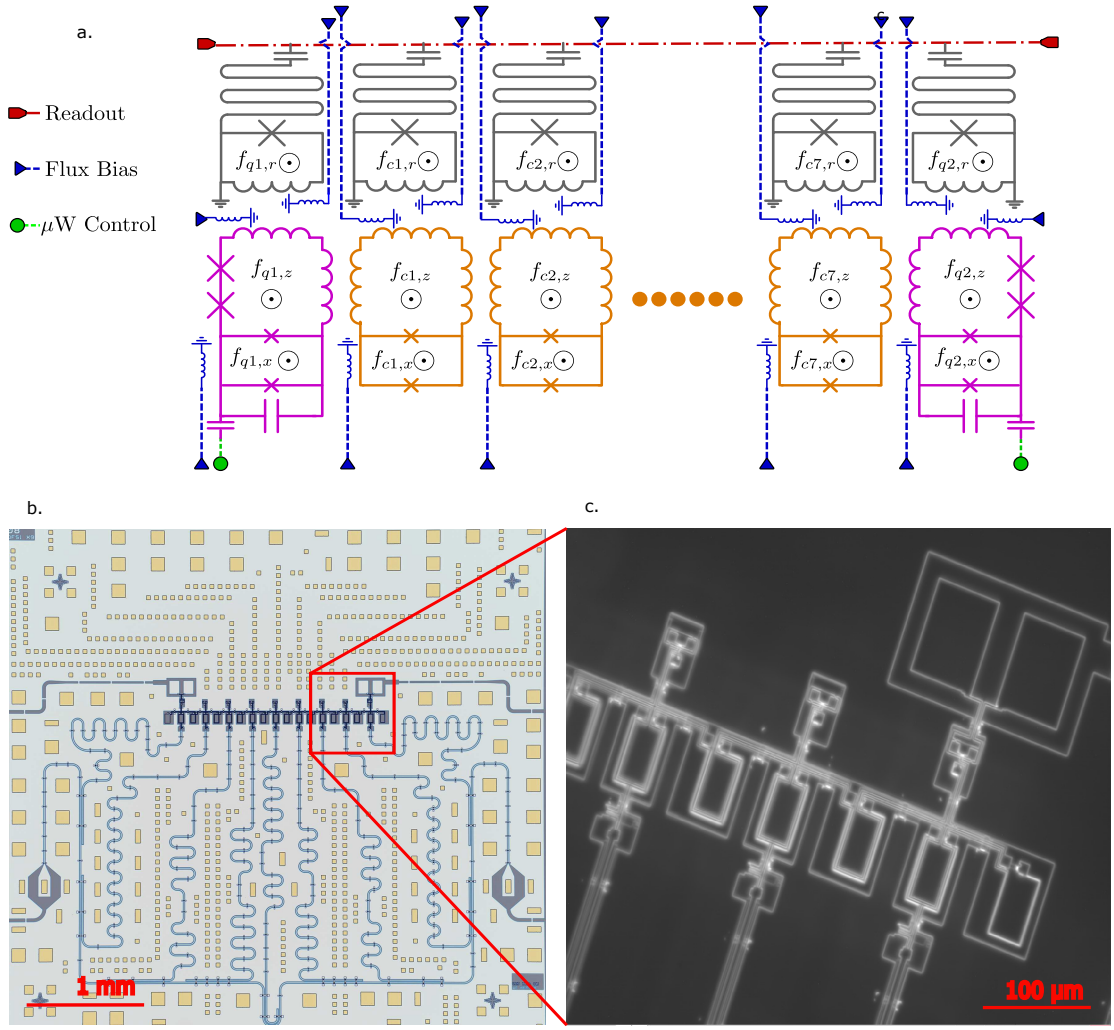

Figure 4.1: Coupler Chain Device. (a)A schematic showing the full device and circuit geometry: two end qubits, shown in magenta, and seven coupler units, shown in orange, each equipped with individual readout resonators. Also indicated are the flux control lines for the qubits, couplers, and readout resonators as well as the microwave control lines for the qubits and the microwave feed-through line for state readout. (b, c) Optical images of the device chip and an expanded view of one end of the coupler chain. The end qubit, capacitively coupled qubit microwave control line, the two adjacent coupler units, and respective readout structures are shown expanded in Panel (c). The readout rf-SQUIDs, connecting to both the qubit and coupler units, terminate at the end of their meandering resonators. The flux control lines are located on the opposing interposer tier.

Sec. 4.5.4 for calculation details). The effective Hamiltonian is

$$\begin{aligned} H^{\text{eff}}_{\text{q}_1,\text{q}_2} &= H_{\text{q}} + J^{\text{eff}}_{\text{q}_1\text{q}_2}\sigma^z_{\text{q}_1}\sigma^z_{\text{q}_2}, \\ J^{\text{eff}}_{\text{q}_1\text{q}_2} &\approx \frac{J_{\text{q}_1\text{c}_1}J_{\text{q}_2\text{c}_7}}{\Omega_{\text{c}}}(\langle 0_{\text{c}}|\sigma^z_{\text{c}_1}|0_{\text{c}}\rangle\langle 0_{\text{c}}|\sigma^z_{\text{c}_7}|0_{\text{c}}\rangle \\ &\quad - \langle 0_{\text{c}}|\sigma^z_{\text{c}_1}\sigma^z_{\text{c}_7}|0_{\text{c}}\rangle), \end{aligned} \tag{4.5}$$

where Ω_{c} is the energy gap between the coupler chain ground and first excited state and $|0_{\text{c}}\rangle$ represents the collective ground state of the unperturbed seven unit coupler chain. Note that an exact expression for the effective coupling between qubits contains the integrals of frequency dependent connected coupler correlation functions. The ground state connected correlation function in Eq. 4.5 is an approximation assuming a large excitation gap, Ω_{c}, and that the coupler chain excitation frequencies are sufficiently degenerate [200, 201]. This approximation is strictly valid for the coupler chain in its paramagnetic phase, where the transverse field on each coupler unit is much larger than the exchange interaction between coupler units. Writing this expression in terms of the zero temperature, bulk susceptibility of the response function in the Lehmann representation, $\widetilde{\chi}_{\text{c}_1\text{c}_7}$, [200] the effective interaction can be expressed as

$$J^{\text{eff}}_{\text{q}_1\text{q}_2} = \widetilde{\chi}_{\text{c}_1\text{c}_7}\, J_{\text{q}_1\text{c}_1}\, J_{\text{q}_2\text{c}_7}. \tag{4.6}$$

The main objective of this work is to measure the quantity $\widetilde{\chi}_{\text{c}_i\text{c}_j}$ as a function of $J_{\text{cc}}/(\Delta_{\text{c}}/2)$, the ratio of the inter-coupler longitudinal coupling strength, proportional to $\sigma^z_{\text{c}_i}\sigma^z_{\text{c}_{i+1}}$, to the individual coupler unit transverse field strength, oriented along $\sigma^x_{\text{c}_i}$, for the homogeneously tuned chain. Long-range coherent coupling becomes possible when the spin chain is tuned to the vicinity of its quantum critical point [225, 226]. In the case presented here, this occurs when the strength of the transverse fields of the coupler spins and inter-unit longitudinal coupling energies between the nearest-neighbor coupler spins become comparable. The coupler chain susceptibility is determined by measuring the response of the longitudinal fields of the coupler units along the chain when a small longitudinal field, $\delta\epsilon$, is applied to the end coupler unit. It is shown that the response truly becomes long-range, that is entirely cross chain, for $J_{\text{cc}}/(\Delta_{\text{c}}/2) \gtrsim 1$, where the system approaches and enters its ordered phase.

The one-dimensional transverse field Ising spin model can be realized by multilevel superconducting Josephson circuits. With the assumption of negligible state occupation of higher levels, the two lowest energy levels of the circuit define the qubit subspace where the transverse and longitudinal components of the unit's spin can be determined as a function of the applied magnetic flux. The individual qubit and coupler circuits utilize inductive couplings for implementing the inter-unit interactions $J_{\text{q}_1\text{c}_1}$, $J_{\text{c}_7\text{q}_2}$, and $J_{\text{c}_i\text{c}_{i+1}}$. Coupling of

this type for single unit coupler circuits has been demonstrated in flux qubits [228, 229, 54, 161], phase qubits [230, 231], and fluxmons [65]. The design choice of independent coupler circuits, as opposed to direct coupling between qubits, is particularly appealing for use in annealing processors where it is necessary to independently control the qubit properties and coupling strengths. This single unit method of identifying both the qubit and coupler's spin components is not as universally applicable as more general means such as the Schrieffer-Wolff transformation [234], particularly in the strong coupling regime. However, as we will restrict our analysis to the weak coupling limit, the results of the two methods coincide [235, 57, 236]. With these assumptions, the behavior of the physical device can be mapped to the one-dimensional, transverse field Ising spin model.

Each coupler circuit can be approximately characterized by its susceptibility, χ, which is the change in current induced by a biasing flux. Assuming the coupler remains in its ground state, this is equivalent to the curvature of the ground state energy with respect to the flux in the coupler's main loop.

$$\chi = \frac{1}{L_{\text{eff}}} = \frac{d\langle I_{\text{c}}^{z}\rangle}{d\, f_z} \approx \frac{d^2 E_{\text{c}}^{0}}{d\, f_z^2} \tag{4.7}$$

In Eq. 4.7, $\langle I_{\text{c}}^{z}\rangle$ represents the ground state expectation value of the current in the coupler's main loop and E_{c}^{0} is the ground state energy of the coupler unit. The character of these two quantities, $\langle I_{\text{c}}^{z}\rangle$ and E_{c}^{0}, is determined by f_x, the magnetic flux in the coupler's small loop. The coupler circuit's susceptibility, χ, is optimized as the unit's $\beta_{\text{c}} \equiv L_{\text{c}}/L_{\text{eff}} = 2\pi L_{\text{c}} I_{\text{c}}^{(c)}/\Phi_0 \approx 1$, where the coupler's local potential minimum is highly sensitive to biasing flux. As shown in Fig. 4.2, this occurs in the same f_x region where $J_{\text{cc}}/(\Delta_{\text{c}}/2) \approx 1$, a design choice made to optimize the generation of long-range correlations across the device. In addition, the device can be operated in a regime such that the coupler's minimum excitation energy, larger than 5 GHz, is much greater than the temperature of the system, approximately 400 MHz, the strength of the qubit-coupler interaction, which is below 1 GHz, and the typical qubit excitation frequency, approximately 2 GHz. This ensures the ground state properties of the coupler dictate its behavior, entanglement between qubits mediated by the coupler is supported, and fast (coupler) and slow (qubit) modes can be separated to preserve the qubit subspace.

The same notions of susceptibility and design constraints can also be applied to a long but finite chain of couplers. The current induced in coupler j when a flux is applied to coupler i is expressed as $\chi_{\text{c}_i\text{c}_j}$, the inter-chain susceptibility. The design constraints are slightly more involved for the chain when compared to a single coupler. For example, the length of the chain has a closing effect on the size of the gap as the fundamental mode frequency of the chain decreases with length. This introduces a trade-off between the

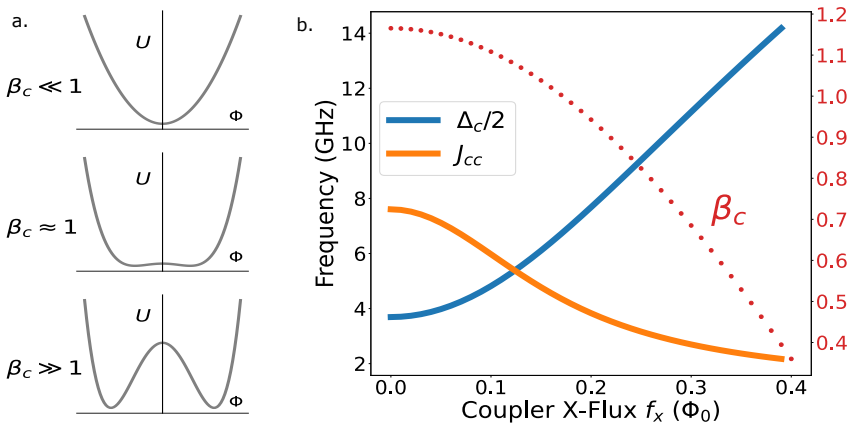

Figure 4.2: Single Coupler Behavior. (a) The ratio of the Josephson inductance to the geometrical inductance, β_c, dictates the shape of the potential energy of the tunable rf-SQUID coupler circuit. When the geometrical inductance dominates, $\beta_c \ll 1$, the potential energy landscape is approximately harmonic. When the Josephson inductance dominates, $\beta_c \gg 1$, the energy landscape becomes double-welled with each minimum representing oppositely circulating current states. Due to the large energy barrier between the states, moderate changes in f_z do not change the current state of the circuit. The coupling is optimized when the geometrical and Josephson inductances are approximately equal. This results in a wide, shallow energy minimum where even slight changes in f_z can induce strong fluctuations between the oppositely circulating current states of the coupler circuit. (b) Both the single coupler transverse field, $\Delta_c/2$, and the inter-coupler interaction energy, $J_{c_i c_{i+1}} = M_{c_i c_{i+1}} I^z_{c_i} I^z_{c_{i+1}}$, are displayed as a function of the coupler f_x when $f_z = \Phi_0/2$. These parameters are calculated in single coupler simulations and then transcribed into spin model parameters. The equality of these two terms appearing in the transverse field Ising model for $f_x \simeq 0.14\,\Phi_0$ signals the location of the quantum critical point, in the vicinity of which we expect long-range correlations to emerge. In addition, the dependence of β_c is displayed as a function of the coupler's f_x for $f_z = \Phi_0/2$. By design, the optimum coupling point, $\beta_c \approx 1$, coincides with the coupler f_x value where we expect critical behavior in the coupler chain.

physical range of interaction and the need to preserve the excitation energy gap of the chain [237].

Taking the same concept of single coupler susceptibility to hold for the coupler chain, as well as adhering to the extra constraints introduced by the many-body chain system, it is possible to construct the form of the effective qubit-qubit interaction, Eq. 4.5, in terms of circuit parameters. Assuming the coupler gap is much greater than the qubit working frequencies allows one to separate the device spectrum into 'slow' qubit-like states and 'fast' coupler-like states. Invoking the Born-Oppenheimer approximation restricts the coupler spectrum to its unperturbed ground state [238]. Further restricting our analysis to the weak coupling limit, $M_{\mathrm{qc}}/L_{\mathrm{c}} \ll 1$, allows us to write the qubit-chain interaction, in general a complicated nonlinear quantity, as an inductive interaction between qubit currents [65, 56], given by

$$\begin{aligned} H_{\mathrm{int}} &= \chi_{\mathrm{c_1c_7}}(M_{\mathrm{q_1c_1}}\hat{I}^z_{\mathrm{q_1}})(M_{\mathrm{q_2c_7}}\hat{I}^z_{\mathrm{q_2}}) \\ &= \widetilde{\chi}_{\mathrm{c_1c_7}}(J_{\mathrm{q_1c_1}})(J_{\mathrm{q_2c_7}})\,\sigma^z_{\mathrm{q_1}}\sigma^z_{\mathrm{q_2}}. \end{aligned} \tag{4.8}$$

The final line of Eq. 4.5 connects the circuit model of the coupler chain to the spin chain model by recognizing that the two versions of the susceptibility are related by $\widetilde{\chi}_{\mathrm{c_1c_7}} = \frac{\chi_{\mathrm{c_1c_7}}}{I^{\mathrm{p}}_{\mathrm{c_1}} I^{\mathrm{p}}_{\mathrm{c_7}}}$. The symbol $I^{\mathrm{p}}_{\mathrm{c_i}}$ refers to the persistent current of the i^{th} coupler, which, when operated at $f_z = \Phi_0/2$, is simply the current dipole moment $\langle 0|\hat{I}^z_{\mathrm{c_i}}|1\rangle$ [57].

Now that the long-range, effective interaction between the two qubits is expressed in terms of circuit parameters, it is possible to measure the response function, $\chi_{\mathrm{c_1c_7}}$, of the coupler chain in a quantitative manner. This task is accomplished by performing two similar measurements. Firstly, only the behavior of the coupler chain units is considered. This measurement is performed with both flux qubits placed at a magnetic flux bias operating point where the circuit has its maximum transition frequency which is much greater than the operating frequencies of the remaining chain units. This decouples the qubits from the coupler chain dynamics and allows the coupler susceptibility to be characterized. Secondly, with knowledge of the chain susceptibility, the two flux qubits are brought into an interacting flux operating point and cross-chain qubit-qubit interactions are demonstrated. Finally, to quantitatively measure the effective qubit-qubit interaction strength, $J^{\mathrm{eff}}_{\mathrm{q_1q_2}}$, we revisit the coupler chain only measurements in more detail to extract the cross-chain susceptibility, $\chi_{\mathrm{c_1c_7}}$. We find that our measurements of $J^{\mathrm{eff}}_{\mathrm{q_1q_2}}$ through susceptibility measurements agree well with full device simulations of the qubit-qubit spectral line splitting.

4.2 Results

4.2.1 Device details and control

The coupler chain device consists of two capacitively shunted, tunable flux qubits and seven tunable rf-SQUIDs, all equipped with individual readout resonators. The measurement setup is the same as the experiments done in Chapter 3 (see also Appendix B). Device characterization and circuit parameter extraction are presented in Sec. 4.5.3. The device is fabricated using the architecture described in Ref. [180], and consists of two separate chips – called the qubit layer and the interposer layer. The interposer layer, seated on the device package's printed circuit board cavity and wire-bonded to the exterior control lines, holds the flux bias lines. The qubit layer, hosting the qubits, couplers, resonators, and co-planar waveguide, is Indium bump bonded atop. The indium bumps provide structural stability, common ground paths between layers, and a conduit for microwave signals originating on the interposer layer, running through the bumps, and continuing on the qubit layer. This device environment allows greater flexibility than planar devices for distributing flux bias lines, represents a step towards full 3-D integration, and supports an electromagnetic environment suitable for quantum annealing controls.

Each unit, qubit or coupler, possesses a meandering resonator terminated in an rf-SQUID for purposes of readout and calibration. These resonators, when their terminating rf-SQUID is biased to a flux-sensitive region, act as magnetic flux detectors, capable of discerning the qubit or coupler unit's persistent current state. When the terminating rf-SQUID is biased to its flux-insensitive operating point, the resonator is exclusively sensitive to the unit's energy level occupation through the resonator-unit dispersive interaction [62]. Being able to operate in these two modes alleviates the need for multiple readout structures, further freeing up space on the chip.

Gaining full flux control of a device of this size is a difficult task for a number of reasons. Complete individual control of each unit requires 27 flux bias control lines corresponding to the 27 Josephson flux loops. Current in one control line provides magnetic flux for its target Josephson loop but also couples to nearby loops. Hence, it is necessary to determine the full 27×27 element mutual inductance matrix before one can expect adequate control of this device. In addition, these inductive elements need to be determined while in the presence of spurious interactions between units. Strong inter-unit interactions can easily mask the linear line-loop inductive interaction. In order to address these points, scalable, device-independent, automated methods have been developed and implemented to characterize the bias line to circuit flux inductive matrix to within acceptable errors for device control [239].

4.2.2 Determination of the cross-chain susceptibility

To explore the behavior of long-range qubit interactions mediated by the coupler chain, it is necessary to characterize the inter-coupler susceptibility, $\chi_{c_i c_j}$. To isolate the coupler chain dynamics, we first flux bias the two end qubits to their high frequency, uncoupled state. Every coupler unit is operated such that its main loop is flux biased at one-half magnetic flux quanta and its small loops are uniformly biased with f_x^c. In this configuration, Coupler 7's f_z is swept across its half quanta point for a range of uniformly biased coupler f_x^c values. Instead of directly measuring the current response in the target unit, we observe the shift of the target unit's effective main loop half-quanta point (see Sec. 4.4 for experimental methods). As the unit's main loop half-quanta flux operating point corresponds to its minimum transition frequency, the dispersive interaction with the unit's resonator provides an accurate determination of the unit's effective half-quanta point in the presence of strong inter-unit and unit-resonator interactions.

The magnitude of the induced fluxes for each coupler unit are displayed in Fig. 4.3. Recall that f_x^c simultaneously controls the unit's transverse field, Δ_c, in the Ising spin model picture as well as the magnitude of the unit's persistent current, thus the longitudinal coupling strength, $J_{cc} = M_{cc} I_{c_i}^z I_{c_{i+1}}^z$. For larger values of f_x^c, the flux propagation signal attenuates over short length scales, up to a few coupler units. As shown in Fig. 4.2(b), this is the regime where the transverse field dominates and the chain system is in its paramagnetic state. For $f_x^c \leq 0.18\,\Phi_0$, long-range correlations are supported across the entire chain. This is where the critical region of the underlying Ising spin model is expected to be located.

The critical region of the Ising spin model is determined by single coupler properties. To further validate our results, full device simulations of the experimental protocol were performed. To perform simulations of a device with such a large Hilbert space, a hierarchical scheme is employed [240]. First, the low energy spectrum, eigenstates, and other operator eigenvalues are computed for individual units. These eigenstates then form the initial basis for computing the energy spectrum of two- and three-unit systems comprising subsections of the full device. Finally, the subsections are appropriately coupled together and the full device energy spectrum, eigenstates, and relevant operator eigenvalues are calculated. At each step of this procedure, necessary mode occupation numbers are included in the calculation such that the low-lying energy and other operator spectra are well converged. Simulating the identical procedure as the measurement protocol allows us to track the target unit's effective main loop half-quanta point yielding results that match well with the experimental outcome (see Fig. 4.6(b-e)).

With the derived information on the chain susceptibility, we now place the two end qubits at flux operating points where it is possible to couple to the adjacent chain unit.

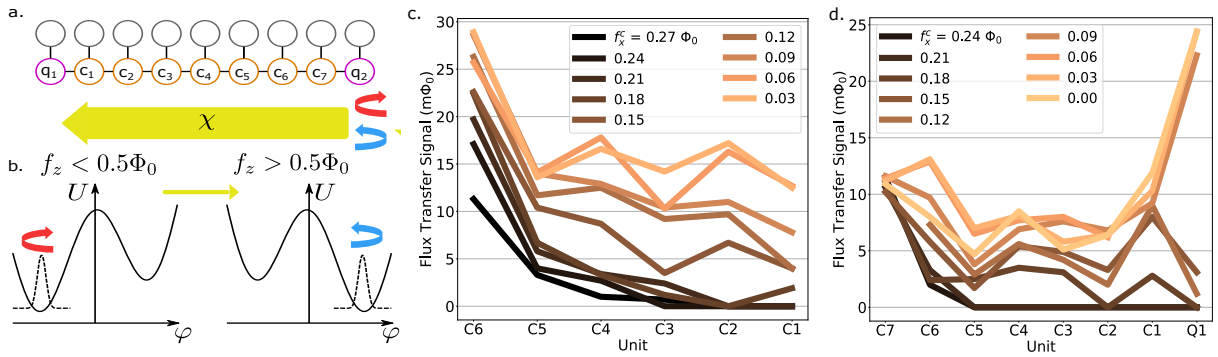

Figure 4.3: The Flux Propagation Experiment. (a) A schematic depicting the flux propagation experiment. Either Coupler 7 [results in (c)], or Qubit 2 [results in (d)], act as the source unit generating the flux signal. The flux response is then measured in the different units along the chain. (b) The flux signal is generated by sweeping the f_z of the source unit across its one-half magnetic flux bias point causing that unit's circulating current to change direction. (c,d) The magnitude of the experimentally measured flux signal is displayed for different homogeneously tuned coupler f_x values for the coupler-only (c) and full device (d). The displayed signal is the difference in effective $f_z = \Phi_0/2$ point when the source unit is placed at $f_z = \Phi_0/2 \pm 20\,\mathrm{m}\Phi_0$. Based on full device simulations, this range fully captures the transition of the target unit's flux response (see Fig. 4.6(f)). This prediction is further validated by measurements extending to larger f_z offsets of the source unit. As the strong coupling between the tunable resonator and the qubit (coupler) makes it challenging to model the resonator response, we therefore resort to image processing techniques to determine the effective symmetry point of the qubit (coupler) unit. This sets the uncertainty of the extracted flux signal to be on the order of the pixel size of the scan, 2.4 $\mathrm{m}\Phi_0$. In the case of both the coupler-only and qubit-to-qubit measurements, the cross-chain signal becomes non-zero in the vicinity of the coupler chain's predicted critical region.

Qubit 1, the target qubit, is operated such that its main loop is flux biased at one-half magnetic flux quantum and its smaller x-loop is flux biased such that its transverse field has strength $\Delta_{q_1} = 2.3$ GHz, approximately where the qubit's potential becomes double-welled. Qubit 2, the source qubit, is placed at its minimum $\Delta_{q_2} \simeq 10$ MHz, deep in its double well regime, and its flux bias f_z is swept across its one-half magnetic flux quantum point. This measurement protocol is repeated for the different coupler chain operating points described in the coupler chain susceptibility experiment.

The results of the qubit-qubit interaction experiment are shown in Fig. 4.3. This figure displays the magnitude of the flux signal propagating along the coupler chain and ultimately into the opposite qubit. These results agree well with full device simulations of the equivalent protocol. As shown in Fig. 4.3(c, d), long-range, cross-chain interactions become supported at approximately $f_x^c \sim 0.15 - 0.18\,\Phi_0$ in both the coupler chain susceptibility and long-range qubit interaction experiments.

Furthermore, the full results of the coupler-only susceptibility measurements can be used to predict the strength of the effective qubit coupling, $J^{\text{eff}}_{q_1 q_2}$, mediated by the chain. Equations (4.9, 4.10) show how the measured coupler susceptibility, $\frac{df^z_{c_1}}{df^z_{c_7}}$, determines the effective qubit interaction strength.

$$J^{\text{eff}}_{q_1 q_2} = \chi_{c_1 c_7} (M_{q_1 c_1} I^z_{q_1})(M_{q_2 c_7} I^z_{q_2}) \tag{4.9}$$

$$\chi_{c_1 c_7} = \frac{d\langle I^z_{c_1}\rangle}{df^z_{c_7}} = \frac{d\langle I^z_{c_1}\rangle}{df^z_{c_1}} \frac{df^z_{c_1}}{df^z_{c_7}} \tag{4.10}$$

Shown in Fig. 4.4 are the effective one-half magnetic flux quantum points of Coupler 1's main loop as a function of Coupler 7's f_z for various homogeneous coupler unit settings. As expected, for the flux regime where the transverse fields dominate, Coupler 1's effective half quanta point is unaffected by the f_z of Coupler 7. As the transverse field is lowered and the coupler-coupler longitudinal coupling strength increases, the effect of Coupler 7's f_z on Coupler 1 becomes more pronounced. The slope at the center of these curves, $\frac{df^z_{c_1}}{df^z_{c_7}}$, can then be extracted. The remaining factors, $I^z_{q_i}$ and $\frac{d\langle I^z_{c_1}\rangle}{df^z_{c_1}}$, are determined from single unit simulations (see Fig. 4.13).

A proper comparison of the qubit interaction strength, $J^{\text{eff}}_{q_1 q_2}$, derived from both full device simulations and the measured coupler susceptibility, is necessary to confirm that the coupler susceptibility is a valid measure of qubit coupling strength. As illustrated in

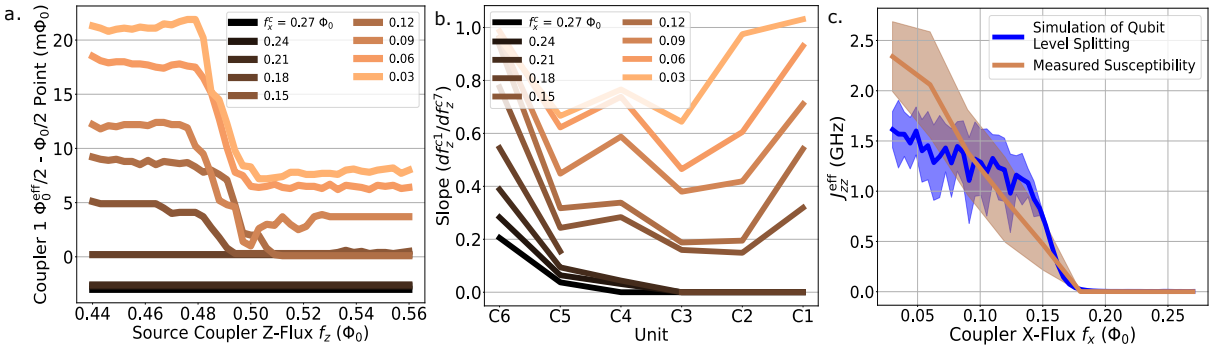

Figure 4.4: Cross Chain Susceptibility. (a)The effective one-half magnetic flux quantum points for Coupler 1's main loop as a function of Coupler 7's f_z for different homogeneous coupler f_x settings. The response becomes non-zero in the vicinity of the couplers' $f_x = 0.15\,\Phi_0$. The offset of both Coupler 1's $\Phi_0^{\text{eff}}/2 - \Phi_0/2$ average value from zero and the inflection point of Coupler 1's flux response from Coupler 7's $f_z = \Phi_0/2$ is due to slight mistuning of the couplers' longitudinal fields. It is the change in Coupler 1's $\Phi_0^{\text{eff}}/2 - \Phi_0/2$ with respect to Coupler 7's f_z that is the relevant quantity. The uncertainty in the extracted values is identical to those in Fig.4.3. (b) The curves in Panel (a), and the corresponding figures for the other units, were then fit to a sigmoid function. Displayed here is the midpoint slope extracted from those fits for all units for different homogeneous coupler f_x settings. The error bars were generated by repeating this procedure many times with small offsets picked from a normal distribution with a standard deviation of 1.2 mΦ_0 applied to the nominal effective symmetry point values. The error bars are the resultant standard deviation of the large array of slopes extracted from the fit sigmoid function. (c) Using the slopes from Panel (b) for Coupler 1, the effective coupling between the two qubits is calculated via Eq. 4.9 and displayed. This is compared to $J^{\text{eff}}_{q_1q_2}$ calculated from the splitting of the otherwise degenerate qubit transitions as predicted by full device simulations incorporating reasonable levels of flux noise. The strong agreement between the two different measures of $J^{\text{eff}}_{q_1q_2}$ indicates that the optimal operating region of the chain is coupler $0.15 \lesssim f_x \leq 0.18\,\Phi_0$, where there is significant coupling strength and, as shown in Fig. 4.5, both the detrimental effects of flux noise and the qubit-coupler state mixing is negligible.

Fig. 4.5, The effective qubit-qubit interaction strength is derivable from full device simulations by noting the energy level splitting between the two end qubits' previously degenerate energy spectrum. This is done by first setting both qubits to have the same finite transverse field and zero longitudinal field. As the cross-chain coupling is increased by lowering the f_x^c of all couplers, the initially degenerate qubit states, $|+-\rangle$ and $|-+\rangle$, develop a splitting that, for weak coupling, is twice the coupling strength $2J^{\text{eff}}_{q_1 q_2}$. A comparison can then be made between the qubit interaction strength, $J^{\text{eff}}_{q_1 q_2}$, as measured in the flux signal propagation experiment, and the qubit level splitting exhibited in full device simulations. As shown in Fig. 4.4, the simulated results find strong agreement with the results of our coupler susceptibility measurements in the weak interaction limit. The quantitative divergence of these two results is expected in the strong coupling regime, for the coupler flux biases $f_x^c < 0.15\,\Phi_0$. In this case, the weak interaction limit assumed in Eq. 4.8 breaks down and the effective qubit-qubit interaction can no longer be described as a linear inductive coupling. Additionally, in the strong coupling regime shown in Fig. 4.5, the qubit energy levels become dressed by the coupler levels. Hence, the two lowest energy levels can no longer be identified as purely qubit-like and their spectral distance no longer represents a simple qubit-qubit interaction.

4.2.3 Analysis of the impact of noise on cross-chain correlations

Low-frequency flux noise is expected to play a detrimental role in the coherence-preserving properties of this long-range interaction. As demonstrated, flux signals can be transported and even amplified in certain coupler flux operating regimes. Therefore, it is crucial to identify a flux operating regime for the coupler units where strong, long-range coupling is present and the detrimental effects of flux noise are not amplified across the device.

With this goal in mind, full device simulations were performed with realistic values of low-frequency flux noise. Flux noise has been measured, across many different platforms and frequencies [241, 48, 242], to be approximately $1/f^\alpha$ in nature, $\alpha \sim 0.9$, with magnitude $1 - 5\,\mu\Phi_o \text{Hz}^{-1/2}$. For moderate-frequency measurements, the effect of this low-frequency noise is to effectively add a small random flux offset to the flux operating point of the measurement. This small random flux offset is sampled from a Gaussian distribution whose standard deviation is determined by integrating the noise spectrum over the appropriate frequency range, from measurement repetition rate to pertinent experimental frequencies, as well as accounting for the circuit geometry. This amounts to a typical random flux offset in the tens of $\mu\Phi_o$.

Simulations of this type were performed repeatedly to determine the behavior of the device energy level structure in the presence of low-frequency flux noise. As shown in Fig. 4.5,

the energy spectrum of the device is highly susceptible to flux noise in its deeply coupled state. Significant line broadening occurs for the uniformly tuned coupler f_x^c between 0 - 0.15 Φ_0. This allows us to identify a region of flux operation, coupler f_x^c from 0.15 to 0.18 Φ_0 where significant long-range interactions are present yet the detrimental effects of flux noise are still minimal.

Another source of experimental imperfection is caused by device fabrication variations. In particular, expected variations in Josephson junction critical currents from device to device can cause offsets both in the targeted Δ_c and inter-unit coupling strengths, causing inhomogeneities across the coupler chain. Note that these errors are set at fabrication, unlike the flux offsets due to low-frequency flux noise which are fluctuating. Spin model simulations of the effective long-range coupling strength and flux propagation experiments were performed with random inhomogeneities added to the targeted values of Δ_{c_i}, $J_{c_i c_{i+1}}$, $J_{q_1 c_1}$, and $J_{q_2 c_7}$. For errors typical of measured devices, both the energy level splitting and flux propagation signal are robust against these imperfections (see Sec. 4.5.5).

4.3 Discussion

Quantum annealing processors stand to benefit from higher dimensional qubit networks, expanded connectivity, and improved qubit coherence. Accomplishing this will require long-range qubit interactions that do not degrade qubit behavior. The use of spin chains as a quantum bus is a promising venue for this. Presented here is a preliminary step in this direction in the context of a superconducting Josephson system. To build on this idea, there have been proposals to generalize one-dimensional spin chains, capable of entangling end qubits, to both paramagnetic trees [146, 144] and two-dimensional spin networks capable of providing entanglement amongst a perimeter of qubits [243, 144]. However, as we look to scale this coupling architecture to larger processors, there are important scientific questions to answer. In particular, it is an open question as to how the effective coupling scales with respect to the chain length when operating in the weak coupling, paramagnetic regime. Nonetheless, the coupler chain architecture holds promise for use in scalable, coherent quantum annealing devices with high graph dimensionality.

Susceptibility measurements in quantum systems, such as those performed in this study, have been considered as a possible measure of the system's entanglement [244]. The susceptibility experiment's close agreement with full device simulations, which also demonstrate qubit energy level splitting in the presence of expected noise levels, suggests the qubits can be prepared in an entangled doublet state. In this view, the susceptibility measurements

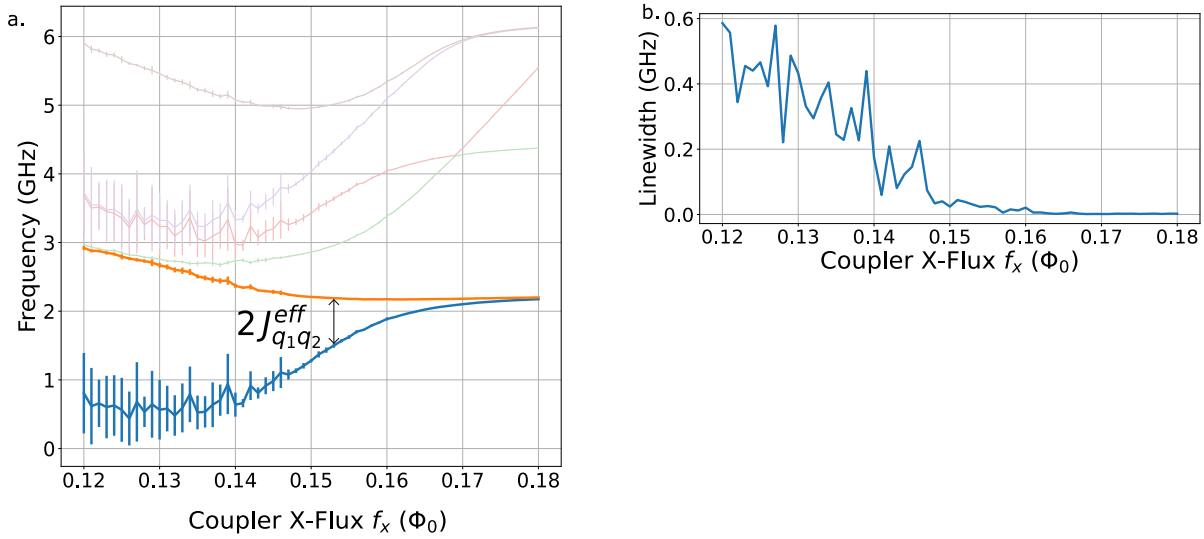

Figure 4.5: Effects of Low Frequency Flux Noise. (a) Average energy levels of the full device versus coupler X-flux f_x, compiling ten separate calculations with random flux operating point offsets (see text). At small coupling, or large f_x, the orange and blue energy levels are identified as the two initially degenerate qubit levels, $|+-\rangle$ and $|-+\rangle$. As the coupler f_x is lowered and cross-chain coupling becomes significant, the previously degenerate qubit levels, split in the presence of cross-chain coupling. The lightly faded color lines are the few next higher energy levels of the full device consisting of a mixture of the coupler and higher qubit levels. Note that the coupler chain and the qubit levels have become comparable in frequency by coupler $f_x \lesssim 0.15\,\Phi_0$. In this region, what were initially qubit-like energy levels, are now dressed by the coupler levels and the splitting of these two energy states no longer represents the effective qubit-qubit interaction strength. In addition, a coupler chain state anti-crosses with the qubit state $|\uparrow\uparrow\rangle$ at approximately coupler $f_x = 0.17$ mΦ_0. While this does appear to violate our previous assumptions concerning the separation of coupler chain and qubit operating frequencies, for adiabatic annealing protocols the $|\uparrow\uparrow\rangle$ state should rarely be accessed. Additionally, this property can be improved upon in future design iterations. (b) Shown is the linewidth of the lower qubit-like level, calculated as the standard deviation of the transition frequency over multiple simulation runs in the presence of realistic flux noise. There is a region, $f_x = 0.15 - 0.18\,\Phi_0$, where significant cross-chain coupling is present but where the effects of flux noise do not significantly broaden the lower qubit-like level's linewidth. For $f_x < 0.15\,\Phi_0$, the calculated linewidth suggests the coherence times of the qubit have deteriorated to the nanosecond scale.

presented here are a consequence and valid measure of a coherent long-range qubit interaction. This view, however, needs further experimental validation. Future experimental work will address the measurement of the coherent coupling enabled by this method using spectroscopic characterization as well as adiabatic transfer protocols. Additionally, the detection of entanglement can be augmented by measuring other observables and witnesses for interacting quantum spin systems [245].

In closing, we have demonstrated long-range interactions in a superconducting Josephson spin bus by probing the device's response function. Simulations of the device, which agree well with measured quantities, predict significant long-range interaction simultaneous with satisfactory qubit coherence. This device has immediate application in near-term quantum annealing devices where both long-range and coherent qubit couplings are necessary for quantum computation speedup.

4.4 Experimental Methods

Both the coupler-only susceptibility measurement and full device qubit interaction demonstration experiments were conducted in a similar fashion. Either Coupler 7, for the coupler-only, or Qubit 2, in the full device, acted as the source unit. For uniformly tuned coupler units, all couplers at their z-symmetry point and homogeneously tuned x-flux settings, the source unit's z-flux is swept across its z-symmetry point, causing the source unit to transition from its 'left' to 'right' circulating current state. This acts to shift the effective z-symmetry point of the remaining units in a manner dependent on the coupler units' x-flux.

The response of the target units is measured by observing the dispersive shift in the target units' resonator. The target units' resonators are maintained at zero flux, or their high-frequency point. The dispersive interaction between the unit and the resonator can be used to ascertain the unit's z-symmetry point. So, for each source unit's z-flux setting, the target unit's resonator is probed over a range of frequencies for a range of the target unit's z-flux settings. In this way, the target unit's effective z-symmetry point can be tracked as a function of the source unit's z-flux setting.

This procedure was applied iteratively starting with the unit adjacent to the source unit, and then continued down the chain. Applying this process iteratively also allowed us to fine-tune the target units' z-flux. As the coupler units' x-flux is lowered and the inter-coupler interactions become stronger, slight mistuning of the unit's z-flux away from their symmetry point can shift the effective symmetry point of nearby units. Applying the

measurement/fine-tuning procedure iteratively allows the units to be tuned correctly even in the presence of slight imperfections further down the chain.

Simulations using the platform described in Sec. 4.5.2 were used to validate the experimental flux signal propagation results. The f_z symmetry point of the target unit is defined as the unit's f_z where the ground state expectation value of the z-loop current equals zero. To track the magnitude of the flux signal, we recorded the difference in the target unit's z-symmetry point when the source unit was 20 $m\Phi_0$ on either side of the z-symmetry point. This protocol was followed in both simulation and experiment.

4.5 Additional details on device modeling and characterization

4.5.1 Circuit model

The Coupler Chain device consists of 7 tunable rf-SQUIDS coupled through their z-loop mutual inductance with the two end couplers coupled mutually to two capacitively shunted flux qubits. Shown in Fig. 4.7 are schematics of the qubit and coupler design. The qubit and coupler are divided into four and three floating islands respectively. Design work utilized Ansys Maxwell finite element electromagnetic simulations supplemented with simulations run in Sonnet to correctly account for higher frequency inductive effects. Effort was made to reproduce effective circuit parameters found in [48, 161]. The results of these simulations are displayed in Table. 4.1.

4.5.2 Simulation framework

Upon attaining all lumped element circuit parameters from the classical electromagnetic Ansys Maxwell and Sonnet simulations, quantum simulations of the lumped element single qubit and coupler units and full device were performed using the MIT-Lincoln Laboratory developed JJSim quantum circuit simulation package [240]. With this software package, energy spectra and operator matrix elements can be extracted. Single unit simulations are performed by identifying internal modes and evaluating the circuit Hamiltonian in the harmonic level basis for high enough levels of internal modes such that the operator expectation values in the low energy qubit subspace converge.

For full device simulations, individual units were grouped and coupled to one another in a hierarchical structure. The end qubits remain their own two subgroups. The coupler

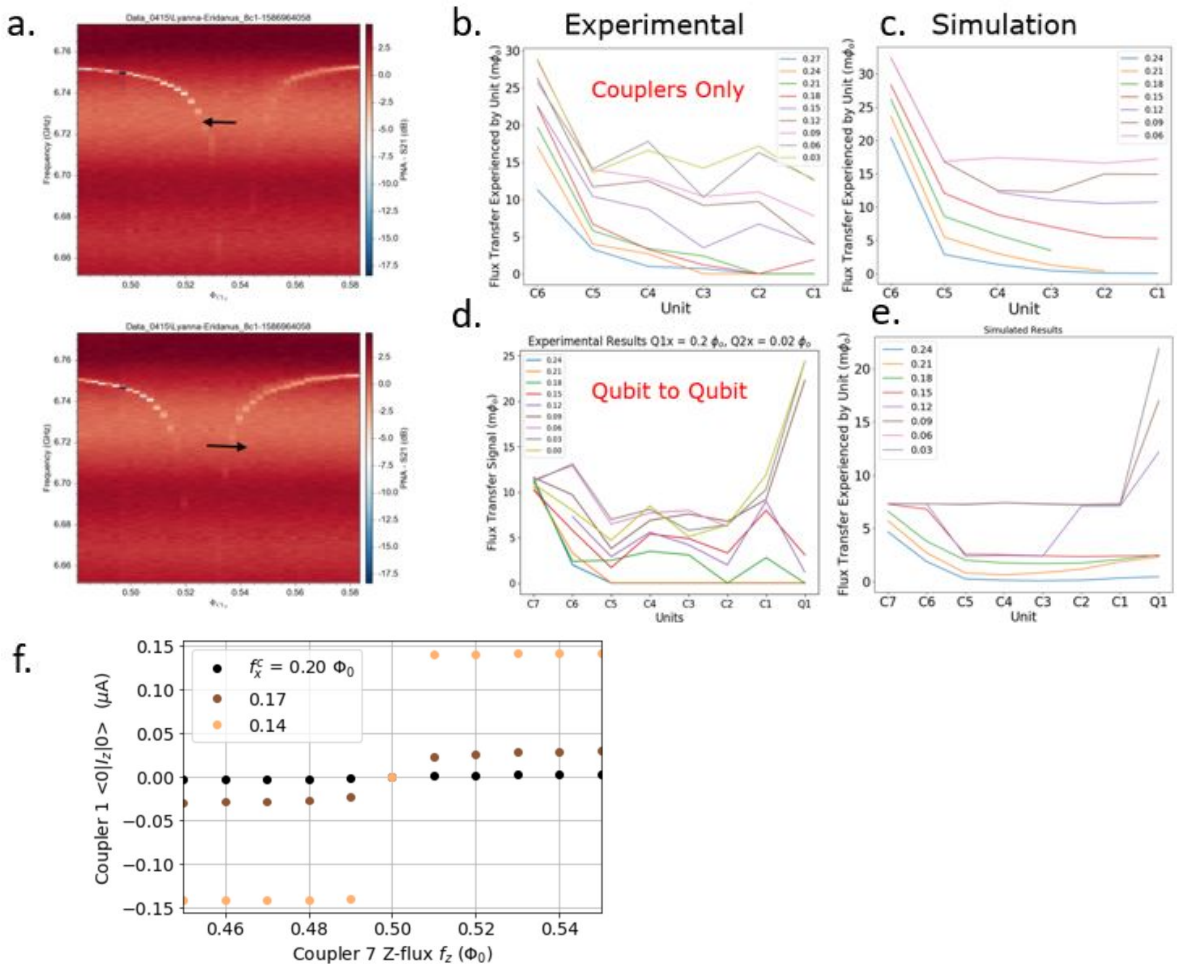

Figure 4.6: Flux Propagation Signal Methods. (a) Shown are the target unit's resonator for the source unit being in its 'Left' and 'Right' circulating current state. The resonator is maintained at $f_r = 0$ while the unit f_z is swept. The dispersive unit-resonator interaction leads to the frequency dip and can be used to ascertain the unit's $\Phi_0/2$ point. (b, c) The experimental and simulated results showing the magnitude of the coupler-only flux signal at the different units for various homogeneously tuned coupler f_x settings. (d, e) The experimental and simulated results showing the magnitude of the full device flux signal at the different units for various homogeneously tuned coupler f_x settings. (f) The induced ground state expectation value of Coupler 1's z-loop current with respect to Coupler 7's z-flux bias is displayed for different coupler x-flux biases. The induced ground state expectation value of the target coupler unit reaches its maximum value in less than 20 mΦ_0 from the source unit's z-flux symmetry point, warranting the use of this value in the flux signal propagation experiment.

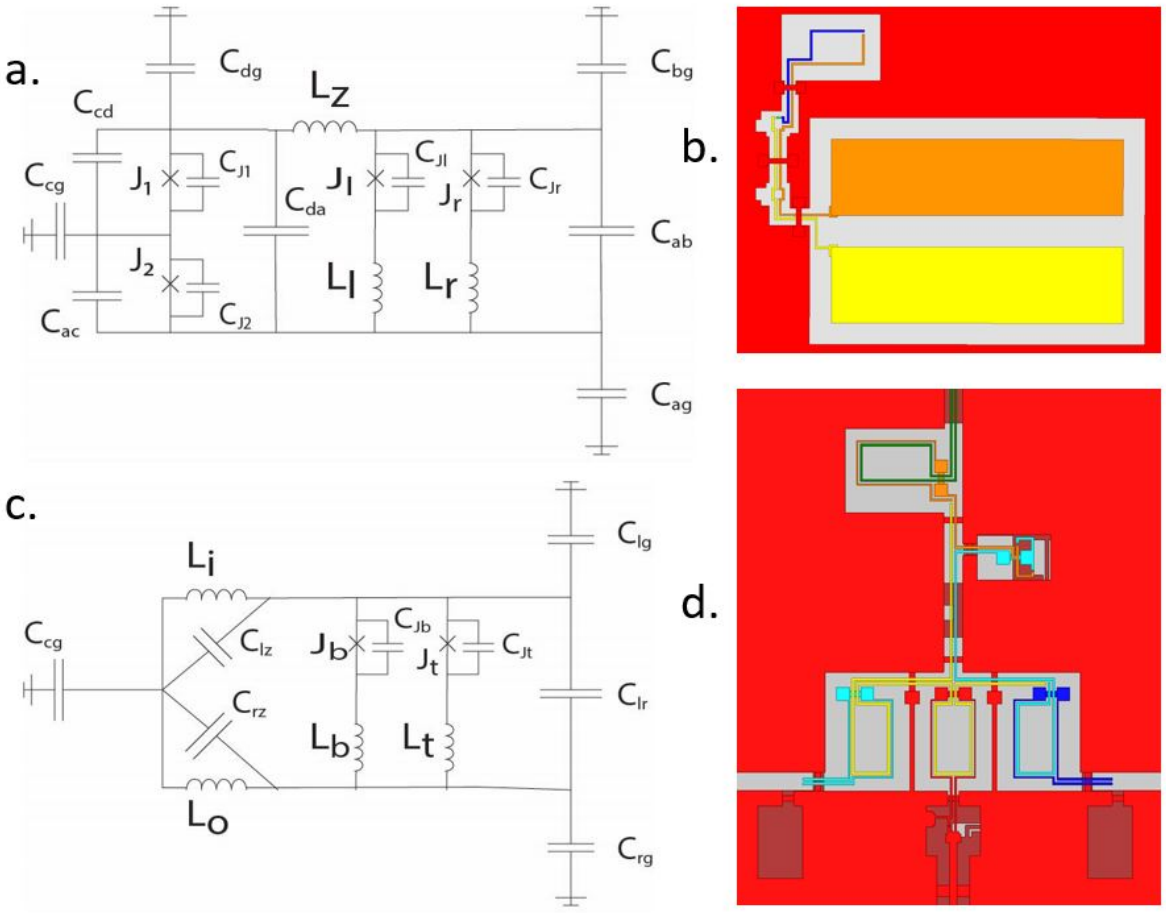

Figure 4.7: Qubit and Coupler Details. (a, b) Shown is the schematic and layout of the capacitively shunted flux qubit. (c, d) Shown is the schematic and layout of the coupler unit.

Qubit Properties		Coupler Properties	
I_c^L	210 nA	I_c	240 nA
I_c^S	90 nA		
C_{ga}	97.4 fF	C_{gr}	32.7 fF
C_{gb}	62.0 fF	C_{gl}	25.8 fF
C_{gc}	0.17 fF	C_{gz}	49.5 fF
C_{gd}	30.4 fF		
C_{ab}	9.81 fF	C_{rl}	6.54 fF
C_{ac}	0.032 fF	C_{rz}	7.22 fF
C_{ad}	2.49 fF	C_{lz}	7.19 fF
C_{cd}	0.29 fF		
$L_l = L_r$	78 pH	L_x	31.4 pH
L_z	690 pH	$L_i = L_o$	378 pH
M_{qc}	62.6 pH	M_{cc}	64.2 pH

Table 4.1: Designed and simulated values for the circuit model parameters of the qubit and the coupler

chain was partitioned into groups of couplers (1,2), (3,4,5), and (6,7). These individual groups then underwent convergence tests exploring how many group energy levels need to be included in simulations such that the low energy operator expectation values converge. Each of the 5 groups was then coupled together for the full device simulations. Again, convergence tests were performed at this final level. Finally, to validate our simulated results with our agreed upon energy level structure, energy levels at lower levels of the hierarchy were varied to double check the validity of the simulated results.

The JJSim lumped element simulations were then incorporated into the full simulation workflow, from classical electromagnetic simulations of the physical device to energy spectrum simulations of the derived lumped element circuits, to optimize the device design. Once the device design was finalized, an additional simulation platform calling JJSim was then developed. This enables an efficient means of adding variation in circuit parameters and flux value assignment in order to account for low-frequency flux noise and fabrication uncertainties, as well as visual result presentation.

4.5.3 Device calibration and parameter extraction

Single unit coherence and annealing measurements have been performed in the two-stack environment. Coherence times measured match well with measurements taken on similar qubits in a single planar tier [178]. Single qubit annealing experiments, as shown in Fig. 4.8, were also performed yielding comparable transition widths as those performed on planar devices [166].

In addition to these encouraging results, the two-stack qubit environment [180], also provides a 'clean' electromagnetic environment. Initial annealing experiments on single-tier qubit environments were hindered by long electromagnetic ring-down times following annealing flux control pulses. As shown in Fig. 4.9, this could be measured by tracking the flux-dependent frequency of the readout resonator. Settling times for the planar geometry devices could reach 100s of μs. Repeating these measurements in the two-stack environment yields settling times of approximately a microsecond. Our initial investigations into this effect broadly agree with the results of [246], i.e., that the long ring down times can be attributed to charge redistribution of the normal metal ground plane but that the superconducting ground planes on both tiers of the two-stack effectively shield the Josephson elements from this effect.

Each qubit/coupler unit is equipped with its readout resonator. These resonators are quarter wavelength meandering resonators terminated with an rf-SQUID. To model this component we consider a quarter wave transmission line resonator [67] terminated in a

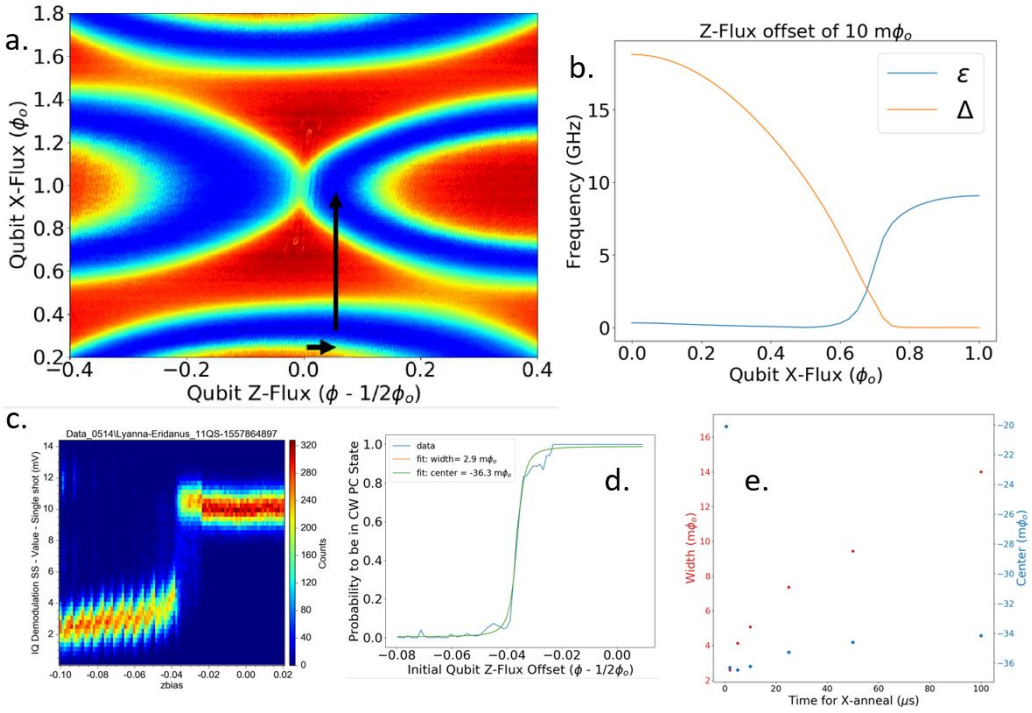

Figure 4.8: Single Qubit Annealing Experiments. (a) Shown is a 'topographical' map of the qubit in flux space. The arrows indicate the path in flux space for a typical annealing experiment. First, a small offset in f_z is applied. Then the change in f_x is applied. (b) Shown are the dynamics of the Ising coefficients during the f_x journey. Initially, the qubit is dominated by the transverse field. As the f_x journey continues the transverse field turns off while the longitudinal field increases. There is a minimum gap at $\simeq 0.68\,\Phi_o$ where these two energy scales are equal and the nature of the qubit ground state transitions between the $\hat{\sigma}_x$ and $\hat{\sigma}_z$ basis. (c) Single shot data showing the histogrammed output voltage of 10,000 runs as a function of initial qubit f_z. The bi-modal distribution of output voltages corresponds to the measuring frequency being on-resonance with the qubit in its 'left' circulating current state and then off-resonance with the qubit in its 'right' circulating current state. (d) The output voltages are then thresholded and the ground state probability is displayed as a function of qubit f_z. (e) The center f_z and transition widths are plotted as a function of f_x journey time. The shift in the center is a reflection of the qubit x-loop junction asymmetry. For a range of longer annealing times, the system thermally exits its ground state at different points along the anneal, shifting the effective f_z symmetry point. These annealing pulses were conducted through low-frequency lines, acting as low-pass filters of approximately 20 MHz. The optimal annealing time of ~ 1 μs results in a width of ~ 3 mΦ_0, similar to previously reported time and widths on these flux bias lines [166].

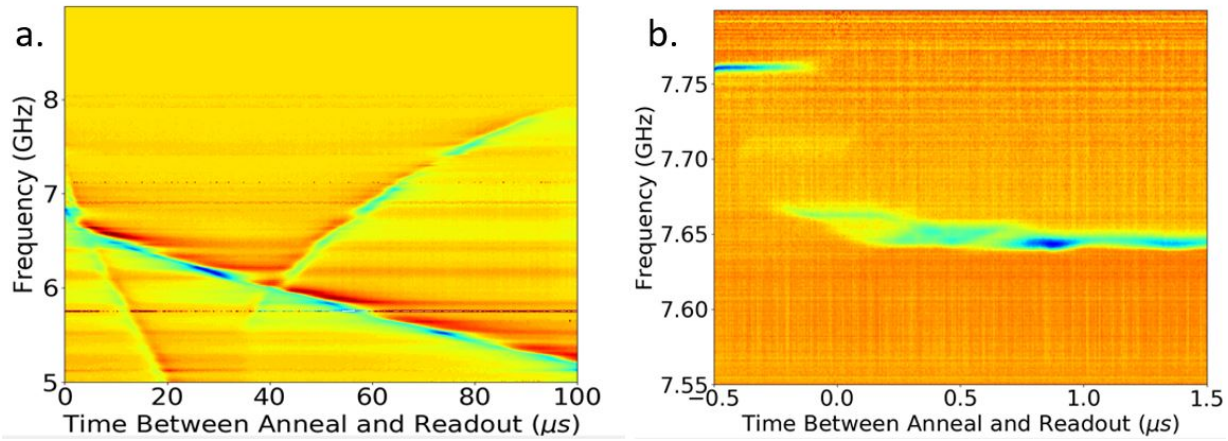

Figure 4.9: Flux Transient Measurements. The dynamic resonator response is measured in both a single-tier (a) and two-stack (b) device environment following a typical annealing-type flux pulse. The single-tier devices have electromagnetic ring-down times of $100s$ of μs whereas the double stack environment is shielded from this effect, settling into its equilibrium flux within 1 μs.

variable inductor whose value is dictated by the rf-SQUID properties [247]. Bare resonator frequencies came out slightly higher than design values by 0.5-2%. To investigate this discrepancy, three-parameter fits, involving resonator length, junction critical current, and geometrical inductance in one case and a common phase velocity, junction critical current, and geometrical inductance in another were applied to the resonator spectra. In the first case, the resonator lengths came out consistently 2% lower than design values, while in the second case, the phase velocity turned out to be 2.4% larger than design. Both cases showed a similar spread in values of critical currents and geometric inductances.

Qubit 2's circuit parameter values were extracted by matching spectroscopy measurements to single unit circuit simulations described above. Qubit 1 suffered an unresponsive capacitive drive line during the experimental run. Displayed in Fig. 4.10, the data are well fit to the simulation and extracted values agree well with the design.

From coupler 'topographical' scans, i.e., probing the coupler resonator at a fixed frequency while varying the coupler's two flux bias currents as shown in Fig. 4.11, we are able to extract couplers' x-loop junction asymmetry, $d = \frac{J_{x_1} - J_{x_2}}{J_{x_1} + J_{x_2}}$. Even small asymmetries of a few percent, due to fabrication imperfections, can appreciably shift the z-symmetry point of the qubit/coupler unit.

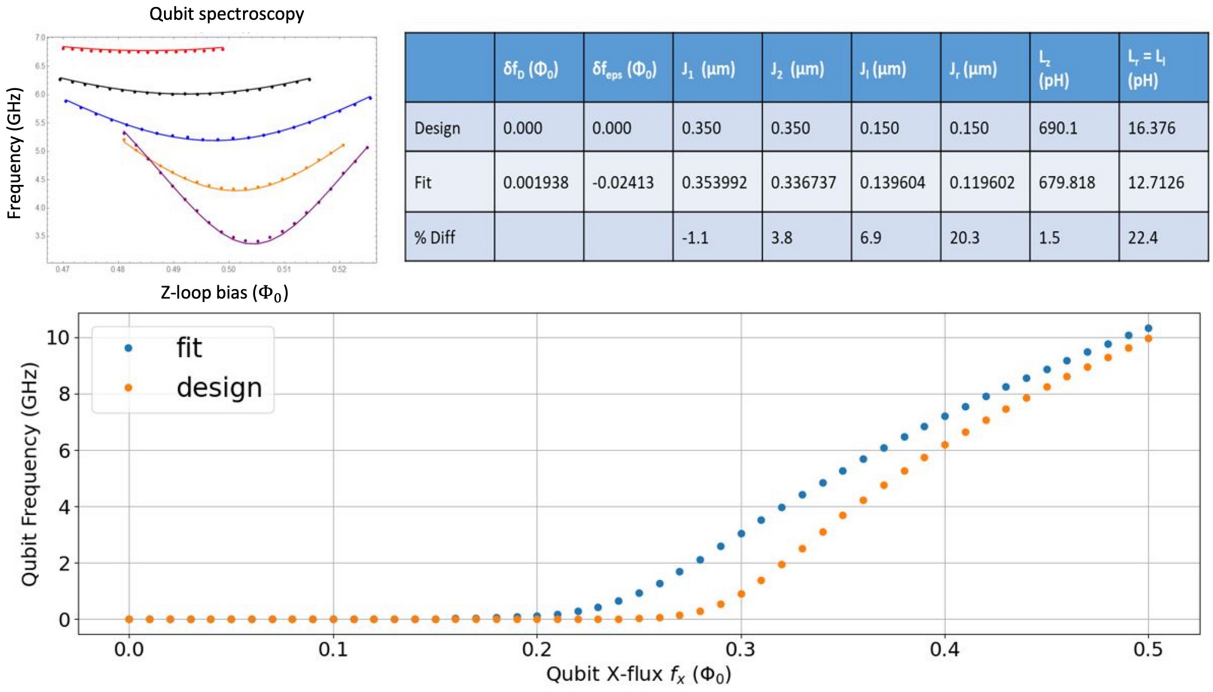

	δf_D (Φ_0)	δf_{eps} (Φ_0)	J_1 (μm)	J_2 (μm)	J_l (μm)	J_r (μm)	L_z (pH)	$L_r = L_l$ (pH)
Design	0.000	0.000	0.350	0.350	0.150	0.150	690.1	16.376
Fit	0.001938	-0.02413	0.353992	0.336737	0.139604	0.119602	679.818	12.7126
% Diff			-1.1	3.8	6.9	20.3	1.5	22.4

Figure 4.10: Qubit 2 Parameter Extraction. Top Left Panel. Two-tone spectroscopy measurements were taken for Qubit 2 for a range of f_x values. Using a rejection sampling method, multi-variable fits were performed on various circuit parameters. Top Right Panel. As shown in the table, all parameters match well with design values. Bottom Panel. Shown are the Qubit 2 0-1 transition frequencies predicted by design and extracted from the parameter fits. We assume the frequency variation in Qubit 2 is typical of other devices in the study.

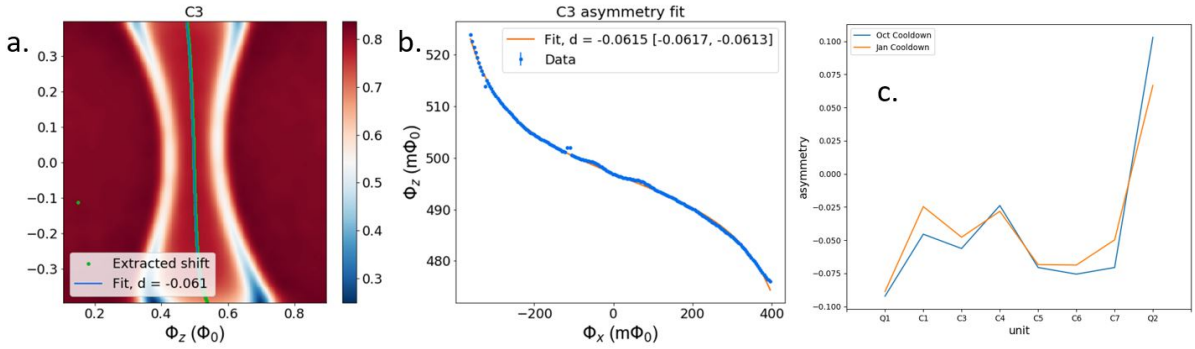

Figure 4.11: Coupler X-Loop junction asymmetry. (a) A 'topographical' scan of Coupler 3. By performing inversion symmetry analysis on these data sets [239], it is possible to extract the effective $\Phi_0/2$ points. (b) These points are well fit by the x-loop junction asymmetry model. (c) Shown are the asymmetry parameters for the coupler units measured approximately 4 months apart during different dilution refrigerator cooldowns.

4.5.4 Spin chain model

For the derivation of the effective qubit-qubit interaction strength, we assume that the coupler chain is operated in its paramagnetic regime such that its ground state is non-degenerate and the energy gap to its first excited state is sufficiently larger than the temperature of the system, the qubit-coupler interaction strength, and the qubit operating frequencies. As the chain approaches its critical region, where we expect long-range correlations to emerge, the gap does become smaller. But, as shown in Fig. 4.5 of the main text, the gap still exceeds these other energy scales.

Treating the qubit-chain interaction as a small perturbation on the coupler chain system allows us to write

$$H_{\text{eff}} \simeq \sum_{i=1}^{2} \overline{H}_{q_i} + J^{\text{eff}}_{q1q2} \sigma^z_{q_1} \sigma^z_{q_2}. \tag{4.11}$$

First-order perturbation expansion shifts the longitudinal field of the qubits,

$$\overline{H}_{q_i} = \frac{\overline{\epsilon}_{q_i}}{2} \sigma^z_{q_i} + \frac{\Delta_{q_i}}{2} \sigma^x_{q_i}, \tag{4.12}$$

$$\overline{\epsilon}_{q_i} = \epsilon_{q_i} + J_{q_i c_{\text{adj}}} \langle 0_c | \sigma^z_{c_{\text{adj}}} | 0_c \rangle, \tag{4.13}$$

where $J_{q_i c_{\mathrm{adj}}} = J_{q_1 c_1}$ or $J_{q_2 c_7}$. The effective qubit-qubit interaction, mediated by virtual excitations of the chain out of its ground state, can be calculated to second order in perturbation theory as

$$\begin{aligned} J^{\mathrm{eff}}_{q_1 q_2} &= -J_{q_1 c_1} J_{q_2 c_7} \sum_{n_c=1}^{2^7-1} \frac{\langle 0_c|\sigma^z_{c_1}|n_c\rangle\langle n_c|\sigma^z_{c_7}|0_c\rangle}{\omega_{0,n_c}} \\ &\simeq -J_{q_1 c_1} J_{q_2 c_7} \sum_{n_c=1}^{2^7-1} \frac{\langle 0_c|\sigma^z_{c_1}|n_c\rangle\langle n_c|\sigma^z_{c_7}|0_c\rangle}{\Omega}, \end{aligned} \tag{4.14}$$

where $\Omega \equiv \omega_{01}$, the energy gap between the ground and the first excited state. In Eq. 4.14 it is recognized that there is a band of $N = 7$ approximately degenerate excited states with gap Ω and finite matrix elements from the ground state. The higher coupler chain levels past this have, at best, exponentially (in energy difference) small $\sigma^z_{c_i}$ matrix elements from the ground state and can be neglected. Now the outer product of states, $\sum_{n_c=1}^{2^7-1} |n_c\rangle\langle n_c|$ can be written as $\mathbb{1} - |0_c\rangle\langle 0_c|$. The effective coupling strength then reduces to

$$J^{\mathrm{eff}}_{q_1 q_2} = \frac{J_{q_1 c_1} J_{q_2 c_7}}{\Omega}(\langle 0_c|\sigma^z_{c_1}|0_c\rangle\langle 0_c|\sigma^z_{c_7}|0_c\rangle - \langle 0_c|\sigma^z_{c_1}\sigma^z_{c_7}|0_c\rangle). \tag{4.15}$$

4.5.5 Spin model simulations

Spin model simulations, based on Eq. (4.1-4.4) of the main text, of the qubit level splittings and the flux propagation experiments were performed using QuTiP [248] to compare to the full circuit simulations and to test the robustness of the long-range coupling to device variations. As displayed in Fig. 4.12(a, b), by using values of Δ_c, J_{cc}, and J_{qc} predicted by the single unit simulations in Fig. 4.13, we find quantitatively similar results for the effective long-range coupling and flux propagation signal as those found for the full device. In Fig. 4.12(c, d), the same simulations were repeated 10 times with random offsets in the spin model parameters on the order of the variation shown in Fig. 4.10, of $\pm$ 500 MHz. Displayed are the repeated instances of the results over the 10 trials. These simulations show that the effective long-range coupling is tolerant to the typical fabrication variations of these devices.

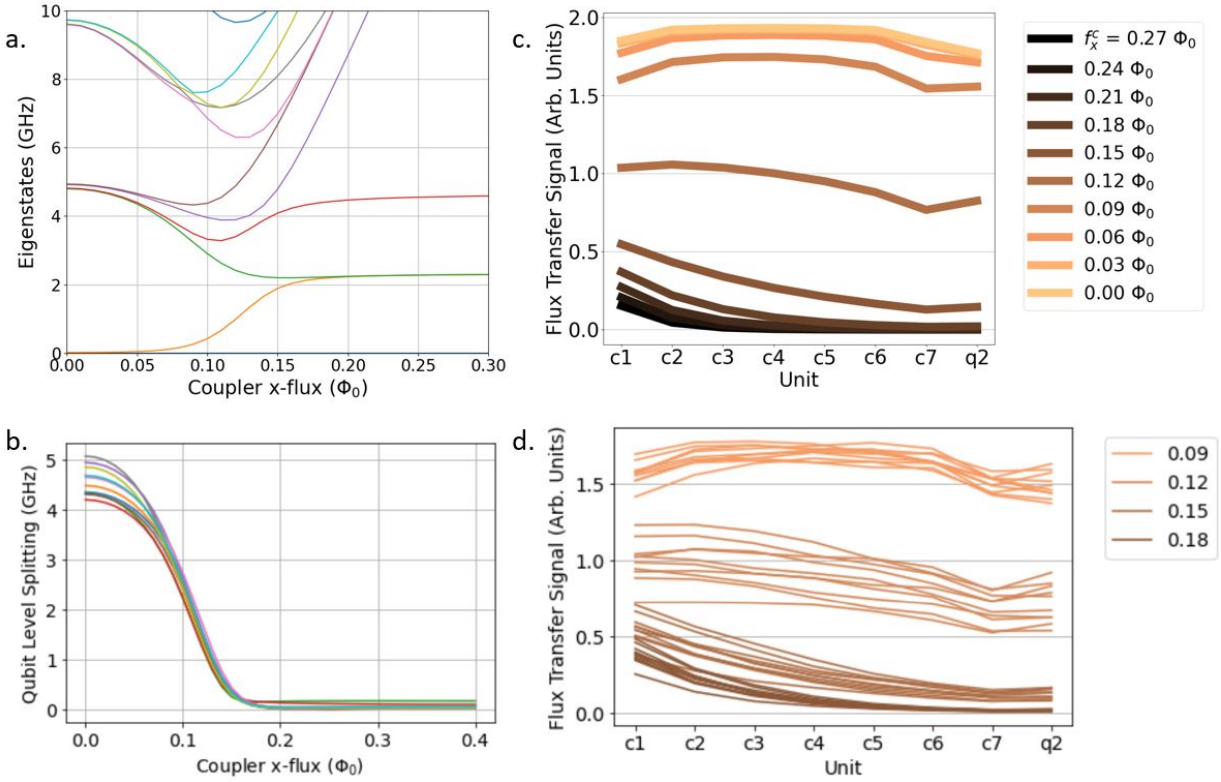

Figure 4.12: Spin model simulation. (a, c) The effective coupling between the two qubit-like states, analogous to Fig. 4.5 in the main text, and the flux signal propagation, analogous to Fig. 4.3(d), are quantitatively similar to the circuit model simulations. (b, d) Random variations, similar in magnitude to that shown in Fig. 4.10, are added to Δ_c, J_{cc}, and J_{qc} over 10 different trial simulations. Shown are repeated instances of trials with these random offsets. Both the long-range effective coupling, as shown in the splitting of the qubit-like levels, and the flux propagation signal are robust with respect to these typical device parameter variations.

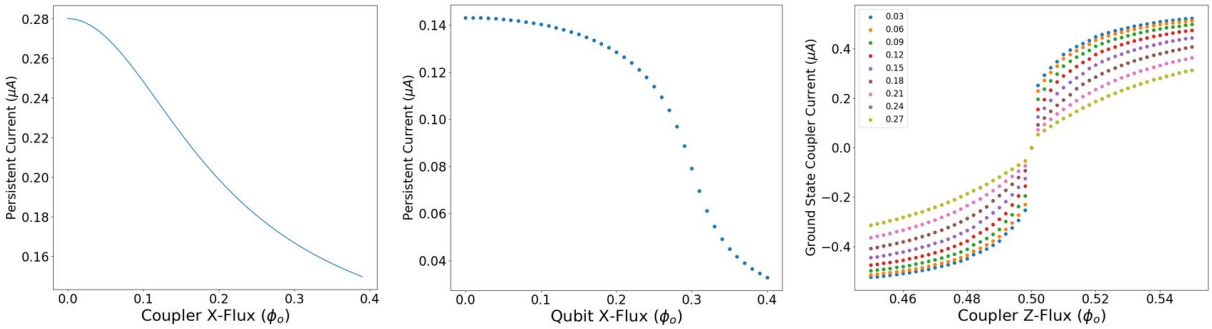

Figure 4.13: Calculation of $J^{\text{eff}}_{q_1 q_2}$. Left Panel. The longitudinal coupling strength between coupler units, the persistent current of the coupler, proportional to the square of $\langle 0|I_z|1\rangle$, along the coupler's $f_z = \Phi_o/2$ was calculated by single coupler simulations. Center Panel. The persistent current of the qubit, $\langle 0|I_z|1\rangle$, along the qubit's $f_z = \Phi_o/2$ was calculated by single qubit simulations. Right Panel. The ground state expectation value of the z-loop current of the coupler, $\langle 0|I_z|0\rangle$, was calculated for a number of coupler f_x values, by single coupler simulations. This sweep was then fit to a sigmoid function and the slope at the z-loop symmetry point, $\frac{d\langle I^z_{c_1}\rangle}{df^z_{c_1}}$, was extracted.

Chapter 5

Decoherence of a tunable capacitively shunted flux qubit

In this chapter, we present a comprehensive study of the coherence of a tunable capacitively-shunted flux qubit, designed for coherent quantum annealing. The measured relaxation and pure dephasing rates are shown to be mainly due to intrinsic flux noise in the qubit control loops, with considerable contributions from the control signal designed to execute fast annealing. The flux bias dependency of the dephasing time also reveals noise correlation between the two control loops and hence the transverse and longitudinal noise of the qubit. Our results are relevant for ongoing efforts on building quantum annealers with increased coherence.

5.1 Introduction

Quantum annealing (QA) is a computational paradigm that shows promise for outperforming classical computers in solving hard optimization problems [20, 88, 30]. In comparison to the more commonly pursued gate-model quantum computation (GMQC), QA is advantageous in that it doesn't require precisely calibrated pulses delivered to each qubit, and hence it is more amenable to scaling up in the near term. Outside the context of optimization, QA also offers potential quantum advantages in machine learning and quantum simulation [249, 250]. Moreover, QA is motivated by the fact that the closed-system version of QA, adiabatic quantum computation [16], is equivalent to GMQC [17].

Superconducting circuits are one of the most prominent physical platforms for both QA and GMQC, owing to a large engineering space and fabrication techniques that build

on conventional electronics [22, 251]. In the context of QA, superconducting flux qubits efficiently implement the transverse field Ising Hamiltonian [50, 65, 178], and can be programmed to solve NP-hard optimization problems [89]. Quantum annealers based on this architecture have been made commercially available by D-Wave, with the latest generation devices containing as many as 5000 qubits [31]. Recent experiments with these devices demonstrate a scaling advantage over Monte-Carlo methods for solving spin glass problems, showing great potential for quantum-enhanced optimization [133].

Decoherence, or the loss of information from a system to its environment, is an important problem both in GMQC and QA [252, 253, 16]. For a single qubit, decoherence is usually characterized by two time scales- T_1 and T_ϕ, which correspond to the time it takes for the system to lose energy (relaxation) to the environment, and to lose phase coherence between different eigenstates (dephasing), respectively. In the limit of weak-coupling to an environment, the Bloch-Redfield theory [254, 255] applies and the relaxation and dephasing times are given by [256]

$$\frac{1}{T_1} = \frac{1}{\hbar^2}\left|\langle e|\frac{\partial H_q}{\partial \lambda}|g\rangle\right|^2 \left[S_\lambda(\omega_q) + S_\lambda(-\omega_q)\right], \tag{5.1}$$

$$\frac{1}{T_\phi} \approx \left(\frac{\partial \omega_q}{\partial \lambda}\right)^2 S_\lambda(0). \tag{5.2}$$

Here $|g(e)\rangle$ is the qubit ground (excited) state, H_q is the qubit Hamiltonian, ω_q is the qubit angular frequency, λ is the noise operator, and S_λ is the noise power spectral density (PSD). The approximate sign in Eq. 5.2 becomes exact when the noise is white (Markovian limit). It can be seen that decoherence is determined by both the quadratic qubit sensitivity term and the strength of the noise, characterized by its noise PSD.

Studying and improving the decoherence time of superconducting qubits is critical for building practically relevant quantum computers. The rf-SQUID flux qubit was one of the first superconducting circuits that were identified to behave as a two-state quantum system, a qubit [257, 258]. Over the last three decades, a few variants of flux qubits have been explored, including the persistent current qubit [46, 45, 232], the capacitively-shunted flux qubits [259, 260, 48, 261], and the fluxonium [51, 204, 262]. A continuous effort on understanding the mechanisms of noise in flux qubits has led to an increase of the coherence times from nanoseconds in the first implementations to a millisecond in recent designs [22]. The key to this progress has been the investigation and understanding of a wide range of noise sources, including intrinsic $1/f$ flux noise [241, 263, 264, 265, 266, 235, 242], photon noise in the readout resonator [267, 268, 269, 48, 270], dielectric loss [271, 272, 273, 262, 274, 275, 276] and junction critical current noise [277, 278]. In spite of the above improvements,

the coherence time for the rf-SQUID qubit used in the DWave annealers has been estimated to be about $\sim$ 10 ns [89], due to a number of reasons, including requirements to simplify control calibration and allow large coupling strength for annealing application [50].

The role of decoherence in QA is an open question under active research. Theoretical studies have suggested that in the limit of weak coupling to the environment, decoherence occurs in the instantaneous energy eigenbasis and is not detrimental so long as the system remains in its ground state during the computation [124, 253, 207]. However, in the strong coupling limit, the situation is more complex and decoherence times as given in Eqs. (5.1,5.2) are no longer well-defined as the system and environment becomes highly correlated. While some previous research suggests that strong coupling to the environment renders quantum annealing impossible [207], other work points out that quantum-assisted tunneling is still possible, which could still lead to a quantum advantage [130].

Most previous experimental studies of coherence in the context of quantum annealing focused on D-Wave devices [126, 82, 279]. While they offer valuable insight about coherence for a large quantum processor, they often rely on assumptions about the sources of the noise and how strongly coupled they are to the system, which cannot be verified independently. Furthermore, the relatively short coherence time compared to the typically available bandwidth in D-Wave devices (control timescales of the order of μs) limits the parameter space that could be explored. That being said, recent work by D-Wave on annealing a 2000-qubit spin chain through its paramagnetic to ferromagnetic transition has shown good agreement with a coherent model when annealing is performed on the time scale of the order of 10 ns [280]. This highlights the importance of expanding by the parameter space to be explored, for example by increasing the control flexibility.

In this work presented in this chapter, we study the coherence of a single tunable capacitively-shunted flux qubit (CSFQ), designed to be incorporated in a large-scale annealer. The CSFQ is a variant of the persistent-current qubit, and features higher coherence when compared to the rf-SQUID flux qubit used in D-Wave devices, by combining high-quality capacitive shunts and reduced influence of flux noise due to the lower persistent current [48]. We measure the coherence times of the CSFQ for a wide range of flux biases, and model the results with a comprehensive list of noise sources. Although the measured coherence times only apply to the weak-coupling limits, the inferred noise power provides a solid basis for future coherence studies in more complex settings. We found that relaxation is dominated by $1/f$ flux noise at lower frequencies and flux bias line thermal noise at higher frequencies, while dephasing is mostly dominated by intrinsic flux noise. In addition, we point out that control with high bandwidth introduces challenges to dephasing. Our results are immediately relevant to upcoming experiments that explore coherent QA based on CSFQs, and could inform the design of other variants of flux qubits, such as

fluxoniums.

This chapter is organized as follows. In Sec. 5.2 we introduce the CSFQ, including the control and readout circuitry. This is followed by a discussion of the basic characterization measurement of the CSFQ. In Sec. 5.4 we present the main results of this chapter, which are the coherence time measurements, and discuss the various noise sources considered. In Sec. 5.5 we comment on the effect of flux noise on the parameters used to define an annealing Hamiltonian, followed by conclusions in Sec. 5.6.

5.2 The CSFQ device

The measured CSFQ, together with the control and readout circuitry is schematically shown in Fig. 5.1(a). The CSFQ has a main loop and a secondary split junction loop. In the two-state approximation, the CSFQ has the Hamiltonian

$$H_{\mathrm{q}} = -\frac{\Delta(\Phi_x)}{2}\sigma_x - I_p(\Phi_x)(\Phi_z - \Phi_z^{\mathrm{sym}})\sigma_z, \tag{5.3}$$

where I_p is the persistent current in the qubit main loop, Δ is the tunneling amplitude between the two persistent current states, Φ_z^{sym}[1] is the effective flux bias symmetry point, and $\sigma_{z,x}$ are the qubit Pauli operators in the persistent current basis. The flux bias Φ_x is the externally applied flux in the secondary loop. The flux bias Φ_z is the effective flux bias in the main loop, defined such that the native crosstalk from the X loop $\Phi_x/2$ is accounted for [45]. To a large extent Φ_z controls the longitudinal field strength while Φ_x controls the transverse field strength, hence the name Z and X respectively. The X loop has a symmetrized design, allowing nearly independent control of the qubit's transverse and longitudinal field (see Appendix D).

The external flux biases are controlled by currents through on-chip flux bias lines, which are supplied by DC voltage sources and arbitrary waveform generators (AWGs) at room temperature, combined through cryogenic bias-Ts. In the experiment reported here, the high-frequency port of the bias-T that controls the X loop was unresponsive, and is hence neglected in the schematic in Fig. 5.1(a). In addition to flux biasing, the CSFQ is capacitively coupled to an rf source, allowing microwave excitation of the qubit.

Readout of the qubit is achieved by coupling the qubit Z loop inductively to an rf-SQUID terminated $\lambda/4$-resonator, coupled to a transmission line. The external flux bias of

[1] We use $\Phi_{x,z}$ in this and the next chapter, as opposed to the reduced biases $f_{z,x}$ used in the previous two chapters, as f is used for frequency here.

the rf-SQUID, Φ_r is controlled by current through the on-chip bias line. When $\Phi_r = 0$, the resonator is at its maximum frequency and the qubit-resonator coupling is linear. At this point, the resonator experiences a qubit-state dependent dispersive shift. Away from zero bias, the resonator has a flux-sensitive resonance, which can be used for persistent current basis readout of the qubit (see Sec.. 2.1.5 for more details regarding the qubit-resonator interaction).

The device is fabricated at MIT Lincoln Laboratory using a flip-chip process [180], combining a high-coherence qubit chip hosting the CSFQ, and a control chip that hosts the readout and control circuitry. Optical images of the two chips are shown in Fig. 5.1(b).

5.3 Device characterization

In this section, we discuss the characterization measurements for the CSFQ, focusing on aspects that concern annealing implementation with the CSFQ.

Experiments were performed with the device cooled down in a dilution refrigerator, with a base temperature of 10 mK (see Appendix C for the measurement setup). The crosstalk between the flux bias lines was measured using the iterative procedure introduced in Chapter 3. After three iterations, the error in flux biasing is expected to be about 1 mΦ_0/Φ_0 (see Sec. 6.5.1 for additional information on crosstalk characterization). In Fig. 5.2 we show the transmission through the line coupled to the resonator, at a frequency near the resonator maximum frequency versus the calibrated external fluxes Φ_z, Φ_x. This measurement shows that the Φ_z symmetry point has a non-linear dependence on Φ_x. This is due to the asymmetry between the two junctions in the DC-SQUID, which results in an effective contribution of the X loop flux to the Z loop [166]. Assuming negligible X loop inductance, the Z loop symmetry point is given by [235]

$$\Phi_z^{\text{sym}} = 0.5 + \arctan\left[d \tan(\frac{\pi \Phi_x}{\Phi_0})\right], \tag{5.4}$$

where d is the asymmetry between the two DC-SQUID junctions and Φ_0 is the flux quantum. The symmetry point can be extracted by checking the point of reflection symmetry for each trace of the transmission measurement at each value of Φ_x, and the fitted asymmetry is $d = 0.069 \pm 0.001$. To verify the effect of finite X loop inductance, we use a full circuit model (see Sec. 6.5.2) to numerically extract the symmetry points and compare them with the analytical expression. As shown in Fig. 5.2(b), using the same junction asymmetry d, the discrepancy between the numerically simulated and analytical Φ_z^{sym} grows larger as Φ_x

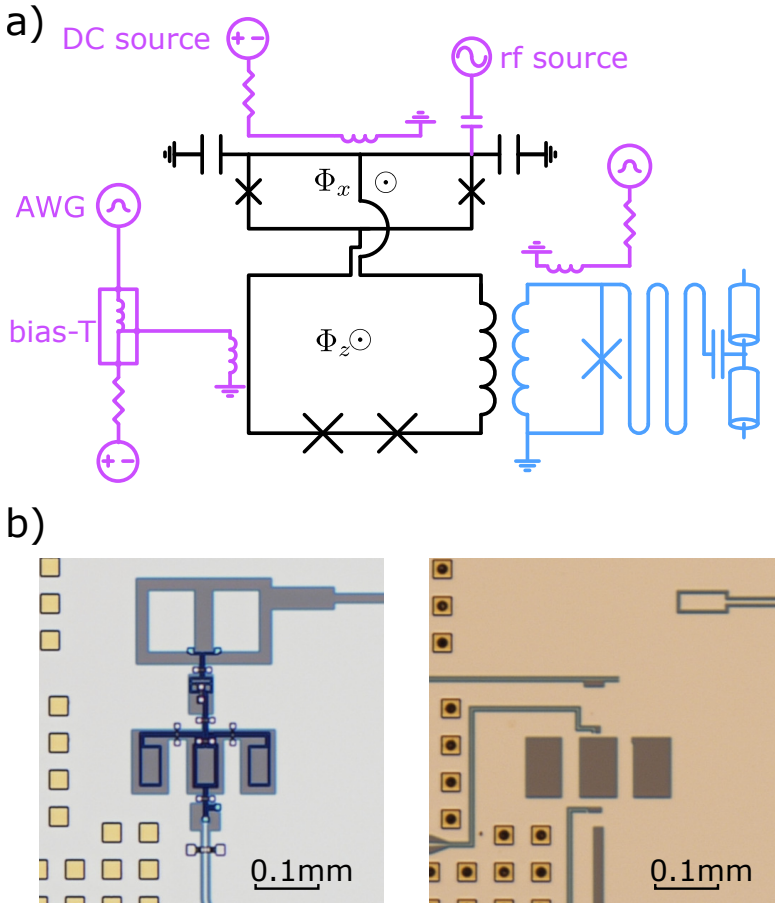

Figure 5.1: (a)Schematic of the CSFQ (black), as well as the readout (blue) and the control (purple) circuit. (b)Optical images of the qubit and interposer chips, around the CSFQ. These two chips face each, with indium bumps to hold them in place.

increases, but always remain below 1 mΦ_0 for the relevant range where the experiments were performed, justifying the use of the analytical expression.

Once the crosstalk and junction asymmetry are calibrated, spectroscopy of the qubit is performed at a range of Φ_z and Φ_x biases, with the resonator SQUID biased at $\Phi_r = 0$. A circuit model of the device is fitted to the transition frequencies between ground, first, and second excited states. The model includes the full capacitance matrix between islands, the loop inductances, and the Josephson junction critical currents, and is simulated using a package developed in Ref. [240] (see Sec. 6.5.2 for circuit model parameter values).

Using the circuit model, the qubit persistent current I_p and tunneling amplitude Δ versus the flux bias in the X loop Φ_x can be obtained. The persistent current I_p can be calculated using two different methods. In the first method, we rely on the operator matrix element defined on the CSFQ circuit

$$I_{p,\mathrm{c}} = \langle 0_\mathrm{c}| \frac{\partial H_\mathrm{c}}{\partial \Phi_z} |1_c\rangle, \tag{5.5}$$

where $|0_\mathrm{c}(1_\mathrm{c})\rangle$ is the circuit ground (excited) state, and H_c is the circuit Hamiltonian, all evaluated at the symmetry point Φ_z^{sym}. In the second method, we find the ground to excited states transition frequencies and fit to the qubit frequencies given by the two-state Hamiltonian Eq. 5.3. The corresponding persistent current is denoted as $I_{p,\mathrm{q}}$. In Fig. 5.3 we show $I_{p,\mathrm{c}}, I_{p,\mathrm{q}}$ versus Φ_x. It can be seen that they agree with each other for small values of Φ_x. At larger Φ_x, $I_{p,\mathrm{q}}$ becomes smaller than $I_{p,\mathrm{c}}$. This can be seen as a result of the breakdown of the two-state approximation, as the lowest energy states of the circuit are no longer spanned by the two persistent current states as Φ_x (or equivalently the tunneling amplitude) increase. Nevertheless, this breakdown of the two-state approximation is not expected to affect annealing, since the system largely remains in the ground state for large values of Δ.

When compared with rf-SQUID flux qubits used in commercially available annealers, the CSFQ presented here has persistent current that is at least an order of magnitude smaller, hence reducing its sensitivity to flux noise. The smaller I_p also leads to smaller interaction strength between qubits, which potentially limits the optimization problems that can be mapped to the annealer. We note that this could be compensated by galvanic coupling, using shared sections of lines [161], and even shared junction or junction arrays between the circuits that need to be coupled.

The tunneling amplitude Δ, also the qubit frequency at the symmetry point, is shown in Fig. 5.3. To implement a standard annealing experiment, the CSFQ is initialized at a large Δ, around$\Phi_x \approx 0.5$, and then the tunneling amplitude is gradually reduced following

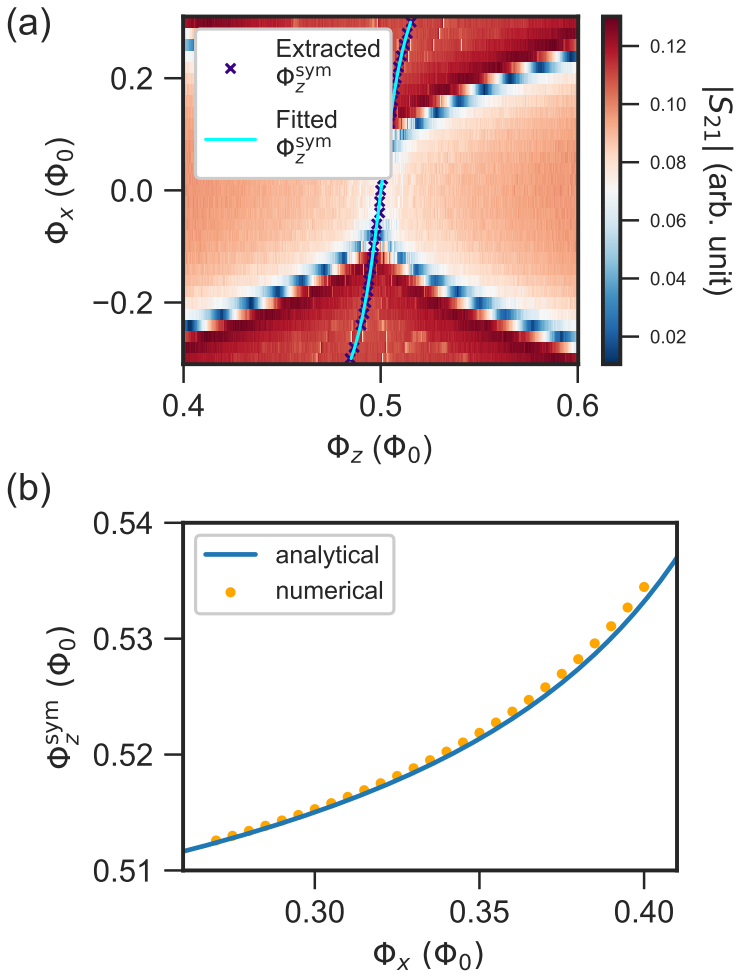

Figure 5.2: (a)Transmission measurement versus the qubit external flux biases Φ_z, Φ_x. The green dots correspond to extracted Φ_z^{sym} by finding the point of reflection symmetry for each Φ_x trace in the transmission measurement, and the blue line is a fit to the analytical expression. (b)Z loop bias symmetry point Φ_z^{sym} as a function of Φ_x, calculated from the analytical (blue line) and numerical (orange dots) model respectively.

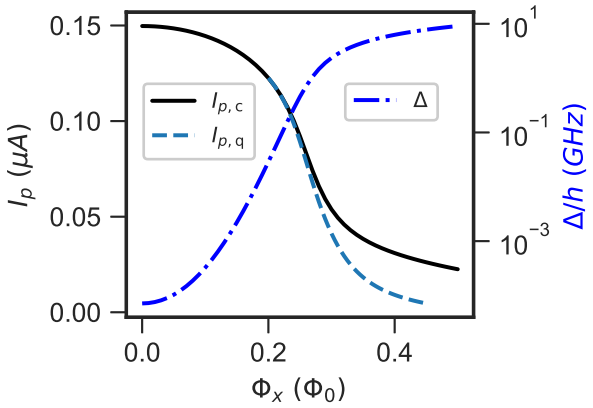

Figure 5.3: Left axis, the qubit persistent current I_p versus X loop external flux bias Φ_x, obtained using the circuit operator (black) and fitting to qubit approximation (light blue dashed) (see text for detail). Right axis, the qubit tunneling amplitude Δ versus X loop external flux bias Φ_x.

a specific annealing schedule. The CSFQ has a more gentle dependence of Δ on Φ_x as compared to the rf-SQUID qubit. Given the same resolution in the biasing sources, this Δ dependence allows finer control of the annealing schedule, and assists in future experimental demonstrations of the novel annealing protocols, such as those proposed in Refs. [222, 236].

5.4 Characterization of decoherence and discussion of results

In this section, we present the measurements of the relaxation and dephasing times T_1, T_ϕ of the CSFQ. We note that T_1, T_ϕ coherence times are only well-defined when the system is weakly coupled to the environment, which is commonly the case in devices made for GMQC. In the context of annealing, the validity of the weak-coupling approximation depends on the relative strength of the qubit fields and the noise. In this work, we only measure the coherence times for qubit $\Delta \gtrsim 1$GHz, limited by the poorer efficiency of state preparation and microwave excitation at lower Δ. In this regime, we do not expect signatures of strong coupling. However, these measurements serve as a useful benchmark to compare with other qubit architectures. Furthermore, the noise amplitude extracted from the coherence time measurements can be used to predict the qubit dynamics in the strong coupling limit, as

is done in the work presented in Chapter 6.

5.4.1 Relaxation time measurements

We first discuss the T_1 relaxation data, which is shown in Fig. 5.4. The relaxation time T_1 was measured by initializing the qubit to the first excited state with a π pulse and then performing the readout with a variable delay time. The relaxation time T_1 is measured both as a function of Φ_x, at the Z loop symmetry point, as shown in Fig. 5.4(a), and as a function of Φ_z near the symmetry point at three different Φ_x, as shown in Fig. 5.4(c). Each relaxation measurement (and dephasing measurement presented later) is repeated 30 times and the average value is reported. It can be seen that as Φ_x varies from 0.27 to 0.4, corresponding to Δ changing from 1 GHz to 6.2 GHz, the T_1 at the Z loop symmetry point increases at first, reaching a maximum at $\Phi_x = 0.32$ ($\Delta/h = 3.2$ GHz), and then decreases. This is similar to other coherence studies on flux qubits and fluxoniums [48, 235, 276], where the qubit coherence is limited by $1/f$ flux noise at low frequency, and transitions to a different noise channel at frequencies higher than ~ 1 GHz.

To better understand the relaxation data, we consider several relaxation channels and show their individual and combined relaxation times in Fig. 5.4, including intrinsic flux noise in the Z loop, thermal noise from the Z bias line, and Purcell decay. We assume the intrinsic flux noise has noise PSD of $2\pi A_{\Phi_z}/\omega$, with ω being the angular frequency and the noise coefficient A_{Φ_z} set by fitting to the dephasing time (see Section 5.4.2). The flux bias line can be modeled as a 50 Ω impedance in parallel with a bias inductor which is coupled to the qubit loops. The noise temperature of the bias line can be estimated based on the attenuations used along the signal line [281]. The Purcell lifetime is estimated by [282]

$$T_1^{\text{Purcell}} = \frac{g^2}{(\omega_r - \omega_{01})^2}\kappa. \tag{5.6}$$

Here ω_r, ω_q, and g are the resonator, qubit transition frequencies and the linear coupling strength between the qubit and the resonator. The coupling strength g is calculated using the circuit model parameters (see Sec. 2.1.5 for the qubit-resonator interaction model and Sec. 6.5.2 for the circuit parameter values), and is found to range from about 100 MHz to 200 MHz depending on the flux bias. The resonator decay rate κ is estimated based on resonator linewidth measurement. At the readout point, the resonator frequency and decay rate are $\omega_r = 7.89 \times 2\pi$ GHz and $\kappa = 12.2$ MHz. Besides the above noise channels, we also note that the intrinsic flux in the X loop has a negligible contribution to relaxation. The microwave port of the X bias line is found to be unresponsive in the experiments,

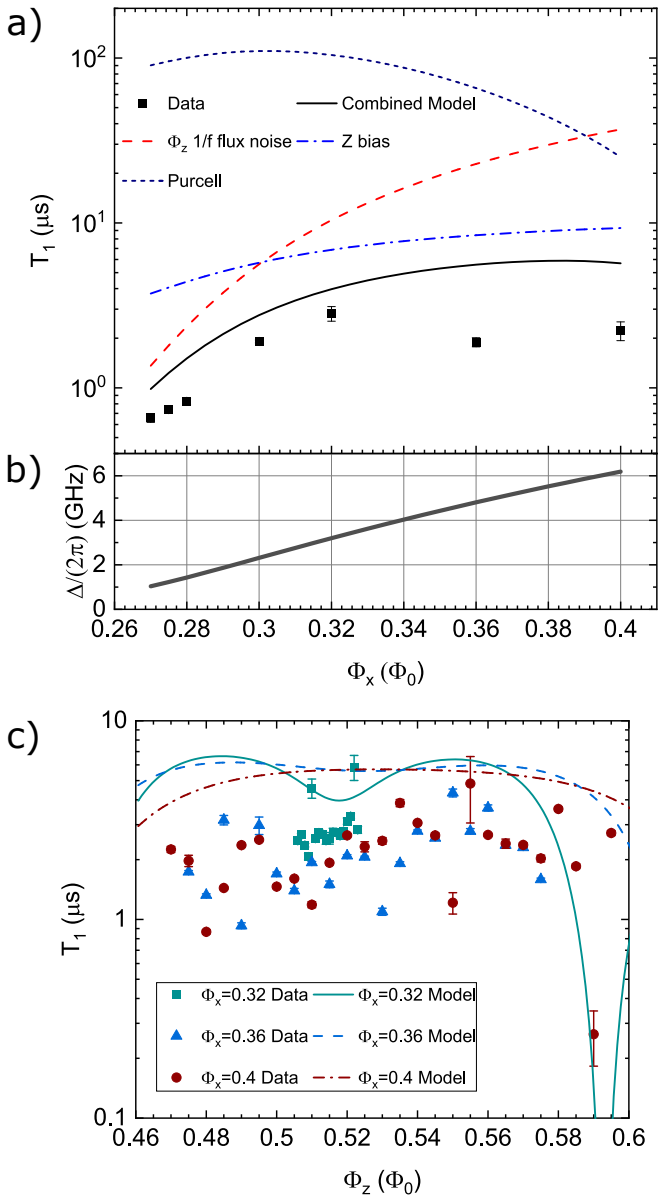

Figure 5.4: (a) Measured (black square markers) and simulated T_1 values as a function of Φ_x, at the Φ_z symmetry point. Each measured point is the result of averaging 30 repeated measurements. The simulated T_1 considered contributions from different sources, with the combined simulated T_1 shown in black. (b) Simulated qubit frequency Δ as a function of Φ_x, at the Φ_z symmetry point. (c) Measured (solid markers) and simulated (lines) T_1 as a function of Φ_z at multiple values of Φ_x. The simulated T_1 combines all noise sources shown in panel (a).

and therefore we do not expect noise at qubit frequency to enter through the X bias line. Details of the relaxation calculations are given in Sec. 5.7.2. As shown in Fig. 5.4(b), at each X flux bias, the predicted relaxation time by combining the above known sources of noise comes within a factor of 2 of the highest T_1 measured at that value of X flux bias.

We discuss the potential causes for the disagreement between the experimental data and the model used for energy relaxation. First, at lower Φ_x, the $1/f$ noise power could differ from the noise power extrapolated using the dephasing time fits based on the simple $1/f$ dependence. Indeed, measurements done on devices fabricated using a similar process show that the actual flux noise has $1/f^{\alpha}$ dependence, with $0.9 < \alpha < 1$ [48, 242]. This means that the flux noise power at the qubit frequency is potentially higher than that assuming $\alpha = 1$. Second, at higher Φ_x, there could be additional high-frequency (super)ohmic flux or charge noise, as found in previous coherence measurements on flux qubits [278, 235, 275, 276]. In this work, it is found that there is significant scatter in the measured T_1 data, especially at values of $\Phi_x > 0.32$. This can be seen from the T_1 versus Φ_z measurements shown in Fig. 5.4, where the measured relaxation varies by as large a factor of 4 between neighboring points. This makes it difficult to determine the nature of the high-frequency noise.

The scatter in the T_1 data could be due to non-equilibrium quasi-particles or coupling to a bath of two-level systems (TLS). Quasi-particle tunneling is known to cause fluctuations in T_1 [283] over time. However, as the spread of the repeated T_1 measurements at the Z symmetry point is small (see Fig. 5.4(a)), fluctuations due to quasi-particles are likely not significant enough to explain the scatter completely (see also Sec. 5.7.3 for repeated T_1 measurement analysis). On the other hand, although the underlying physical nature of TLSs is still under active investigation [284], resonant coupling to TLSs usually leads to variations in T_1 over qubit frequencies [285], and sometimes fluctuations over time [286]. This is also in line with recent measurements on fluxoniums, showing that TLSs indeed have a strong contribution to relaxation [276].

5.4.2 Dephasing time measurements

We next discuss the dephasing measurement, which is also performed at a range of X and Z loop biases. T_ϕ times were measured using a Ramsey oscillation protocol (see Ref. [256], for example) which consists of initializing the qubit with a $\pi/2$ pulse (detuned approximately 10 MHz from the qubit transition frequency) and then applying a second pulse after a variable delay time just before performing readout. As shown in Fig. 5.5(a), at the Z loop symmetry point, the Ramsey pure dephasing time T_ϕ varies from ~ 200 ns to ~ 100 ns as Φ_x is reduced from 0.4 to 0.27. The spin-echo dephasing time T_ϕ^E, measured

with a sequence that has an additional π pulse in between the two $\pi/2$ pulses [256], shows an improvement of about a factor of 5. This improvement, and the fact that all the phase decay have been well-fitted with a Gaussian envelope, are consistent with dephasing dominated by $1/f$ noise. When examining the Φ_z dependence of T_ϕ, it is found that the maximum dephasing time occurs near, but to the left of the Z loop symmetry point Φ_z^{sym}, which stands in contrast to the non-tunable flux qubit.

To model dephasing, we assume $1/f$ flux noises in the Z and X loops are the only sources of dephasing, with noise power spectral density $S_{\Phi_z} = 2\pi A_{\Phi_z}/\omega$ and $S_{\Phi_x} = 2\pi A_{\Phi_x}/\omega$ respectively, with ω the angular frequency. In addition, we assume the flux noises in the Z and X loops have correlated noise PSD $C_{\Phi_z\Phi_x}$, represented by the dimensionless coefficient, $c_{zx} = C_{\Phi_z\Phi_x}/\sqrt{S_{\Phi_z}S_{\Phi_x}}$. The frequency sensitivity to flux noise is determined directly from the circuit model, without the two-state approximation. The noise power that fit the measured T_ϕ best are $\sqrt{A_{\Phi_z}} = 13.3\ \mu\Phi_0/\sqrt{\text{Hz}}$, $\sqrt{A_{\Phi_x}} = 7.6\ \mu\Phi_0/\sqrt{\text{Hz}}$. These numbers are consistent with previous devices fabricated using a similar process [161], considering flux noise scales as length over the width of the loop wires [265, 242].

The best fit of the dephasing times indicates a correlation coefficient of $c_{zx} = 0.47$. Flux noise correlation in tunable flux qubits have been measured previously [287, 276], and it has been pointed out that positive (negative) correlation shifts the maximum dephasing time to the left (right) of the symmetry point. Assuming flux noise arises from uniformly distributed environmental spins on the metal surface of the superconducting loop, Ref. [287] suggests that the correlation could be understood in terms of spins that occupy the shared arm between the Z and X loops. However, given the symmetrized X loop design used here, the expected correlation using this simple model for flux noise is zero, and hence does not explain the measured correlation.

Junction asymmetry could also lead to an offset between the maximum dephasing time and the qubit symmetry point. To see this, one could define another effective Z flux bias $\Phi_{\tilde{z}}$, such that the symmetry point in $\Phi_{\tilde{z}}$ is independent of Φ_x. This means

$$\Phi_{\tilde{z}} = \Phi_z - F(\Phi_x), \tag{5.7}$$

where F is given by Eq. 5.4 when X loop inductance is negligible. Then it can be found that the noise correlation coefficient between $\Phi_{\tilde{z}}$ and Φ_x is given by (see Appendix D)

$$c_{\tilde{z}x} = c_{zx} - \frac{dF}{d\Phi_x}\frac{S_{\Phi_x}}{\sqrt{S_{\Phi_z}S_{\Phi_x}}}. \tag{5.8}$$

Therefore, for negligible c_{zx}, as would be the case if noise purely comes from uniformly distributed spins on the metal surface, $c_{\tilde{z}x}$ would be negative given a positive junction

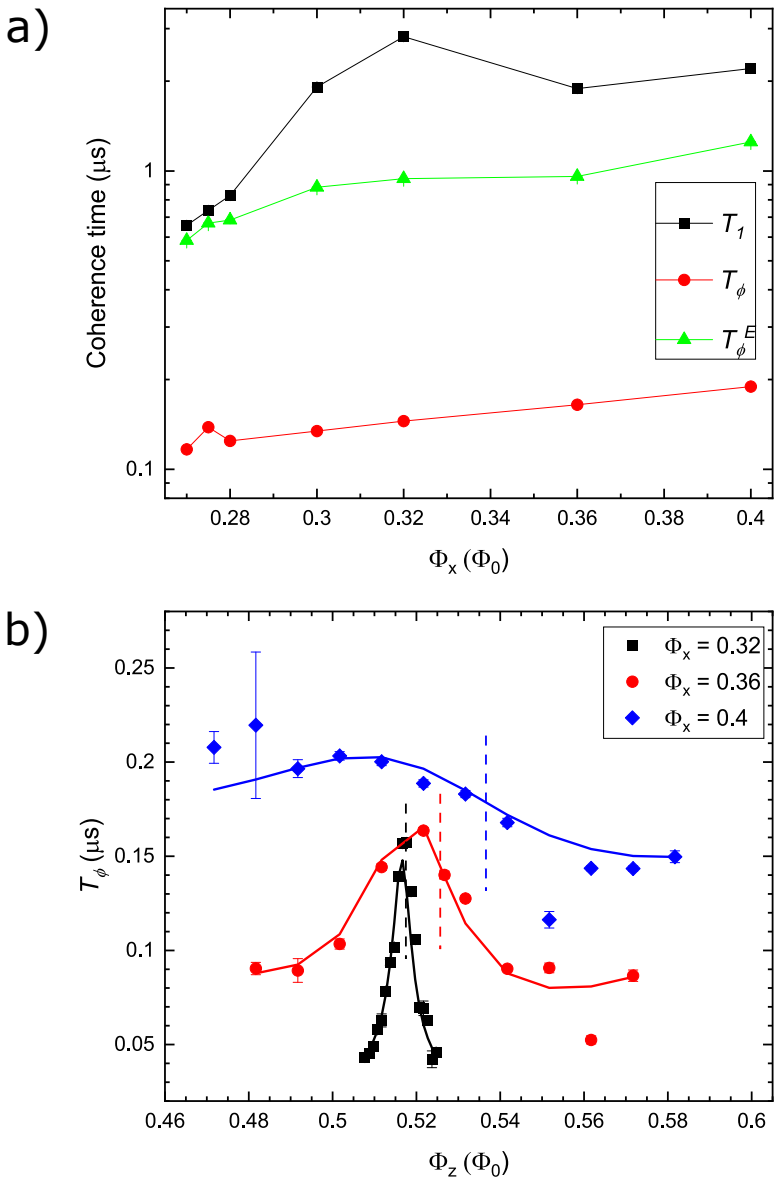

Figure 5.5: (a) Measured relaxation time T_1 (black squares), Ramsey T_ϕ (red dots) and spin-echo T_ϕ^E (green triangles) dephasing times, as a function of Φ_x, with Φ_z set at the symmetry point. Each point is the result of averaging 30 repeated measurements. (b)Measured (solid points) and calculated values (solid lines) of T_ϕ as a function of Φ_z at three values of Φ_x. The vertical dashed lines indicate the position of the symmetry point at each value of Φ_x.

asymmetry d. In other words, the effect of junction asymmetry in the device is to shift the point of maximum dephasing time to the right of the symmetry point, which is the opposite of what is observed experimentally. We note that this apparent offset should not be confused with the fitted correlation c_{zx}, as the fitting uses numerically extracted frequency sensitivity to Φ_z and Φ_x, which implicitly contains information about the asymmetry.

To further investigate the source of this correlation, we considered additional sources of dephasing, including bias line thermal noise, voltage noise of the bias source, photon shot noise, second order coupling to flux noise, charge noise, and junction critical current noise (see Sec. 5.7.4). We found that using previously reported values of $1/f$ noise of the critical current of the junctions, its contribution to dephasing can be non-negligible compared to dephasing due to first-order coupling to flux noise. Furthermore, junction critical current noise leads to maximum dephasing time to the left of Φ_z^{sym}, hence could contribute to the apparent positive correlation between the two flux biases.

We also observed over multiple cooldowns of the dilution fridge and changes to the setup that the choice of bias source could have an impact on the coherence times as well. Experiments performed during earlier cooldowns used AWGs as the DC bias sources for the device. After switching from using AWGs to a lower noise DC bias source for the X bias, we found the measured Ramsey pure dephasing time at $\Phi_x = 0.32$ improved from $\sim$ 80 ns initially to $\sim$ 150 ns after the switch. In Sec. 5.7.4, we show that by assuming the AWG has a $1/f$ and white noise combined at low frequency, it alone could lead to a dephasing time of $T_\phi \sim 350$ ns. This is roughly consistent with the reduction in Ramsey dephasing time when the AWG is used, given the crude model on the AWG noise. As the DC bias source does not support fast annealing, strategies need to be developed to mitigate the noise from the AWG. This could be done by either using a cryogenic bias-T to combine the DC and fast signal, allowing smaller coupling strength of the more noisy signal, or simply applying heavier low-pass filtering to the fast signal.

5.5 Noise in annealing parameters

It is useful to put the measured noise here in the context of annealing applications. For a "single-qubit anneal" [166, 288], the qubit Hamiltonian starts with a large value of Δ, at which the qubit is initialized in the ground state, and the qubit Hamiltonian is gradually changed to a target Hamiltonian where Δ close to zero. The only parameter defining the target Hamiltonian is the qubit longitudinal field

$$\epsilon = 2I_p(\Phi_z - \Phi_{z,\text{sym}}). \tag{5.9}$$

Noise in the control fluxes gives rise to noise in the annealing parameters ϵ, Δ, with the same frequency dependence. We focus on the intrinsic $1/f$ flux noise, assuming noise arising from wiring and electronics can be minimized through careful engineering. Using the qubit approximation Hamiltonian Eq. 5.3, we can find the individual and correlated $1/f$ noise in ϵ, Δ, given by

$$A_\epsilon = \left(\frac{\partial \epsilon}{\partial \Phi_z}\right)^2 A_{\Phi_z} + \left(\frac{\partial \epsilon}{\partial \Phi_x}\right)^2 A_{\Phi_x} + 2\frac{\partial \epsilon}{\partial \Phi_z}\frac{\partial \epsilon}{\partial \Phi_x} A_{\Phi_z \Phi_x}, \tag{5.10}$$

$$A_\Delta = \left(\frac{\partial \Delta}{\partial \Phi_x}\right)^2 A_{\Phi_x}, \tag{5.11}$$

$$A_{\Delta\epsilon} = \frac{\partial \epsilon}{\partial \Phi_z}\frac{\partial \Delta}{\partial \Phi_x} A_{\Phi_z \Phi_x} + \frac{\partial \epsilon}{\partial \Phi_x}\frac{\partial \Delta}{\partial \Phi_x} A^2_{\Phi_x}, \tag{5.12}$$

where $A_{\Phi_z \Phi_x} = c_{zx}\sqrt{A_{\Phi_z} A_{\Phi_x}}$ is the $1/f$ amplitude of the flux noise correlation. In Fig. 5.6 we show these three quantities versus the transverse field Δ, for the target longitudinal field $\epsilon = 0$, noting these quantities are weakly dependent on ϵ. It can be seen that the ϵ noise, A_ϵ is always the dominant noise factor. The correlated noise $A_{\Delta\epsilon}$ is mainly due to the measured flux noise correlation, and is about an order of magnitude lower than A_ϵ. The noise in A_Δ is comparable to $A_{\Delta\epsilon}$ for large Δ, but diminishes quickly with decreasing Δ. The role of the relative strength of the noises would be explored in future work. One interesting direction is to extend previous analysis of the effect of correlated noise on single qubit Landau-Zener tunneling [289], to the general case of multi-qubit annealing.

5.6 Conclusion

We have presented a detailed characterization of coherence in a CSFQ design relevant for quantum annealing. We measured the T_1 relaxation and T_ϕ dephasing times and modeled them considering all relevant noise sources. We find that the T_1 values are influenced primarily by $1/f$ flux noise with additional contributions from the thermal noise from the bias lines, while the T_ϕ is dominated by $1/f$ flux noise, with a possible contribution from $1/f$ noise in junction critical current. We point out that for annealing application, the external flux biases can introduce significant relaxation and dephasing as compared to the intrinsic noises of the qubit. This suggests that future annealing experiments that aim to combine high coherence and high control flexibility need to carefully evaluate the trade-off between the added noise and the improved control bandwidth.

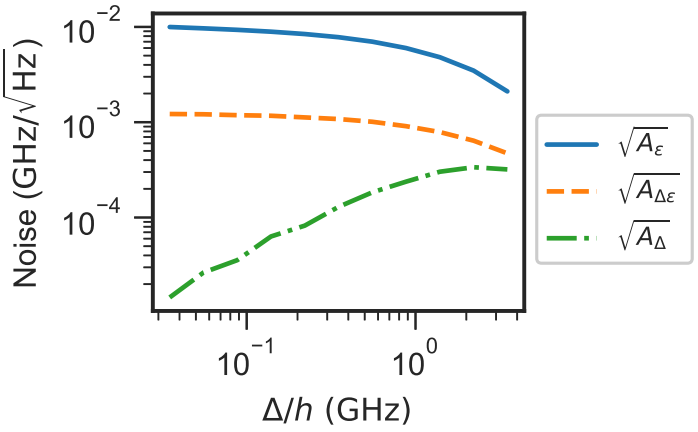

Figure 5.6: Individual and correlated $1/f$ noise amplitude at 1Hz for the annealing parameters ϵ, Δ as a function of the transverse field Δ, calculated from the measured $1/f$ flux noise in the two control loops.

Additionally, we observe a positive correlation between the X and Z control flux noise, as manifested in the maximum dephasing time versus Φ_z occurring on the left of the symmetry point. This correlation may arise due to a combination of correlations between intrinsic flux noise in the two loops, and junction critical current noise. Future experiments that are able to distinguish the different sources of $1/f$ noise are needed to quantitatively determine the origin of this noise correlation.

Our work provides a detailed characterization of noise sources of a flux qubit, relevant for future analysis of coherent annealers based on CSFQs. Besides quantum annealing, the work presented here is also relevant for flux qubit devices made for GMQC, such as fluxonium qubits. Future extension of the work will be directed at extending the coherence characterization to the strong coupling limit, multi-qubit systems, as well as studying coherence in a dynamic setting, which will lead to a deeper understanding of the role of coherence in quantum annealing.

5.7 Additional details on decoherence modeling

5.7.1 Noise spectrum and decoherence

In this work, we define the noise power spectral density (PSD) of a random variable $\delta\lambda$ as the Fourier transform of its auto-correlation function,

$$S_\lambda(\omega) = \int_{-\infty}^{\infty} \mathrm{d}\tau e^{i\omega\tau} \langle \delta\lambda(\tau)\delta\lambda(0)\rangle. \tag{5.13}$$

If the noise arises from a quantum bath, the noise PSD is asymmetric in positive and negative frequencies. However, our noise measurement is only sensitive to the symmetrized noise spectrum, which we define as

$$S_\lambda^+(\omega) = \frac{1}{2}\int_{-\infty}^{\infty} \mathrm{d}\tau e^{i\omega\tau} \langle \delta\lambda(\tau)\delta\lambda(0) + \delta\lambda(0)\delta\lambda(\tau)\rangle \tag{5.14}$$

$$= \frac{1}{2}\left(S_\lambda(\omega) + S_\lambda(-\omega)\right). \tag{5.15}$$

The symmetrized correlation between two random variables $\delta\kappa$ and $\delta\lambda$ is given by the cross power spectral density

$$C_{\lambda\kappa}(\omega) = \frac{1}{2}\int_{-\infty}^{\infty} \mathrm{d}t e^{i\omega t} \left(\langle \delta\lambda(t)\delta\kappa(0) + \delta\lambda(0)\delta\kappa(t)\rangle\right) \tag{5.16}$$

$$\equiv c_{\lambda\kappa}\sqrt{S_\lambda^+(\omega)S_\kappa^+(\omega)}, \tag{5.17}$$

where $c_{\lambda\kappa}$ is a dimensionless number describing the relative correlation between the two noise variables.

5.7.2 Relaxation

We considered qubit relaxation time T_1 in general to be given by

$$\frac{1}{T_1} = \frac{1}{T_1^{\mathrm{Purcell}}} + \frac{1}{T_1^{\mathrm{z1f}}} + \frac{1}{T_1^{\mathrm{x1f}}} + \frac{1}{T_1^{\mathrm{zb}}} + \frac{1}{T_1^{\mathrm{xb}}} \tag{5.18}$$

$$+ \frac{1}{T_1^{\mathrm{QOhmic}}} + \frac{1}{T_1^{\mathrm{zOhmic}}} + \frac{1}{T_1^{\mathrm{xOhmic}}}, \tag{5.19}$$

where T_1^{Purcell} is the resonator induced Purcell decay rate, $T_1^{\text{z(x)1f}}$ is the relaxation time due to the intrinsic $1/f$ flux noise in the $Z(X)$ loops, $T_1^{\text{z(x)b}}$ are the relaxation time due to Johnson-Nyquist noise in the $Z(X)$ bias lines, and $T_1^{\text{Q(z,x)Ohmic}}$ are additional ohmic noise that couples to the qubit charge degrees of freedom [290, 48, 235].

The Purcell lifetime is estimated by [282]

$$T_1^{\text{Purcell}} = \frac{g^2}{(\omega_r - \omega_{01})^2}\kappa, \tag{5.20}$$

where g is the exchange interaction strength between the qubit and the resonator, ω_r is the resonator frequency and κ is the resonator decay rate.

For the rest of the noise channels, we assume the noise is weak and the decay rates from the Bloch-Redfield theory (or equivalently the Fermi's Golden rule) is given by,

$$\frac{1}{T_1^\lambda} = |\langle 1|\frac{\partial H_q}{\partial \lambda}|0\rangle|^2 \left(S_\lambda(\omega_{01}) + S_\lambda(-\omega_{01})\right), \tag{5.21}$$

where $\frac{\partial H_q}{\partial \lambda}$ is understood as the qubit operator that is coupled to the noise, and $S_\lambda(\omega_{01})$ is the noise PSD of λ at qubit frequency ω_{01}. For the intrinsic flux noise, we assume they are of the form $2\pi A_\lambda/\omega$, with the same noise amplitude as found in the pure dephasing rate fits. For the Johnson-Nyquist noise, we considered the bias line as an inductor with inductance L_b shunted by an impedance of $Z_0 = 50\Omega$. The current noise is given by

$$S_I(\omega) = \frac{\hbar\omega \text{Re}[Z_b](1 + \coth\frac{\hbar\omega}{2k_B T_N})}{\omega^2 L_b^2}, \tag{5.22}$$

$$\text{where } \frac{1}{Z_b} = \frac{1}{Z_0} + \frac{1}{i\omega L_b}, \tag{5.23}$$

and $L_b = 25$ pH based on electromagnetic simulation. For the noise temperature T_N of the bias lines, we use the formula

$$T_N^{i+1} = \frac{T_N^i - T^{i+1}}{A^{i+1}} + T^{i+1} \tag{5.24}$$

to propagate the noise down the different stages of the dilution. Here T^i, T_N^i and A_i are respectively the fridge temperature, incoming noise temperature and attenuation used at that stage. In particular for the Z bias, we used 20, 10, 10 dB attenuation at the 3 K, 0.5 K and 20 mK stages of the dilution fridge. This attenuation scheme leads to an effective noise

temperature of 123 mK, which is relatively large compared to the base temperature of the fridge.

For the additional $Q(z,x)$ ohmic noise, we assume they are of the form

$$S_{\text{Ohmic}} = B\omega|\omega|^{\gamma-1}(1+\coth\frac{\hbar\omega}{2k_BT}), \tag{5.25}$$

with $\gamma = 1$ and the different noise coefficients B^Q, B^z, B^x corresponding to charge noise, Φ_z flux noise and Φ_x flux noise. Previous experiments on flux qubits have found that the dominant relaxation channel at higher qubit frequencies($\gtrsim$ 1 GHz) could be either ohmic charge or (super)ohmic flux noise [48, 235, 276]. In our experiments, due to the relatively significant scatter in our T_1 data, we do not investigate the possibilities of any additional (super)ohmic noises.

5.7.3 Fluctuations in relaxation time due to quasi-particles

In addition to the above mentioned relaxation channels, inelastic quasiparticle tunneling across the qubit junctions could lead to additional qubit energy decay. Modeling the number of quasiparticle tunneling events in each shot of the T_1 measurement as a Poisson distribution, the average qubit excited state decay follows [283],

$$\langle P(t)\rangle = \mathrm{e}^{\lambda_{\text{qp}}\left(\exp\left(-t/\tilde{T}_{1\text{qp}}\right)-1\right)}\mathrm{e}^{-t/T_{1\text{R}}}, \tag{5.26}$$

where $\langle P(t)\rangle$ is the excited state population averaged over many shots, λ_{qp} is the average quasiparticle tunneling event., $T_{1\text{qp}}$ is the qubit relaxation rate due to one quasiparticle tunneling and $T_{1\text{R}}$ is the qubit relaxation time due to all other noise channels. Due to fluctuations in the quasiparticle numbers, the qubit decay measurement also experiences fluctuations. To investigate this, we perform 100 repetitions of T_1 measurements at the symmetry point at $\Phi_x = 0.32$. Each repetition is averaged over 10 thousand shots, with a repetition time of 100 μs. The result of each repetition is then fitted to Eq. 5.26, with λ_{qp} being independent in each measurement and $T_{1\text{qp}}$ and $T_{1\text{R}}$ shared for all the repetitions. This gives $T_{1\text{qp}} = 3.6$ μs, $T_{1\text{R}} = 3.4$ μs. The average number of quasiparticle tunneling events for each repetition is shown in Fig. 5.7, with an average of 0.43 and a standard deviation of 0.097, which is slightly larger than previous measurements on CSFQs [48, 261].

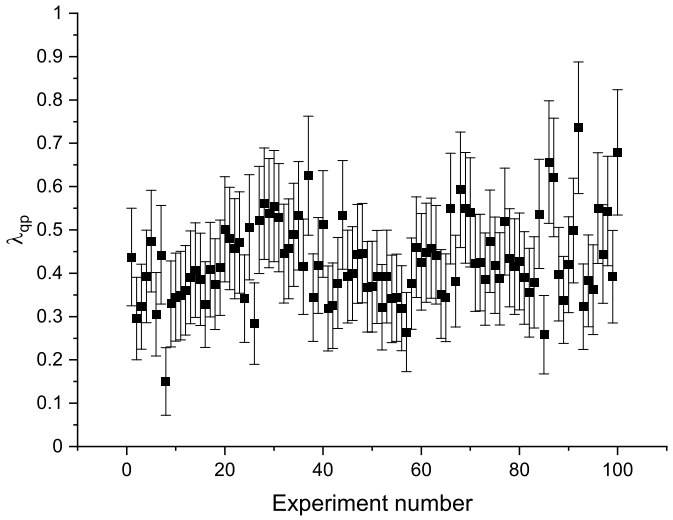

Figure 5.7: Fitted average number of quasiparticle tunneling event λ_{qp} over 100 hundred repetitions of T_1 measurements, performed at the Φ_z symmetry point with $\Phi_x = 0.32$.

5.7.4 Pure dephasing

Dephasing is caused by low-frequency fluctuations in the qubit energy splitting ω_{01} due to various noise sources. The noise spectrum of the the qubit ω_{01} is given by

$$S^{+}_{\omega_{01}} = \sum_{\lambda} \left(\frac{\partial \omega_{01}}{\partial \lambda} \right)^2 S^{+}_{\lambda} + 2 \sum_{\lambda \neq \kappa} \frac{\partial \omega_{01}}{\partial \lambda} \frac{\partial \omega_{01}}{\partial \kappa} C_{\lambda\kappa}, \tag{5.27}$$

where the summation runs over the noise sources under consideration. For classical noise, dephasing can be described by the decay $\langle \exp(-\chi(\tau)) \rangle$, where χ is given by

$$\chi(\tau) = \frac{\tau^2}{2\pi} \int_{\omega_{\mathrm{low}}}^{\infty} \mathrm{d}\omega S^{+}_{\omega_{01}}(\omega) g_N(\omega\tau). \tag{5.28}$$

Here $g_N(\omega\tau)$ is the filter function for the specific coherence measurement, and ω_{low} is a low-frequency cut-off determined by the total experiment time. We have $N = 0$ for Ramsey

and $N = 1$ for spin-echo measurement. Their respective filter functions are

$$g_0 = \text{sinc}^2\left(\frac{\omega\tau}{2}\right) \text{ and} \tag{5.29}$$

$$g_1 = \text{sinc}^2\left(\frac{\omega\tau}{4}\right)\sin^2\left(\frac{\omega\tau}{4}\right). \tag{5.30}$$

In general the decay of $\chi(\tau)$ is not exponential. We associate the pure dephasing time T_ϕ as the $1/e$ decay time, where $\langle \exp\left(-\chi(\tau = T_\phi)\right)\rangle = 1/e$.

Noises that couple via the fluxes

In order to realize the large energy scale required for annealing, the tunable CSFQs have relatively large superconducting loops and flux sensitivities. This large sensitivity, together with the measured flux noise correlation, motivate grouping the noises that couple to control fluxes together. We consider three different such sources, intrinsic flux noise, Johnson-Nyquist noise of the bias lines and noise due to biasing sources. Denoting the intrinsic flux noises on the two fluxes as $S^{\text{int}}_{\Phi_z}, S^{\text{int}}_{\Phi_x}$, the Johnson-Nyquist current noise on the two bias lines as S_{I_z}, S_{I_x} and the voltage noise from the bias sources as S_{V_z}, S_{V_x}, the self and cross PSD of the two flux biases are

$$S_{\Phi_z} = S^{\text{int}}_{\Phi_z} + M^2_{zz}(\frac{S_{V_z}}{R^2_z} + S_{I_z}) + M^2_{zx}(\frac{S_{V_x}}{R^2_x} + S_{I_x}), \tag{5.31}$$

$$S_{\Phi_x} = S^{\text{int}}_{\Phi_x} + M^2_{xz}(\frac{S_{V_z}}{R^2_z} + S_{I_z}) + M^2_{xx}(\frac{S_{V_x}}{R^2_x} + S_{I_x}) \text{ and} \tag{5.32}$$

$$C_{\Phi_z\Phi_x} = C^{\text{int}}_{\Phi_z\Phi_x} + M_{zz}M_{xz}(\frac{S_{V_z}}{R^2_z} + S_{I_z}) \tag{5.33}$$

$$+ M_{zx}M_{xx}(\frac{S_{V_x}}{R^2_x} + S_{I_x}), \tag{5.34}$$

where $M_{z(x)z(x)}$ are the mutuals between the bias line and the fluxes, and $R_{z(x)}$ are the resistances between the source and the bias line on the chip. We note that the intrinsic flux noise is non-negligible at both low and high frequencies. The voltage noise from the bias sources is only strong at low frequencies, as the bias source is coupled to the device through a low-pass filter, and the Johnson-Nyquist current noise is only apparent at high frequencies.

Dephasing due to intrinsic flux noise alone

The intrinsic flux noise usually has a noise PSD of the form

$$S_\lambda^+(\omega) = A_\lambda^2 \left(\frac{2\pi}{|\omega|}\right)^\alpha, \tag{5.35}$$

for $\lambda \in [\Phi_z, \Phi_x]$, where $\alpha \sim 1$. If dephasing is dominated by flux noise, we can assume $S_{\omega_{01}}^+$ has the same frequency dependence, with

$$S_{\omega_{01}}^+ = A_{\omega_{01}}^2 \left(\frac{2\pi}{|\omega|}\right)^\alpha. \tag{5.36}$$

In this case, the integral in Eq. (5.28) can be simplified, which leads to dephasing time

$$\frac{1}{T_\phi} = \left(A_{\omega_{01}} \eta_N^{1/2}\right)^{2/(1+\alpha)}. \tag{5.37}$$

Following Ref. [161], for Ramsey and spin-echo measurements, the factors η_0, η_1 are determined numerically by

$$\eta_0 = (2\pi)^{\alpha-1} \int_{\omega_{\text{low}} t}^\infty \frac{dz}{z^\alpha} \left(\frac{\sin(z/2)}{z/2}\right)^2, \tag{5.38}$$

$$\eta_1 = (2\pi)^{\alpha-1} \int_0^\infty \frac{dz}{z^\alpha} \left(\frac{\sin(z/4)}{z/4}\right)^2 \sin^2(z/4), \tag{5.39}$$

where t is the typical free evolution time in a single Ramsey sequence. The fitting result shown in Sec. 5.4.2 corresponds to $\omega_{\text{low}} = 10\text{Hz} \times 2\pi$ and $t = 100\text{ns}$.

Dephasing due to biasing sources

During a separate cooldown of the device, a different measurement setup was used and the coherence time of the device dropped significantly. Among other changes in the setup, we found that biasing the qubit circuit using an AWG is the likely cause of the lower coherence. In this section, we present the estimated dephasing rate due to typical noise from the AWG (Keysight model M3202a).

The AWG can be considered to have a classical voltage noise source, with a noise PSD that is close to a combination of $1/f$ and white noise. For low-frequency biasing, the noise

is also low-pass filtered at some cutoff frequency ω_l. This motivates a simple voltage noise PSD for the AWG, given by

$$S_V^+(\omega) = \left[A_V^2 \left(\frac{2\pi}{|\omega|}\right) + S_{V0}\right] \frac{1}{1 + (|\omega|/\omega_l)^2}, \tag{5.40}$$

where A_V is related to the noise amplitude of the $1/f$ part, S_{I0} describes the white noise power and we assumed the filter is first-order for simplicity.

For the numerical computation, we take $A_V = 8 \times 10^{-7}\mathrm{V}/\sqrt{\mathrm{Hz}}$ and $S_{V0} = 7.9 \times 10^{-17}\mathrm{V}^2/\mathrm{Hz}$, for both the Z and Z low frequency bias. Ignoring other sources of noise, we show the estimated flux bias noise PSD for two different low-frequency cutoffs, 32 kHz and 100 MHz in Fig. 5.8. The dephasing rate is computed numerically for a range of Φ_z at $\Phi_x = 0.32$, by solving $\chi(\tau = T_\phi) = -1$ from Eq. 5.28, which is shown in Fig. 5.8(b). It can be seen that when the low-frequency cutoff is 100 MHz, the dephasing rate becomes close to the intrinsic flux noise limited rate shown in Sec. 5.4.2. When the low-frequency cutoff is 32 kHz, the dephasing rate due to voltage noise is about an order of magnitude larger.

For the data presented in Sec. 5.4.2, the DC bias has a low-frequency cutoff of 32 kHz, and the biasing source is a Yokogawa DC voltage source (model GS200), which is expected to have lower noise than the AWG. On the other hand, the microwave port of Z couples about 20 times more weakly than the DC port. The microwave port of X is unused. These considerations allow us to eliminate the effect of the biasing sources on the dephasing.

Estimated dephasing for other noise sources

In this section, we consider a number of additional sources of dephasing.

First, we briefly note that the thermal noise of the bias lines at low frequency leads to a dephasing time of about 1 ms and can be neglected.

It was previously observed in high-coherence CSFQ that the dominant noise channel at the symmetry point is photon-shot noise [48], with a dephasing rate given by

$$\Gamma_\phi^{\mathrm{th}} = \frac{\kappa^2}{\kappa^2 + 4\chi^2} \frac{4\chi^2}{\kappa} \bar{n}, \tag{5.41}$$

where κ is the resonator decay rate and χ is the qubit-induced dispersive shift of the resonator, and $\bar{n}$ is the average thermal photon in the resonator. In our experiments, at $\Phi_x = 0.4$, we found a dispersive shift of $\chi \sim 0.8$ MHz, and a resonator decay rate of 0.7 MHz. To obtain a dephasing rate of 5 MHz, the required average thermal photon

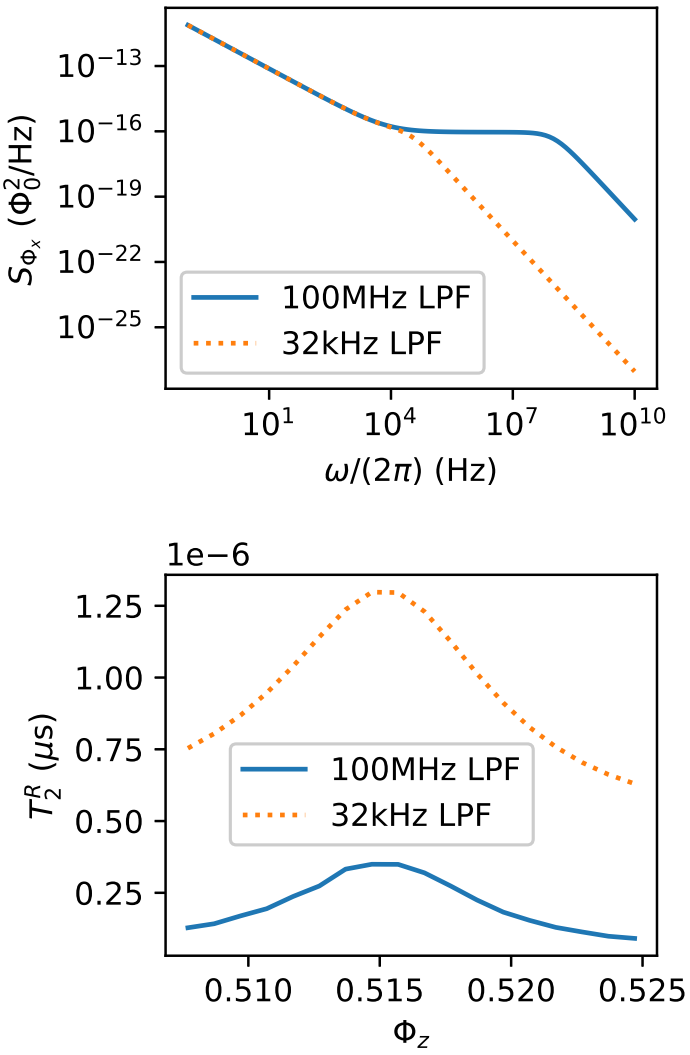

Figure 5.8: (a)Z-flux noise PSD due to the AWGs used to bias the circuit, when using a 100 MHz (blue solid) or a 32 kHz (orange dotted) low-pass filter (LPF). (b) Ramsey pure dephasing time as a function of Φ_z for $\Phi_x = 0.32$, due to AWG noise with the 100 MHz (blue solid) or 32 kHz (orange dotted) LPF.

number is $\bar{n} \approx 2$, much higher than than the expected value, given the readout resonator should be reasonably well thermalized with the readout line in the fridge. Therefore photon-shot noise is unlikely to be dominant in our device.

We also consider the second-order coupling of flux noise following [256]. Given our typical experimental timescales, we take the quasistatic limit flux noise and found the second-order coupling to flux noise contributes to dephasing rate

$$\Gamma_{\phi}^{\mathrm{f2nd}} \approx 1.6 \frac{\partial^2 \omega_{01}}{\partial \lambda^2} A_{\lambda}. \tag{5.42}$$

Using the numerically simulated qubit spectrum and the fitted $1/f$ flux noise amplitudes, we estimate that the second order coupling to flux noise leads to $\Gamma_{\phi}^{\mathrm{f2nd}} \sim 1$ kHz, which is negligible compared to the dephasing due to first order coupling.

It has also been reported that quasi-particles could lead to frequency fluctuation in certain flux qubits [291]. We checked the fluctuation in ω_{01} in our circuit as a function of charge offsets in each island, and found a maximum of 100 kHz, which is much smaller than the observed Γ_{ϕ}. Therefore dephasing due to quasi-particles or charge noise is likely negligible.

Defects in the junction tunneling barrier could lead to $1/f$ noise of the critical current of the junctions [277] and have been shown to be the main source of dephasing at the symmetry point in some earlier flux qubit[278]. To estimate the critical-current noise induced dephasing, we follow Ref. [278] to assume a normalized critical current noise of $A_{\mathrm{ic}} = 4.0 \times 10^{-6}$ on each of the four junctions independently. The noise sensitivity to junction i^{th} critical current $\partial \omega_{01} / \partial I_{ci}$ can be computed numerically from the circuit model, and leads to a noise sensitivity to the normalized critical current noise defined as

$$\frac{\partial \omega_{01}}{\partial i_{\mathrm{c}}} = \sqrt{\sum_i \left(\frac{\partial \omega_{01}}{\partial i_{\mathrm{ci}}} \right)^2}. \tag{5.43}$$

where i_{ci} is junction i^{th} critical current normalized by its nominal value I_{ci}. In Fig. 5.9 we show the critical current noise sensitivity and the corresponding dephasing time over different biases. It can be seen that the dephasing rate can be a substantial fraction of the measured dephasing rate. We also note that for each Φ_x, the Φ_z bias corresponding to the minimum sensitivity, and hence maximum dephasing time, is to the left of the symmetry point. This trend is qualitatively in line with the experimentally measured Ramsey dephasing versus Φ_z. Therefore the critical current noise could be a potential explanation for the apparent correlation between the Z and X loop flux noise, although further understanding and investigations into the physical origin of these noises are required to distinguish them.

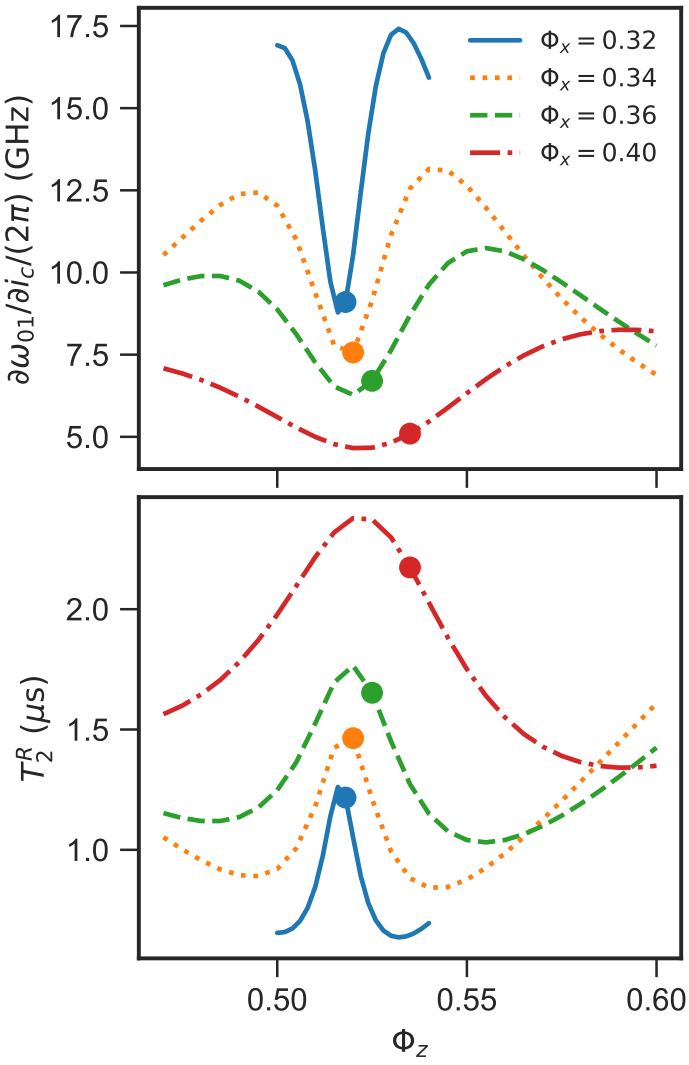

Figure 5.9: (a)Qubit frequency sensitivity to normalized critical current versus Φ_z for different Φ_x. The Φ_z coordinates of the dots indicate the symmetry point for different Φ_x biases. (b)Ramsey pure dephasing time versus Φ_z for different Φ_x, due to $1/f$ critical current noise.

Chapter 6

Dissipative Landau-Zener tunneling: crossover from weak to strong environment coupling

Landau-Zener tunneling, which describes transitions in a two-level system during the passage through an anti-crossing, is a model applicable to a wide range of physical phenomena. Dissipation due to the coupling between the system and environment is an important factor in determining the transition rates. Using a superconducting tunable capacitively shunted flux qubit, we observe the crossover from weak to strong coupling to the environment. The weak coupling limit corresponds to small system-environment coupling and leads to environment-induced thermalization. In the strong coupling limit, environmental polarizations dress the system and incoherent tunneling occurs between the dressed states. Our results confirm previous theoretical studies of dissipative Landau-Zener tunneling in the weak and strong coupling limits, and motivate further work on understanding the intermediate regime. The work presented in this chapter is relevant for understanding the role of open system effects in quantum annealing, where Landau-Zener transitions at small gaps, occurring in large-scale systems, are important for the success probability.

This chapter is organized as follows. In Sec. 6.1, we review previous literature on Landau-Zener transitions and summarize our results. Then we will present the main experimental and numerical results in Sec. 6.2, followed by a discussion in Sec. 6.3. The methods used, as well as various experimental and numerical details are left in Sec. 6.4-6.7.

6.1 Introduction

Landau-Zener (LZ) tunneling [292, 293, 294, 295] describes non-adiabatic transitions in a two-state quantum system when it is swept through an anti-crossing with linearly changing energy separation. The LZ tunneling model is applicable to a wide range of physical phenomena, such as atomic collisions [296], chemical reactions [297], and molecular magnets [298] and has been extensively studied theoretically and experimentally [299, 300, 301, 302, 303, 304, 305]. In experiments with superconducting systems, single or repeated LZ transitions have been used to demonstrate phase coherence [301, 306], to realize quantum gates [307] and to validate theories of incoherent tunneling (MRT) in the presence of strong $1/f$ noise [308, 309].

In the closed-system case, analytical solutions for transition probabilities were obtained in Ref. [292, 293, 294, 295]. Specifically, for a given tunneling amplitude (or minimum gap size) Δ and sweep velocity v, the probability for the system to tunnel from one to the other diabatic state is $1 - P_{\mathrm{LZ}}$, where P_{LZ} is the non-adiabatic transition probability and in the coherent limit is given by

$$P_{\mathrm{LZ}} = \exp\left(-\frac{\pi\Delta^2}{2\hbar v}\right). \tag{6.1}$$

In the open system case, analytical results have been obtained in various limiting cases for the temperature and coupling strength of the environment [299, 300, 310]. In the particular case of longitudinal coupling (coupling to the diabatic basis) to high-frequency noise, the transition probability, for fast sweep, is unchanged when compared to the coherent case. For the slow sweep, the transition probability remains unchanged if the noise temperature of the environment is low compared to the minimum gap size [311, 299, 310, 312, 289], and approaches the asymptotic value of 1/2 when the noise temperature is high [313, 314, 300]. At intermediate temperatures, numerical studies found that high-frequency longitudinal noise leads to non-monotonic dependence of the tunneling probability versus sweep rate, due to the competition between adiabaticity, thermal excitation near the anti-crossing, and thermal relaxation after the anti-crossing [315, 316].

More, recently, there is growing interest in studying dissipative LZ transitions in the context of quantum annealing [20, 317]. The success probability for a quantum annealer to find the target ground state crucially depends on the system tunneling across the minimum gap between the instantaneous ground and excited state, a situation well-described by the LZ model [124, 309, 126, 222]. Therefore, studying LZ tunneling in the presence of realistic environment is an important step towards understanding the computational capability of a quantum annealer.

One of the most prominent realizations of large-scale quantum annealer is based on superconducting flux qubits. The dominant source of noise in the flux qubit is usually the ubiquitous low-frequency flux noise that couples longitudinally to the qubit. The long correlation time of such noise presents a considerable difficulty for numerical study, although analytical results exist in some limiting cases. First, if the noise correlation time is longer than a relevant time window in which LZ tunneling occurs, the noise does not alter the transition when compared to the coherent case [313]. Second, in the limit of small tunneling and strong low-frequency noise, the polaron transformation can be applied, which leads to incoherent macroscopic resonant tunneling (MRT) between diabatic states [308, 318]. This analysis was applied to an earlier measurement of LZ transition in flux qubits, which showed that the LZ tunneling rate is the same as in the coherent limit, provided the integrated power of the low-frequency noise is much larger than the noise temperature [309].

In this work, we perform the LZ transition measurement with tunable flux qubit for a wide range of minimum gap Δ and sweep velocity v. We find that for large enough Δ, the experimental data agree with previous numerical studies which show a non-monotonic dependence of transition probability versus sweep time [315, 316]. For small Δ, we find our results agree with the previous LZ measurement on flux qubit [309], where the measured transition probability is close to the coherent limit transition probability. The two respective limits are modeled using the master equations introduced in Sec. 2.2. To model the full range of experimental data, we explore using a quantum spin bath to represent the low-frequency noise. Preliminary simulation results using this model show good agreement with the experiments, and suggest that the crossover happens when the time taken for the qubit to tunnel from one diabatic state to the other, set by Δ, becomes comparable to the timescale at which the environment reorganizes itself as the qubit tunnels.

6.2 Results

Our experiments are performed using a two-level quantum system implemented using a tunable superconducting flux qubit. A schematic of the experiment setup is shown in Figure 6.1(a). The qubit circuit consists of two flux loops, designated as z, x respectively, including Josephson tunnel junctions. Under suitable flux bias conditions, the circuit has a double-well potential energy landscape, with the two wells corresponding to persistent currents flowing in opposite directions in the z loop. At energies lower than the plasma frequencies of both wells, the system is confined to the ground states of the two wells, described by the two-state (qubit) Hamiltonian

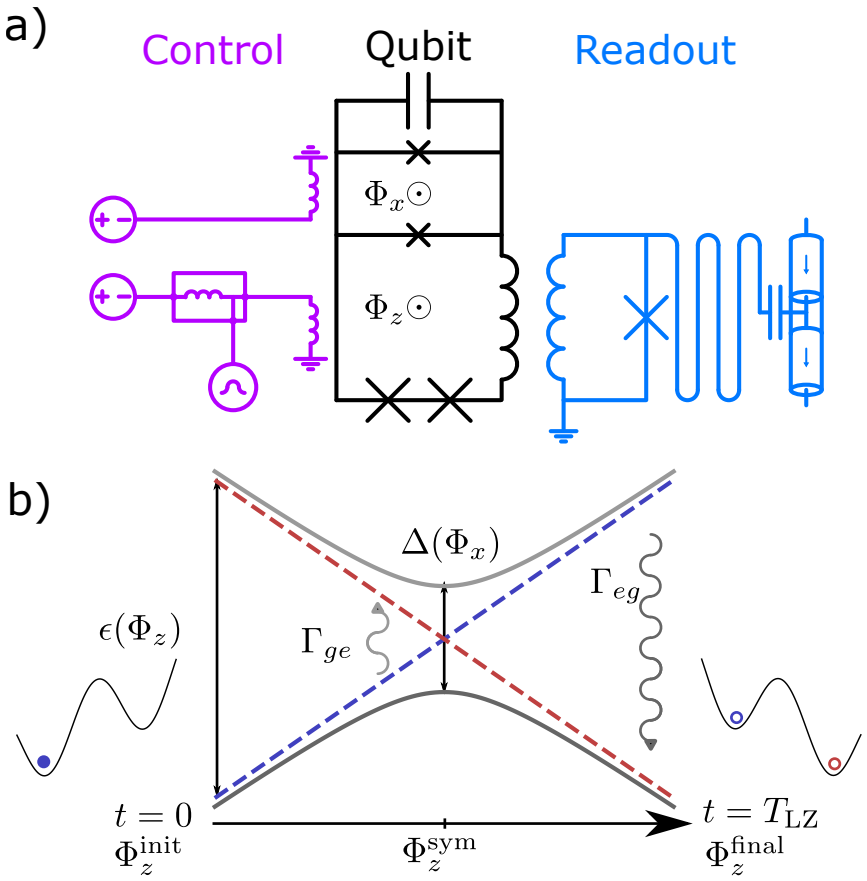

Figure 6.1: The flux qubit and the dissipative LZ transition. (a) Schematic of the tunable capacitively-shunted flux qubit and the control and readout circuitry. The flux biases Φ_x, Φ_z are each supplied by a DC voltage source and the Φ_z is further controlled by a fast arbitrary waveform generator, joined to the DC control through a bias-tee. Readout is done by measuring the transmission through an rf-SQUID terminated waveguide resonator coupled inductively to the qubit. (b) Schematic representation of the LZ sequence. The blue and red dashed lines indicate the energies of the diabatic states, which are separated by $\epsilon(\Phi_z) = 2I_p(\Phi_z - \Phi_z^{\text{sym}})$. The grey lines indicate the eigenenergies of the qubit, which has a minimum gap of Δ at the symmetry point Φ_z^{sym}. The curly arrows indicate the dominant open system effects in the LZ measurements in the weak-coupling limit, which are excitations around the symmetry point and relaxation after the symmetry point. The double-well plots on either side of the energy level diagram are a representation of the qubit potential at the beginning and end of the LZ sweep.

$$H_q = -\frac{\epsilon(\Phi_z)}{2}\sigma_z - \frac{\Delta(\Phi_x)}{2}\sigma_x, \tag{6.2}$$

with $\sigma_{z,x}$ being the Pauli operators. Here $\epsilon = 2I_p(\Phi_z - \Phi_z^{\text{sym}})$ and Δ are respectively the bias and tunneling amplitude between persistent current states, I_p is the persistent current, $\Phi_{z(x)}$ is the flux bias in the $z(x)$ loop, and Φ_z^{sym} is the Φ_z bias which gives a symmetric double-well potential. The Φ_x, Φ_z biases are controlled by DC voltage sources and the Φ_z bias is additionally coupled to a fast arbitrary waveform generator (AWG), combined with the DC control through a bias-tee. Readout of persistent current states is done by inductively coupling the qubit z loop to a flux-sensitive resonator. The circuit is also capacitively coupled to a waveguide used to send microwave signals, allowing resonant excitation of the circuit. Spectroscopically measured transition frequencies are fit using a circuit network model, which allows for finding the circuit parameters (see Sec. 6.5.2). The two-state model parameters I_p and Δ can then be obtained from the circuit model at arbitrary flux bias near the symmetry point $\Phi_z = \Phi_z^{\text{sym}}$.

6.2.1 Short-time limit

A diagram representation for the LZ measurement is shown in Figure 6.1(b). At $t = 0$, the qubit is prepared in the left well at $\Phi_z^{\text{init}} \approx -0.005\Phi_0 + \Phi_z^{\text{sym}}$. Then the qubit z flux Φ_z is linearly swept to $\Phi_z^{\text{final}} \approx 0.005\Phi_0 + \Phi_z^{\text{sym}}$ over the duration T_{LZ}. The initial and final values of Φ_z ensure the LZ sweep starts and ends far enough from the anti-crossing so that the qubit energy eigenstates approximately overlap with the persistent current states. The qubit state population after the sweep is read out by measuring the state-dependent transmission through the resonator. The sequence is repeated for a range of Φ_x and T_{LZ} values. With decreasing Φ_x, Δ decreases nearly exponentially whereas I_p increases by about 10% over the entire range.

The measured final excited state probabilities P_e versus T_{LZ} at short times are shown in Figure 6.2(a). In the weak-coupling limit, the system is expected to behave nearly coherently for short sweep times, implying that the final excited state probabilities are well described by Eq. 6.1 with v the sweep velocity, given by $v = 2I_p(\Phi_z^{\text{final}} - \Phi_z^{\text{init}})/T_{\text{LZ}}$. To confirm the coherent-limit behavior, we fit an exponential decay to the short-time decay of the measured final excited probabilities, and then convert the decay constant to an effective gap Δ_{LZ} assuming I_p given by the circuit model. The extracted values of the effective gap Δ_{LZ} are compared to values of Δ given by the circuit model in Figure 6.2(b). There is excellent agreement for the full range of Φ_x measured in LZ experiments, with Δ in the

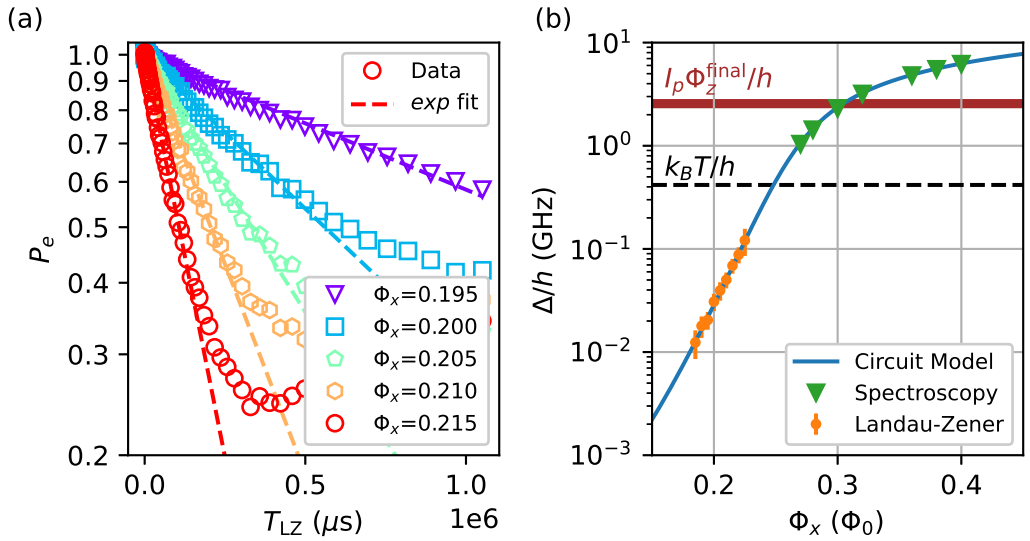

Figure 6.2: LZ data in the short sweep time range and fitted effective gap. (a) Experimental data (open markers) and exponential fits (dashed lines) to P_e versus T_{LZ}. The maximum sweep time included in the fit is determined adaptively, by first starting from 30 ns and then increasing until the mean square loss of the fit exceeds 0.01. (b) The minimum gap Δ versus x-bias flux Φ_x from spectroscopy (green triangle), LZ (orange dots) and circuit model (blue line). Error bars in the LZ data represent standard error propagated from the exponential decay fit error. The circuit model is a result of fitting spectroscopy data for a range of Φ_x, Φ_z (not shown here). The black dashed line indicates the noise temperature, which is assumed to be the base temperature of the dilution fridge, $T = 20\,\mathrm{mK}$. The brown horizontal band indicates the qubit energy splitting at the end of the LZ sweep.

range of $12 - 120\,\mathrm{MHz}$. This range of Δ corresponds to a(n) (non-)adiabatic time scale that approaches the lower and upper limit of the flux control bandwidth.

6.2.2 Long-time limit

After confirming the short-time behavior, we observe the dynamics at longer sweep times, where coupling to the environment is expected to affect the LZ transition. We first discuss the characterization of the environment. Measurement of the noise spectrum is done based on its effect on qubit relaxation and dephasing at $\Delta/h \gtrsim 1\mathrm{GHz}$, where the weak coupling limit holds. We find that the coherence is flux noise limited and can be explained by a noise

power spectral density (PSD) consistent with previous work [48, 235, 290], where the noise power varies to a good approximation as $1/f$, with f the frequency, up to 1 GHz, combined with quasi-ohmic noise at higher frequencies. Our noise measurements, which are sensitive to the symmetrized noise power, combined with the assumption that the environment is in thermal equilibrium at the fridge base temperature, allow us to write the quantum noise PSD (unsymmetrized) as

$$S_\lambda(\omega) = S_{\lambda,1/f}(\omega) + S_{\lambda,\text{ohmic}}(\omega), \tag{6.3}$$

$$S_{\lambda,1/f}(\omega) = \frac{A_\lambda \omega}{|\omega|^\alpha}\left[1 + \coth\left(\frac{\beta\hbar\omega}{2}\right)\right] \text{ and} \tag{6.4}$$

$$S_{\lambda,\text{ohmic}}(\omega) = B_\lambda \omega |\omega|^{\gamma-1}\left[1 + \coth\left(\frac{\beta\hbar\omega}{2}\right)\right], \tag{6.5}$$

with $\lambda \in \{\Phi_x, \Phi_z\}$. Here $\beta = 1/k_B T$ is the inverse temperature and $A_\lambda(B_\lambda)$ and $\alpha(\gamma)$ characterize the strength and frequency dependence of the $1/f$(quasi-ohmic) component respectively[1]. Given the smaller noise power and coupling matrix elements of the Φ_x noise for flux biases probed in the LZ measurement, we only consider Φ_z noise from here onward.

The measured final ground state probabilities $P_g = 1 - P_e$ for different Φ_x are shown in Figure 6.3(a,b), versus the full range of sweep time T_{LZ} and the dimensionless time $\tau = \Delta^2/\hbar v$, with Δ being the predicted value from the circuit model. Analyzing the dependence on both the actual time T_{LZ}, and dimensionless time τ allows us to make complementary observations about the changes in the effect of the environment as Φ_x, or equivalently Δ, is tuned.

6.2.3 Master equations

The weak-coupling limit between the system and the environment is expected to apply when the system-environment coupling strength is much smaller than the system's own energy scale, in this case, Δ. In the weak coupling limit, the adiabatic master equation (AME) [77] can be applied, where the environment is in thermal equilibrium and does not have memories of the system's states in the past (Markovian environment). The dominant environmental effects are thermal transitions and decoherence between the energy eigenstates of the system. The AME-simulated final ground state probabilities are shown in Figure 3(c,d). For large Φ_x, P_g increases non-monotonically with T_{LZ}. This can be

[1] see Sec. 6.6 for details of the noise PSD definition and the noise parameters

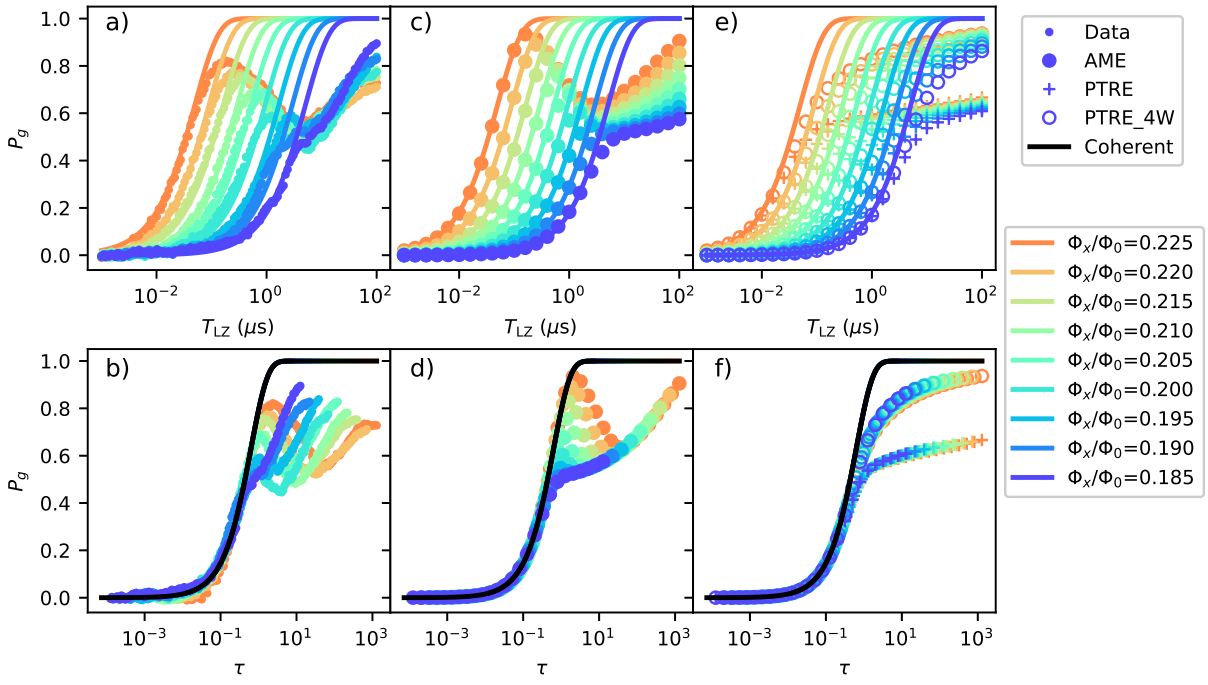

Figure 6.3: LZ data for the full range of Φ_x and sweep time, and comparison with simulation. Final ground-state probability P_g versus the sweep time T_{LZ} (top) and the dimensionless sweep time $\tau = \Delta^2/\hbar v$ (bottom), for (a, b) experimental data, (c,d) Adiabatic master equation simulation (labeled as AME) results with nominal noise parameters and (e,f) Polaron-transformed Redfield equation simulation with nominal noise parameters (labeled as PTRE) and 4 times larger MRT width W (labeled as PTRE_4W). All panels also contain the coherent limit given by $P_g = 1 - P_{\mathrm{LZ}}$.

interpreted in terms of the competition between thermal excitation around the minimum gap and relaxation after the minimum gap at intermediate and long time scales, as seen in previous numerical studies of dissipative LZ [315, 319, 316]. As the total sweep time increases, P_g first increases following the coherent limit, until the qubit has enough time to thermalize around the minimum gap and P_g starts to decrease. Further increase of the total sweep time allows the qubit to relax after crossing the minimum gap, increasing the final ground state probabilities again. Since the instantaneous matrix element of the Φ_z noise is proportional to $\Delta/\sqrt{\Delta^2+\epsilon(t)^2}$, thermal relaxation after the minimum gap is only significant at very long sweep times, and becomes very slow at smaller Φ_x.

Comparing the experimental data and AME simulation, we find qualitative agreement at large Φ_x. The experimental data show smaller P_g local maxima, which could indicate that the noise experienced by the qubit in LZ sweep is larger than the extrapolated noise values based on qubit decoherence measurements. There is significant disagreement between the data and the AME simulation at smaller Φ_x. Looking at the T_{LZ} dependence, while the AME predicts P_g to nearly settle at 0.5, the experimental data shows P_g to continue increasing with increasing sweep time. In fact, the experimental final ground state probability P_g for different Φ_x crosses at long times and the highest P_g is obtained at the lowest Φ_x. Furthermore, when looking at the τ dependence, it can be seen that for $\tau \gg 1$, where relaxation after the gap is expected to dominate, the simulated P_g curves for different Φ_x collapse onto the same τ dependence. This is contrasted with experimental data, where the P_g curves shift left towards the coherent limit as Φ_x is reduced. These signatures indicate that the weak-coupling limit breaks down as the minimum gap Δ is reduced.

To understand the data in the strong-coupling limit, the polaron-transformed master equation (PTRE) is used [320, 318]. PTRE incorporates strong system-environment coupling by transforming into the dressed polaron frame and treats the tunneling parameter Δ perturbatively. The noise PSD in the polaron frame is separated into low- and high-frequency components. Particularly, the low-frequency part is characterized by two parameters,

$$W^2 = 2I_p^2 \int \frac{d\omega}{2\pi} S^{+}_{\Phi_z,1/\mathrm{f}}(\omega), \text{ and} \tag{6.6}$$

$$\epsilon_p = 2I_p^2 \int \frac{d\omega}{2\pi} \frac{S^{-}_{\Phi_z,1/\mathrm{f}}(\omega)}{\hbar\omega}, \tag{6.7}$$

which are known as the MRT width and reorganization energy respectively [308]. The functions $S^{-(+)}_{\Phi_z}$ are the (anti-) symmetrized low frequency Φ_z noise. The PTRE is expected

to hold when the environment-induced dephasing is much larger than the qubit's minimum energy gap, or $W \gg \Delta$. By integrating the $1/f$ noise obtained from dephasing time measurements, we obtain $W/h \approx 48 - 59\,\mathrm{MHz}$. Assuming the environment is in thermal equilibrium, ϵ_p is related to W via the fluctuation-dissipation theorem $\epsilon_p = W^2/2k_BT$. The result of PTRE simulations is shown in Figure 6.3(e,f). The final ground-state probability P_g first increases with increasing sweep time, closely following the coherent LZ probabilities until around $P_g = 0.5$ where it flattens. It is found through numerical experiments that increasing W while keeping T unchanged, or equivalently increasing ϵ_p/W, brings the PTRE results closer to the coherent LZ probabilities. Indeed, it has been demonstrated previously that for a flux qubit strongly coupled to low-frequency noise, the LZ transition probability recovers the coherent LZ probability when $\epsilon_p \gg W$ [309].

In the experimental data, the transition probabilities approach the coherent limit as Φ_x or Δ is reduced, indicating a strong coupling between the qubit and the environment. At the smallest Φ_x, the measured P_g does not flatten near 0.5, contrasting the PTRE prediction with nominal noise values, but is closer to the PTRE prediction with larger MRT width W. This suggests that the noise seen by the qubit is larger than the integrated $1/f$ noise. This is not entirely surprising, given that previous MRT measurements on superconducting flux qubits also revealed larger W than the integrated power of $1/f$ flux noise (see Sec. 6.6).

6.2.4 Spin bath model for the crossover regime

To further understand the result in the crossover regime, we propose a hybrid noise model, that incorporates both the high-frequency noise and the low-frequency noise through an explicit spin bath. The spin bath is chosen because it is an appropriate physical model for the underlying origin of low-frequency flux noise [321, 322, 140], although simplification is needed for the simulation to be computationally feasible. Specifically, we consider N_s spins coupled to the qubit via the interaction

$$H_{qS} = \sum_{i}^{N_s} J_i \sigma_z \tau_{z,i}, \tag{6.8}$$

where $\tau_{z,i}$ is the i'th spin's Pauli Z operator and J_i is its coupling strength to the qubit. The bath spins do not have internal dynamics, but each of them is transversely coupled to its own environment, at a temperature that we assume to be the same as the qubit's environment, T. This environment leads to thermal transitions between the spin states, with depolarization rate γ_i. For appropriately chosen distribution of γ_i and J_i, the noise

PSD due to the spins effectively represents the $1/f$ noise seen by the qubit in the chosen frequency range (see Sec. 6.7 for details of the model).

The spin bath model is simulated using the AME, with the high-frequency noise defined in the same as the single-qubit AME, and the parameters defining the spin bath are the number of spins, the minimum and maximum depolarization rate γ_i of the spins, and the target low-frequency noise amplitude. As a preliminary demonstration, we choose a model with three spins, with uniform J, and γ_i distributed between $1-10$ MHz to match a target low frequency $1/f^{\alpha}$ flux noise. This range of γ_i is chosen such that they are lower than the minimum qubit frequency, and therefore can be characterized as low-frequency noise, but they are not too slow to the extent that they do not display any dynamics within the LZ sweep time. As shown in Fig. 6.4, it is found that if the target low-frequency noise amplitude is 8 times larger than the noise amplitude deduced from decoherence measurements, corresponding to $J_i/h = J/h = -0.09$ GHz, the simulated ground state probabilities versus sweep time at different Φ_x qualitatively matches the experimental results, including the crossover regime. Specifically, for large Φ_x or Δ, the spin bath simulation results display the non-monotonic dependence of ground state probability P_g versus the dimensionless sweep time τ, and is almost indistinguishable from the single qubit AME result. However, at smaller Φ_x or Δ, the spin bath simulation result displays a monotonic increase of P_g with increasing sweep time τ, which is similar to the PTRE. The spin bath simulation results also differ from both AME and PTRE in that the P_g curves for different Φ_x at large τ do not collapse.

Further intuition about the spin bath model can be obtained by observing the evolution of the polarization of the qubit and the spin bath during the LZ sweep. The collective effect of the spins can be captured by the parameter

$$\epsilon_{\mathrm{SB}} = -\sum J_i \langle \tau_{z,i} \rangle, \tag{6.9}$$

which is the effective longitudinal bias applied by the spins on the qubit. In Fig. 6.4(d, e) we show the evolution of the qubit polarization $\langle \sigma_z \rangle$ and the effective bias ϵ_{SB} for $\tau \sim 10$ at two different X flux bias. It can be seen that for $\Phi_x = 0.225$, the effective bias ϵ_{SB} changes slowly after the qubit has tunneled. Therefore the spin bath presents negligible influence on the qubit dynamics. For $\Phi_x = 0.185$, the change in ϵ_{SB} almost overlaps with the changes in qubit polarization $\langle \sigma_z \rangle$. This is because for the same dimensionless sweep time τ, the depolarization rate of the spins becomes much shorter as compared to the tunneling time of the qubit [2] as Φ_x or Δ reduces. In other words, the spins quickly reorganize themselves

[2] This is roughly the adiabatic timescale, or the time required for the qubit to adiabatically transition from one to the other persistent current/diabatic state

to align with the new qubit polarization, due to their ferromagnetic interaction. This fast change in ϵ_{SB}, together with its relatively large magnitude as compared to Δ, effectively shifts the qubit away from the anti-crossing as soon as the qubit has tunneled to the opposite polarization. Away from the anti-crossing, the qubit rarely experiences thermal excitation, hence the non-monotonic P_g dependence disappears and P_g continues to increase with sweep time as it has more time to complete the tunneling. If however the noise is not strong and does not induce a large enough ϵ_{SB} to shift the qubit away from the anti-crossing, thermalization excitation would still occur, and P_g would barely increase above 0.5, similar to the single-qubit AME when Δ is small (see Sec. 6.7 for the simulation results with weaker low-frequency noise).

6.3 Discussion

In summary, we experimentally characterized the LZ transition probability in a superconducting flux qubit with a wide range of sweep velocities v and minimum gap sizes Δ, and we showed that the dominant physics of coupling to the environment shows a crossover from weak coupling to high-frequency noise to strong coupling to low-frequency noise. We found that for large gap Δ, the competition between adiabaticity and environment-induced thermalization leads to non-monotonic dependence of the final ground state probability P_g on sweep time, which can be reproduced by a weak-coupling model, the AME. However, as Δ becomes smaller, the non-monotonicity gradually disappears and P_g becomes closer to the coherent LZ transition rate, which is consistent with a strong-coupling model, the PTRE. These findings confirm previous analytical and numerical results on the dissipative LZ dynamics in the weak- and strong-coupling limits.

We also explored a spin bath model that qualitatively reproduces the full range of experimental data. The spin bath model explicates that the crossover depends on the relative timescale between the tunneling time of the qubit, and the time taken for the environment to reorganize itself after the qubit has tunneled. At large Δ, the qubit tunneling time is short and the low-frequency environment does not respond to, and hence has no impact on the qubit dynamics. As Δ decreases, the environment reorganization time becomes comparable and eventually shorter than the qubit tunneling time. If coupling to the environment is strong enough, the reorganized environment exerts a large effective bias which shifts the qubit away from the symmetry point, preventing the qubit from thermalizing near the anti-crossing.

The spin bath model presented in this chapter is still at a preliminary stage. The next step would be to explore the parameters of the spin bath more systematically, including

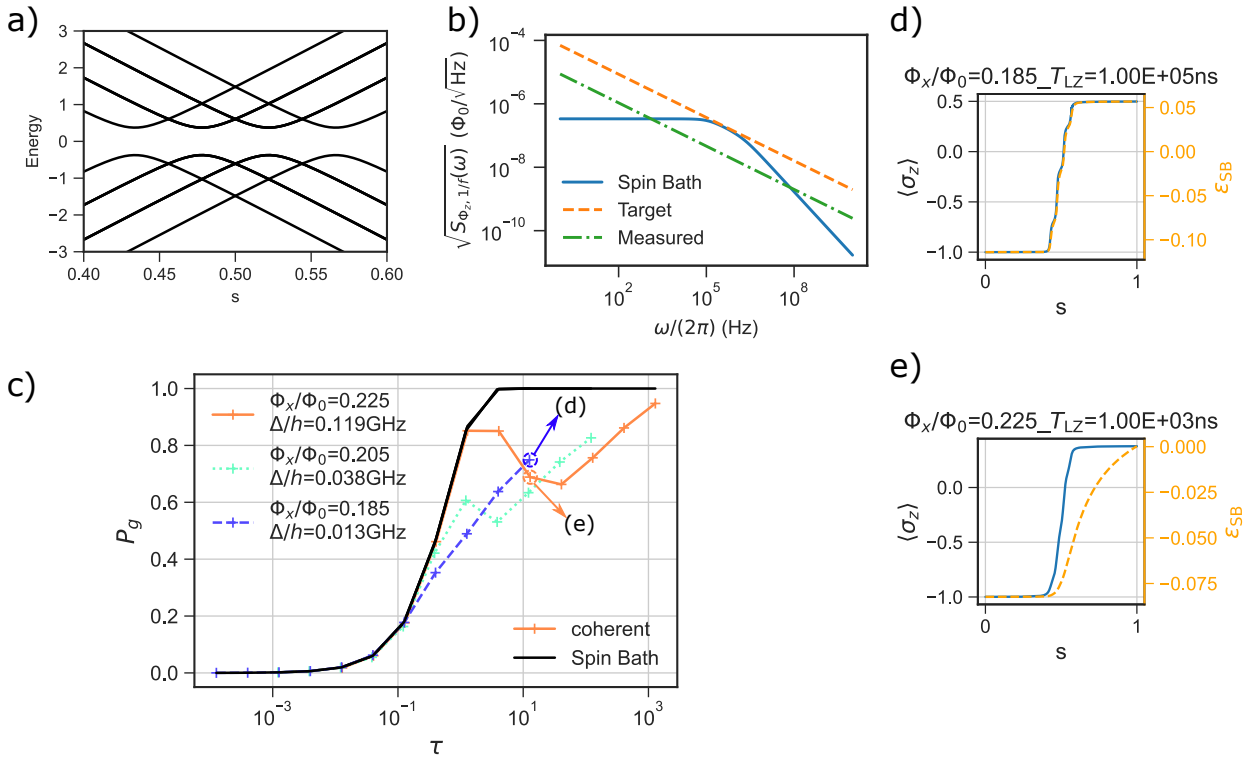

Figure 6.4: Simulation results of the spin bath model. (a) The energy spectra of the qubit LZ transition with 3 spins ferromagnetically coupled to the qubit, versus the normalized time $s \in [0, 1]$, for $\Phi_x = 0.225$. There are 4 distinct levels visible in the manifold of the qubit being in the left state, corresponding to 0, 1, 2, and 3 spins aligned with the qubit (with degeneracies of 1, 3, 3, and 1 respectively). Each of them anti cross with the corresponding state in the manifold of the qubit being in the right state. Energy levels of states with different numbers of aligned spins cross each other, as there is no matrix element coupling them. (b) The symmetrized $1/f^\alpha$ flux noise PSD as measured by the decoherence measurement (green dash-dotted line), the equivalent flux noise PSD generated by the spins (blue solid line), calculated by summing the individual contribution using Eq. 6.40, as well as the targeted noise PSD (orange dash line) that the spin bath is set to match, which has 8 times larger magnitude than the measured. (c) The simulated final ground state probabilities versus dimensionless sweep time τ, using the spin bath model with 3 spins targeting the noise PSD shown in (b). (d, e) The instantaneous evolution of the qubit polarization and effective bias by the spin bath, versus the normalized time s, for $\Phi_x = 0.185$ and $\Phi_x = 0.225$ respectively. Both plots correspond to $\tau \approx 10$ (see text for discussion).

the number of spins, the range of their polarization rates, and possibly different noise temperatures for the low and high-frequency noise. Ideally, the spin bath model parameters should be completely specified by the actual environment of the flux qubit, in terms of the noise PSD, and other experimentally measured properties, such as the environment polarization time [140]. This requires both further experimental characterization of the noise properties over a wide range of frequencies, as well as expanding the simulation capabilities.

The dissipative LZ transition studied here can be considered a toy model for dynamics in quantum annealing, where small gap anti-crossings between the lowest two energy eigenstates are expected to play an important role [124, 82]. Our results thus contribute to the understanding of the role of open system effects in a quantum annealer [126, 127, 82, 323, 324]. In the weak-coupling limit, although thermal relaxation helps the system to reach the ground state, the rate of this process is only proportional to the minimum gap Δ, which is expected to close for hard annealing problems. On the other hand, remaining in the strong coupling limit is not necessarily detrimental, as the experimental data and PTRE simulation show a counter-intuitive result that higher ground state probabilities can be achieved in the intermediate to strong coupling limit, as compared to the weak-coupling limit, when ϵ_p/W is large enough. It should be noted that coupling to classical noise gives $\epsilon_p = 0$, which would limit the maximum P_g to 0.5.

We expect future work employing more complex annealing protocols, such as those involving repeated LZ transitions or locally adiabatic annealing schedule [10] could build on the understanding developed here and reveal more information about the qubit environment. It would be interesting to see if there is a general relationship between the annealing rate and the relevant environmental noise. An optimistic outcome would be the discovery of annealing protocols similar to dynamical decoupling, which have been extensively used in GMQC to reduce the impact of low-frequency noise. Another interesting direction is engineered environment. For the simple LZ problem, it is known that transverse coupling to low-temperature noise could enhance the ground state probability beyond the limit posed by adiabaticity [325]. To implement this idea for an annealer, the generalization of transverse noise needs to be developed for multi-qubit cases, and the enhancement needs to be verified in the presence of strong low-frequency noise, as is the case studied here.

6.4 Methods

6.4.1 Qubit control and readout

The qubit x, z flux biases are each controlled using on-chip flux bias lines, with current supplied by a DC voltage source and a fast AWG. The DC source has a stronger coupling to the qubit loops to achieve flux biasing of more than a flux quantum. The AWG has weaker coupling to the flux biases, corresponding to a bias range of about 100 mΦ_0, where Φ_0 is the flux quantum.

Before the LZ sweep, the qubit needs to be prepared in its ground state. Passive cooling is not possible when the tunneling barrier between persistent current states is large. We use a cooling protocol similar to that demonstrated in Ref. [326]. Using the large tunneling amplitude between the ground state of the higher well and the excited state of the opposite well, residual excited populations can be adiabatically transferred to the lower well and the system quickly relaxes to the ground state. Additional details of the energy spectrum and this cooling method are discussed in Sec. 6.5.5.

The qubit state is read by measuring the state-dependent transmission through the tunable resonator. When doing spectroscopy and coherence measurements, the resonator is biased at a flux-insensitive position (0 flux in the SQUID), and readout is in the qubit energy eigenbasis, due to dispersive interaction between the qubit and resonator. During the LZ measurement, the resonator is biased at a flux-sensitive position (-0.15 Φ_0 flux in the SQUID), which allows measuring the qubit's persistent current states. Since the readout point of the LZ experiment is far from the qubit's symmetry point, the persistent current basis and energy eigenbasis of the qubit nearly coincide, with more than 99% overlap, and we do not distinguish the two bases at the readout point.

6.4.2 Master equation simulation

The master equation simulations were performed using HOQST, a Julia package for open system dynamics with time-dependent Hamiltonians [320]. The simulation takes the qubit Hamiltonian in Eq. (6.2), with I_p, Δ given by the circuit model. The qubit-bath interaction considered is

$$H_{\text{int}} = -I_p \sigma_z \otimes Q, \tag{6.10}$$

where σ_z acts on the qubit and Q acts on the environment degrees of freedom which causes the qubit z loop flux noise.

The AME is a time-dependent version of the frequency form Redfield equation. Although a rigorous upper bound on the error of the AME is only small in the adiabatic limit [327], it is likely that the error is still small in the non-adiabatic limit, as shown in previous literature where the master equation results are compared to numerically exact path integral based simulation results [319, 316]. Specifically, the form used in this work is the one-sided AME that first appeared in [77], given by

$$\begin{aligned}\dot{\rho}_q(t) &= -\frac{i}{\hbar}[H_q(t), \rho_q(t)] \\ &+ \frac{1}{\hbar^2}\sum_{\omega} \Gamma_{\Phi_z}(\omega)\left[L_\omega(t)\rho_q, I_p\sigma_z\right] + h.c.,\end{aligned}$$

where ρ_q is the reduced density matrix of the qubit,

$$\Gamma_{\Phi_z}(\omega) = \frac{1}{2}S_{\Phi_z}(\omega) + i\gamma_{\Phi_z}(\omega) \tag{6.11}$$

$$\gamma_{\Phi_z}(\omega) = \frac{1}{2\pi}\int_{-\infty}^{\infty} S_{\Phi_z}(\omega')\mathcal{P}\left(\frac{1}{\omega-\omega'}\right)d\omega', \tag{6.12}$$

with $\mathcal{P}$ denoting the Cauchy principal value[3]. The operators L_ω are given by

$$L_\omega(t) = \sum_{E_\beta - E_\alpha = \omega} \langle\alpha(t)|I_p\sigma_z|\beta(t)\rangle|\alpha(t)\rangle\langle\beta(t)|, \tag{6.13}$$

where $E_{\alpha(\beta)}$ and $|\alpha(\beta)\rangle$ are the system's instantaneous energy eigenvalues and eigenstates, and $\alpha, \beta \in \{g, e\}$.

The PTRE is a model that accounts for strong system-environment coupling and has been found to explain experimental data in quantum annealers coupled strongly to low-frequency noise [309, 318]. The form of PTRE we use here has Lindblad form, given by

$$\begin{aligned}\dot{\tilde{\rho}}_q(t) &= -\frac{i}{\hbar}[\tilde{H}_q(t), \tilde{\rho}_q(t)] \\ &+ \frac{1}{\hbar^2}\sum_{\omega,\lambda} \tilde{S}(\omega)\left[\tilde{L}_{\omega,\lambda}\tilde{\rho}_q\tilde{L}^\dagger_{\omega,\lambda} - \frac{1}{2}\left\{\tilde{L}^\dagger_{\omega,\lambda}\tilde{L}_{\omega,\lambda}, \tilde{\rho}_q\right\}\right],\end{aligned}$$

[3]Note the notations for real and imaginary components of the Fourier transform of the noise correlation function change from the those presented in Chapter 2.2. This is to stay in line with the experimental convention of using S to denote noise PSD.

where tilde is used to denote operators in the polaron frame. Specifically,

$$\tilde{H}_q = -I_p(\Phi_z - \Phi_z^{\text{sym}})\sigma_z, \tag{6.14}$$

$$\tilde{L}_{\omega,\lambda\in\{+,-\}} = \frac{\Delta}{2} \sum_{E_i - E_j = \hbar\omega} \langle i|\sigma_\lambda|j\rangle |i\rangle\langle j|, \tag{6.15}$$

where $\sigma_{+(-)}$ are the qubit Pauli raising and lowering operators and $i, j \in \{0, 1\}$ are the qubit persistent current state index. The low- and high-frequency parts of the noise give a convolutional form for the PSD in the polaron frame

$$\tilde{S}(\omega) = \int \frac{\mathrm{d}\omega'}{2\pi} G_L(\omega - \omega') G_H(\omega'), \tag{6.16}$$

where G_L and G_H are contributions from the low- and high-frequency noise respectively, given by

$$G_L(\omega) = \sqrt{\frac{2\pi\hbar^2}{W^2}} \exp\left[-\frac{(\hbar\omega - \epsilon_p)^2}{2\hbar^2 W^2}\right] \tag{6.17}$$

$$G_H(\omega) = \frac{4S_{\Phi_z,\text{ohmic}}(\omega) I_p^2/\hbar^2}{\omega^2 + 4[S_{\Phi_z,\text{ohmic}}(0)/\hbar^2]^2 I_p^4}. \tag{6.18}$$

6.5 Additional details on the experiment

6.5.1 Crosstalk calibration

DC flux crosstalk between different bias lines and flux loops is calibrated using the CISCIQi method developed in Ref. [239]. We first measure the flux bias dependent resonator spectrum and the crosstalk into the resonator from other bias lines. This allows us to fix the resonator bias to measure the qubit-bias-dependent transmission through the resonator. The procedure is iterated a few times until the crosstalk is compensated to within $1\,\mathrm{m}\Phi_0$ accuracy. The full crosstalk matrix is shown in Figure 6.5(a).

Crosstalk from the fast pulses sent to the qubit z loop to other loops is not compensated due to bandwidth limitations on other bias lines. For the small pulse amplitude used for the LZ sweep, reaching up to $10\,\mathrm{m}\Phi_0$, the induced flux on the x, r loop should be inconsequential.

6.5.2 Circuit model

The device used in this experiment consists of a capacitively-shunted flux qubit coupled to a tunable rf-SQUID terminated resonator. The coupling between these two circuits is done via the mutual inductance between the qubit z loop and the rf-SQUID loop. A lumped element representation of the qubit and resonator circuit is shown in Figure 6.5(b). The qubit eigenstates and eigenvalues are obtained using the numerical tools developed in Ref. [240]. The circuit persistent current I_p and gap Δ were verified experimentally via qubit spectroscopy, as shown in Figure 6.5(c). The simulated I_p and Δ values are plotted as a function of Φ_x in Figure 6.5(d).

The parameters of the resonator rf-SQUID were determined by fitting the experimental values of the resonator frequency versus resonator flux bias Φ_r, shown in Figure 6.6(a). The resonator model allows for the extraction of the value of the screening current in the rf-SQUID, which was used to determine the shift in the symmetry point of the qubit, induced by the rf-SQUID when biased away from zero. In order to confirm this value experimentally, spectroscopy curves were taken at a fixed value of Φ_x at two different values of resonator bias Φ_r at zero and -0.15, the value used for persistent current readout. The two spectroscopy curves are shown in Figure 6.6(b). The circuit parameters are summarized in Table 6.1.

6.5.3 Fast flux line coupling characterization

As described in Section C, fast voltage pulses are applied to the qubit z loop via a bias tee in order to control the flux bias of the qubit during the LZ sweep. In order to determine the transfer function between the voltage of the AWG and the flux fed to the qubit loop, a procedure using Ramsey interferometry was used.

The protocol is shown in Figure 6.7(a). Two $\pi/2$ pulses are applied using the capacitively coupled waveguide, separated by the time τ_{delay}. During the interval between the two $\pi/2$ pulses, a trapezoidal flux pulse with 1 ns rise and fall time is applied to the z loop of the qubit. This flux pulse adiabatically changes the qubit frequency, depending on the pulse amplitude and duration, which induces an additional phase for the superposition created by the first $\pi/2$ pulse, inducing an oscillation whose period depends on the flux amplitude. An example is shown in Figure 6.7(b) for the case of no flux pulse applied (i.e. pure Ramsey with no detuning) and with a 60 mV pulse applied.

The above sequence is repeated at a range of pulse amplitudes such that the detuning varied between approximately from 0 to 60 MHz. This detuning versus flux pulse am-

L_r	16.4pH
L_l	16.4pH
L_z	799.8pH
I_{cr}	77.6nA
I_{cl}	89.1nA
I_{c1}	244.7nA
I_{c2}	244.7nA
C_{cd}	0.4fF
C_{ad}	3.6fF
C_{ac}	0.04fF
C_{ab}	14.2fF
C_{gd}	44.1fF
C_{gc}	0.2fF
C_{ga}	141.4fF
C_{gb}	90.0fF
SQUID inductance L_s	238.7pH
SQUID junction I_s	1187nA
resonator length l_r	3.364mm
Mutual between qubit and SQUID M	60.3pH

Table 6.1: Best fit circuit parameter values for the qubit and resonator circuits.

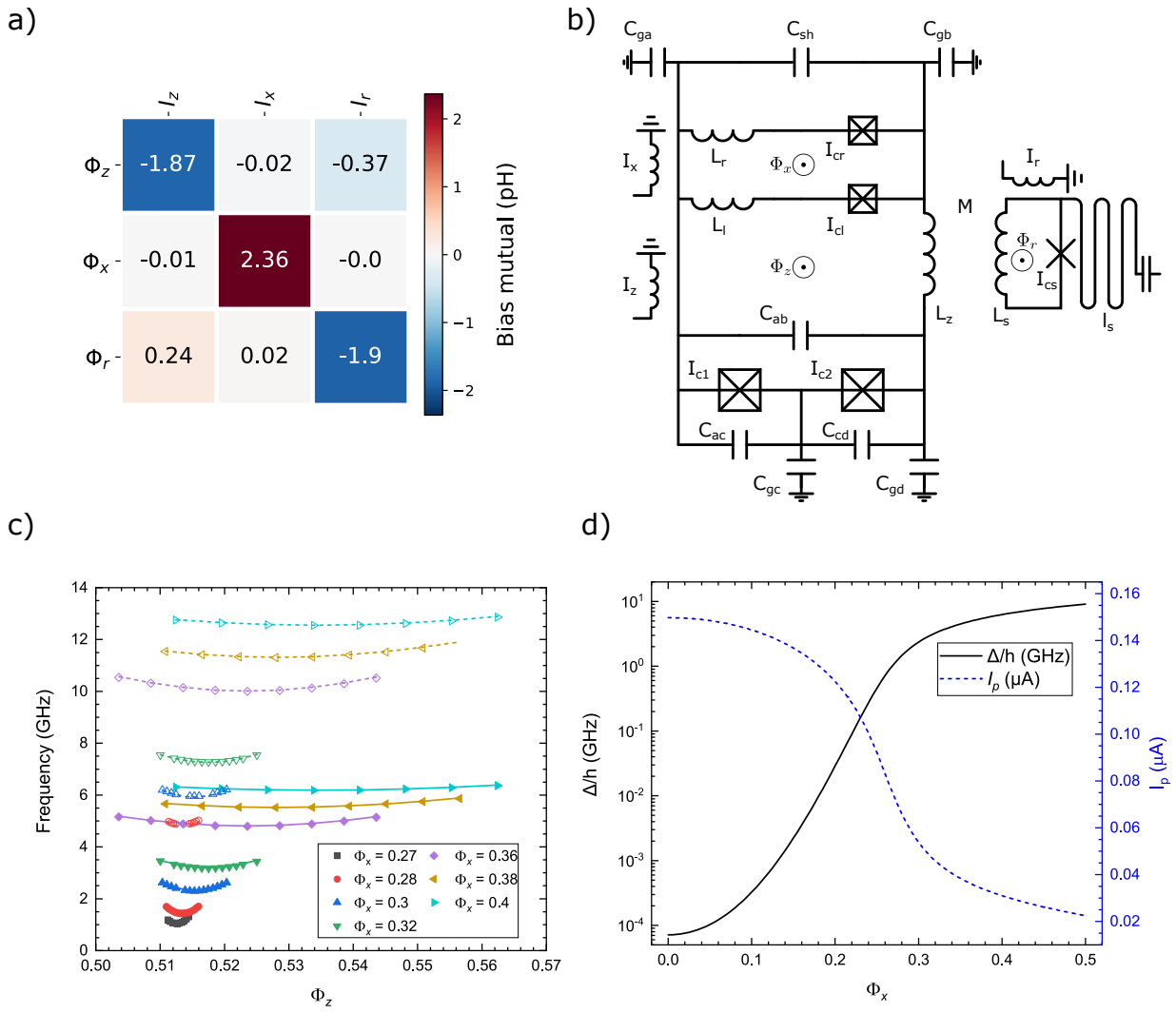

Figure 6.5: a) Matrix of mutual inductances between on-chip bias lines and flux loops. b) Circuit diagram for the qubit and coupler. c) Experimentally measured qubit transition frequency and simulated qubit transition frequencies for the best-fit parameters, as a function of the biases Φ_x and Φ_z, and comparison with experiment. Filled symbols (solid lines) correspond to the experimentally obtained (simulated) transition frequencies between the ground and the first excited state. Open symbols (dashed lines) correspond to the experimental (simulated) transition frequencies between the ground and the second excited state. d) Simulated minimum gap (left axis, solid curve) and persistent current (right axis, dashed curve) values as a function of the bias Φ_x.

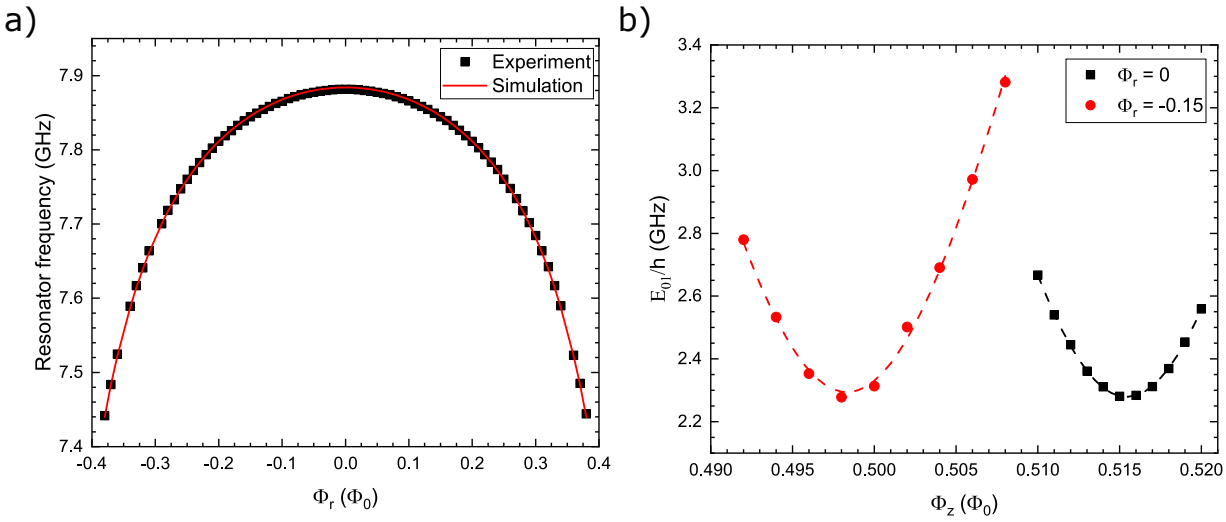

Figure 6.6: a) Readout resonator resonance frequency vs bias: experiment (solid points) and simulation with best-fit parameters (solid line). b) Experimentally measured shift of the qubit z symmetry point due to the SQUID screening current. Solid symbols correspond to qubit frequencies determined from spectroscopy, and dashed lines correspond to a fit using a two-level system anticrossing relation.

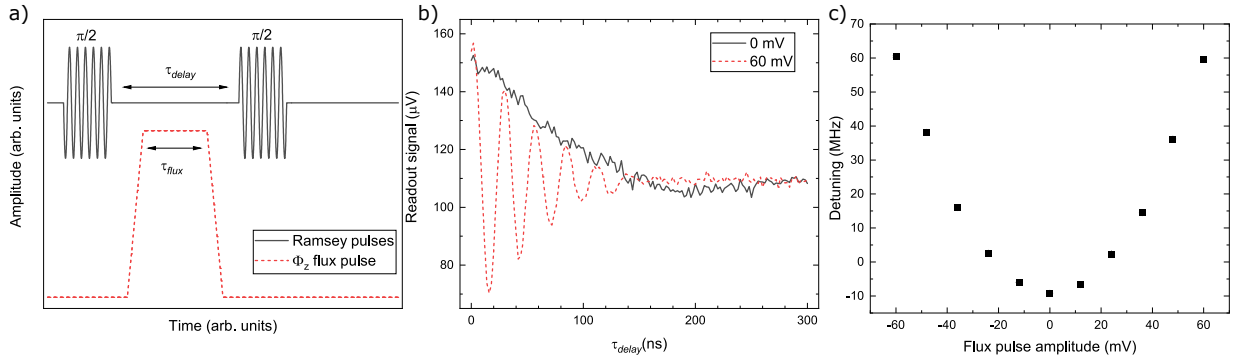

Figure 6.7: Bias line characterization using a Ramsey protocol. a) Pulse sequence for Ramsey measurements. The qubit is initialized in a superposition using a $\pi/2$ pulse, then a flux pulse applied to the qubit Z bias adiabatically detunes the qubit away from the symmetry point. The spacing between the two $\pi/2$ pulses τ_{delay} equal to the pulse duration τ_{flux} plus the rise and fall times. The qubit acquires a phase dependent on the amplitude and duration of the pulse. b) Ramsey oscillation curves with $V_z = 0$ and 60 mV. c) Fitted detuning as a function of pulse amplitude.

plitude is shown in Figure 6.7(c). Combining the detuning and the drive frequency gives the effective qubit frequency during the delay time in the Ramsey sequence. Comparing the qubit frequency versus flux pulse amplitudes allows us to deduce the voltage-to-flux conversion for the fast flux line.

6.5.4 Fast flux line pulse distortion characterization

During the LZ measurement sequence, time-dependent flux pulses are applied to the qubit via a bias tee, as discussed in Sections C and 6.5.3. As the experiment involved the application of long pulses (duration > 1 μs), we characterize the transmission of the AC port of the bias tee to check for possible frequency-dependent attenuation effects that would distort the pulse shape.

In order to check for distortion effects, we used an experimental protocol based on a Ramsey sequence, shown in Figure 6.8(a). Two microwave $\pi/2$ pulses are applied with a fixed delay time τ_{delay}. The delay time is chosen to correspond to the inflection point of one of the Ramsey oscillations, so that the readout signal is maximally sensitive, and responds linearly to changes in qubit frequency and hence the flux pulse amplitude. The spacing between the Ramsey sequence and readout is fixed. In addition, a square pulse from Φ_z

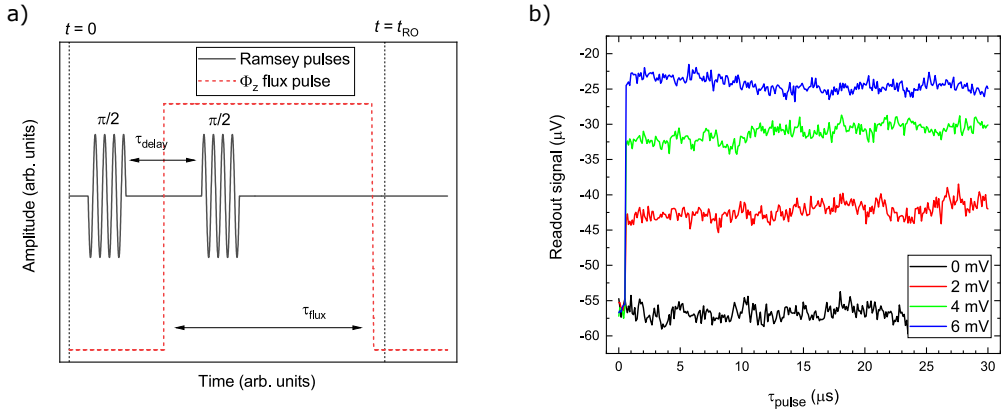

Figure 6.8: Characterization of pulse distortion from the bias tee. a) Schematic of Ramsey-based sequence used to quantify the pulse distortion. b) Readout voltage as a function of pulse duration τ_{flux}. The flat profile of the readout voltages out to several tens of μs shows that the bias tee negligibly distorts the pulse shape.

fast line is applied with duration τ_{flux}. The position of the rising edge of the square pulse is varied, spanning a range of times relative to the Ramsey pulses, from the rising edge following the first $\pi/2$ pulse to preceding the first $\pi/2$ pulse. This is done by increasing τ_{flux} while keeping the falling edge and the Ramsey pulses at a fixed position relative to the readout pulse.

The readout signal as a function of pulse duration is shown in Figure 6.8(b) for several values of pulse amplitudes. For short pulse duration, the pulse starts after the Ramsey sequence and does not change the readout signal. As the pulse duration increases, the leading edge of the pulse moves past the second and then the first $\pi/2$ pulse. The flux pulse experienced by the qubit in between the two $\pi/2$ pulses changes the phase of the Ramsey oscillation, causing a sharp change in the measured signal, with a width corresponding to τ_{delay}. The Ramsey signal shown in Figure 6.8(b) is flat up to a pulse duration as long as 30 μs, indicating that the pulse is negligibly distorted at these time scales.

6.5.5 State preparation and readout calibration

In this section, we describe the protocol for preparing the qubit in its ground state and the method for calibrating the readout voltage to obtain the state populations.

The qubit can in general be prepared in the ground state by waiting long enough. However, for some of the small gap Δ values used in the Landau- Zener experiments, the

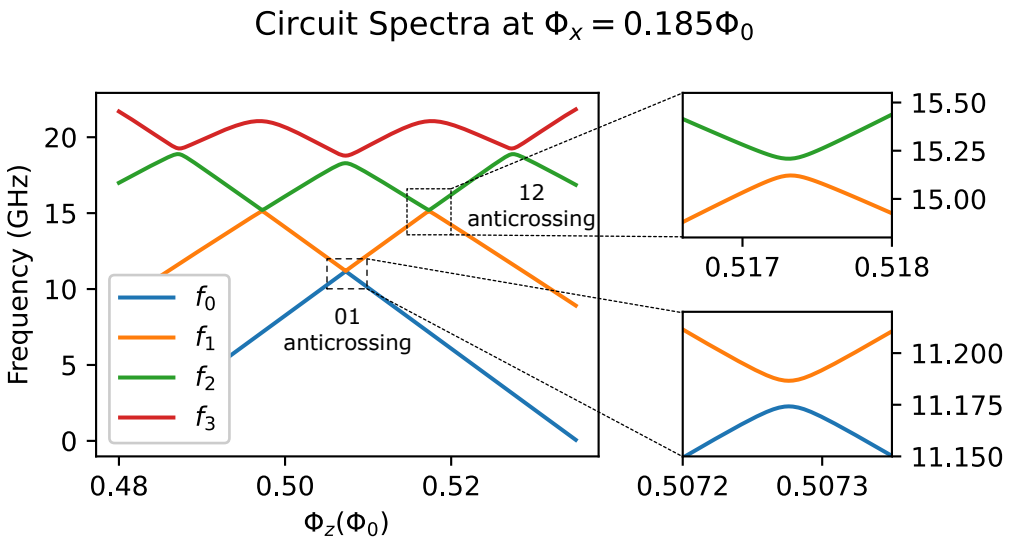

Figure 6.9: Energy Spectrum of the qubit circuit at $\Phi_x = 0.185\Phi_0$, with close up of the 01 and 12 anticrossing

transition rate between the ground states of the two wells is very slow. Therefore, to prepare the qubit in the ground state before the LZ measurements, we use a sideband cooling method similar to that used in Ref. [326] A plot of the qubit energy levels is shown in Figure 6.9. The qubit is prepared in its ground state at a bias about $\Phi_z - \Phi_{z,\text{sym}} \approx 0.005$ away from the symmetry point, as follows. A sinusoidal pulse is applied which, on its positive side, sweeps the qubit further away from the symmetry point and past the anti-crossing between the first and second excited states. Prior to this sinusoidal pulse, the qubit is in a mixture of the ground and excited states. Due to the larger anti-crossing between the higher levels, the excited state can be adiabatically transferred into the same well as the ground state, which allows fast relaxation back to the ground state. By repeated sweeping across the anti-crossing between the first and second excited state, it is possible to prepare the qubit in the ground state. In our experiments, the qubit was cycled 5-10 times in order to prepare the ground state prior to the LZ sweep.

Next, we discuss the calibration of the readout signal. Given a fixed readout frequency, the transmission measured is given by a complex number $V_g(V_e)$ for the qubit at the ground (excited) state. For a qubit in the mixed state, the readout voltage is given by $V = V_g + P_e(V_e - V_g)$ where we assume populations beyond the qubit states are negligible. Therefore to obtain the qubit excited state population we need to obtain V_g and V_e.

For the LZ measurements, V_g and V_e are calibrated at each Φ_x. To measure V_g we prepare the qubit in the ground state at the readout point (at the end of the LZ sweep) using the cooling procedure discussed above. To measure V_e, we prepare the qubit in the excited state by preparation in the ground state at the opposite side of the symmetry point, followed by a fast, 1 ns long, LZ sweep through the minimum gap. Taking the qubit model parameters and the coherent LZ formula, a 1 ns LZ is expected to lead to a final excited state probability larger than 99% for even the largest Δ measured in our experiments.

6.6 Additional details on noise parameters and master equation simulation

In this section, we discuss the noise model used in the master equation simulation. We first introduce the general form of noise and then discuss some specificities regarding including them in the adiabatic master equation (AME) and polaron-transformed Redfield equation (PTRE). For reference, we also provide a comparison of the noise parameters used in this work with noises measured in three other flux-qubit-based quantum annealing devices, as summarized in Table 6.2.

As the qubit circuit has relatively large flux loops, we assume the flux noise in the qubit x and z loops are the dominant sources of noise. The noises lead to fluctuation in the circuit Hamiltonian via

$$\delta H_{\mathrm{c}}(\Phi_z, \Phi_x) = \sum_{\lambda \in \{\Phi_z, \Phi_x\}} \frac{\partial H_{\mathrm{c}}}{\partial \lambda} \delta\lambda. \tag{6.19}$$

In particular for $\lambda = \Phi_z$, in the two level approximation $\frac{\partial H_{\mathrm{c}}}{\partial \Phi_z} = -I_p \sigma_z$. Note here when the noise source is quantum, $\delta\lambda$ is a quantum operator of the environment.

The noise power spectral density (PSD) due to $\delta\lambda$ is given by the Fourier transform of its auto-correlation function,

$$S_\lambda(\omega) = \int_{-\infty}^{\infty} \mathrm{d}\tau e^{i\omega\tau} \langle \delta\lambda(\tau)\delta\lambda(0) \rangle. \tag{6.20}$$

Various previous measurements have shown that flux noise has roughly 1/f dependence, with f being frequency, up to around 1GHz, and then a quasi-ohmic spectrum at higher frequencies [48, 235, 290]. Furthermore, we follow Ref. [235] to consider a quantum noise

PSD with the positive and negative frequency components related by a phenomenological thermodynamic model. These considerations lead to the noise PSD given by

$$S_\lambda = S_{\lambda,1/\mathrm{f}} + S_{\lambda,\mathrm{ohmic}} \tag{6.21}$$

$$S_{\lambda,1/\mathrm{f}} = \frac{A_\lambda \omega}{|\omega|^\alpha}\left[1 + \coth\left(\frac{\beta\hbar\omega}{2}\right)\right], \tag{6.22}$$

$$S_{\lambda,\mathrm{ohmic}} = B_\lambda \omega |\omega|^{\gamma-1}\left[1 + \coth\left(\frac{\beta\hbar\omega}{2}\right)\right], \tag{6.23}$$

where $\beta = 1/k_B T$ is the inverse temperature, A_λ, B_λ determines the noise strength and α, γ determine the frequency dependence. For 1/f noise, $\alpha = 1$ and for ohmic noise $\gamma = 1$. The temperature is assumed to be the base temperature of the fridge, $T = 20\,\mathrm{mK}$.

The parameters of 1/f noise are obtained by measuring the flux bias dependent Ramsey dephasing times. The Ramsey dephasing time probes symmetrized 1/f noise in the low-frequency limit, satisfying $\hbar\omega \ll k_B T$. In this limit, we have

$$S^+_{\lambda,1/f}(\omega) = \frac{1}{2}\left(S_{\lambda,1/f}(\omega) + S_{\lambda,1/f}(-\omega)\right) \tag{6.24}$$

$$\approx \frac{A_\lambda \omega}{|\omega|^\alpha}\frac{2}{\hbar\omega\beta} \tag{6.25}$$

$$= A^*_\lambda \left(\frac{2\pi}{|\omega|}\right)^\alpha, \tag{6.26}$$

where we defined $A^*_\lambda = 2A_\lambda/[\hbar\beta(2\pi)^\alpha]$ to relate to the more commonly used expression for 1/f flux noise, used in for example Ref. [161]. Given the similarity between our device and the device used in Ref. [161], we assume $\alpha = 0.91$ and found $A^*_{\Phi_z} = (8.7 \times 10^{-6})^2\,\Phi_0^2/\mathrm{Hz}$, $A^*_{\Phi_x} = (5. \times 10^{-6})^2\,\Phi_0^2/\mathrm{Hz}$ fits the measured Ramsey dephasing time best [4].

The quasi-ohmic component of the flux noise mainly contributes to qubit relaxation. It is more difficult to give a quantitative estimate of the quasi-ohmic noise power as it leads to similar flux bias dependence of relaxation rates as other noise sources, such as ohmic charge noise [48, 235]. For this reason, we use the reported ohmic noise strength measured in Ref. [235] and scale it according to the ratio of the 1/f noise strength at 1Hz between the two devices. This gives $\gamma = 1$ and $B_{\Phi_z} \approx 1.3 \times 10^{-30}\Phi_0^2/\mathrm{Hz}^2$, $B_{\Phi_x} \approx 4.1 \times 10^{-31}\Phi_0^2/\mathrm{Hz}^2$. These

[4] Note that we used $\alpha = 0.91$ here but assumed $\alpha = 1$ in Chapter 5, and the corresponding fitted noise amplitudes differ. This might appear contradictory, but the essential features of the LZ simulation are not expected to change based on the exact frequency dependence

	This work	Quintana et. al [5]	DWave CJJ qubit [6]	DWave CCJJ qubit [7]
$A^*_{\Phi_z}$ (Φ_0^2/Hz)	$(8.7 \times 10^{-6})^2$	$\sim (5 \times 10^{-6})^2/2$		$(1.3 \times 10^{-6})^2/2$
α	0.91	$0.96 - 1.05$		0.95
$I_p(\mu\text{A})$	$0.104 - 0.129$	~ 0.5		~ 1.0
W/h(predicted)(GHz)	$0.048 - 0.059$	~ 0.16		0.05
W/h(measured)(GHz)		~ 0.25	2.6	1.4
T_{eff}(mK)[8]	20	20	21	53
ηg[29]	6.8×10^{-6}	$\sim 5 \times 10^{-5}$		~ 0.065[290]

Table 6.2: Comparison of noise parameters used for simulation in this work and other work using flux qubits for quantum annealing.

values give reasonable agreement with the qubit T_1 relaxation times we have measured. In Table 6.2, we also provide these numbers in terms of the dimensionless coupling constant η that is often discussed in spin-boson literature. We also want to note that the simulation result is largely unchanged if the ohmic component of the noise spectrum is not included.

6.6.1 Effect of X-noise coupling

In the master equation simulations, noise from Φ_x is not included. This is justified based on three considerations. Firstly, the noise power of Φ_x is less than half the noise power in Φ_z. Secondly, as plotted in Figure. 6.10, the matrix elements of the flux operators between the circuit energy eigenstates $\langle\alpha|\partial H/\partial\Phi_x|\beta\rangle$ is smaller than $\langle\alpha|\partial H/\partial\Phi_z|\beta\rangle$ by a factor of 50. Finally, Φ_x noise only primarily leads to transverse noise assuming small Φ_x and small x loop junction asymmetry. Previous studies suggested that for transverse noise to have similar dissipative effects, its coupling strength needs to be at least about 1/10 of the longitudinal noise [325]; this condition is far from being satisfied in our case.

[5] The numbers are based on Ref. [235].

[6] The numbers are based on Ref. [309] where the LZ experiment is performed.

[7] The numbers are based on Refs. [203, 290].

[8] This is the effective temperature that describes the MRT data assuming low-frequency noise is at thermal equilibrium.

[9] ηg^2 is defined such that, the system bath coupling is given as $gA \otimes B$, where A, B are norm-1 system and bath operators respectively and the noise PSD of B is given as $S(\omega) = 2\pi\eta\hbar^2\omega\frac{\exp(-|\omega|/\omega_c)}{1-\exp(-\beta\hbar\omega)}$. See for example Ref. [77] for more details.

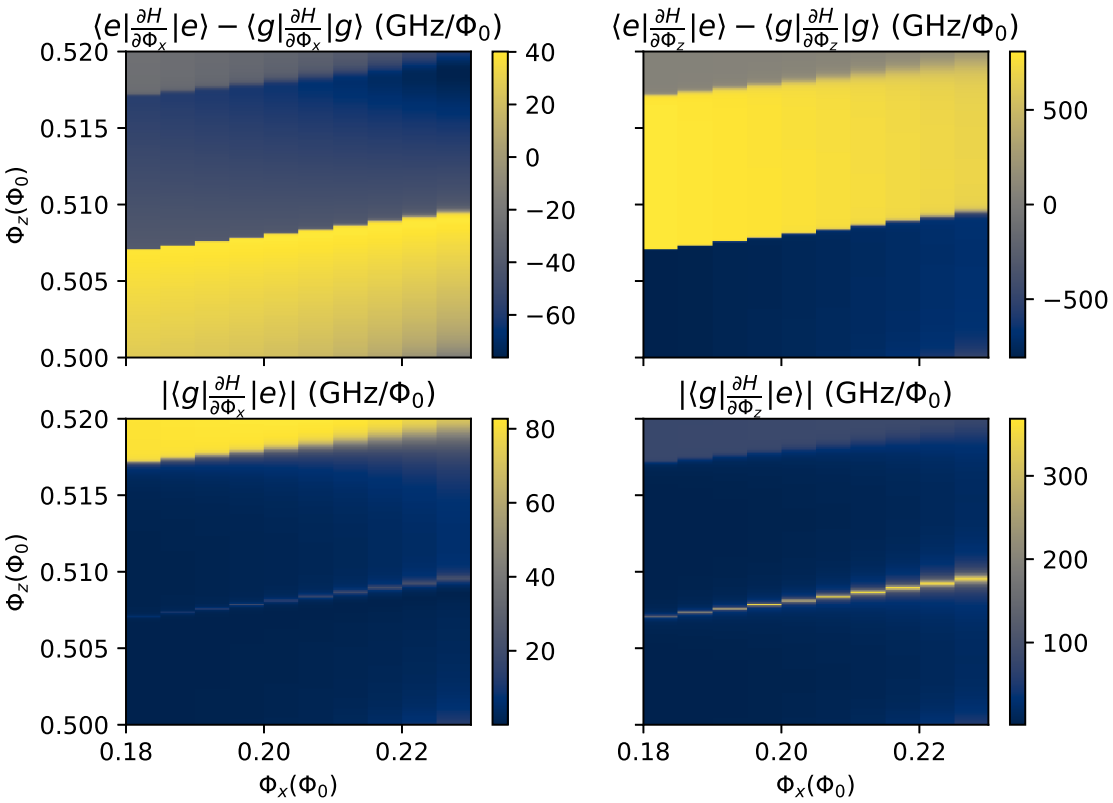

Figure 6.10: Matrix elements for the x and z flux biases

6.6.2 Adiabatic master equation (AME)

In order to implement in AME the noise PSD in Eq. (6.21), additional low- and high-frequency cutoffs ω_l and ω_h are added to avoid divergence. This introduces $S_{\Phi_z}^{\mathrm{AME}}$, the PSD used in AME simulations, defined as

$$S_{\Phi_z}^{\mathrm{AME}} = \begin{cases} S_{\Phi_z,1/\mathrm{f}}(\omega)\exp\left(\frac{-|\omega|}{\omega_h}\right) + S_{\Phi_z,\mathrm{ohmic}}(\omega)\exp\left(\frac{-|\omega|}{\omega_h}\right) & |\omega| > \omega_l \\ S_{\Phi_z,1/\mathrm{f}}(\omega_l)\exp\left(\frac{-|\omega_l|}{\omega_h}\right) + S_{\Phi_z,\mathrm{ohmic}}(\omega)\exp\left(\frac{-|\omega|}{\omega_h}\right) & |\omega| \leq \omega_l. \end{cases} \tag{6.27}$$

The high-frequency cutoff is chosen to be $\omega_h/2\pi = 10$GHz, which is roughly the characteristic oscillation frequency in either of the qubit potential wells. For the low-frequency cutoff, given that we are primarily concerned with thermalization effects, we choose $\omega_l/2\pi=$ 10MHz, which corresponds to the minimum qubit frequency for the LZ measurement presented in this work.

6.6.3 Polaron-transformed master equation (PTRE)

In the PTRE simulation, the noise model consists of an ohmic noise just as in AME, and the 1/f noise is represented by the MRT parameters W and ϵ_p [308]. The MRT width W characterizes the integrated effect of the symmetrized low-frequency noise,

$$W^2 = 2I_p^2 \int_{\omega_{\mathrm{low}}}^{\omega_{\mathrm{high}}} \frac{d\omega}{2\pi} S^{+}_{\Phi_z,1/\mathrm{f}}(\omega). \tag{6.28}$$

The anti-symmetrized low frequency noise $S^{-}_{\Phi_z,1/\mathrm{f}}(\omega) = 1/2(S_{\Phi_z,1/\mathrm{f}}(\omega) - S_{\Phi_z,1/\mathrm{f}}(-\omega))$ gives the reorganization energy ϵ_p

$$\epsilon_p = 2I_p^2 \int_{\omega_{\mathrm{low}}}^{\omega_{\mathrm{high}}} \frac{d\omega}{2\pi} \frac{S^{-}_{\Phi_z,1/\mathrm{f}}(\omega)}{\hbar\omega}. \tag{6.29}$$

For the integration limit, we choose $\omega_{\mathrm{low}}/2\pi = 4\,\mathrm{Hz}$ based on the experiment time taken for all the repetitions at each Φ_x and T_{LZ}, and $\omega_{\mathrm{high}}/2\pi = 10\,\mathrm{GHz}$ based on the characteristic oscillation frequency in the qubit potential wells. We assume that the low-frequency noise is in thermal equilibrium, which relates W and ϵ_p via the fluctuation-dissipation theorem,

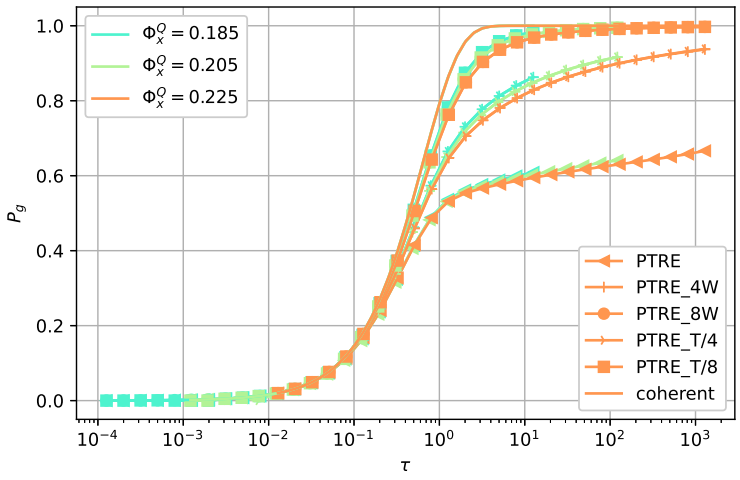

Figure 6.11: Final ground state probabilities versus the dimensionless sweep time $\tau = \Delta^2/\hbar v$ for different PTRE parameters.

$W^2 = 2k_BT\epsilon_p$. We also note that 1/f noise has a significant contribution to the noise power at high frequency, up to around 1 GHz. This contribution breaks the normalization condition for the high-frequency noise in the current numerical implementation of PTRE (see discussion around Eq. [16] of Ref. [318]). The effect of the high-frequency component of 1/f noise in the strong coupling limit is to be explored in future work.

As discussed in Sec. 6.2, the values of W or T need to be adjusted for better agreement between PTRE simulation and the experiment data at low Φ_x. The results are shown in Figure 6.11. Interestingly, it is found that increasing W by 4(8) times is equivalent to decreasing T by 4(8) times. This indicates that the ratio ϵ/W is most critical to the result, with increasing ϵ_p/W leading to closer to the coherent limit of the ground state population.

6.6.4 Symmetric versus asymmetric LZ Sweep

As discussed in Section 6.5.2, the screening current in the rf-SQUID leads to an effective bias to the qubit z loop. Due to an initial inaccurate estimation of this effect, the LZ data presented in Sec. 6.2 has an asymmetric scan range, with initial and final z loop bias being $\Phi_{z,\text{init}} = -3.1 \times 10^{-3}\Phi_0$ and $\Phi_{z,\text{final}} = 6.9 \times 10^{-3}\Phi_0$. This was later identified via the spectroscopy method mentioned in Section 6.5.2, but leaving insufficient time to repeat the full range of LZ experiments. However, with this asymmetric scan range, the

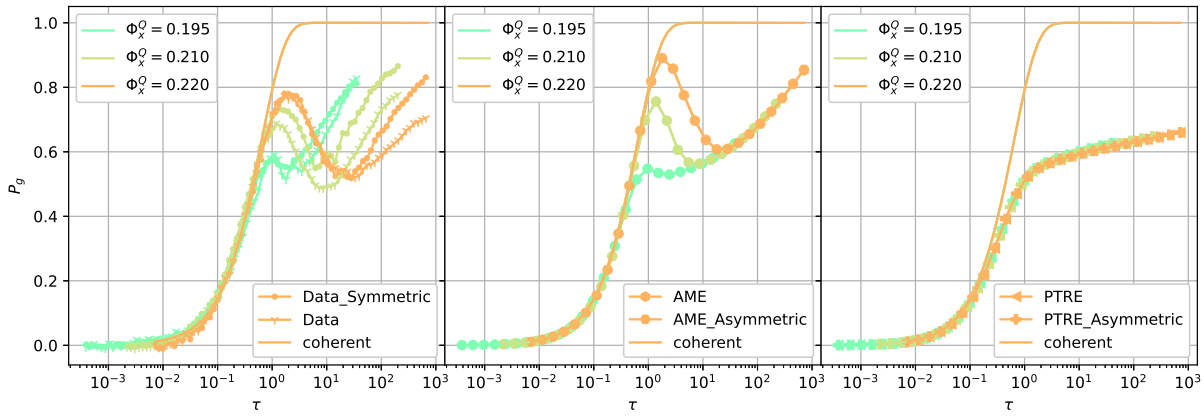

Figure 6.12: Final ground state probabilities comparing the symmetric and asymmetric sweep around Φ_z symmetry point, for experiment data on the left panel, AME simulation on the center panel and PTRE simulation on the right panel. The simulated results use the nominal noise parameters discussed in Sec. 6.6 and the symmetric and asymmetric sweep overlap. The experiment data presented in Sec. 6.2 is asymmetric in range and the simulated data is symmetric in range.

validity of the LZ model is not affected, since the initial and final longitudinal fields are still much larger than the tunneling amplitude. In Figure 6.12, we compare the measured and simulated results for symmetric and asymmetric Φ_z sweep range. The experiment data show some differences but the qualitative features discussed in Sec. 6.2 remain the same. In particular, the symmetric data also show that as Φ_x decreases, P_g becomes closer to the coherent limit behavior. The simulated results using either AME or PTRE for the symmetric and asymmetric sweep range do not differ significantly.

6.7 Additional details on the spin bath model

Given the Markovian master equations, AME and PTRE failed to capture the crossover from the weak to strong coupling limit in the experiment data, it is natural to ask whether this crossover can be captured by simulating the experiment incorporating an explicit quantum environment. The spin bath is a natural choice for this quantum environment. First, the dominant noise in the experiment, 1/f flux noise, has long been thought to originate from either clusters of coupled spins or randomly distributed two-level systems, which are also essentially spins. Second, spins ferromagnetically coupled to the qubit offer

an intuitive picture of the MRT phenomenon, a canonical example of the strong coupling limit. The non-zero expectation of the spins' polarization acts as an environmental bias to the qubit, resembling the reorganization energy in MRT. Fluctuations of this polarization due to the internal dynamics of the spins effectively dephase and broaden the longitudinal bias seen by the qubit, analogous to the MRT width.

6.7.1 Single spin

The simplest toy model for a quantum environment coupled to the system is a single spin ferromagnetically coupled to the system qubit, with an additional bath that causes depolarization of the spin. This system can be described by the Hamiltonian

$$H = H_q + H_{qb} + H_{qS} + H_{SB} + H_S + H_b + H_B, \tag{6.30}$$
$$H_{qb} = I_p \sigma_z Q_{\Phi_z}, \tag{6.31}$$
$$H_{qS} = J \sigma_z \tau_z, \tag{6.32}$$
$$H_S = 0, \tag{6.33}$$
$$H_{SB} = \tau_x Q', \tag{6.34}$$
$$S_{Q_{\Phi_z}}(\omega) = S^{\mathrm{AME}}_{\Phi_z}(\omega) \text{ and} \tag{6.35}$$
$$S_{Q'}(\omega) = \hbar^2 \lambda \frac{1}{1 + \exp\left(-\beta\hbar\omega\right)} \exp\left(-\frac{\omega}{\omega_c}\right), \tag{6.36}$$

where N_s is the total number of spins in the bath. The model Hamiltonian is understood as follows. First, the high-frequency, Markovian part of the noise is captured by the noise PSD used in the previous AME simulation. On top of this, a single spin is added to capture the effect of a strong low-frequency noise. The qubit is ferromagnetically coupled to the spin with coupling strength J. The environmental spin does not have internal dynamics, but it is transversely coupled to its own environment. This environment is nearly a white noise, but with the induced relaxation and excitation rate of the spin satisfying detailed balance. The strength of this noise λ is essentially the depolarization rate of the spin, in the limit where the qubit-spin coupling approaches zero. Similar to the noise PSD describing the environment of the qubit, the noise PSD for the environment of the spin also has an exponential cutoff, the role of which is essentially to ensure numerical convergence.

Next, assuming the temperature and the cutoff frequency of the spin's environment are the same as the qubit's environment, there are only two parameters to the model, the coupling strength J and the free spin depolarization rate λ. We numerically simulate the LZ experiment with the above model, initializing the system in the ground state (initialization

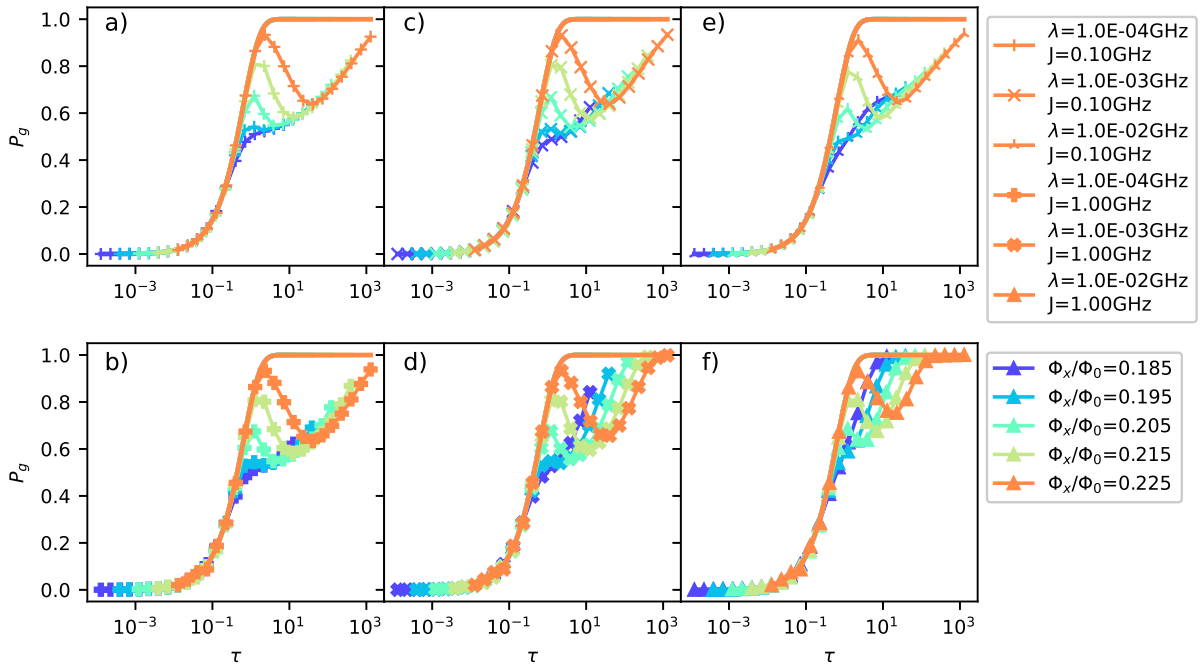

Figure 6.13: Final ground state probabilities versus the dimensionless sweep time τ, using the single spin bath model (see text). Parameters for the single spin are $\lambda = 0.0001, 0.001, 0.01$ GHz from left to right and $J/h = 0.1(1.0)$ GHz on the top(bottom).

in the thermal state doesn't give significant changes to the result). The result is shown in Fig. 6.13, with a range of J and λ taken in geometric steps. It can be seen that for small J and λ, the result of the single spin bath model is almost the same as the qubit AME result. This can be understood from two perspectives. First, small λ corresponds to the spin being nearly coherent and has no dynamics. Therefore its effect is to merely shift the location of the anticrossing to $\epsilon + 2J = 0$. Second, for small J, the thermal equilibrium state of the spin always has its polarization $\langle \tau_z \rangle \approx 0$, irrespective of the qubit state. Therefore it has a negligible impact on the qubit. As λ and J increase the spin bath model predicts a behavior that closely resembles the experimental data. For large Φ_x, the single spin bath model simulated ground state probably has a non-monotonic dependence versus LZ sweep time, but as Φ_x decreases, the dependence becomes monotonic and approaches the coherent limit. Among the parameters simulated, there is a good qualitative agreement between the simulated and experiment data for $\lambda = 0.001$ GHz and $J/h = 1.0$ GHz.

Further insight into the model can be obtained by looking at the instantaneous state

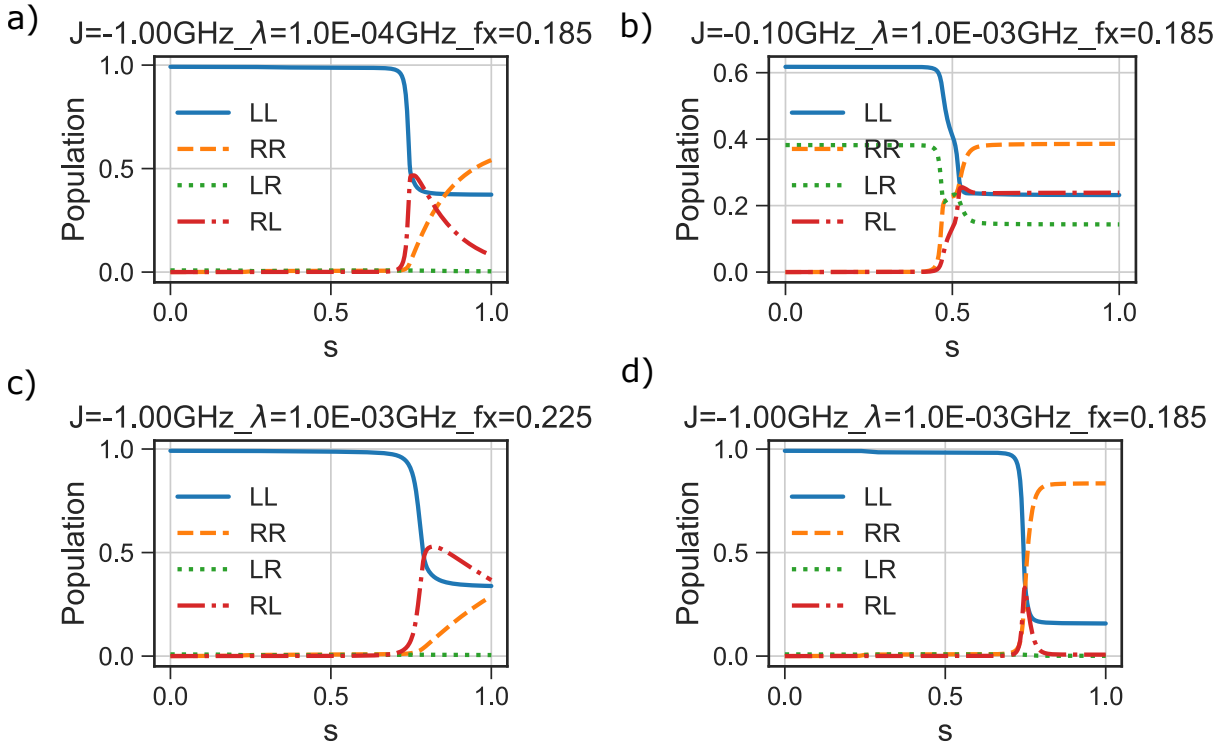

Figure 6.14: Evolution of the instantaneous qubit and spin states as a function of the normalized time $s \in [0, 1]$, for different parameters of the qubit and the spin.

probabilities, which are shown in Fig. 6.14. First, when λ is small (Fig. 6.13(a)), the spin is nearly coherent and simply adds an additional bias J to the qubit. This effectively shifts the position of the anti-crossing seen by the qubit, but does not change the final ground state probabilities, as long as J is well within the initial and final Z bias of the qubit. For small J such that $\beta|J| \ll 1$(Fig. 6.13(b)), the thermal average of the spin's polarization is almost always close to zero, regardless of the state of the qubit, or the depolarization rate λ, Therefore the spin has a negligible effect on the qubit.

Finally, for $\beta J \gtrsim 1$, a qualitative difference arises for small and large Δ. When Δ is large (Fig. 6.13(c)), the qubit completes the tunneling before the spin has time to re-align with the qubit. Therefore the qubit sees a static effective bias due to the spin, which allows thermalization to happen across the energy eigenstates of the qubit near the anti-crossing. This leads to a local minimum of ground state probability $P_g \approx 0.5$ as sweep time increases. However, when Δ is small (Fig. 6.13(d)), the spin quickly relaxes to the

opposite state, following the qubit. After the spin has relaxed, the qubit effectively sees a Z bias of $-2J$, which suppresses thermalization induced by the qubit's own environment. Therefore for small Δ, as the sweep time increases, ground state probability no longer has a local minimum around 0.5.

6.7.2 Multiple spins

A general spin bath has a large parameter space, such as the distribution of their longitudinal and transverse fields, the distribution of couplings among them, and the distribution of couplings of them to their respective environments. While some of these parameters can be motivated based on plausible models of flux noise, these models often assume a macroscopic number of spins, and it is not clear whether they have an efficient numerical representation [321, 322]. Given this complexity, we leave it as future work to systematically explore the parameters of the spin bath and its relation to the physical 1/f flux noise. In this work, we adopt a simplified approach which can be seen as a quantum extension of simulating classical 1/f noise with two-level fluctuators [328].

In the multi-spin model, the Hamiltonian changes from the single-spin model by making the changes given by

$$H_{qS} = \sum_{i}^{N_s} J_i \sigma_z \tau_{z,i}, \tag{6.37}$$

$$H_{SB} = \sum_{i}^{N_s} \tau_{x,i} Q'_i, \text{ and} \tag{6.38}$$

$$S_{Q'_i}(\omega) = \hbar^2 \lambda_i \frac{1}{1+\exp\left(-\beta\hbar\omega\right)} \exp\left(-\frac{\omega}{\omega_c}\right). \tag{6.39}$$

The spin bath parameters J_i and λ_i can be chosen based on the measured 1/f flux noise strength. To see this, we first consider the large N_s, weak coupling limit, where the effect of the spin bath can be well captured by the noise PSD. Following Refs. [321, 329], the symmetrized noise PSD of the i'th spin is

$$S_i(\omega) = (1 - \langle \tau_i \rangle) \frac{2\gamma_i J_i^2}{\omega^2 + \gamma_i^2}, \tag{6.40}$$

where $\langle \tau_i \rangle$ is the expectation value of spin i's longitudinal polarization, and γ_i is its depolarization rate. In general, the expectation value and the depolarization rate depend on

the instantaneous qubit Hamiltonian. However, for a small enough coupling between the qubit and the spin, the effect of the qubit on the spin is an effective longitudinal bias with strength, $-J_i\langle\sigma_z\rangle/2$. In this case, the expectation value and the depolarization rate are

$$\langle\tau_i\rangle = \tanh\left(\beta\langle\sigma_z\rangle J_i\right), \tag{6.41}$$

$$\gamma_i = \lambda_i \exp\left(-\beta|J_i|\langle\sigma_z\rangle\right). \tag{6.42}$$

Then to obtain 1/f like noise with exponent α, we assume that the distribution of λ for all the spins is given by

$$P_\lambda(\lambda) = \frac{1}{N_\lambda}\frac{1}{\lambda^\alpha}, \tag{6.43}$$

$$N_\lambda = \left(\frac{1}{-\alpha+1}\right)\left(\lambda_{\max}^{-\alpha+1} - \lambda_{\min}^{-\alpha+1}\right), \tag{6.44}$$

where $\lambda_{\min}, \lambda_{\max}$ can be chosen based on the frequency range of the noise PSD that we are interested in simulating. For simplicity, we also assume that the ferromagnetic coupling is constant for all spins, $J_i = J$. Then the collective noise PSD of the spin bath is

$$S_S(\omega) = N_s(1-\langle\tau\rangle)\int_{\lambda_{\min}}^{\lambda_{\max}} P_\lambda(\lambda)\frac{2\gamma_i(\lambda)J^2}{\omega^2+\gamma^2(\lambda)} \tag{6.45}$$

$$= (1-\langle\tau\rangle)\frac{N_s J^2}{N_\lambda}c^{\alpha-1}\frac{1}{\omega^\alpha}\mathcal{I} \tag{6.46}$$

where we have introduced

$$\langle\tau\rangle = \tanh\left(\beta\langle\sigma_z\rangle J_i\right) \tag{6.47}$$

$$c = \exp(-\beta|J_i|) \tag{6.48}$$

$$\mathcal{I} = \int_{c\lambda_{\min}/\omega}^{c\lambda_{\max}/\omega} \frac{x^{1-\alpha}}{1+x^2}dx, \tag{6.49}$$

and $x = c\lambda$. We can notice that for $\beta J \to 0$, the J dependence of the noise PSD primarily comes from the J^2 term. This allows us to set J based on the measured flux noise power. Comparing $S_S(\omega)$ with the symmetrized flux noise power we have

$$J = \sqrt{\frac{A_{\Phi_z}^* N_\lambda}{\mathcal{I} N_s}} I_p. \tag{6.50}$$

In the above expression, the integral $\mathcal{I}$ can evaluate at a typical ω in between $\lambda_{\max}$ and $\lambda_{\min}$, and it is always close to 1.

To confirm the intuition that the spin bath captures the MRT parameters, we can compare the following two expressions. First, from the fluctuation-dissipation theorem and the definition of MRT width using symmetrized noise PSD in Eq. 6.28, we have

$$\epsilon_p = \frac{\beta}{2} W^2 \tag{6.51}$$

$$= \beta I_p^2 A_{\Phi_z}^* \frac{1}{-\alpha+1} \left[\left(\frac{\omega_{\text{high}}}{2\pi} \right)^{-\alpha+1} - \left(\frac{\omega_{\text{low}}}{2\pi} \right)^{-\alpha+1} \right]. \tag{6.52}$$

On the other hand, the effective bias applied to the qubit by the spin bath is

$$N_s J \tanh \beta J \approx N_s \beta J^2 \tag{6.53}$$

$$= \beta A_{\Phi_z}^8 I_p^2 \frac{1}{\mathcal{I}} \frac{1}{-\alpha+1} \left[\left(\frac{\lambda_{\text{high}}}{2\pi} \right)^{-\alpha+1} - \left(\frac{\lambda_{\text{low}}}{2\pi} \right)^{-\alpha+1} \right]. \tag{6.54}$$

Therefore, if we choose $\lambda_{\text{max}} \gtrsim \omega_{\text{max}}$ and $\lambda_{\text{min}} \lesssim \omega_{\text{min}}$, these two expressions, Eq. 6.52 and 6.54 indeed match each other, up to a constant $\mathcal{I}$ that is close to unity.

As mentioned in Sec. 6.7, when the low-frequency noise is not large enough, the spin bath simulation results closely resemble that of the single-qubit AME. This is exemplified in Fig. 6.15, where the spin bath parameters are chosen to target an $1/f^\alpha$ noise spectrum with the same amplitude as deduced from the decoherence measurements, therefore being 8 times smaller than the simulation presented in Sec. 6.7.

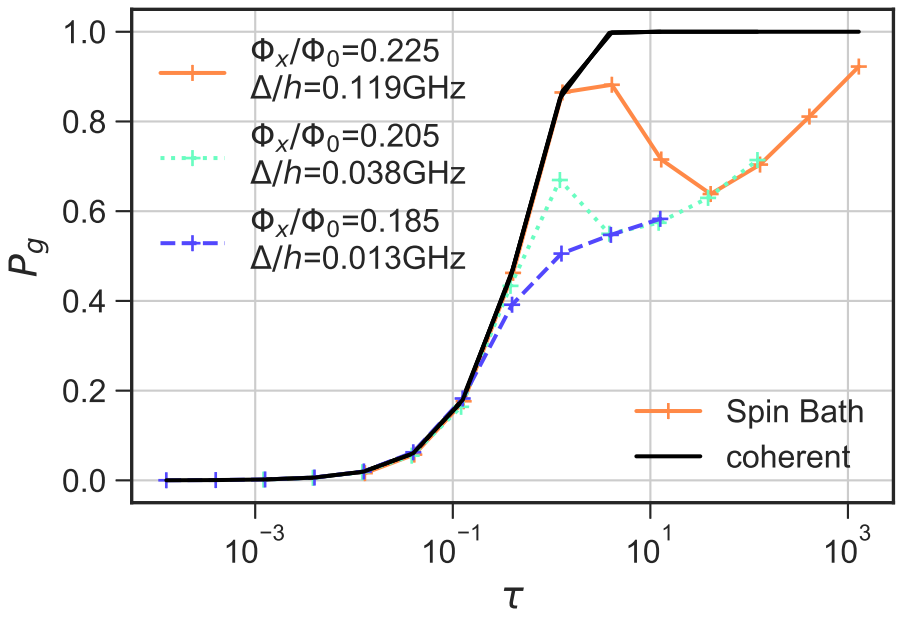

Figure 6.15: Simulated LZ final ground state probabilities versus the dimensionless sweep time τ for different Φ_x or Δ, using the spin bath model, with 3 spins and targeting the nominal $1/f$ noise amplitude.

Chapter 7

Conclusion

We have studied components of a quantum annealer based on capacitively-shunted flux qubits and tunable rf-SQUID couplers. This new architecture has two essential features. First, the qubits and couplers have individual bias lines that in principle allow annealing in the nanosecond timescale, with independent control of each qubit and coupler. Second, the CSFQs have coherence times on the order of hundreds of nanoseconds. These two features combined together open the possibility of exploring high-coherence, high control flexibility annealing, beyond the capabilities of commercially available quantum annealers.

Realizing a highly-controllable annealer requires careful calibration of control crosstalk, which is challenging for the strongly interacting circuits studied here. This is tackled by the two crosstalk calibration methods presented in Chapter 3 of this thesis. We have demonstrated these methods on superconducting flux circuits with various sizes. The accuracies of these methods are comparable to contemporary gate-model devices, and also approach the lower bound posed by fluctuations due to intrinsic flux noise. An important future direction on crosstalk calibration is to address the frequency-dependence of crosstalk, which is relevant for high-bandwidth control of the annealing schedule.

Long-range and high-degree connectivity is another desired quality in a quantum annealer. In Chapter. 4 we presented a device made of a chain of couplers, used to realize long-range coupling between flux qubits without degrading qubit coherence. Susceptibility measurements were performed, showing that the coupler chain can indeed support effective coupling between qubits at the two ends of the chain, even considering realistic fluctuations due to flux noise. A relevant next step is to demonstrate the effective qubit coupling through coherent driving, and characterize the qubit coherence as a function of chain size and coupling strength.

There is little doubt that improving coherence is beneficial in harnessing the quantum advantage. However, the role of noise and coherence in quantum annealing is not so clear, especially going beyond the weak coupling limit of the system and the environment. In Chapter. 5 we measure and model the coherence times of a single CSFQ designed for annealing. While the concept of coherence time is in general not well defined for an annealer, these measurements allow us to characterize the dominant noise channel in the system, which is intrinsic 1/f flux noise. The coherence times measured also serve as a useful benchmark when considering future improvements to annealing-compatible qubits, for example a tunable fluxonium. In Chapter. 6 we extrapolate these measured noise strengths to interpret the Landau-Zener tunneling measurement for the CSFQ. Landau-Zener tunneling is a toy model for a large annealer going through its minimum gap, and by tuning the minimum gap, it allows going beyond the weak-coupling limit of system-environment coupling in a controllable manner. The measurement result confirms previous predictions and experiments in the weak and strong coupling limits.

The experiment also reveals the cross-over regime of weak to strong coupling, which has not been explored before in either theory or experiments. We proposed a phenomenological quantum spin bath model, which we have numerically simulated and found qualitative agreement with the experiment results. The spin bath hints at an important concept that needs to be further studied, that is the timescale over which the bath reorganizes itself as the system tunnels to a new state. Further experiments, for example repeated Landau-Zener crossings are needed to systematically explore this concept and further validate the spin bath model. A better understanding in this respect could lead to novel protocols that evade noise and speed up quantum tunneling, bringing us closer to solving optimization problems with a quantum speedup.

References

[1] Jonathan P. Dowling and Gerard J. Milburn. Quantum Technology: The Second Quantum Revolution. *Philosophical Transactions: Mathematical, Physical and Engineering Sciences*, 361(1809):1655–1674, 2003.

[2] Iulia Georgescu. Nobel Prize 2012: Haroche & Wineland. *Nature Physics*, 8(11):777–777, November 2012.

[3] R. Alléaume, C. Branciard, J. Bouda, T. Debuisschert, M. Dianati, N. Gisin, M. Godfrey, P. Grangier, T. Länger, N. Lütkenhaus, C. Monyk, P. Painchault, M. Peev, A. Poppe, T. Pornin, J. Rarity, R. Renner, G. Ribordy, M. Riguidel, L. Salvail, A. Shields, H. Weinfurter, and A. Zeilinger. Using quantum key distribution for cryptographic purposes: A survey. *Theoretical Computer Science*, 560:62–81, December 2014.

[4] C. L. Degen, F. Reinhard, and P. Cappellaro. Quantum sensing. *Reviews of Modern Physics*, 89(3):035002, July 2017.

[5] Michael A. Nielsen and Isaac L. Chuang. *Quantum Computation and Quantum Information*. Cambridge University Press, Cambridge ; New York, 10th anniversary ed edition, 2010.

[6] Richard P. Feynman. Simulating physics with computers. *International Journal of Theoretical Physics*, 21(6):467–488, June 1982.

[7] David Deutsch and Richard Jozsa. Rapid Solution of Problems by Quantum Computation. *Proceedings: Mathematical and Physical Sciences*, 439(1907):553–558, 1992.

[8] Lov K. Grover. A fast quantum mechanical algorithm for database search. In *Proceedings of the Twenty-Eighth Annual ACM Symposium on Theory of Computing*, STOC '96, pages 212–219, New York, NY, USA, July 1996. Association for Computing Machinery.

[9] Peter W. Shor. Polynomial-Time Algorithms for Prime Factorization and Discrete Logarithms on a Quantum Computer. *SIAM Journal on Computing*, 26(5):1484–1509, October 1997.

[10] Jérémie Roland and Nicolas J. Cerf. Quantum search by local adiabatic evolution. *Physical Review A*, 65(4):042308, March 2002.

[11] Aram W. Harrow, Avinatan Hassidim, and Seth Lloyd. Quantum Algorithm for Linear Systems of Equations. *Physical Review Letters*, 103(15):150502, October 2009.

[12] Ashley Montanaro. Quantum algorithms: An overview. *npj Quantum Information*, 2(1):1–8, January 2016.

[13] P.W. Shor. Algorithms for quantum computation: Discrete logarithms and factoring. In *Proceedings 35th Annual Symposium on Foundations of Computer Science*, pages 124–134, November 1994.

[14] H. J. Briegel, D. E. Browne, W. Dür, R. Raussendorf, and M. Van den Nest. Measurement-based quantum computation. *Nature Physics*, 5(1):19–26, January 2009.

[15] David Elieser Deutsch and Roger Penrose. Quantum computational networks. *Proceedings of the Royal Society of London. A. Mathematical and Physical Sciences*, 425(1868):73–90, 1989.

[16] Tameem Albash and Daniel A. Lidar. Adiabatic quantum computation. *Reviews of Modern Physics*, 90(1):015002, January 2018.

[17] Dorit Aharonov, Wim van Dam, Julia Kempe, Zeph Landau, Seth Lloyd, and Oded Regev. Adiabatic Quantum Computation Is Equivalent to Standard Quantum Computation. *SIAM Rev.*, 50:755–787, November 2008.

[18] B. Apolloni, C. Carvalho, and D. de Falco. Quantum stochastic optimization. *Stochastic Processes and their Applications*, 33(2):233–244, December 1989.

[19] A. B. Finnila, M. A. Gomez, C. Sebenik, C. Stenson, and J. D. Doll. Quantum annealing: A new method for minimizing multidimensional functions. *Chemical Physics Letters*, 219:343–348, November 1993.

[20] Tadashi Kadowaki and Hidetoshi Nishimori. Quantum annealing in the transverse Ising model. *Phys. Rev. E*, 58(5):5355–5363, 1998.

[21] S. Kirkpatrick, C. D. Gelatt, and M. P. Vecchi. Optimization by Simulated Annealing. *Science*, 220(4598):671–680, May 1983.

[22] Morten Kjaergaard, Mollie E. Schwartz, Jochen Braumüller, Philip Krantz, Joel I.-J. Wang, Simon Gustavsson, and William D. Oliver. Superconducting Qubits: Current State of Play. *Annual Review of Condensed Matter Physics*, 11(1):369–395, March 2020.

[23] Lieven M. K. Vandersypen and Mark A. Eriksson. Quantum computing with semiconductor spins. *Physics Today*, 72(8):38–45, August 2019.

[24] Colin D. Bruzewicz, John Chiaverini, Robert McConnell, and Jeremy M. Sage. Trapped-ion quantum computing: Progress and challenges. *Applied Physics Reviews*, 6(2):021314, June 2019.

[25] Fulvio Flamini, Nicolò Spagnolo, and Fabio Sciarrino. Photonic quantum information processing: A review. *Reports on Progress in Physics*, 82(1):016001, November 2018.

[26] M. Saffman, T. G. Walker, and K. Mølmer. Quantum information with Rydberg atoms. *Reviews of Modern Physics*, 82(3):2313–2363, August 2010.

[27] John Clarke and Frank K. Wilhelm. Superconducting quantum bits. *Nature*, 453(7198):1031–1042, June 2008.

[28] Y. Nakamura, Yu A. Pashkin, and J. S. Tsai. Coherent control of macroscopic quantum states in a single-Cooper-pair box. *Nature*, 398(6730):786–788, April 1999.

[29] Frank Arute, Kunal Arya, Ryan Babbush, Dave Bacon, Joseph C. Bardin, Rami Barends, Rupak Biswas, Sergio Boixo, Fernando G. S. L. Brandao, David A. Buell, et al. Quantum supremacy using a programmable superconducting processor. *Nature*, 574(7779):505–510, October 2019.

[30] Philipp Hauke, Helmut G. Katzgraber, Wolfgang Lechner, Hidetoshi Nishimori, and William D. Oliver. Perspectives of quantum annealing: Methods and implementations. *Reports on Progress in Physics*, 83(5):054401, May 2020.

[31] QPU-Specific Characteristics — D-Wave System Documentation documentation. https://docs.dwavesys.com/docs/latest/doc_physical_properties.html#doc-qpu-characteristics.

[32] E. J. Crosson and D. A. Lidar. Prospects for quantum enhancement with diabatic quantum annealing. *Nature Reviews Physics*, 3(7):466–489, July 2021.

[33] Atanu Rajak, Sei Suzuki, Amit Dutta, and Bikas K. Chakrabarti. Quantum annealing: An overview. *Philosophical Transactions of the Royal Society A: Mathematical, Physical and Engineering Sciences*, 381(2241):20210417, December 2022.

[34] J. Bardeen, L. N. Cooper, and J. R. Schrieffer. Microscopic Theory of Superconductivity. *Physical Review*, 106(1):162–164, April 1957.

[35] J. Bardeen, L. N. Cooper, and J. R. Schrieffer. Theory of Superconductivity. *Physical Review*, 108(5):1175–1204, December 1957.

[36] B. D. Josephson. Possible new effects in superconductive tunnelling. *Physics Letters*, 1(7):251–253, July 1962.

[37] Juan José García Ripoll. *Quantum Information and Quantum Optics with Superconducting Circuits*. Cambridge University Press, first edition, July 2022.

[38] M.H. Devoret. *Quantum Fluctuations in Electrical Circuits*. Edition de Physique, France, 1997.

[39] Guido Burkard, Roger H. Koch, and David P. DiVincenzo. Multilevel quantum description of decoherence in superconducting qubits. *Physical Review B*, 69(6):064503, February 2004.

[40] Andrew J. Kerman. Efficient numerical simulation of complex Josephson quantum circuits. *arXiv:2010.14929 [quant-ph]*, October 2020.

[41] Simon E. Nigg, Hanhee Paik, Brian Vlastakis, Gerhard Kirchmair, S. Shankar, Luigi Frunzio, M. H. Devoret, R. J. Schoelkopf, and S. M. Girvin. Black-Box Superconducting Circuit Quantization. *Physical Review Letters*, 108(24):240502, June 2012.

[42] Zlatko K. Minev, Zaki Leghtas, Shantanu O. Mundhada, Lysander Christakis, Ioan M. Pop, and Michel H. Devoret. Energy-participation quantization of Josephson circuits. *npj Quantum Information*, 7(1):1–11, August 2021.

[43] F. London and H. London. The electromagnetic equations of the supraconductor — Proceedings of the Royal Society of London. Series A - Mathematical and Physical Sciences. *Proceedings of the Royal Society of London. Series A - Mathematical and Physical Sciences*, 149(866):71, 1935.

[44] Bascom S. Deaver and William M. Fairbank. Experimental Evidence for Quantized Flux in Superconducting Cylinders. *Physical Review Letters*, 7(2):43–46, July 1961.

[45] T. P. Orlando, J. E. Mooij, Lin Tian, Caspar H. van der Wal, L. S. Levitov, Seth Lloyd, and J. J. Mazo. Superconducting persistent-current qubit. *Physical Review B*, 60(22):15398–15413, December 1999.

[46] J. E. Mooij, T. P. Orlando, L. Levitov, Lin Tian, Caspar H. van der Wal, and Seth Lloyd. Josephson Persistent-Current Qubit. *Science*, 285(5430):1036–1039, August 1999.

[47] David J. Griffiths and Darrell F. Schroeter. *Introduction to Quantum Mechanics*. Cambridge University Press, 3 edition, 2018.

[48] Fei Yan, Simon Gustavsson, Archana Kamal, Jeffrey Birenbaum, Adam P. Sears, David Hover, Ted J. Gudmundsen, Danna Rosenberg, Gabriel Samach, S. Weber, Jonilyn L. Yoder, Terry P. Orlando, John Clarke, Andrew J. Kerman, and William D. Oliver. The flux qubit revisited to enhance coherence and reproducibility. *Nat. Commun*, 7:12964, November 2016.

[49] Jonathan R. Friedman, Vijay Patel, W. Chen, S. K. Tolpygo, and J. E. Lukens. Quantum superposition of distinct macroscopic states. *Nature*, 406(6791):43–46, July 2000.

[50] R. Harris, J. Johansson, A. J. Berkley, M. W. Johnson, T. Lanting, Siyuan Han, P. Bunyk, E. Ladizinsky, T. Oh, I. Perminov, E. Tolkacheva, S. Uchaikin, E. M. Chapple, C. Enderud, C. Rich, M. Thom, J. Wang, B. Wilson, and G. Rose. Experimental demonstration of a robust and scalable flux qubit. *Phys. Rev. B*, 81(13):134510, April 2010.

[51] Vladimir E. Manucharyan, Jens Koch, Leonid I. Glazman, and Michel H. Devoret. Fluxonium: Single Cooper-Pair Circuit Free of Charge Offsets. *Science*, 326(5949):113–116, October 2009.

[52] Aaron Somoroff, Quentin Ficheux, Raymond A. Mencia, Haonan Xiong, Roman V. Kuzmin, and Vladimir E. Manucharyan. Millisecond coherence in a superconducting qubit. *arXiv:2103.08578 [cond-mat, physics:quant-ph]*, March 2021.

[53] S. H. W. van der Ploeg, A. Izmalkov, Alec Maassen van den Brink, U. Hübner, M. Grajcar, E. Il'ichev, H.-G. Meyer, and A. M. Zagoskin. Controllable Coupling of Superconducting Flux Qubits. *Physical Review Letters*, 98(5):057004, February 2007.

[54] R. Harris, A. J. Berkley, M. W. Johnson, P. Bunyk, S. Govorkov, M. C. Thom, S. Uchaikin, A. B. Wilson, J. Chung, E. Holtham, J. D. Biamonte, A. Yu. Smirnov, M. H. S. Amin, and Alec Maassen van den Brink. Sign- and Magnitude-Tunable Coupler for Superconducting Flux Qubits. *Physical Review Letters*, 98(17):177001, April 2007.

[55] R. Harris, T. Lanting, A. J. Berkley, J. Johansson, M. W. Johnson, P. Bunyk, E. Ladizinsky, N. Ladizinsky, T. Oh, and S. Han. Compound Josephson-junction coupler for flux qubits with minimal crosstalk. *Physical Review B*, 80(5):052506, August 2009.

[56] Dvir Kafri, Chris Quintana, Yu Chen, Alireza Shabani, John M. Martinis, and Hartmut Neven. Tunable inductive coupling of superconducting qubits in the strongly nonlinear regime. *Physical Review A*, 95(5):052333, May 2017.

[57] Gioele Consani and Paul A. Warburton. Effective Hamiltonians for interacting superconducting qubits: Local basis reduction and the Schrieffer–Wolff transformation. *New Journal of Physics*, 22(5):053040, May 2020.

[58] Mostafa Khezri, Xi Dai, Rui Yang, Tameem Albash, Adrian Lupascu, and Daniel A. Lidar. Customized Quantum Annealing Schedules. *Physical Review Applied*, 17(4):044005, April 2022.

[59] Caspar H. van der Wal, A. C. J. ter Haar, F. K. Wilhelm, R. N. Schouten, C. J. P. M. Harmans, T. P. Orlando, Seth Lloyd, and J. E. Mooij. Quantum Superposition of Macroscopic Persistent-Current States. *Science*, 290(5492):773–777, October 2000.

[60] A. Lupaşcu, C. J. M. Verwijs, R. N. Schouten, C. J. P. M. Harmans, and J. E. Mooij. Nondestructive Readout for a Superconducting Flux Qubit. *Physical Review Letters*, 93(17), October 2004.

[61] A. Lupaşcu, S. Saito, T. Picot, P. C. de Groot, C. J. P. M. Harmans, and J. E. Mooij. Quantum non-demolition measurement of a superconducting two-level system. *Nature Physics*, 3(2):119–125, February 2007.

[62] Jeffrey A. Grover, James I. Basham, Alexander Marakov, Steven M. Disseler, Robert T. Hinkey, Moe Khalil, Zachary A. Stegen, Thomas Chamberlin, Wade DeGottardi, David J. Clarke, et al. Fast, Lifetime-Preserving Readout for High-Coherence Quantum Annealers. *PRX Quantum*, 1(2):020314, November 2020.

[63] Alexandre Blais, Ren-Shou Huang, Andreas Wallraff, S. M. Girvin, and R. J. Schoelkopf. Cavity quantum electrodynamics for superconducting electrical circuits: An architecture for quantum computation. *Physical Review A*, 69:062320, June 2004.

[64] J.-L. Orgiazzi, C. Deng, D. Layden, R. Marchildon, F. Kitapli, F. Shen, M. Bal, F. R. Ong, and A. Lupascu. Flux qubits in a planar circuit quantum electrodynamics architecture: Quantum control and decoherence. *Physical Review B*, 93(10):104518, March 2016.

[65] Christopher M Quintana. *Superconducting flux qubits for high-connectivity quantum annealing without lossy dielectrics*. PhD thesis, UC Santa Barbara, 2017.

[66] J. Clarke and A. I. Braginski, editors. *The SQUID Handbook*. Wiley-VCH, Weinheim, 2004.

[67] David M. Pozar. *Pozar, David M - Microwave Engineering-Wiley (2012).Pdf*. John Wiley & Sons, Inc., 2011.

[68] Heinz-Peter Breuer and F. Petruccione. *The Theory of Open Quantum Systems*. Oxford University Press, Oxford ; New York, 2002.

[69] Ulrich Weiss. *Quantum Dissipative Systems*. World Scientific, 2012.

[70] Sadao Nakajima. On Quantum Theory of Transport Phenomena: Steady Diffusion. *Progress of Theoretical Physics*, 20(6):948–959, December 1958.

[71] Robert Zwanzig. Ensemble Method in the Theory of Irreversibility. *The Journal of Chemical Physics*, 33(5):1338–1341, November 1960.

[72] R. P Feynman and F. L Vernon. The theory of a general quantum system interacting with a linear dissipative system. *Annals of Physics*, 24:118–173, October 1963.

[73] Yoshitaka Tanimura and Ryogo Kubo. Time Evolution of a Quantum System in Contact with a Nearly Gaussian-Markoffian Noise Bath. *Journal of the Physical Society of Japan*, 58(1):101–114, January 1989.

[74] Ryogo Kubo, Morikazu Toda, and Natsuki Hashitsume. *Statistical Physics II*, volume 31 of *Springer Series in Solid-State Sciences*. Springer Berlin Heidelberg, Berlin, Heidelberg, 1991.

[75] Morikazu Toda, Ryōgo Kubo, N. Saitō, and N. Hashitsume. *Statistical Physics*. Number 30-31 in Springer Series in Solid-State Sciences. Springer-Verlag, Berlin ; New York, 2nd ed edition, 1991.

[76] A. G. Redfield. On the theory of relaxation processes. *IBM Journal of Research and Development*, 1(1):19–31, January 1957.

[77] Tameem Albash, Sergio Boixo, Daniel A. Lidar, and Paolo Zanardi. Quantum adiabatic Markovian master equations. *New J. Phys.*, 14(12):123016, 2012.

[78] Huo Chen and Daniel A. Lidar. Hamiltonian open quantum system toolkit. *Communications Physics*, 5(1):1–10, May 2022.

[79] Dazhi Xu and Jianshu Cao. Non-canonical distribution and non-equilibrium transport beyond weak system-bath coupling regime: A polaron transformation approach. *Frontiers of Physics*, 11(4):110308, May 2016.

[80] A. J. Leggett, S. Chakravarty, A. T. Dorsey, Matthew P. A. Fisher, Anupam Garg, and W. Zwerger. Dynamics of the dissipative two-state system. *Reviews of Modern Physics*, 59(1):1–85, January 1987.

[81] H. Dekker. Noninteracting-blip approximation for a two-level system coupled to a heat bath. *Physical Review A*, 35(3):1436–1437, February 1987.

[82] Sergio Boixo, Vadim N. Smelyanskiy, Alireza Shabani, Sergei V. Isakov, Mark Dykman, Vasil S. Denchev, Mohammad H. Amin, Anatoly Yu Smirnov, Masoud Mohseni, and Hartmut Neven. Computational multiqubit tunnelling in programmable quantum annealers. *Nature Communications*, 7:10327, January 2016.

[83] Anatoly Yu Smirnov and Mohammad H. Amin. Theory of open quantum dynamics with hybrid noise. *New J. Phys.*, 20(10):103037, October 2018.

[84] Gerald D. Mahan. *Many-Particle Physics*. Physics of Solids and Liquids. Plenum Press, New York, 2nd ed edition, 1990.

[85] M. H. S. Amin and Dmitri V. Averin. Macroscopic Resonant Tunneling in the Presence of Low Frequency Noise. *Phys. Rev. Lett.*, 100(19), May 2008.

[86] Giuseppe E. Santoro, Roman Martoňák, Erio Tosatti, and Roberto Car. Theory of Quantum Annealing of an Ising Spin Glass. *Science*, 295(5564):2427–2430, March 2002.

[87] J. Brooke, D. Bitko, T. F. Rosenbaum, and G. Aeppli. Quantum Annealing of a Disordered Magnet. *Science*, 284(5415):779–781, April 1999.

[88] Edward Farhi, Jeffrey Goldstone, Sam Gutmann, Joshua Lapan, Andrew Lundgren, and Daniel Preda. A Quantum Adiabatic Evolution Algorithm Applied to Random Instances of an NP-Complete Problem. *Science*, 292(5516):472–475, April 2001.

[89] M. W. Johnson, M. H. S. Amin, S. Gildert, T. Lanting, F. Hamze, N. Dickson, R. Harris, A. J. Berkley, J. Johansson, P. Bunyk, E. M. Chapple, C. Enderud, J. P. Hilton, K. Karimi, E. Ladizinsky, N. Ladizinsky, T. Oh, I. Perminov, C. Rich, M. C. Thom, E. Tolkacheva, C. J. S. Truncik, S. Uchaikin, J. Wang, B. Wilson, and G. Rose. Quantum annealing with manufactured spins. *Nature*, 473:194–198, May 2011.

[90] S. Ebadi, A. Keesling, M. Cain, T. T. Wang, H. Levine, D. Bluvstein, G. Semeghini, A. Omran, J.-G. Liu, R. Samajdar, X.-Z. Luo, B. Nash, X. Gao, B. Barak, E. Farhi, S. Sachdev, N. Gemelke, L. Zhou, S. Choi, H. Pichler, S.-T. Wang, M. Greiner, V. Vuletić, and M. D. Lukin. Quantum optimization of maximum independent set using Rydberg atom arrays. *Science*, 376(6598):1209–1215, June 2022.

[91] R. Islam, C. Senko, W. C. Campbell, S. Korenblit, J. Smith, A. Lee, E. E. Edwards, C.-C. J. Wang, J. K. Freericks, and C. Monroe. Emergence and Frustration of Magnetism with Variable-Range Interactions in a Quantum Simulator. *Science*, 340(6132):583–587, May 2013.

[92] Andrew D. King and William Bernoudy. Performance benefits of increased qubit connectivity in quantum annealing 3-dimensional spin glasses, September 2020.

[93] Sheir Yarkoni, Elena Raponi, Thomas Bäck, and Sebastian Schmitt. Quantum annealing for industry applications: Introduction and review. *Reports on Progress in Physics*, 85(10):104001, September 2022.

[94] Subir Sachdev. *Quantum Phase Transitions*. Cambridge University Press, Cambridge, transferred to digital printing edition, 2009.

[95] M Amin and V Choi. First-order quantum phase transition in adiabatic quantum computation. *APS*, 80:062326, December 2009.

[96] Ralf Schützhold and Gernot Schaller. Adiabatic quantum algorithms as quantum phase transitions: First versus second order. *Physical Review A*, 74(6):060304, December 2006.

[97] Junichi Tsuda, Yuuki Yamanaka, and Hidetoshi Nishimori. Energy Gap at First-Order Quantum Phase Transitions: An Anomalous Case. *Journal of the Physical Society of Japan*, 82(11):114004, November 2013.

[98] C. R. Laumann, R. Moessner, A. Scardicchio, and S. L. Sondhi. Quantum Adiabatic Algorithm and Scaling of Gaps at First-Order Quantum Phase Transitions. *Physical Review Letters*, 109(3):030502, July 2012.

[99] Sergey Knysh. Zero-temperature quantum annealing bottlenecks in the spin-glass phase. *Nature Communications*, 7:12370, August 2016.

[100] Edward Farhi, Jeffrey Goldston, David Gosset, Sam Gutmann, Harvey B. Meyer, and Peter Shor. Quantum adiabatic algorithms, small gaps, and different paths. *Quantum Information & Computation*, 11(3):181–214, March 2011.

[101] Neil G. Dickson and M. H. S. Amin. Does Adiabatic Quantum Optimization Fail for NP-Complete Problems? *Physical Review Letters*, 106(5):050502, February 2011.

[102] Trevor Lanting, Andrew D. King, Bram Evert, and Emile Hoskinson. Experimental demonstration of perturbative anticrossing mitigation using nonuniform driver Hamiltonians. *Physical Review A*, 96(4):042322, October 2017.

[103] Yuki Susa, Yu Yamashiro, Masayuki Yamamoto, and Hidetoshi Nishimori. Exponential Speedup of Quantum Annealing by Inhomogeneous Driving of the Transverse Field. *Journal of the Physical Society of Japan*, 87(2):023002, January 2018.

[104] Edward Farhi, Jeffrey Goldstone, and Sam Gutmann. Quantum Adiabatic Evolution Algorithms with Different Paths, August 2002.

[105] Tameem Albash and Matthew Kowalsky. Diagonal catalysts in quantum adiabatic optimization. *Physical Review A*, 103(2):022608, February 2021.

[106] Tameem Albash. Role of nonstoquastic catalysts in quantum adiabatic optimization. *Physical Review A*, 99(4):042334, April 2019.

[107] Alejandro Perdomo-Ortiz, Salvador E. Venegas-Andraca, and Alán Aspuru-Guzik. A study of heuristic guesses for adiabatic quantum computation. *Quantum Information Processing*, 10(1):33–52, February 2011.

[108] Masaki Ohkuwa, Hidetoshi Nishimori, and Daniel A. Lidar. Reverse annealing for the fully connected p-spin model. *Physical Review A*, 98(2):022314, August 2018.

[109] Andrew D. King, Juan Carrasquilla, Jack Raymond, Isil Ozfidan, Evgeny Andriyash, Andrew Berkley, Mauricio Reis, Trevor Lanting, Richard Harris, Fabio Altomare, Kelly Boothby, Paul I. Bunyk, Colin Enderud, Alexandre Fréchette, Emile Hoskinson, Nicolas Ladizinsky, Travis Oh, Gabriel Poulin-Lamarre, Christopher Rich, Yuki Sato, Anatoly Yu Smirnov, Loren J. Swenson, Mark H. Volkmann, Jed Whittaker, Jason Yao, Eric Ladizinsky, Mark W. Johnson, Jeremy Hilton, and Mohammad H. Amin. Observation of topological phenomena in a programmable lattice of 1,800 qubits. *Nature*, 560(7719):456–460, August 2018.

[110] Andrew D. King, Jack Raymond, Trevor Lanting, Sergei V. Isakov, Masoud Mohseni, Gabriel Poulin-Lamarre, Sara Ejtemaee, William Bernoudy, Isil Ozfidan, Anatoly Yu Smirnov, Mauricio Reis, Fabio Altomare, Michael Babcock, Catia Baron, Andrew J. Berkley, Kelly Boothby, Paul I. Bunyk, Holly Christiani, Colin Enderud, Bram Evert, Richard Harris, Emile Hoskinson, Shuiyuan Huang, Kais Jooya, Ali Khodabandelou, Nicolas Ladizinsky, Ryan Li, P. Aaron Lott, Allison J. R. MacDonald, Danica Marsden, Gaelen Marsden, Teresa Medina, Reza Molavi, Richard Neufeld, Mana Norouzpour, Travis Oh, Igor Pavlov, Ilya Perminov, Thomas Prescott, Chris Rich, Yuki Sato, Benjamin Sheldan, George Sterling, Loren J. Swenson, Nicholas Tsai, Mark H. Volkmann, Jed D. Whittaker, Warren Wilkinson, Jason Yao, Hartmut Neven, Jeremy P. Hilton, Eric Ladizinsky, Mark W. Johnson, and Mohammad H. Amin. Scaling advantage over path-integral Monte Carlo in quantum simulation of geometrically frustrated magnets. *Nature Communications*, 12(1):1113, February 2021.

[111] Mustafa Demirplak and Stuart A. Rice. Assisted Adiabatic Passage Revisited. *The Journal of Physical Chemistry B*, 109(14):6838–6844, April 2005.

[112] Dries Sels and Anatoli Polkovnikov. Minimizing irreversible losses in quantum systems by local counterdiabatic driving. *Proceedings of the National Academy of Sciences*, 114(20):E3909–E3916, May 2017.

[113] David P. Landau and K. Binder. *A Guide to Monte Carlo Simulations in Statistical Physics*. Cambridge University Press, Cambridge ; New York, 2nd ed edition, 2005.

[114] Sergei V. Isakov, Guglielmo Mazzola, Vadim N. Smelyanskiy, Zhang Jiang, Sergio Boixo, Hartmut Neven, and Matthias Troyer. Understanding Quantum Tunneling through Quantum Monte Carlo Simulations. *Physical Review Letters*, 117(18):180402, October 2016.

[115] Sergey Bravyi and Barbara Terhal. Complexity of Stoquastic Frustration-Free Hamiltonians. *SIAM Journal on Computing*, 39(4):1462–1485, January 2010.

[116] Matthew B. Hastings. Obstructions to classically simulating the quantum adiabatic algorithm. *Quantum Information and Computation*, 13(11&12):1038–1076, November 2013.

[117] Jacob D. Biamonte and Peter J. Love. Realizable Hamiltonians for universal adiabatic quantum computers. *Physical Review A*, 78(1):012352, July 2008.

[118] I. Ozfidan, C. Deng, A.Y. Smirnov, T. Lanting, R. Harris, L. Swenson, J. Whittaker, F. Altomare, M. Babcock, C. Baron, A.J. Berkley, K. Boothby, H. Christiani, P. Bunyk, C. Enderud, B. Evert, M. Hager, A. Hajda, J. Hilton, S. Huang, E. Hoskinson, M.W. Johnson, K. Jooya, E. Ladizinsky, N. Ladizinsky, R. Li, A. MacDonald, D. Marsden, G. Marsden, T. Medina, R. Molavi, R. Neufeld, M. Nissen, M. Norouzpour, T. Oh, I. Pavlov, I. Perminov, G. Poulin-Lamarre, M. Reis, T. Prescott, C. Rich, Y. Sato, G. Sterling, N. Tsai, M. Volkmann, W. Wilkinson, J. Yao, and M.H. Amin. Demonstration of a Nonstoquastic Hamiltonian in Coupled Superconducting Flux Qubits. *Physical Review Applied*, 13(3):034037, March 2020.

[119] Andrew J Kerman. Superconducting qubit circuit emulation of a vector spin-1/2. *New Journal of Physics*, 21(7):073030, July 2019.

[120] Yuya Seki and Hidetoshi Nishimori. Quantum annealing with antiferromagnetic fluctuations. *Physical Review E*, 85(5):051112, May 2012.

[121] Elizabeth Crosson, Tameem Albash, Itay Hen, and A. P. Young. De-Signing Hamiltonians for Quantum Adiabatic Optimization. *Quantum*, 4:334, September 2020.

[122] Stephen P. Jordan, David Gosset, and Peter J. Love. Quantum-Merlin-Arthur–complete problems for stoquastic Hamiltonians and Markov matrices. *Physical Review A*, 81(3):032331, March 2010.

[123] Dave Wecker, Matthew B. Hastings, and Matthias Troyer. Training a quantum optimizer. *Physical Review A*, 94(2):022309, August 2016.

[124] M. H. S. Amin, Peter J. Love, and C. J. S. Truncik. Thermally Assisted Adiabatic Quantum Computation. *Physical Review Letters*, 100(6):060503, February 2008.

[125] R. Harris, M. W. Johnson, T. Lanting, A. J. Berkley, J. Johansson, P. Bunyk, E. Tolkacheva, E. Ladizinsky, N. Ladizinsky, T. Oh, F. Cioata, I. Perminov, P. Spear,

C. Enderud, C. Rich, S. Uchaikin, M. C. Thom, E. M. Chapple, J. Wang, B. Wilson, M. H. S. Amin, N. Dickson, K. Karimi, B. Macready, C. J. S. Truncik, and G. Rose. Experimental investigation of an eight-qubit unit cell in a superconducting optimization processor. *Physical Review B*, 82(2):024511, July 2010.

[126] N. G. Dickson, M. W. Johnson, M. H. Amin, R. Harris, F. Altomare, A. J. Berkley, P. Bunyk, J. Cai, E. M. Chapple, P. Chavez, F. Cioata, T. Cirip, P. deBuen, M. Drew-Brook, C. Enderud, S. Gildert, F. Hamze, J. P. Hilton, E. Hoskinson, K. Karimi, E. Ladizinsky, N. Ladizinsky, T. Lanting, T. Mahon, R. Neufeld, T. Oh, I. Perminov, C. Petroff, A. Przybysz, C. Rich, P. Spear, A. Tcaciuc, M. C. Thom, E. Tolkacheva, S. Uchaikin, J. Wang, A. B. Wilson, Z. Merali, and G. Rose. Thermally assisted quantum annealing of a 16-qubit problem. *Nature Communications*, 4:1903, May 2013.

[127] Tameem Albash and Daniel A. Lidar. Decoherence in adiabatic quantum computation. *Physical Review A*, 91(6):062320, June 2015.

[128] Jeffrey Marshall, Davide Venturelli, Itay Hen, and Eleanor G. Rieffel. Power of Pausing: Advancing Understanding of Thermalization in Experimental Quantum Annealers. *Physical Review Applied*, 11(4):044083, April 2019.

[129] Huo Chen and Daniel A. Lidar. Why and When Pausing is Beneficial in Quantum Annealing. *Physical Review Applied*, 14(1):014100, July 2020.

[130] Vasil S. Denchev, Sergio Boixo, Sergei V. Isakov, Nan Ding, Ryan Babbush, Vadim Smelyanskiy, John Martinis, and Hartmut Neven. What is the Computational Value of Finite-Range Tunneling? *Physical Review X*, 6(3):031015, August 2016.

[131] Yuki Bando, Ka-Wa Yip, Huo Chen, Daniel A. Lidar, and Hidetoshi Nishimori. Breakdown of the Weak-Coupling Limit in Quantum Annealing. *Physical Review Applied*, 17(5):054033, May 2022.

[132] Andrew D. King, Sei Suzuki, Jack Raymond, Alex Zucca, Trevor Lanting, Fabio Altomare, Andrew J. Berkley, Sara Ejtemaee, Emile Hoskinson, Shuiyuan Huang, Eric Ladizinsky, Allison J. R. MacDonald, Gaelen Marsden, Travis Oh, Gabriel Poulin-Lamarre, Mauricio Reis, Chris Rich, Yuki Sato, Jed D. Whittaker, Jason Yao, Richard Harris, Daniel A. Lidar, Hidetoshi Nishimori, and Mohammad H. Amin. Coherent quantum annealing in a programmable 2,000 qubit Ising chain. *Nature Physics*, 18(11):1324–1328, November 2022.

[133] Andrew D. King, Jack Raymond, Trevor Lanting, Richard Harris, Alex Zucca, Fabio Altomare, Andrew J. Berkley, Kelly Boothby, Sara Ejtemaee, Colin Enderud, Emile Hoskinson, Shuiyuan Huang, Eric Ladizinsky, Allison J. R. MacDonald, Gaelen Marsden, Reza Molavi, Travis Oh, Gabriel Poulin-Lamarre, Mauricio Reis, Chris Rich, Yuki Sato, Nicholas Tsai, Mark Volkmann, Jed D. Whittaker, Jason Yao, Anders W. Sandvik, and Mohammad H. Amin. Quantum critical dynamics in a 5000-qubit programmable spin glass, July 2022.

[134] Daniel A. Lidar. Arbitrary-time error suppression for Markovian adiabatic quantum computing using stabilizer subspace codes. *Physical Review A*, 100(2):022326, August 2019.

[135] Milad Marvian and Daniel A. Lidar. Error Suppression for Hamiltonian-Based Quantum Computation Using Subsystem Codes. *Physical Review Letters*, 118(3):030504, January 2017.

[136] Tameem Albash, Victor Martin-Mayor, and Itay Hen. Analog errors in Ising machines. *Quantum Science and Technology*, 4(2):02LT03, April 2019.

[137] Kristen L. Pudenz, Tameem Albash, and Daniel A. Lidar. Error-corrected quantum annealing with hundreds of qubits. *Nature Communications*, 5:ncomms4243, February 2014.

[138] Adam Pearson, Anurag Mishra, Itay Hen, and Daniel A. Lidar. Analog errors in quantum annealing: Doom and hope. *npj Quantum Information*, 5(1):107, December 2019.

[139] Jemma Bennett, Adam Callison, Tom O'Leary, Mia West, Nicholas Chancellor, and Viv Kendon. Using copies to improve precision in continuous-time quantum computing, August 2022.

[140] T. Lanting, M. H. Amin, C. Baron, M. Babcock, J. Boschee, S. Boixo, V. N. Smelyanskiy, M. Foygel, and A. G. Petukhov. Probing Environmental Spin Polarization with Superconducting Flux Qubits. *arXiv:2003.14244 [cond-mat, physics:quant-ph]*, April 2020.

[141] Vicky Choi. Minor-embedding in adiabatic quantum computation: I. The parameter setting problem. *Quantum Information Processing*, 7(5):193–209, October 2008.

[142] Vicky Choi. Minor-embedding in adiabatic quantum computation: II. Minor-universal graph design. *Quantum Information Processing*, 10(3):343–353, June 2011.

[143] Erica Grant and Travis S. Humble. Benchmarking embedded chain breaking in quantum annealing*. *Quantum Science and Technology*, 7(2):025029, March 2022.

[144] Andrew Kerman. Design and simulation of complex superconducting circuits for advanced quantum annealing hardware. In *APS March Meeting Abstracts*, volume 2018, pages C26–001, 2018.

[145] Wolfgang Lechner, Philipp Hauke, and Peter Zoller. A quantum annealing architecture with all-to-all connectivity from local interactions. *Science Advances*, 1(9):e1500838, October 2015.

[146] Steven Weber, Gabriel Samach, Danna Rosenberg, Jonilyn Yoder, David Kim, Andrew Kerman, and William Oliver. Hardware considerations for high-connectivity quantum annealers. In *APS March Meeting Abstracts*, volume 2018, pages A33–008, 2018.

[147] Shruti Puri, Christian Kraglund Andersen, Arne L. Grimsmo, and Alexandre Blais. Quantum annealing with all-to-all connected nonlinear oscillators. *Nature Communications*, 8:15785, June 2017.

[148] Tim Menke, Florian Häse, Simon Gustavsson, Andrew J. Kerman, William D. Oliver, and Alán Aspuru-Guzik. Automated design of superconducting circuits and its application to 4-local couplers. *npj Quantum Information*, 7(1):1–8, March 2021.

[149] Tim Menke, William P. Banner, Thomas R. Bergamaschi, Agustin Di Paolo, Antti Vepsäläinen, Steven J. Weber, Roni Winik, Alexander Melville, Bethany M. Niedzielski, Danna Rosenberg, Kyle Serniak, Mollie E. Schwartz, Jonilyn L. Yoder, Alán Aspuru-Guzik, Simon Gustavsson, Jeffrey A. Grover, Cyrus F. Hirjibehedin, Andrew J. Kerman, and William D. Oliver. Demonstration of Tunable Three-Body Interactions between Superconducting Qubits. *Physical Review Letters*, 129(22):220501, November 2022.

[150] Yu Chen, C. Neill, P. Roushan, N. Leung, M. Fang, R. Barends, J. Kelly, B. Campbell, Z. Chen, B. Chiaro, et al. Qubit Architecture with High Coherence and Fast Tunable Coupling. *Phys. Rev. Lett.*, 113(22):220502, November 2014.

[151] Matthew Reagor, Christopher B. Osborn, Nikolas Tezak, Alexa Staley, Guenevere Prawiroatmodjo, Michael Scheer, Nasser Alidoust, Eyob A. Sete, Nicolas Didier, Marcus P. da Silva, et al. Demonstration of universal parametric entangling gates on a multi-qubit lattice. *Science Advances*, 4(2):eaao3603, February 2018.

[152] B. Foxen, C. Neill, A. Dunsworth, P. Roushan, B. Chiaro, A. Megrant, J. Kelly, Zijun Chen, K. Satzinger, R. Barends, et al. Demonstrating a Continuous Set of Two-Qubit Gates for Near-Term Quantum Algorithms. *Phys. Rev. Lett.*, 125(12):120504, September 2020.

[153] Yuan Xu, Ji Chu, Jiahao Yuan, Jiawei Qiu, Yuxuan Zhou, Libo Zhang, Xinsheng Tan, Yang Yu, Song Liu, Jian Li, Fei Yan, and Dapeng Yu. High-Fidelity, High-Scalability Two-Qubit Gate Scheme for Superconducting Qubits. *Phys. Rev. Lett.*, 125(24):240503, December 2020.

[154] Youngkyu Sung, Leon Ding, Jochen Braumüller, Antti Vepsäläinen, Bharath Kannan, Morten Kjaergaard, Ami Greene, Gabriel O. Samach, Chris McNally, David Kim, et al. Realization of High-Fidelity CZ and ZZ-Free iSWAP Gates with a Tunable Coupler. *Phys. Rev. X*, 11(2):021058, June 2021.

[155] J. Stehlik, D. M. Zajac, D. L. Underwood, T. Phung, J. Blair, S. Carnevale, D. Klaus, G. A. Keefe, A. Carniol, M. Kumph, et al. Tunable Coupling Architecture for Fixed-Frequency Transmon Superconducting Qubits. *Phys. Rev. Lett.*, 127(8):080505, August 2021.

[156] V. Negîrneac, H. Ali, N. Muthusubramanian, F. Battistel, R. Sagastizabal, M. S. Moreira, J. F. Marques, W. J. Vlothuizen, M. Beekman, C. Zachariadis, et al. High-Fidelity Controlled-Z Gate with Maximal Intermediate Leakage Operating at the Speed Limit in a Superconducting Quantum Processor. *Phys. Rev. Lett.*, 126(22):220502, June 2021.

[157] Peng Zhao, Kehuan Linghu, Zhiyuan Li, Peng Xu, Ruixia Wang, Guangming Xue, Yirong Jin, and Haifeng Yu. Quantum Crosstalk Analysis for Simultaneous Gate Operations on Superconducting Qubits. *PRX Quantum*, 3(2):020301, April 2022.

[158] M. S. Allman, F. Altomare, J. D. Whittaker, K. Cicak, D. Li, A. Sirois, J. Strong, J. D. Teufel, and R. W. Simmonds. Rf-SQUID-Mediated Coherent Tunable Coupling between a Superconducting Phase Qubit and a Lumped-Element Resonator. *Phys. Rev. Lett.*, 104(17):177004, April 2010.

[159] S. J. Srinivasan, A. J. Hoffman, J. M. Gambetta, and A. A. Houck. Tunable Coupling in Circuit Quantum Electrodynamics Using a Superconducting Charge Qubit with a V -Shaped Energy Level Diagram. *Phys. Rev. Lett.*, 106(8):083601, February 2011.

[160] A. Baust, E. Hoffmann, M. Haeberlein, M. J. Schwarz, P. Eder, J. Goetz, F. Wulschner, E. Xie, L. Zhong, F. Quijandría, et al. Tunable and switchable coupling between two superconducting resonators. *Phys. Rev. B*, 91(1):014515, January 2015.

[161] Steven J. Weber, Gabriel O. Samach, David Hover, Simon Gustavsson, David K. Kim, Alexander Melville, Danna Rosenberg, Adam P. Sears, Fei Yan, Jonilyn L. Yoder, William D. Oliver, and Andrew J. Kerman. Coherent coupled qubits for quantum annealing. *Phys. Rev. Appl.*, 8:014004, jul 2017.

[162] Tim Menke, William P. Banner, Thomas R. Bergamaschi, Agustin Di Paolo, Antti Vepsäläinen, Steven J. Weber, Roni Winik, Alexander Melville, Bethany M. Niedzielski, Danna Rosenberg, et al. Demonstration of tunable three-body interactions between superconducting qubits. *arXiv:2205.04542*, May 2022.

[163] P. V. Klimov, J. Kelly, Z. Chen, M. Neeley, A. Megrant, B. Burkett, R. Barends, K. Arya, B. Chiaro, Yu Chen, et al. Fluctuations of Energy-Relaxation Times in Superconducting Qubits. *Phys. Rev. Lett.*, 121(9):090502, August 2018.

[164] M. W. Johnson, P. Bunyk, F. Maibaum, E. Tolkacheva, A. J. Berkley, E. M. Chapple, R. Harris, J. Johansson, T. Lanting, I Perminov, E. Ladizinsky, T. Oh, and G. Rose. A scalable control system for a superconducting adiabatic quantum optimization processor. *Supercond. Sci. Technol.*, 23(6):065004, 2010.

[165] Mostafa Khezri, Xi Dai, Rui Yang, Tameem Albash, Adrian Lupascu, and Daniel A. Lidar. Customized quantum annealing schedules. *arXiv:2103.06461*, 2021.

[166] Mostafa Khezri, Jeffrey A. Grover, James I. Basham, Steven M. Disseler, Huo Chen, Sergey Novikov, Kenneth M. Zick, and Daniel A. Lidar. Anneal-path correction in flux qubits. *npj Quantum Inf.*, 7(1):26, February 2021.

[167] Juan I. Adame and Peter L. McMahon. Inhomogeneous driving in quantum annealers can result in orders-of-magnitude improvements in performance. *Quantum Sci. Technol.*, 5(3):035011, jun 2020.

[168] Yuki Susa, Yu Yamashiro, Masayuki Yamamoto, Itay Hen, Daniel A. Lidar, and Hidetoshi Nishimori. Quantum annealing of the p-spin model under inhomogeneous transverse field driving. *Phys. Rev. A*, 98(4):042326, oct 2018.

[169] Tameem Albash and Matthew Kowalsky. Diagonal catalysts in quantum adiabatic optimization. *arXiv:2009.05726*, sep 2020.

[170] M. Kounalakis, C. Dickel, A. Bruno, N. K. Langford, and G. A. Steele. Tuneable hopping and nonlinear cross-Kerr interactions in a high-coherence superconducting circuit. *Npj Quantum Inf.*, 4(1):1–7, August 2018.

[171] C. Neill, P. Roushan, K. Kechedzhi, S. Boixo, S. V. Isakov, V. Smelyanskiy, A. Megrant, B. Chiaro, A. Dunsworth, K. Arya, et al. A blueprint for demonstrating quantum supremacy with superconducting qubits. *Science*, 360(6385):195–199, April 2018.

[172] Deanna M. Abrams, Nicolas Didier, Shane A. Caldwell, Blake R. Johnson, and Colm A. Ryan. Methods for Measuring Magnetic Flux Crosstalk between Tunable Transmons. *Phys. Rev. Appl.*, 12(6):064022, December 2019.

[173] Sebastian Krinner, Nathan Lacroix, Ants Remm, Agustin Di Paolo, Elie Genois, Catherine Leroux, Christoph Hellings, Stefania Lazar, Francois Swiadek, Johannes Herrmann, et al. Realizing Repeated Quantum Error Correction in a Distance-Three Surface Code. *arXiv:2112.03708*, December 2021.

[174] P. I. Bunyk, E. M. Hoskinson, M. W. Johnson, E. Tolkacheva, F. Altomare, A. J. Berkley, R. Harris, J. P. Hilton, T. Lanting, A. J. Przybysz, and J. Whittaker. Architectural considerations in the design of a superconducting quantum annealing processor. *IEEE Trans. Appl. Supercond.*, 24(4):1–10, aug 2014.

[175] Fritz London. *Superfluids. Volume 1. Macroscopic Theory of Superconductivity.* Dover, New York, 1961.

[176] N. Byers and C. N. Yang. Theoretical Considerations Concerning Quantized Magnetic Flux in Superconducting Cylinders. *Phys. Rev. Lett.*, 7(2):46–49, July 1961.

[177] Jochen Braumüller, Amir H. Karamlou, Yariv Yanay, Bharath Kannan, David Kim, Morten Kjaergaard, Alexander Melville, Bethany M. Niedzielski, Youngkyu Sung, Antti Vepsäläinen, Roni Winik, Jonilyn L. Yoder, Terry P. Orlando, Simon Gustavsson, Charles Tahan, and William D. Oliver. Probing quantum information propagation with out-of-time-ordered correlators. *Nat. Phys.*, 18(2):172–178, February 2022.

[178] S. Novikov, R. Hinkey, S. Disseler, J. I. Basham, T. Albash, A. Risinger, D. Ferguson, D. A. Lidar, and K. M. Zick. Exploring More-Coherent Quantum Annealing. In *2018 IEEE International Conference on Rebooting Computing (ICRC)*, pages 1–7, November 2018.

[179] A. J. Berkley, M. W. Johnson, P. Bunyk, R. Harris, J. Johansson, T. Lanting, E. Ladizinsky, E. Tolkacheva, M. H. S. Amin, and G. Rose. A scalable readout system for a superconducting adiabatic quantum optimization system. *Supercond. Sci. Technol.*, 23(10):105014, 2010.

[180] D. Rosenberg, D. Kim, R. Das, D. Yost, S. Gustavsson, D. Hover, P. Krantz, A. Melville, L. Racz, G. O. Samach, S. J. Weber, F. Yan, J. L. Yoder, A. J. Kerman, and W. D. Oliver. 3D integrated superconducting qubits. *Npj Quantum Inf.*, 3(1):1–5, October 2017.

[181] D. R. W. Yost, M. E. Schwartz, J. Mallek, D. Rosenberg, C. Stull, J. L. Yoder, G. Calusine, M. Cook, R. Das, A. L. Day, E. B. Golden, D. K. Kim, A. Melville, B. M. Niedzielski, W. Woods, A. J. Kerman, and W. D. Oliver. Solid-state qubits integrated with superconducting through-silicon vias. *npj Quantum Inf.*, 6(1):1–7, 2020.

[182] Norbert Marwan, M. Carmen Romano, Marco Thiel, and Jürgen Kurths. Recurrence plots for the analysis of complex systems. *Phys. Rep.*, 438(5):237–329, jan 2007.

[183] P. F. Alcantarilla, A. Bartoli, and A. J. Davison. KAZE features. In *Eur. Conf. on Computer Vision (ECCV)*, 2012.

[184] Stéfan van der Walt, Johannes L. Schönberger, Juan Nunez-Iglesias, François Boulogne, Joshua D. Warner, Neil Yager, Emmanuelle Gouillart, and Tony Yu. Scikit-image: image processing in python. *PeerJ*, 2:e453, jun 2014.

[185] Manuel Guizar-Sicairos, Samuel T. Thurman, and James R. Fienup. Efficient subpixel image registration algorithms. *Opt. Lett.*, 33(2):156, jan 2008.

[186] Deanna M. Abrams, Nicolas Didier, Shane A. Caldwell, Blake R. Johnson, and Colm A. Ryan. Methods for measuring magnetic flux crosstalk between tunable transmons. *Phys. Rev. Appl.*, 12(6):064022, dec 2019.

[187] D. R. W. Yost, M. E. Schwartz, J. Mallek, D. Rosenberg, C. Stull, J. L. Yoder, G. Calusine, M. Cook, R. Das, A. L. Day, et al. Solid-state qubits integrated with superconducting through-silicon vias. *Npj Quantum Inf.*, 6(1):1–7, July 2020.

[188] Eric Brochu, Vlad M. Cora, and Nando de Freitas. A Tutorial on Bayesian Optimization of Expensive Cost Functions, with Application to Active User Modeling and Hierarchical Reinforcement Learning. *arXiv:1012.2599*, December 2010.

[189] Lars Buitinck, Gilles Louppe, Mathieu Blondel, Fabian Pedregosa, Andreas Mueller, Olivier Grisel, Vlad Niculae, Peter Prettenhofer, Alexandre Gramfort, Jaques Grobler, et al. Api design for machine learning software: experiences from the scikit-learn project. *arXiv:1309.0238*, 2013.

[190] X. Dai, D.M. Tennant, R. Trappen, A.J. Martinez, D. Melanson, M.A. Yurtalan, Y. Tang, S. Novikov, J.A. Grover, S.M. Disseler, et al. Calibration of Flux Crosstalk in Large-Scale Flux-Tunable Superconducting Quantum Circuits. *PRX Quantum*, 2(4):040313, October 2021.

[191] J.C. Spall. Multivariate stochastic approximation using a simultaneous perturbation gradient approximation. *IEEE Transactions on Automatic Control*, 37(3):332–341, March 1992.

[192] Ilya Sutskever, James Martens, George Dahl, and Geoffrey Hinton. On the importance of initialization and momentum in deep learning. In *Proceedings of the 30th International Conference on Machine Learning*, pages 1139–1147. PMLR, May 2013.

[193] Zhaoqi Leng, Pranav Mundada, Saeed Ghadimi, and Andrew Houck. Robust and efficient algorithms for high-dimensional black-box quantum optimization. *arXiv:1910.03591*, October 2019.

[194] N. Otsu. A threshold selection method from gray-level histograms. *IEEE Trans. Syst. Man Cybern. Syst.*, 9(1):62–66, jan 1979.

[195] Helmut G. Katzgraber, Firas Hamze, and Ruben S. Andrist. Glassy chimeras could be blind to quantum speedup: Designing better benchmarks for quantum annealing machines. *Phys. Rev. X*, 4:021008, Apr 2014.

[196] Sergey Bravyi, David Gosset, and Ramis Movassagh. Classical algorithms for quantum mean values. *Nat. Phys.*, 17(3):337–341, Mar 2021.

[197] L Campos Venuti, C Degli Esposti Boschi, and Marco Roncaglia. Long-distance entanglement in spin systems. *Phys. Rev. Lett.*, 96(24):247206, 2006.

[198] Mark Friesen, Asoka Biswas, Xuedong Hu, and Daniel A. Lidar. Efficient multiqubit entanglement via a spin bus. *Phys. Rev. Lett.*, 98(23):230503, 2007.

[199] L Campos Venuti, C Degli Esposti Boschi, and M Roncaglia. Qubit teleportation and transfer across antiferromagnetic spin chains. *Phys. Rev. Lett.*, 99(6):060401, 2007.

[200] Aires Ferreira and J. M. B. Lopes dos Santos. Analytic results on long-distance entanglement mediated by gapped spin chains. *Phys. Rev. A*, 77(3):034301, 2008.

[201] Sangchul Oh, Mark Friesen, and Xuedong Hu. Even-odd effects of Heisenberg chains on long-range interaction and entanglement. *Phys. Rev. B*, 82:140403, Oct 2010.

[202] Sangchul Oh et al. Heisenberg spin bus as a robust transmission line for quantum-state transfer. *Phys. Rev. A*, 84(2):022330, 2011.

[203] R. Harris, J. Johansson, A. J. Berkley, M. W. Johnson, T. Lanting, Siyuan Han, P. Bunyk, E. Ladizinsky, T. Oh, I. Perminov, E. Tolkacheva, S. Uchaikin, E. M. Chapple, C. Enderud, C. Rich, M. Thom, J. Wang, B. Wilson, and G. Rose. Experimental demonstration of a robust and scalable flux qubit. *Phys. Rev. B*, 81(13), April 2010.

[204] Long B. Nguyen, Yen-Hsiang Lin, Aaron Somoroff, Raymond Mencia, Nicholas Grabon, and Vladimir E. Manucharyan. High-Coherence Fluxonium Qubit. *Phys. Rev. X*, 9(4):041041, November 2019.

[205] Bruno Apolloni, Nicolò Cesa-Bianchi, and Diego De Falco. A numerical implementation of quantum annealing. In *Stochastic Processes, Physics and Geometry: Proceedings of the Ascona-Locarno Conference*, pages 97–111, 1990.

[206] Arnab Das and Bikas K. Chakrabarti. Colloquium: Quantum annealing and analog quantum computation. *Rev. Mod. Phys.*, 80:1061–1081, Sep 2008.

[207] Tameem Albash and Daniel A. Lidar. Decoherence in adiabatic quantum computation. *Phys. Rev. A*, 91(6):062320, June 2015.

[208] T. Lanting et al. Entanglement in a quantum annealing processor. *Phys. Rev. X*, 4:021041, May 2014.

[209] R. Harris et al. Phase transitions in a programmable quantum spin glass simulator. *Science*, 361(6398):162–165, 2018.

[210] Kazuki Ikeda, Yuma Nakamura, and Travis S. Humble. Application of quantum annealing to nurse scheduling problem. *Sci. Rep.*, 9(1):12837, Sep 2019.

[211] Daisuke Inoue, Akihisa Okada, Tadayoshi Matsumori, Kazuyuki Aihara, and Hiroaki Yoshida. Traffic signal optimization on a square lattice with quantum annealing. *Sci. Rep.*, 11(1):3303, Feb 2021.

[212] Richard Y. Li, Rosa Di Felice, Remo Rohs, and Daniel A. Lidar. Quantum annealing versus classical machine learning applied to a simplified computational biology problem. *npj Quantum Inf.*, 4(1):14, Feb 2018.

[213] Helmut G Katzgraber. Viewing vanilla quantum annealing through spin glasses. *Quantum Sci. Tech.*, 3(3):030505, jun 2018.

[214] Bettina Heim, Troels F Rønnow, Sergei V Isakov, and Matthias Troyer. Quantum versus classical annealing of Ising spin glasses. *Science*, 348(6231):215–217, 2015.

[215] Davide Venturelli et al. Quantum optimization of fully connected spin glasses. *Phys. Rev. X*, 5:031040, Sep 2015.

[216] Sergey Novikov, Roy Murray, Edward Leonard, Alexander Marakov, Thomas Chamberlin, James Basham, Jeffrey Grover, Steven Disseler, Rabindra Das, David Kim, et al. 3d-integrated 25-qubit quantum annealing processor with high coherence, individualized control, and modular architecture. part 1: design. In *APS March Meeting Abstracts*, volume 2021, pages C30–001, 2021.

[217] Kelly Boothby, Paul Bunyk, Jack Raymond, and Aidan Roy. Next-generation topology of D-Wave quantum processors. *Preprint at http://arXiv.org/abs/2003.00133*, 2020.

[218] Andrew Lucas. Ising formulations of many NP problems. *Front. Phys.*, 2:5, 2014.

[219] G Passarelli, V Cataudella, and P Lucignano. Improving quantum annealing of the ferromagnetic p-spin model through pausing. *Phys. Rev. B*, 100(2):024302, 2019.

[220] Tameem Albash and Daniel A Lidar. Demonstration of a scaling advantage for a quantum annealer over simulated annealing. *Phys. Rev. X*, 8(3):031016, 2018.

[221] Rolando D Somma, Daniel Nagaj, and Mária Kieferová. Quantum speedup by quantum annealing. *Phys. Rev. Lett.*, 109(5):050501, 2012.

[222] Humberto Munoz-Bauza, Huo Chen, and Daniel Lidar. A double-slit proposal for quantum annealing. *Npj Quantum Inf.*, 5(1):51, December 2019.

[223] Melvin A Ruderman and Charles Kittel. Indirect exchange coupling of nuclear magnetic moments by conduction electrons. *Phys. Rev.*, 96(1):99–102, 1954.

[224] Haifeng Qiao et al. Long-distance superexchange between semiconductor quantum-dot electron spins. *Phys. Rev. Lett.*, 126(1):017701, 2021.

[225] Tobias J Osborne and Michael A Nielsen. Entanglement in a simple quantum phase transition. *Phys. Rev. A*, 66(3):032110, 2002.

[226] Guifre Vidal, José Ignacio Latorre, Enrique Rico, and Alexei Kitaev. Entanglement in quantum critical phenomena. *Phys. Rev. Lett.*, 90(22):227902, 2003.

[227] Qing Ai, Tao Shi, Guilu Long, and C. P. Sun. Induced entanglement enhanced by quantum criticality. *Phys. Rev. A*, 78:022327, Aug 2008.

[228] Alec Maassen van den Brink, A. J. Berkley, and M. Yalowsky. Mediated tunable coupling of flux qubits. *New Journal of Physics*, 7(1):230, 2005.

[229] V Zakosarenko et al. Realization of a classical counterpart of a scalable design for adiabatic quantum computation. *Appl. Phys. Lett.*, 90(2):022501, 2007.

[230] Michael S Allman et al. rf-SQUID-mediated coherent tunable coupling between a superconducting phase qubit and a lumped-element resonator. *Phys. Rev. Lett.*, 104(17):177004, 2010.

[231] Michael Shane Allman et al. Tunable resonant and nonresonant interactions between a phase qubit and LC resonator. *Phys. Rev. Lett.*, 112(12):123601, 2014.

[232] Caspar H. Van Der Wal, A. C. J. Ter Haar, F. K. Wilhelm, R. N. Schouten, CJPM Harmans, T. P. Orlando, Seth Lloyd, and J. E. Mooij. Quantum superposition of macroscopic persistent-current states. *Science*, 290(5492):773–777, 2000.

[233] F. G. Paauw, A Fedorov, C. J. P. M. Harmans, and J. E. Mooij. Tuning the gap of a superconducting flux qubit. *Phys. Rev. Lett.*, 102(9):090501, 2009.

[234] Sergey Bravyi, David P. DiVincenzo, and Daniel Loss. Schrieffer–Wolff transformation for quantum many-body systems. *Annals of Physics*, 326(10):2793–2826, October 2011.

[235] C. M. Quintana, Yu Chen, D. Sank, A. G. Petukhov, T. C. White, Dvir Kafri, B. Chiaro, A. Megrant, R. Barends, B. Campbell, Z. Chen, A. Dunsworth, A. G. Fowler, R. Graff, E. Jeffrey, J. Kelly, E. Lucero, J. Y. Mutus, M. Neeley, C. Neill, P. J. J. O'Malley, P. Roushan, A. Shabani, V. N. Smelyanskiy, A. Vainsencher, J. Wenner, H. Neven, and John M. Martinis. Observation of Classical-Quantum Crossover of \$1/f\$ Flux Noise and Its Paramagnetic Temperature Dependence. *Phys. Rev. Lett.*, 118(5):057702, January 2017.

[236] Mostafa Khezri, Xi Dai, Rui Yang, Tameem Albash, Adrian Lupascu, and Daniel A. Lidar. Customized Quantum Annealing Schedules. *Phys. Rev. Appl.*, 17(4):044005, April 2022.

[237] Florian Meier, Jeremy Levy, and Daniel Loss. Quantum computing with antiferromagnetic spin clusters. *Phys. Rev. B*, 68(13):134417, 2003.

[238] Denis Melanson, Antonio J Martinez, Salil Bedkihal, and Adrian Lupascu. Tunable three-body coupler for superconducting flux qubits. *Preprint at http://arXiv.org/abs/1909.02091*, 2019.

[239] X. Dai, D.M. Tennant, R. Trappen, A.J. Martinez, D. Melanson, M.A. Yurtalan, Y. Tang, S. Novikov, J.A. Grover, S.M. Disseler, J.I. Basham, R. Das, D.K. Kim, A.J. Melville, B.M. Niedzielski, S.J. Weber, J.L. Yoder, D.A. Lidar, and A. Lupascu. Calibration of Flux Crosstalk in Large-Scale Flux-Tunable Superconducting Quantum Circuits. *PRX Quantum*, 2(4):040313, October 2021.

[240] Andrew J. Kerman. Efficient numerical simulation of complex Josephson quantum circuits, October 2020.

[241] F. Yoshihara, K. Harrabi, A. O. Niskanen, Y. Nakamura, and J. S. Tsai. Decoherence of Flux Qubits due to $1/f$ Flux Noise. *Phys. Rev. Lett.*, 97(16):167001, October 2006.

[242] Jochen Braumüller, Leon Ding, Antti P. Vepsäläinen, Youngkyu Sung, Morten Kjaergaard, Tim Menke, Roni Winik, David Kim, Bethany M. Niedzielski, Alexander Melville, Jonilyn L. Yoder, Cyrus F. Hirjibehedin, Terry P. Orlando, Simon Gustavsson, and William D. Oliver. Characterizing and Optimizing Qubit Coherence Based on SQUID Geometry. *Phys. Rev. Appl.*, 13(5):054079, May 2020.

[243] Stefano Zippilli, Salvatore Marco Giampaolo, and Fabrizio Illuminati. Surface entanglement in quantum spin networks. *Phys. Rev. A*, 87:042304, Apr 2013.

[244] Philipp Hauke, Markus Heyl, Luca Tagliacozzo, and Peter Zoller. Measuring multipartite entanglement through dynamic susceptibilities. *Nat. Phys.*, 12(8):778–782, Aug 2016.

[245] L.-A. Wu, S. Bandyopadhyay, M. S. Sarandy, and D. A. Lidar. Entanglement observables and witnesses for interacting quantum spin systems. *Phys. Rev. A*, 72:032309, Sep 2005.

[246] B Foxen, JY Mutus, E Lucero, E Jeffrey, D Sank, R Barends, K Arya, B Burkett, Yu Chen, Zijun Chen, et al. High speed flux sampling for tunable superconducting qubits with an embedded cryogenic transducer. *Superconductor Science and Technology*, 32(1):015012, 2018.

[247] Michael Tinkham. *Introduction to superconductivity*. Courier Corporation, 2004.

[248] J Robert Johansson, Paul D Nation, and Franco Nori. Qutip: An open-source python framework for the dynamics of open quantum systems. *Computer Physics Communications*, 183(8):1760–1772, 2012.

[249] Mohammad H. Amin, Evgeny Andriyash, Jason Rolfe, Bohdan Kulchytskyy, and Roger Melko. Quantum Boltzmann Machine. *Phys. Rev. X*, 8(2):021050, May 2018.

[250] Andrew D. King, Jack Raymond, Trevor Lanting, Sergei V. Isakov, Masoud Mohseni, Gabriel Poulin-Lamarre, Sara Ejtemaee, William Bernoudy, Isil Ozfidan, Anatoly Yu Smirnov, Mauricio Reis, Fabio Altomare, Michael Babcock, Catia Baron, Andrew J. Berkley, Kelly Boothby, Paul I. Bunyk, Holly Christiani, Colin Enderud, Bram Evert, Richard Harris, Emile Hoskinson, Shuiyuan Huang, Kais Jooya, Ali Khodabandelou, Nicolas Ladizinsky, Ryan Li, P. Aaron Lott, Allison J. R. MacDonald, Danica Marsden, Gaelen Marsden, Teresa Medina, Reza Molavi, Richard Neufeld, Mana Norouzpour, Travis Oh, Igor Pavlov, Ilya Perminov, Thomas Prescott, Chris Rich, Yuki Sato, Benjamin Sheldan, George Sterling, Loren J. Swenson, Nicholas Tsai, Mark H. Volkmann, Jed D. Whittaker, Warren Wilkinson, Jason Yao, Hartmut Neven, Jeremy P. Hilton, Eric Ladizinsky, Mark W. Johnson, and Mohammad H. Amin. Scaling advantage over path-integral Monte Carlo in quantum simulation of geometrically frustrated magnets. *Nat. Comm*, 12(1):1113, February 2021.

[251] Alexandre Blais, Arne L. Grimsmo, S. M. Girvin, and Andreas Wallraff. Circuit quantum electrodynamics. *Rev. Mod. Phys.*, 93(2):025005, May 2021.

[252] Irfan Siddiqi. Engineering high-coherence superconducting qubits. *Nat. Rev. Mater.*, 6(10):875–891, October 2021.

[253] M. H. S. Amin, C. J. S. Truncik, and D. V. Averin. Role of single-qubit decoherence time in adiabatic quantum computation. *Phys. Rev. A*, 80(2):022303, August 2009. 00043.

[254] F. Bloch. Generalized Theory of Relaxation. *Phys. Rev.*, 105(4):1206–1222, February 1957.

[255] A. G. Redfield. On the Theory of Relaxation Processes. *IBM J. Res. Dev.*, 1(1):19–31, January 1957.

[256] G. Ithier, E. Collin, P. Joyez, P. J. Meeson, D. Vion, D. Esteve, F. Chiarello, A. Shnirman, Y. Makhlin, J. Schriefl, and G. Schön. Decoherence in a superconducting quantum bit circuit. *Phys. Rev. B*, 72:134519, October 2005.

[257] A. J. Leggett, S. Chakravarty, A. T. Dorsey, Matthew P. A. Fisher, Anupam Garg, and W. Zwerger. Dynamics of the dissipative two-state system. *Rev. Mod. Phys.*, 59(1):1–85, January 1987.

[258] Jonathan R. Friedman, Vijay Patel, W. Chen, S. K. Tolpygo, and J. E. Lukens. Quantum superposition of distinct macroscopic states. *Nature*, 406(6791):43–46, July 2000.

[259] J. Q. You, Xuedong Hu, S. Ashhab, and Franco Nori. Low-decoherence flux qubit. *Phys. Rev. B*, 75(14):140515, April 2007.

[260] Matthias Steffen, Shwetank Kumar, David P. DiVincenzo, J. R. Rozen, George A. Keefe, Mary Beth Rothwell, and Mark B. Ketchen. High-Coherence Hybrid Superconducting Qubit. *Phys. Rev. Lett.*, 105(10):100502, September 2010.

[261] M.A. Yurtalan, J. Shi, G.J.K. Flatt, and A. Lupascu. Characterization of Multilevel Dynamics and Decoherence in a High-Anharmonicity Capacitively Shunted Flux Circuit. *Phys. Rev. Appl.*, 16(5):054051, November 2021.

[262] Aaron Somoroff, Quentin Ficheux, Raymond A. Mencia, Haonan Xiong, Roman V. Kuzmin, and Vladimir E. Manucharyan. Millisecond coherence in a superconducting qubit, March 2021.

[263] K. Kakuyanagi, T. Meno, S. Saito, H. Nakano, K. Semba, H. Takayanagi, F. Deppe, and A. Shnirman. Dephasing of a Superconducting Flux Qubit. *Physical Review Letters*, 98(4):047004, January 2007.

[264] Radoslaw C. Bialczak, R. McDermott, M. Ansmann, M. Hofheinz, N. Katz, Erik Lucero, Matthew Neeley, A. D. O'Connell, H. Wang, A. N. Cleland, and John M. Martinis. $1/f$ Flux Noise in Josephson Phase Qubits. *Physical Review Letters*, 99(18):187006, November 2007.

[265] T. Lanting, A. J. Berkley, B. Bumble, P. Bunyk, A. Fung, J. Johansson, A. Kaul, A. Kleinsasser, E. Ladizinsky, F. Maibaum, R. Harris, M. W. Johnson, E. Tolkacheva, and M. H. S. Amin. Geometrical dependence of the low-frequency noise in superconducting flux qubits. *Phys. Rev. B*, 79(6):060509(R), feb 2009.

[266] Fumiki Yoshihara, Yasunobu Nakamura, Fei Yan, Simon Gustavsson, Jonas Bylander, William D. Oliver, and Jaw-Shen Tsai. Flux qubit noise spectroscopy using Rabi oscillations under strong driving conditions. *Physical Review B*, 89(2):020503, January 2014.

[267] P. Bertet, I. Chiorescu, G. Burkard, K. Semba, C. J. P. M. Harmans, D. P. DiVincenzo, and J. E. Mooij. Dephasing of a Superconducting Qubit Induced by Photon Noise. *Phys. Rev. Lett.*, 95(25):257002, December 2005.

[268] D. I. Schuster, A. Wallraff, A. Blais, L. Frunzio, R.-S. Huang, J. Majer, S. M. Girvin, and R. J. Schoelkopf. Ac Stark Shift and Dephasing of a Superconducting Qubit Strongly Coupled to a Cavity Field. *Physical Review Letters*, 94(12):123602, March 2005.

[269] Chad Rigetti, Jay M. Gambetta, Stefano Poletto, B. L. T. Plourde, Jerry M. Chow, A. D. Córcoles, John A. Smolin, Seth T. Merkel, J. R. Rozen, George A. Keefe, Mary B. Rothwell, Mark B. Ketchen, and M. Steffen. Superconducting qubit in a waveguide cavity with a coherence time approaching 0.1 ms. *Physical Review B*, 86(10):100506, September 2012.

[270] Fei Yan, Dan Campbell, Philip Krantz, Morten Kjaergaard, David Kim, Jonilyn L. Yoder, David Hover, Adam Sears, Andrew J. Kerman, Terry P. Orlando, Simon Gustavsson, and William D. Oliver. Distinguishing Coherent and Thermal Photon Noise in a Circuit Quantum Electrodynamical System. *Physical Review Letters*, 120(26):260504, June 2018.

[271] John M. Martinis, K. B. Cooper, R. McDermott, Matthias Steffen, Markus Ansmann, K. D. Osborn, K. Cicak, Seongshik Oh, D. P. Pappas, R. W. Simmonds, and Clare C. Yu. Decoherence in Josephson Qubits from Dielectric Loss. *Physical Review Letters*, 95(21):210503, November 2005.

[272] C. Wang, C. Axline, Y. Y. Gao, T. Brecht, Y. Chu, L. Frunzio, M. H. Devoret, and R. J. Schoelkopf. Surface participation and dielectric loss in superconducting qubits. *Applied Physics Letters*, 107(16):162601, October 2015.

[273] Jay M. Gambetta, Conal E. Murray, Y.-K.-K. Fung, Douglas T. McClure, Oliver Dial, William Shanks, Jeffrey W. Sleight, and Matthias Steffen. Investigating Surface Loss Effects in Superconducting Transmon Qubits. *IEEE Transactions on Applied Superconductivity*, 27(1):1–5, January 2017.

[274] T. Chang, T. Cohen, I. Holzman, G. Catelani, and M. Stern. Tunable superconducting flux qubits with long coherence times, July 2022.

[275] T. Chang, I. Holzman, T. Cohen, B. C. Johnson, D. N. Jamieson, and M. Stern. Reproducibility and control of superconducting flux qubits, July 2022.

[276] Hantao Sun, Feng Wu, Hsiang-Sheng Ku, Xizheng Ma, Jin Qin, Zhijun Song, Tenghui Wang, Gengyan Zhang, Jingwei Zhou, Yaoyun Shi, Hui-Hai Zhao, and Chunqing Deng. Characterization of loss mechanisms in a fluxonium qubit, February 2023.

[277] D. J. Van Harlingen, T. L. Robertson, B. L. T. Plourde, P. A. Reichardt, T. A. Crane, and John Clarke. Decoherence in Josephson-junction qubits due to critical-current fluctuations. *Phys. Rev. B*, 70(6):064517, August 2004.

[278] Fei Yan, Jonas Bylander, Simon Gustavsson, Fumiki Yoshihara, Khalil Harrabi, David G. Cory, Terry P. Orlando, Yasunobu Nakamura, Jaw-Shen Tsai, and William D. Oliver. Spectroscopy of low-frequency noise and its temperature dependence in a superconducting qubit. *Phys. Rev. B*, 85(17):174521, May 2012.

[279] Yuki Bando, Ka-Wa Yip, Huo Chen, Daniel A. Lidar, and Hidetoshi Nishimori. Breakdown of the Weak-Coupling Limit in Quantum Annealing. *Phys. Rev. Appl.*, 17(5):054033, May 2022.

[280] Andrew D. King, Sei Suzuki, Jack Raymond, Alex Zucca, Trevor Lanting, Fabio Altomare, Andrew J. Berkley, Sara Ejtemaee, Emile Hoskinson, Shuiyuan Huang, and others. Coherent quantum annealing in a programmable 2,000 qubit Ising chain. *Nat. Phys.*, pages 1–5, September 2022.

[281] S. Krinner, S. Storz, P. Kurpiers, P. Magnard, J. Heinsoo, R. Keller, J. Lütolf, C. Eichler, and A. Wallraff. Engineering cryogenic setups for 100-qubit scale superconducting circuit systems. *EPJ Quantum Technology*, 6(1):1–29, December 2019.

[282] A. A. Houck, J. A. Schreier, B. R. Johnson, J. M. Chow, Jens Koch, J. M. Gambetta, D. I. Schuster, L. Frunzio, M. H. Devoret, S. M. Girvin, and R. J. Schoelkopf. Controlling the Spontaneous Emission of a Superconducting Transmon Qubit. *Phys. Rev. Lett.*, 101(8):080502, August 2008.

[283] Ioan M. Pop, Kurtis Geerlings, Gianluigi Catelani, Robert J. Schoelkopf, Leonid I. Glazman, and Michel H. Devoret. Coherent suppression of electromagnetic dissipation due to superconducting quasiparticles. *Nature*, 508(7496):369–372, April 2014.

[284] Clemens Müller, Jared H. Cole, and Jürgen Lisenfeld. Towards understanding two-level-systems in amorphous solids: Insights from quantum circuits. *Rep. Prog. Phys.*, 82(12):124501, October 2019.

[285] R. Barends, J. Kelly, A. Megrant, D. Sank, E. Jeffrey, Y. Chen, Y. Yin, B. Chiaro, J. Mutus, C. Neill, P. O'Malley, P. Roushan, J. Wenner, T. C. White, A. N. Cleland, and John M. Martinis. Coherent Josephson Qubit Suitable for Scalable Quantum Integrated Circuits. *Physical Review Letters*, 111(8):080502, August 2013.

[286] J. H. Béjanin, C. T. Earnest, A. S. Sharafeldin, and M. Mariantoni. Interacting defects generate stochastic fluctuations in superconducting qubits. *Phys. Rev. B*, 104(9):094106, September 2021.

[287] Simon Gustavsson, Jonas Bylander, Fei Yan, William D. Oliver, Fumiki Yoshihara, and Yasunobu Nakamura. Noise correlations in a flux qubit with tunable tunnel coupling. *Phys. Rev. B*, 84(1), 2011.

[288] Zachary Morrell, Marc Vuffray, Andrey Lokhov, Andreas Bärtschi, Tameem Albash, and Carleton Coffrin. Signatures of Open and Noisy Quantum Systems in Single-Qubit Quantum Annealing, August 2022.

[289] Keiji Saito, Martijn Wubs, Sigmund Kohler, Yosuke Kayanuma, and Peter Hänggi. Dissipative Landau-Zener transitions of a qubit: Bath-specific and universal behavior. *Phys. Rev. B*, 75(21):214308, June 2007.

[290] T. Lanting, M. H. S. Amin, M. W. Johnson, F. Altomare, A. J. Berkley, S. Gildert, R. Harris, J. Johansson, P. Bunyk, E. Ladizinsky, E. Tolkacheva, and D. V. Averin. Probing high-frequency noise with macroscopic resonant tunneling. *Phys. Rev. B*, 83(18):180502, May 2011.

[291] M. Bal, M. H. Ansari, J.-L. Orgiazzi, R. M. Lutchyn, and A. Lupascu. Dynamics of parametric fluctuations induced by quasiparticle tunneling in superconducting flux qubits. *Phys. Rev. B*, 91(19):195434, May 2015.

[292] L. D. Landau. Zur Theorie der Energieubertragung II. *Phys. Z. Sowjetunion*, 2:46–51, 1932.

[293] Clarence Zener. Non-adiabatic crossing of energy levels. *Proc. R. Soc. London, Ser. A*, 137(833):696–702, 1932.

[294] Ettore Majorana. Atomi orientati in campo magnetico variabile. *Nuovo. Cim.*, 9(2):43–50, 1932.

[295] Ernst CG Stückelberg. Theory of inelastic collisions between atoms, using two simultaneous differential equations. *Helv. Phys. Acta*, 5:369–422, 1932.

[296] Evgenii E. Nikitin and Stanislav Ya. Umanskii. *Theory of Slow Atomic Collisions*, volume 30 of *Springer Series in Chemical Physics*. Springer Berlin Heidelberg, 1984.

[297] Peter Hänggi, Peter Talkner, and Michal Borkovec. Reaction-rate theory: Fifty years after Kramers. *Rev. Mod. Phys.*, 62(2):251–341, 1990.

[298] Michael N. Leuenberger, Florian Meier, and Daniel Loss. Quantum Spin Dynamics in Molecular Magnets. In Wolfgang Linert and Michel Verdaguer, editors, *Molecular Magnets Recent Highlights*, pages 101–117. Springer, 2003.

[299] Ping Ao and Jo/rgen Rammer. Quantum dynamics of a two-state system in a dissipative environment. *Phys. Rev. B*, 43(7):5397–5418, 1991.

[300] Yosuke Kayanuma and Hiroyuki Nakayama. Nonadiabatic transition at a level crossing with dissipation. *Phys. Rev. B*, 57(20):13099–13112, 1998.

[301] William D. Oliver, Yang Yu, Janice C. Lee, Karl K. Berggren, Leonid S. Levitov, and Terry P. Orlando. Mach-Zehnder Interferometry in a Strongly Driven Superconducting Qubit. *Science*, 310(5754):1653–1657, 2005.

[302] A. Zenesini, H. Lignier, G. Tayebirad, J. Radogostowicz, D. Ciampini, R. Mannella, S. Wimberger, O. Morsch, and E. Arimondo. Time-Resolved Measurement of Landau-Zener Tunneling in Periodic Potentials. *Phys. Rev. Lett.*, 103(9):090403, 2009.

[303] F. Troiani, C. Godfrin, S. Thiele, F. Balestro, W. Wernsdorfer, S. Klyatskaya, M. Ruben, and M. Affronte. Landau-Zener Transition in a Continuously Measured Single-Molecule Spin Transistor. *Phys. Rev. Lett.*, 118(25):257701, 2017.

[304] S. S. Zhang, W. Gao, H. Cheng, L. You, and H. P. Liu. Symmetry-Breaking Assisted Landau-Zener Transitions in Rydberg Atoms. *Phys. Rev. Lett.*, 120(6):063203, 2018.

[305] Guang Yuan Zhu, Yi Qin, Miao Meng, Suman Mallick, Hang Gao, Xiaoli Chen, Tao Cheng, Ying Ning Tan, Xuan Xiao, Mei Juan Han, Mei Fang Sun, and Chun Y. Liu. Crossover between the adiabatic and nonadiabatic electron transfer limits in the Landau-Zener model. *Nat. Commun.*, 12(1):456, 2021.

[306] Mika Sillanpää, Teijo Lehtinen, Antti Paila, Yuriy Makhlin, and Pertti Hakonen. Continuous-Time Monitoring of Landau-Zener Interference in a Cooper-Pair Box. *Phys. Rev. Lett.*, 96(18):187002, 2006.

[307] C. M. Quintana, K. D. Petersson, L. W. McFaul, S. J. Srinivasan, A. A. Houck, and J. R. Petta. Cavity-Mediated Entanglement Generation Via Landau-Zener Interferometry. *Phys. Rev. Lett.*, 110(17):173603, 2013.

[308] M. H. S. Amin and Dmitri V. Averin. Macroscopic Resonant Tunneling in the Presence of Low Frequency Noise. *Phys. Rev. Lett.*, 100(19), 2008.

[309] J. Johansson, M. H. S. Amin, A. J. Berkley, P. Bunyk, V. Choi, R. Harris, M. W. Johnson, T. M. Lanting, Seth Lloyd, and G. Rose. Landau-Zener transitions in a superconducting flux qubit. *Phys. Rev. B*, 80(1):012507, 2009.

[310] Martijn Wubs, Keiji Saito, Sigmund Kohler, Peter Hänggi, and Yosuke Kayanuma. Gauging a Quantum Heat Bath with Dissipative Landau-Zener Transitions. *Phys. Rev. Lett.*, 97(20):200404, 2006.

[311] Ping Ao and Jo?rgen Rammer. Influence of dissipation on the Landau-Zener transition. *Physical Review Letters*, 62(25):3004–3007, June 1989.

[312] V. L. Pokrovsky and D. Sun. Fast quantum noise in the Landau-Zener transition. *Physical Review B*, 76(2):024310, July 2007.

[313] Yosuke Kayanuma. Nonadiabatic Transitions in Level Crossing with Energy Fluctuation. I. Analytical Investigations. *Journal of the Physical Society of Japan*, 53(1):108–117, January 1984.

[314] Yosuke Kayanuma. Population Inversion in Optical Adiabatic Rapid Passage with Phase Relaxation. *Physical Review Letters*, 58(19):1934–1936, May 1987.

[315] P. Nalbach and M. Thorwart. Landau-Zener Transitions in a Dissipative Environment: Numerically Exact Results. *Phys. Rev. Lett.*, 103(22):220401, 2009.

[316] Luca Arceci, Simone Barbarino, Rosario Fazio, and Giuseppe E. Santoro. Dissipative Landau-Zener problem and thermally assisted Quantum Annealing. *Phys. Rev. B*, 96(5):054301, 2017.

[317] E. J. Crosson and D. A. Lidar. Prospects for quantum enhancement with diabatic quantum annealing. *Nat. Rev. Phys.*, 3(7):466–489, 2021.

[318] Anatoly Yu Smirnov and Mohammad H. Amin. Theory of open quantum dynamics with hybrid noise. *New J. Phys.*, 20(10):103037, 2018.

[319] P. Nalbach. Adiabatic-Markovian bath dynamics at avoided crossings. *Phys. Rev. A*, 90(4):042112, 2014.

[320] Huo Chen and Daniel A. Lidar. HOQST: Hamiltonian Open Quantum System Toolkit, 2020.

[321] Alexander Shnirman, Gerd Schön, Ivar Martin, and Yuriy Makhlin. Low- and High-Frequency Noise from Coherent Two-Level Systems. *Physical Review Letters*, 94(12):127002, April 2005.

[322] Lara Faoro and Lev B. Ioffe. Microscopic Origin of Low-Frequency Flux Noise in Josephson Circuits. *Physical Review Letters*, 100(22):227005, June 2008.

[323] Yuki Bando, Ka-Wa Yip, Huo Chen, Daniel A. Lidar, and Hidetoshi Nishimori. Breakdown of the weak coupling limit in experimental quantum annealing, 2021.

[324] Andrew D. King, Sei Suzuki, Jack Raymond, Alex Zucca, Trevor Lanting, Fabio Altomare, Andrew J. Berkley, Sara Ejtemaee, Emile Hoskinson, Shuiyuan Huang, et al. Coherent quantum annealing in a programmable 2000-qubit Ising chain. *arXiv:2202.05847*, February 2022.

[325] S. Javanbakht, P. Nalbach, and M. Thorwart. Dissipative Landau-Zener quantum dynamics with transversal and longitudinal noise. *Phys. Rev. A*, 91(5):052103, May 2015.

[326] Sergio O. Valenzuela, William D. Oliver, David M. Berns, Karl K. Berggren, Leonid S. Levitov, and Terry P. Orlando. Microwave-Induced Cooling of a Superconducting Qubit. *Science*, 314(5805):1589–1592, 2006.

[327] Evgeny Mozgunov and Daniel Lidar. Completely positive master equation for arbitrary driving and small level spacing. *Quantum*, 4:227, 2020.

[328] P. Dutta and P. M. Horn. Low-frequency fluctuations in solids: 1 f noise. *Reviews of Modern Physics*, 53(3):497–516, July 1981.

[329] Xinyuan You, Aashish A. Clerk, and Jens Koch. Positive- and negative-frequency noise from an ensemble of two-level fluctuators. *Physical Review Research*, 3(1):013045, January 2021.

[330] C. Macklin, K. O'Brien, D. Hover, M. E. Schwartz, V. Bolkhovsky, X. Zhang, W. D. Oliver, and I. Siddiqi. A near–quantum-limited josephson traveling-wave parametric amplifier. *Science*, 350(6258):307–310, oct 2015.

[331] F. Yoshihara, Y. Nakamura, and J. S. Tsai. Correlated flux noise and decoherence in two inductively coupled flux qubits. *Phys. Rev. B*, 81(13), 2010.

APPENDICES

Appendix A

Details of circuit quantization

In this section, we discuss details of the numerical simulation of superconducting circuits, complementing the discussion in Sec. 2.1.2.

A.1 Efficient numerical representation

First, we introduce an alternative way to write down the inductive energy that is analogous to the capacitive energy, in anticipation of the fact that they can later be combined to give energy expressions like harmonic oscillators. This is done by first considering the branch inductance matrix $\mathbf{L}_B$, with dimensions $N_B \times N_B$ where N_B is the total number of branches in the circuit. The only non-zero entries of the branch inductance matrix are the inductances of a branch, which are on the diagonals, and mutual inductances between two branches, which are on the off-diagonals. Next, we define an inductive transformation matrix R_{BN}, with dimension $N_B \times N_N$. Its entries are $+1$ for the ending node of an inductive branch, and -1 for the starting node of an inductive branch. Combining $\mathbf{L}_b$ and $\mathbf{R}_{\mathrm{BN}}$, we can define the inverse node inductance matrix

$$\mathbf{L}_n^{-1} = \mathbf{R}_{\mathrm{BN}}^T \mathbf{L}_b^+ \mathbf{R}_{\mathrm{BN}}, \tag{A.1}$$

where the superscript $+$ denotes pseudo inverse. If we have chosen our branching tree such that there are only Josephson junctions in $\mathcal{L}$ (which is always possible as long as there are

no inductor-only loops), we have in terms of $\mathbf{L}_n^{-1}$ the inductive energy [1]

$$U_{\text{ind}} = \frac{\phi_0}{2}(\vec{\varphi_N})^T \mathbf{L}_n^{-1}(\vec{\varphi_N}). \tag{A.2}$$

Following [40], an efficient numerical representation of the circuit Hamiltonian requires distinguishing different types of coordinates

- Harmonic oscillator coordinates. Nodes that are connected to inductors lead to such coordinates. The potential energy goes to ∞ when such coordinates go to ∞.
- Josephson coordinates. Nodes that are connected to Josephson junctions and no inductors lead to such coordinates. The Hamiltonian is invariant under a 2π shift of such coordinates.
- Island coordinates. Nodes that are only connected to capacitors lead to such coordinates. Such coordinates do not appear in the potential energy, and the conjugate momentum is a conserved quantity.

To explicitly keep track of the different types of coordinates, we define a transformation matrix $\mathbf{R}$ that is of size $N_N \times N_N$. This transformation is not unique, but the optimal choice could lead to faster convergence of the numerical simulation. The transformed coordinates and conjugate momentum are

$$\vec{\varphi} = \mathbf{R}\vec{\varphi}_N, \tag{A.3}$$
$$\vec{p} = (\mathbf{R}^T)^{-1}\vec{p}_N. \tag{A.4}$$

Any such transformation should preserve the commutation relations, i.e. $[\varphi_i, p_j] = i\delta_{ij}$. After this transformation, the circuit Hamiltonian is given by

$$\begin{aligned} H_{\text{circ}} = &\frac{1}{2\phi_0^2}\vec{p}^T\mathbf{C}^{-1}\vec{p} \\ &+ \frac{\phi_0}{2}\vec{\varphi}^T\mathbf{L}^{-1}\vec{\varphi} \\ &- \sum_i E_{j,i}\cos\varphi_i, \end{aligned} \tag{A.5}$$

[1] If there are inductors in $\mathcal{L}$, the flux bias needs to go into the expression for the inductive energy of these inductors.

where in the last line, the phase across the i'th Josephson junction can be expressed in the new coordinates using $\vec{\varphi}_N = \mathbf{R}^{-1}\vec{\varphi}$ and applying Eq. 2.11. The new inverse capacitance and inductance matrix are defined as $\mathbf{C}^{-1} = \mathbf{R}\mathbf{C}_N^{-1}\mathbf{R}^T$ and $\mathbf{L}^{-1} = (\mathbf{R}^T)^{-1}\mathbf{L}_N^{-1}\mathbf{R}^{-1}$.

To obtain a concrete matrix representation of the Hamiltonian, different bases are used for different types of coordinates. For Josephson coordinates, the natural basis is the charge basis, where

$$p|n\rangle = \hbar n|n\rangle \tag{A.6}$$

$$\cos\varphi = \frac{1}{2}(\exp(i\varphi) + \exp(-i\varphi)) \tag{A.7}$$

$$= \frac{1}{2}(|n\rangle\langle n+1| + |n+1\rangle\langle n|), \tag{A.8}$$

where $|n\rangle$ corresponds to the state with n Cooper pairs.

For harmonic oscillator coordinates, the natural basis is the Fock basis. Each harmonic oscillator mode is associated with a characteristic frequency and impedance,

$$\omega_i = \sqrt{\mathbf{C}_{ii}^{-1}\mathbf{L}_{ii}^{-1}} \text{ and} \tag{A.9}$$

$$Z_i = \sqrt{\frac{\mathbf{C}_{ii}^{-1}}{\mathbf{L}_{ii}^{-1}}}. \tag{A.10}$$

The operators for harmonic oscillator modes are given by

$$\varphi_i = \frac{1}{\phi_0}\sqrt{\frac{\hbar Z_i}{2}}(a_i^+ + a_i) \text{ and} \tag{A.11}$$

$$p_i = -i\phi_0\sqrt{\frac{\hbar}{2Z_i}}(a_i - a_i^+). \tag{A.12}$$

Besides, the Josephson junction connected to an inductor leads to non-linearity in the harmonic oscillator potential and gives terms of the form

$$\cos(x\varphi_i + 2\pi\delta f), \tag{A.13}$$

where $x, \delta f$ are some constant of order unity arising from the $\mathbf{R}$ transformation. The matrix form of such operator in the harmonic oscillator basis, unlike other operators previously presented, is not sparse. Care needs to be given to the $\mathbf{R}$ transformation matrix to minimize the large computational cost associated with such non-sparsity.

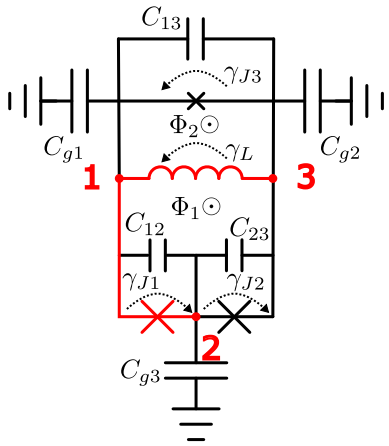

Figure A.1: An example superconducting circuit to illustrate the quantization procedure. The red lines indicate the spanning tree.

To illustrate the above procedure of circuit quantization, we look at the example circuit shown in Fig. A.1. The fluxoid quantization conditions are

$$\gamma_{J1} + \gamma_{J2} + \gamma_L + 2\pi f_1 = 0. \tag{A.14}$$

$$-\gamma_L + \gamma_{J3} + 2\pi f_2 = 0. \tag{A.15}$$

Choosing the spanning tree as highlighted in red, the circuit Hamiltonian in terms of node coordinates are

$$H_{\text{circ}} = \frac{1}{2\phi_0^2}\vec{p}_N^T \mathbf{C}_N^{-1}\vec{p}_N + E_{J1}\cos\left(\varphi_{N2} - \varphi_{N1}\right) + E_{J2}\cos\left(\varphi_{N3} - \varphi_{N2} - 2\pi f_1\right) \tag{A.16}$$

$$+E_{J3}\cos\left(\varphi_{N1} - \varphi_{N3} - 2\pi f_2\right) + \frac{\phi_0^2}{2L}(\varphi_{N1} - \varphi_{N3}), \tag{A.17}$$

where φ_{Ni} are the node generalized flux coordinates, $\vec{p}_N$ is the vector of node conjugate momenta and the node capacitance matrix is given by

$$\mathbf{C}_N = \begin{pmatrix} C_{g1} + C_{12} + C_{13} & -C_{12} & -C_{13} \\ -C_{12} & C_{g2} + C_{12} + C_{23} & -C_{23} \\ -C_{13} & -C_{23} & C_{g3} + C_{13} + C_{23} \end{pmatrix}. \tag{A.18}$$

We then introduce the transformed coordinates

$$\vec{\varphi} = \mathbf{R}\vec{\varphi}_N \tag{A.19}$$

$$\mathbf{R} = \begin{pmatrix} -1 & 1 & 0 \\ 1 & 0 & -1 \\ 1 & 1 & 1 \end{pmatrix}. \tag{A.20}$$

After the transformation, φ_1 is a Josephson mode, φ_2 is a harmonic oscillator mode, and the third mode φ_3 is an island mode corresponding to charge conservation in the island. The Hamiltonian after the transformation is

$$H_{\text{circ}} = \frac{1}{2\phi_0}\vec{p}^T\mathbf{C}^{-1}\vec{p} + \frac{\phi_0^2}{2}\vec{\varphi}^T\mathbf{L}^{-1}\vec{\varphi} + E_{J1}\cos\widetilde{\varphi}_1 + E_{J2}\cos\left(-\varphi_1 - \varphi_2 - 2\pi f_1\right) + E_{J3}\cos\left(\varphi_2 - 2\pi f_2\right), \tag{A.21}$$

where

$$\mathbf{C}^{-1} = \mathbf{R}\mathbf{C}_N^{-1}\mathbf{R}^T \tag{A.22}$$

$$\mathbf{L}^{-1} = (\mathbf{R}^T)^{-1}\begin{pmatrix} \frac{1}{L} & 0 & -\frac{1}{L} \\ 0 & 0 & 0 \\ -\frac{1}{L} & 0 & \frac{1}{L} \end{pmatrix}\mathbf{R}^{-1} \tag{A.23}$$

$$= \begin{pmatrix} 0 & 0 & 0 \\ 0 & \frac{1}{L} & 0 \\ 0 & 0 & 0 \end{pmatrix} \tag{A.24}$$

A.2 Combining subcircuits

When a large circuit is made by coupling a few subcircuits together inductively or capacitively, it is desirable to first numerically diagonalize the subcircuits and then combine them together, to avoid the large computational cost of directly diagonalizing the large coupled circuit. When doing this, it needs to be noted that the coupling, besides generating the interaction terms, also leads to inductive/capacitive loading of each subcircuit.

For example, when considering two superconducting circuits joined capacitively, the combined capacitance matrix can be written in block-matrix form as

$$\mathbf{C}_N = \begin{pmatrix} \mathbf{C}_{N1} & \mathbf{C}_{N12} \\ \mathbf{C}_{N21} & \mathbf{C}_{N2} \end{pmatrix}, \tag{A.25}$$

where $\mathbf{C}_{N1,2}$ are the node capacitance matrix of the respective subcircuit, and $\mathbf{C}_{12} = \mathbf{C}_{21}^T$ describes the capacitive coupling between the subcircuits. Taking the inverse of the above matrix, we obtain

$$\mathbf{C}_N^{-1} = \begin{pmatrix} \overline{\mathbf{C}}_{N1}^{-1} & \overline{\mathbf{C}}_{N12}^{-1} \\ \overline{\mathbf{C}}_{N21}^{-1} & \overline{\mathbf{C}}_{N2}^{-1} \end{pmatrix}, \tag{A.26}$$

where $\overline{\mathbf{C}}_{N1,2}^{-1}$ are in general different from $\mathbf{C}_{N1,2}^{-1}$ and captures the capacitive loading effect.

Similarly for inductive interactions between two subcircuits, we first write down the branch inductance matrix in block matrix form

$$\mathbf{L}_B = \begin{pmatrix} \mathbf{L}_{B1} & \mathbf{L}_{B12} \\ \mathbf{L}_{B21} & \mathbf{L}_{B2} \end{pmatrix}. \tag{A.27}$$

The branch inductance matrix is then converted to the inverse node inductance matrix via

$$\mathbf{L}_N^{-1} = \begin{pmatrix} R_{\mathrm{BN1}} & \mathbf{0} \\ \mathbf{0} & R_{\mathrm{BN2}} \end{pmatrix} \mathbf{L}_B^{+} \begin{pmatrix} R_{\mathrm{BN1}} & \mathbf{0} \\ \mathbf{0} & R_{\mathrm{BN2}} \end{pmatrix} = \begin{pmatrix} \overline{\mathbf{L}}_{N1}^{-1} & \overline{\mathbf{L}}_{N12}^{-1} \\ \overline{\mathbf{L}}_{N21}^{-1} & \overline{\mathbf{L}}_{N2}^{-1} \end{pmatrix}, \tag{A.28}$$

where $R_{\mathrm{BN1,2}}$ are the node-to-branch transformation matrix for subcircuit 1 and 2, and $\overline{\mathbf{L}}_{n1,2}$ are the loaded inverse node inductance matrix.

Appendix B

Measurement setup and wiring for Chapters 3 and 4

In Fig. B.1 we present a diagram of the setup showing the room temperature electronics and the wiring inside the dilution refrigerator. Arbitrary waveform generators (AWG) are used for flux biasing the circuit. The AWGs (Keysight AWG3202A) can supply voltages ranging from $-1.5\,\mathrm{V}$ to $+1.5\,\mathrm{V}$ with 14 bits of precision. The bias current is carried to the packaged chip through twisted wires. Inline resistors of appropriate resistances (typically $1000\,\Omega$) are used to apply current leading to a voltage-to-flux conversion of the order of $1\,\Phi_0/V$. The twisted wires have a limited bandwidth of about $10\,\mathrm{MHz}$. Later generations of the experiment employ customized wiring, which is designed to have higher bandwidth. The qubit can also be driven with a capacitively coupled gate voltage, supplied by an rf source (Rohde-Schwarz SGS100A), through a coaxial cable.

For readout, the output signal from the device first goes through two Quinstar 4-16 GHz isolators. It is then combined with a pump pulse through a Marki 1-16GHz directional coupler, before going into the traveling-wave-parametric-amplifier (TWPA) [330] at the mixing chamber of the dilution refrigerator. The signal goes through another two isolators and a 12GHz low-pass filter, before being amplified again at the 3K stage by an LNF 4-8GHz high-electron-mobility transistor (HEMT) amplifier. At room temperature, two setups are used for readout. In the first, a KeySight N5222a Vector Network Analyzer is used to measure transmission through the device. In the other, the readout pulse is generated by the AWG, which is then upconverted by combining with a stable tone from a microwave synthesizer (Agilent PSG 8275A), through an IQ mixer (Marki MLIQ-0218). The output of the device is then demodulated by another IQ mixer and goes through two

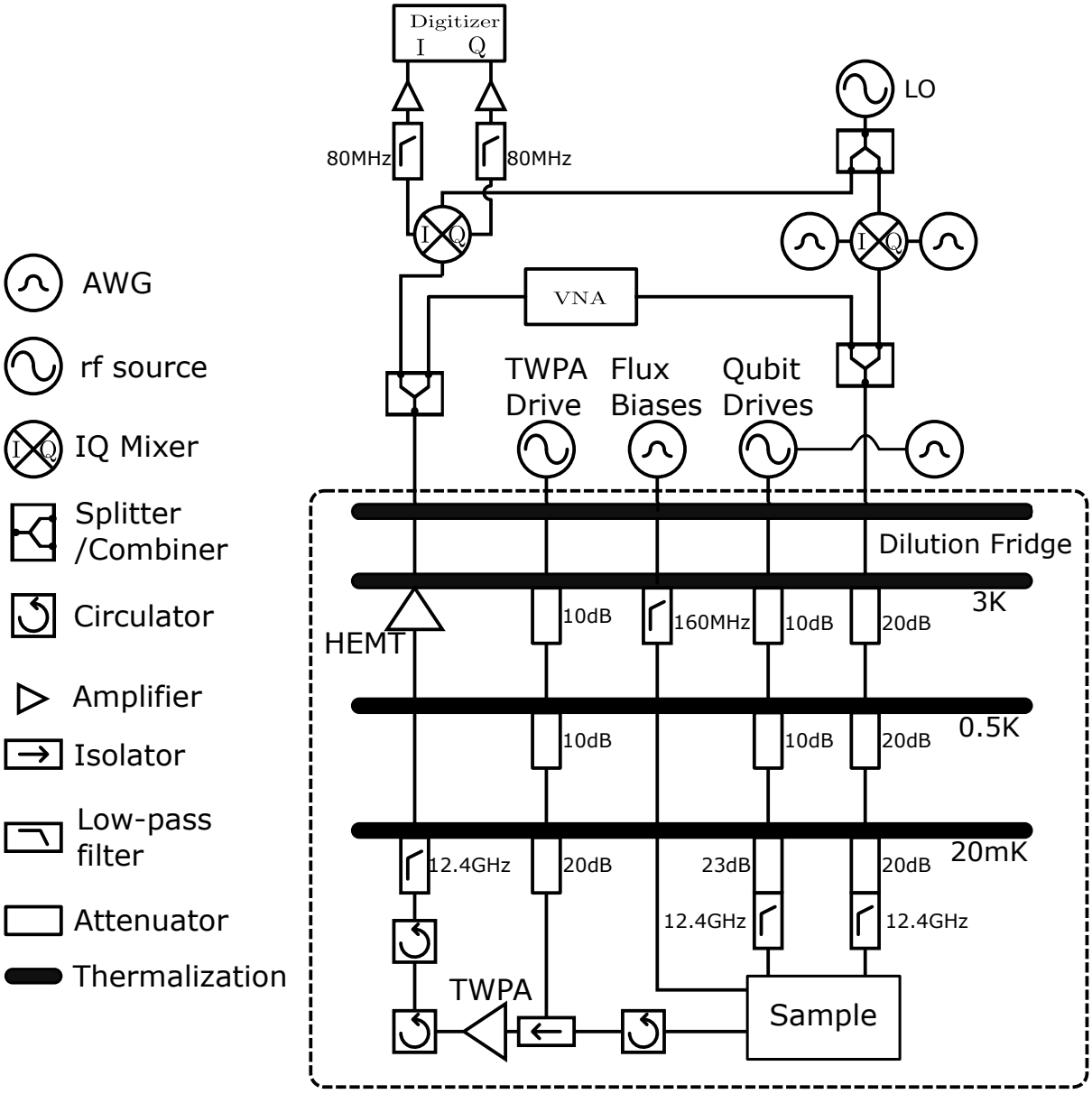

Figure B.1: Measurement Setup for crosstalk calibration and coupler chain experiments.

80MHz filters, after which it gets processed by a field programmable gate array (FPGA) digitizer (KeySight M3102A).

Appendix C

Measurement setup and wiring for Chapters 5 and 6

In Figure C.1 we present a diagram of the room-temperature and cryogenic setup used in the experiments. The qubit flux bias for the x and z loops, Φ_x and Φ_z, are controlled by currents generated by a DC voltage source and a high bandwidth source, combined through a bias tee at the mixing chamber stage of the dilution refrigerator. The DC biases are supplied by Yokogawa GS 200 voltage sources through twisted pair cable and low-pass filtered to below 32 kHz to minimize noise. The high bandwidth components of the current are supplied by a 1 GHz arbitrary waveform generators (AWGs) (Keysight M3202A), through coaxial cables. The fast line coupling to Φ_x suffered from a cold open during the cooldown and is not used for the Landau-Zener experiment. The attenuators and filters on the cable are chosen to allow a sufficiently large current range for driving Rabi oscillation and performing annealing experiments, while minimizing decoherence due to thermal and electronic noise. The resonator SQUID bias is supplied by an AWG (Keysight M3202A), but through twisted pair cable. The qubit can be driven with a capacitively coupled driving line, supplied by an rf source with an integrated IQ modulator, through a coaxial cable. The readout signal is amplified by a traveling-wave-parametric-amplifier (TWPA) [330] at the mixing chamber stage of the fridge, followed by a high-electron mobility transistor amplifier (HEMT) at the 4K stage, and room temperature amplifiers, before being processed by a field-programmable gate array (FPGA) digitizer (Keysight M3102A).

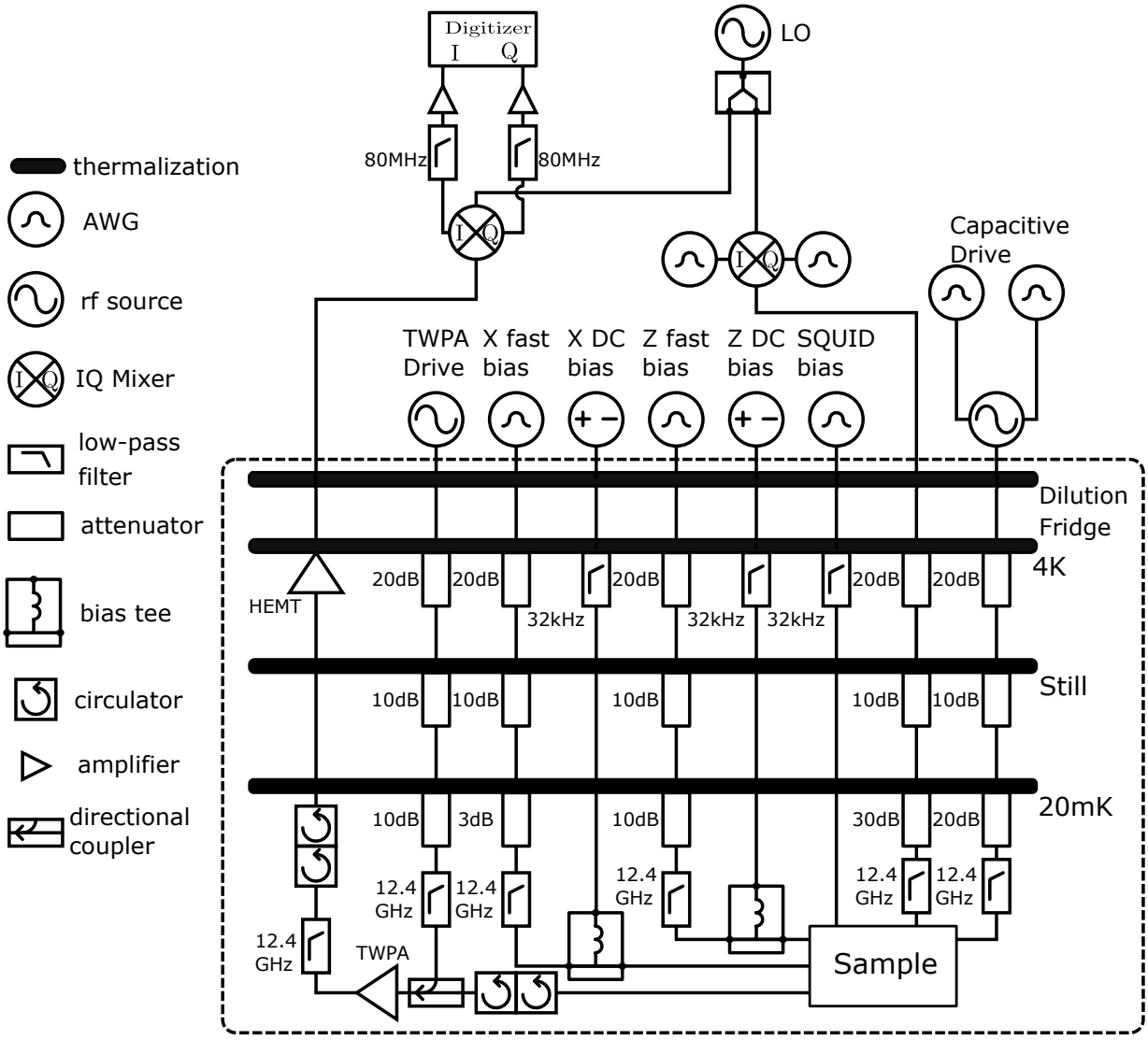

Figure C.1: Measurement setup for decoherence and LZ measurements.

Appendix D

Qubit, coupler and QFP loop geometry

The qubits, couplers, and QFPs used in this thesis all have two fundamental loops, denoted by z', x, and they all share the same symmetrized X loop design. In this appendix, we discuss the reason for this design. Figure D.1 shows the circuit schematic of a two-loop device, using the tunable flux qubit as an example, including the flux bias lines. The panels D.1(a, b) show a planar and a symmetrized X loop geometry respectively. In both cases, the flux biases are applied through the loops labeled x and z'. These loops are defined as follows:

$$x : 1 \xrightarrow{\text{red}} 3 \xrightarrow{\text{yellow}} 1, \text{ and} \tag{D.1}$$

$$z' : 1 \xrightarrow{\text{blue}} 2 \xrightarrow{\text{blue}} 3 \xrightarrow{\text{red}} 1, \tag{D.2}$$

where the numbers are the node indices, as indicated in Fig. D.1. The external fluxes in these two loops are denoted by $\Phi_x, \Phi_{z'}$ respectively.[1]

We also introduced the compensated Z bias flux bias

$$\Phi_z = \Phi_{z'} + \frac{1}{2}\Phi_x. \tag{D.3}$$

As discussed in Sec. 2.1.3, $\Phi_z = (1/2 + n)\Phi_z$ corresponds to the symmetry point of the circuit, provided the two junctions in the x-loop have identical sizes [166]. Around the

[1] Or f_x, $f_{z'}$, which is the flux biases normalized by the flux quantum, Φ_0, as is used in Chapters 3, 4.

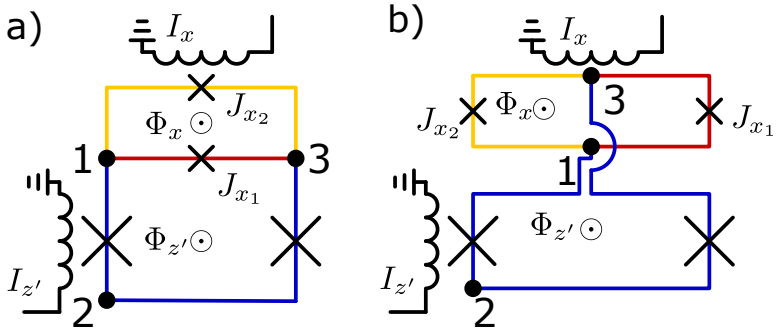

Figure D.1: Schematic of the tunable flux qubit, in a (a) planar geometry and a (b) symmetrized X loop geometry. In both cases, the red and blue arms form the z' loop and the red and yellow arms form the x loop. Bias line currents $I_{z'}, I_x$ induce fluxes in the loops through their mutual inductances to the loops. While the x and z' are intended to induce coupling to their respective loops, unintended crosstalk exists.

symmetry point, the Hamiltonian projected onto the subspace formed by the lowest two energy eigenstates can be written as

$$H = -I_p(\Phi_x)\left(\Phi_z - \Phi_{z,\text{sym}}\right)\sigma_z - \frac{\Delta(\Phi_x)}{2}\sigma_x, \tag{D.4}$$

where I_p is the persistent current and Δ is the gap at the symmetry point. During a typical quantum annealing experiment, one starts with large Δ and ends with minimal $\Delta \approx 0$. This corresponds to varying Φ_x from $1/2\Phi_0$ to 0, while keeping Φ_z close to the symmetry point $\Phi_{z,\text{sym}}$. As the flux qubit energy is very sensitive to Φ_z, it is beneficial to keep the excursion in its corresponding bias current I_z small during the annealing, so that pulse distortion does not cause significant errors. This motivates the symmetrized X-loop design, as used in the coupler design in Ref. [55]. An illustration of the design is shown in Fig. D.1(b). In this geometry, the mutual between the x bias line and z'-loop, $M_{z'x}$, is designed to be about $-1/2$ of the mutual between the x bias line and the x-loop, M_{xx}. The relation between the two control loop fluxes and bias current becomes

$$\begin{pmatrix}\Phi_z\\ \Phi_x\end{pmatrix} = \begin{pmatrix}1 & \frac{1}{2}\\ 0 & 1\end{pmatrix}\begin{pmatrix}\Phi_{z'}\\ \Phi_x\end{pmatrix} \tag{D.5}$$

$$= \begin{pmatrix}1 & \frac{1}{2}\\ 0 & 1\end{pmatrix}\begin{pmatrix}M_{z'z} & M_{z'x}\\ M_{xz} & M_{xx}\end{pmatrix}\begin{pmatrix}I_z\\ I_x\end{pmatrix} \tag{D.6}$$

$$= \begin{pmatrix}M_{z'z} + \frac{1}{2}M_{xz} & M_{z'x} + \frac{1}{2}M_{xx}\\ M_{xz} & M_{xx}\end{pmatrix}\begin{pmatrix}I_z\\ I_x\end{pmatrix}. \tag{D.7}$$

Since $M_{z'x} + \frac{1}{2}M_{xx} \approx 0$ by the symmetrized design, Φ_z remains largely unchanged when I_x pulses are applied. This hence minimizes the excursions in I_z during annealing experiments.

D.1 Bias periodicities during calibration

Since z',x loops are physical loops in the superconducting circuit, properties of the circuit can be considered as a lattice in the $\Phi_{z'}, \Phi_x$ coordinates, with primitive lattice vectors $(1,0)^T$ and $(0,1)^T$. In the flux coordinates Φ_z, Φ_x, the primitive lattice vectors become $(1,0)^T$ and $(1/2,1)^T$. During CISCIQ iterations and error measurements, it is easier to work with another set of independent lattice vectors $(1,0)^T$ and $(0,2)^T$ in the Φ_z, Φ_x coordinates. This means that when periodic steps are used for the crosstalk source bias, the choice of step for x bias becomes $2\,\Phi_0$ instead of $1\,\Phi_0$.

D.2 Flux noise correlations

An asymmetry between the critical currents of the X loop junctions shifts the symmetry point that corresponds to a symmetric double well. Since we are interested in the shift in flux bias corresponding to maximum coherence, relative to the Φ_z symmetry point, it is also useful to define $\Phi_{\tilde{z}}$, a coordinate in which the symmetry point is independent of Φ_x. This is

$$\Phi_{\tilde{z}} = \Phi_z - F(\Phi_x), \tag{D.8}$$

where $F(\Phi_x)$ is the X loop junction asymmetry induced shift.

Next, we relate the flux noise PSDs and correlations among the three different Z flux bias conventions, which further clarifies the role of loop geometry and junction asymmetry on the measured flux noise correlation. To make connection between noise in Φ_z and Φ'_z, we consider small variations in the flux biases,

$$\begin{aligned}\langle \delta\Phi_z \delta\Phi_z \rangle = \langle \delta\Phi_{z'} \delta\Phi_{z'} \rangle + \frac{1}{2}\langle \delta\Phi_{z'} \delta\Phi_x \rangle \\ + \frac{1}{2}\langle \delta\Phi_x \delta\Phi_{z'} \rangle + \frac{1}{4}\langle \delta\Phi_x \delta\Phi_x \rangle.\end{aligned} \tag{D.9}$$

This allows us to calculate the PSD of Φ_z

$$S_{\Phi_z} = S_{\Phi_{z'}} + C_{\Phi_{z'}\Phi_x} + \frac{1}{4}S_{\Phi_x}. \tag{D.10}$$

To obtain the cross PSD between S_{Φ_z} and S_{Φ_x} use

$$\langle \delta\Phi_z \delta\Phi_x \rangle = \langle \delta\Phi_{z'} \delta\Phi_x \rangle + \frac{1}{2}\langle \delta\Phi_x \delta\Phi_x \rangle, \tag{D.11}$$

which gives

$$C_{\Phi_z\Phi_x} = C_{\Phi_{z'}\Phi_x} + \frac{1}{2}S_{\Phi_x} \tag{D.12}$$

$$= c_{zx}\sqrt{S_{\Phi_z} S_{\Phi_x}} \tag{D.13}$$

Similarly, the noise in $\Phi_{\tilde{z}}$ can be related to noise in Φ_z, Φ_x by considering the relation

$$\langle \delta\Phi_{\tilde{z}} \delta\Phi_{\tilde{z}} \rangle = \langle \delta\Phi_z \delta\Phi_z \rangle - \frac{\mathrm{d}F}{\mathrm{d}\Phi_x}\langle \delta\Phi_x \delta\Phi_z \rangle$$
$$- \frac{\mathrm{d}F}{\mathrm{d}\Phi_x}\langle \delta\Phi_z \delta\Phi_x \rangle + \left(\frac{\mathrm{d}F}{\mathrm{d}\Phi_x}\right)^2 \langle \delta\Phi_x \delta\Phi_x \rangle, \tag{D.14}$$

which gives

$$S_{\Phi_{\tilde{z}}} = S_{\Phi_z} - 2\frac{\mathrm{d}F}{\mathrm{d}\Phi_x} C_{\Phi_z\Phi_x} + \left(\frac{\mathrm{d}F}{\mathrm{d}\Phi_x}\right)^2 S_{\Phi_x}. \tag{D.15}$$

For the cross PSD between $S_{\Phi_{\tilde{z}}}$ and S_{Φ_x} we use

$$\langle \delta\Phi_{\tilde{z}} \delta\Phi_x \rangle = \langle \delta\Phi_z \delta\Phi_x \rangle - \frac{\mathrm{d}F}{\mathrm{d}\Phi_x}\langle \delta\Phi_x \delta\Phi_x \rangle, \tag{D.16}$$

which gives

$$C_{\Phi_{\tilde{z}}\Phi_x} = C_{\Phi_z\Phi_x} - \frac{\mathrm{d}F}{\mathrm{d}\Phi_x} S_{\Phi_x}. \tag{D.17}$$

Previous studies [287, 331] suggest that flux noise can be explained by local fluctuating spins uniformly distributed along the surface of the circumference of the qubit loops. This model indicates the scaling of flux noise amplitude with the geometry of superconducting loops as

$$A_{\Phi_\alpha} = B\frac{l_\alpha}{w_\alpha}. \tag{D.18}$$

Here A_{Φ_α} refers to the flux noise amplitude from a particular superconducting loop or arm, B is a constant assumed to be constant for the same fabrication procedure, l_α and w_α are the length and width of a superconducting loop or arm. We can also relate the fluctuations $\delta\Phi_{z'}, \delta\Phi_x$ to the flux fluctuation contributed by spins on each of the arms in our device,

$$\delta\Phi_{z'} = -\delta\Phi_{\text{red}} + \delta\Phi_{\text{blue}} \text{ and} \tag{D.19}$$

$$\delta\Phi_x = \delta\Phi_{\text{red}} + \delta\Phi_{\text{yellow}}. \tag{D.20}$$

Then

$$\begin{aligned}\langle\delta\Phi_{z'}\delta\Phi_x\rangle &= -\langle\delta\Phi_{\text{red}}\delta\Phi_{\text{red}}\rangle - \langle\delta\Phi_{\text{red}}\delta\Phi_{\text{yellow}}\rangle \\ &+ \langle\delta\Phi_{\text{blue}}\delta\Phi_{\text{red}}\rangle + \langle\delta\Phi_{\text{blue}}\delta\Phi_{\text{yellow}}\rangle \qquad \text{(D.21)} \\ &= -\langle\delta\Phi_{\text{red}}\delta\Phi_{\text{red}}\rangle. \qquad \text{(D.22)}\end{aligned}$$

We can also obtain S_{Φ_x} in terms of the contribution from the two arms since

$$\begin{aligned}\langle\delta\Phi_x\delta\Phi_x\rangle &= \langle\delta\Phi_{\text{red}}\delta\Phi_{\text{red}}\rangle + \langle\delta\Phi_{\text{red}}\delta\Phi_{\text{yellow}}\rangle \\ &+ \langle\delta\Phi_{\text{yellow}}\delta\Phi_{\text{red}}\rangle + \langle\delta\Phi_{\text{yellow}}\delta\Phi_{\text{yellow}}\rangle \qquad \text{(D.23)} \\ &= \langle\delta\Phi_{\text{red}}\delta\Phi_{\text{red}}\rangle + \langle\delta\Phi_{\text{yellow}}\delta\Phi_{\text{yellow}}\rangle. \qquad \text{(D.24)}\end{aligned}$$

If the red and yellow arms are of equal length and wire width, then

$$\langle\delta\Phi_{\text{red}}\delta\Phi_{\text{red}}\rangle = \langle\delta\Phi_{\text{yellow}}\delta\Phi_{\text{yellow}}\rangle \tag{D.25}$$

$$\langle\delta\Phi_x\delta\Phi_x\rangle = -2\langle\delta\Phi_{z'}\delta\Phi_x\rangle \text{ and} \tag{D.26}$$

$$S_{\Phi_x} = -2C_{\Phi_{z'}\Phi_x}, \tag{D.27}$$

where in the second line we used Eq. D.22 and Eq. D.24. To summarize the results obtained by assuming the geometric dependence of intrinsic flux noise and symmetric x-loop, we have

$$S_{\Phi_{z'}} = S_{\Phi_{\text{red}}} + S_{\Phi_{\text{blue}}} \tag{D.28}$$

$$S_{\Phi_x} = S_{\Phi_{\text{red}}} + S_{\Phi_{\text{yellow}}} \tag{D.29}$$

$$C_{\Phi_{z'}\Phi_x} = -\frac{1}{2}S_{\Phi_x} \tag{D.30}$$

Combines this with Eq. D.10 and D.12 we get

$$S_{\Phi_z} = S_{\Phi_{z'}} - \frac{1}{2}S_{\Phi_x} = S_{\Phi_{\text{blue}}}, \tag{D.31}$$

$$C_{\Phi_z\Phi_x} = 0. \tag{D.32}$$

Therefore the expected flux noise correlation coefficient c_{zx} is zero, assuming independent and uniform contributions from each superconducting wire segment.